STRUCTURE AND MECHANISM OF A BACTERIAL HOMOLOG OF NEUROTRANSMITTER:SODIUM SYMPORTERS

By

Derek Paul Claxton

Dissertation

Submitted to the Faculty of the

Graduate School of Vanderbilt University

in partial fulfillment of the requirements

for the degree of

DOCTOR OF PHILOSOPHY

in

Molecular Physiology and Biophysics

August, 2010

Nashville, Tennessee

Approved:

Albert H. Beth, Ph.D.

Roger J. Colbran, Ph.D.

Aurelio Galli, Ph.D.

Charles R. Sanders, Ph.D.

Jonathan A. Javitch, M.D., Ph.D.

To my wife Ashley

and

to my parents Windell and Jacqueline

ACKNOWLEDGEMENTS

There are so many things I could say, yet not enough words, to express my sincere gratitude toward those that have contributed to my development as an independent scientist. I wish to thank the National Institute of Neurological Disorders and Stroke for providing me with a pre-doctoral fellowship to financially support the work embodied in this dissertation. I sincerely appreciate the intellectual support and guidance from the members of my dissertation committee: Albert Beth, Roger Colbran, Aurelio Galli, Chuck Sanders and Jonathan A. Javitch. Our conversations stimulated intense thought, creativity and criticisms that are invaluable for a successful career.

I am thankful for the everlasting relationships with each member of the Mchaourab laboratory. My experience at Vanderbilt has been nothing but enjoyable because of our friendships and your willingness to help me and each other. I am especially grateful to Hanane Koteiche for training in molecular biology, and Guangyong Yang and Sanjay Mishra for help in protein expression and purification. I am deeply indebted to my mentor and friend, Hassane, whose passion for life and science knows no bounds.

This work would not be complete without the help and support of our collaborators. Special thanks must be given to Matthias and Fernanda for their efforts in protein expression and functional analysis of an enormous number of mutants. The many conversations with Harel, Lei, Jonathan, Matthias and Hassane will remain engraved permanently in my mind as we labored to uncover this remarkable story. This truly was a memorable journey.

Most importantly, the encouragement and expressed faith from my family, both physical and spiritual, has been unwavering. I have been very fortunate to have wonderful and supportive parents, who graciously implanted the seeds of self-respect, motivation and accomplishment. And I am eternally grateful for the patience, understanding and love from my wife Ashley. This achievement belongs to both of us. Indeed God gives abundantly.

TABLE OF CONTENTS

LIST OF TABLES

Table Page

LIST OF FIGURES

LIST OF ABBREVIATIONS

CNS ..... central nervous system

NSS ..... neurotransmitter sodium:symporter

DAT ..... dopamine transporter

SERT ..... serotonin transporter

NET ..... norepinephrine transporter

GABA ..... gamma-aminobutyric acid

GAT ..... GABA transporter

GlyT ..... glycine transporter

EAAT ..... excitatory amino acid transporter

MPPP 1-methyl-4-phenyl-4-propionoxy-piperidine

MPTP 1-methyl-4-phenyl-1,2,5,6-tetrahydropyridine

MPP^+ 1-methyl-4-phenylpyridinium

VMAT ..... vesicular monoamine transporter

TCA ..... tricyclic antidepressant

SSRI ..... selective serotonin re-uptake inhibitor

MAOI ..... monoamine oxidase inhibitor

TM ..... transmembrane

IL ..... intracellular loop

EL ..... extracellular loop

TMHMM ..... transmembrane hidden Markov model

MTS ..... methanethiosulfonate

PKA ..... protein kinase A

PKC ..... protein kinase

CaMKII ..... Ca^{2+}/calmodulin kinase II

ER ..... endoplasmic reticulum

FRET.....fluorescence resonance energy transfer

CFP ..... cyan fluorescent protein

YFP .....yellow fluorescent protein

LeuT.....leucine transporter

OG..... β-octyl glucoside

DDM ..... *n*-dodecyl-β-D-maltopyranoside

CMI.....clomipramine

SMD..... steered molecular dynamics

EPR ..... electron paramagnetic resonance

NMR ..... nuclear magnetic resonance

CW .....continuous wave

MTSSL.....1-oxyl-2,2,5,5-tetramethylpyrroline-3-methyl)methanethiosulfonate

NiEDDA ..... Ni(II)ethylenediamine diacetic acid

DEER..... double electron electron resonance

S1 ..... primary binding site

S2 .....secondary binding site

SPA ..... scintillation proximity assay

CHAPTER I

STRUCTURE AND FUNCTION OF NEUROTRANSMITTER:SODIUM SYMPORTERS

Physiological significance of neurotransmitter transporters

In the central nervous system (CNS), the termination of neurotransmitter signaling across the chemical synapse is achieved primarily through a high affinity re-uptake mechanism mediated by integral membrane proteins collectively known as neurotransmitter transporters (1). These transporters couple the energy of pre-existing ion gradients to the movement of neurotransmitter from the synaptic cleft to the cytoplasm, thereby controlling the magnitude and duration of post-synaptic receptor stimulation (2). Once in the cytoplasm, neurotransmitter substrates are recycled into vesicular storage compartments (mediated by other specialized transporters), reducing the need for *de novo* transmitter synthesis and preparing the neuron for subsequent rounds of neurotransmitter release (3). Two distinct families of neurotransmitter transporters are responsible for modulating synaptic tone in the CNS, namely the glutamate transporters (SLC1) and the Na^+/Cl^--dependent neurotransmitter transporters (SLC6) (4). These families are distinguished by the transported substrates, protein primary sequence, transport coupling ions and expression sites. The focus of this chapter pertains to the biological significance of Na^+/Cl^--dependent neurotransmitter transporters, although some comparisons will be made with the glutamate transporters.

Biology of neurotransmitter sodium:symporters

The family of Na^+/Cl^--dependent neurotransmitter transporters includes the biogenic monoamine transporters such as those for dopamine (DAT), serotonin (SERT), norepinephrine (NET) and gamma-aminobutyric acid (GABA, GAT) (1). Furthermore, this family includes transporters for amino acids as well as prokaryotic homologs (5). Due to the high intracellular concentration of neurotransmitter relative to the synapse, these transporters and the glutamate

transporters utilize the electrochemical Na^+ gradient established by the plasma membrane ion pump, the Na^+/K^+-ATPase, to catalyze the thermodynamically unfavorable movement of neurotransmitter substrates from the extracellular space into the cytoplasm (6,7). Since the transport of substrate is coupled to the movement of Na^+ ions down their concentration gradient (symport), these secondary active transporters are also known as neurotransmitter:sodium symporters (NSS). In general, substrate transport is strictly coupled to the inwardly directed Na^+ gradient since substitution of this cation with others (e.g. $NMDG^+$, Li^+ or K^+) greatly reduces or eliminates specific transport activity (8,9). Disrupting the physiological Na^+ gradient by elevating the intracellular Na^+ concentration may also inhibit cytoplasmic substrate release from the DAT (8). Glutamate transport is coupled not only to the inwardly directed Na^+ gradient, but to the outwardly directed K^+ gradient as well (10).

Although studies have shown that Cl^- is required for efficient NSS activity, Cl^- may allosterically regulate transport instead of contributing to the energetics of ion-coupled substrate translocation. Indeed the Cl^- equilibrium potential typically approximates the resting membrane potential (-70 mV), conferring little thermodynamic advantage to coupling transport to the Cl^- gradient. However, Cl^- was found to modulate the kinetics of GABA transport by altering the affinity of Na^+ and substrate to the GAT-1 (11). Even though Cl^- associated flux was observed during transport, Cl^- did not contribute to the net charge of a transport event or alter the stoichiometry of Na^+ or GABA. Interestingly, substitution of intracellular Cl^- by $acetate^-$ has been found to reduce the turnover rate of the DAT, suggesting that Cl^- regulates the velocity of DAT turnover (8). Similarly, intracellular Cl^- facilitated serotonin-dependent ionic currents, implying a regulatory role for Cl^- in the transport mechanism of the SERT (12). Some have suggested that Cl^- transport may counterbalance the net positive charge (see below) associated with the coupled translocation of substrate and Na^+, a compensatory mechanism for transport-related membrane depolarization (13,14).

Kinetic experiments indicate that these transporters display variable ion/substrate

stoichiometry associated with transport (9,15). Studies suggest that the DAT and the GAT have an ion-to-substrate stoichiometry of $2Na^+$:$1Cl^-$:1DA(GABA), resulting in electrogenic transport (i.e. possesses a net charge flux) into the cell (9). In contrast, SERT and NET only co-transport one Na^+ and one Cl^- per substrate (15). Additionally, the SERT is also dependent on the efflux of a single K^+ following substrate translocation. Since serotonin is likely to be positively charged at physiological pH, serotonin transport is theoretically electroneutral (1 net positive charge into the cell versus 1 net positive charge out) (16). However, ionic currents mediated by the SERT and other NSS have been observed to exceed (up to 100 fold) the predicted current levels from stoichiometric coupling (17). Electrophysiological experiments have demonstrated that these transporters also possess substrate-induced currents uncoupled from transport and substrate-independent "leak" currents, suggesting that these transporters possess properties of ion channels (12,18-21). A small Cl^- flux not stoichiometrically linked to transport, yet elicited by low dopamine concentrations has been observed for the DAT, a current which may modulate cell excitability (22). Similarly, an uncoupled Cl^- conductance is a feature of glutamate transporters (10,14). These currents may have a significant impact on voltage-dependent events, such as neurotransmitter release and the opening of Ca^{2+} channels. Thus the presence of these currents suggests that neurotransmitter transporters impact the electrical and physiological properties of the neuron besides controlling neurotransmitter homeostasis. Certainly uncoupled currents have led to different hypotheses regarding the mechanism of Na^+-coupled transport, and the corresponding models will be presented later in this chapter.

Regardless of the mechanism of ion/substrate transport, uptake experiments have revealed that NSS display surprisingly slow turnover rates. These transporters typically display turnover rates of 1 to 15 molecules s^{-1}, requiring at least 60 ms for a transporter to bind substrate, release it into the cytoplasm and re-face to the binding-competent configuration (23). In contrast, acetylcholine signal termination by acetylcholinesterase at nicotinic synapses is quite efficient with an observed turnover rate on the order of 10^4 s^{-1} (24,25). Despite slow turnover rates,

neurotransmitter clearance by NSS has been observed to occur within a few milliseconds (23). This rate of clearance necessitates a transporter density at the plasma membrane of about $10^3 \mu m^{-2}$, which has been observed for both the glutamate transporter and NSS systems (26,27). Consistent with electrogenic transport, the uptake velocity is influenced by the plasma membrane potential, emphasizing the thermodynamic dependence of transport on the electrical gradient across the membrane. Indeed, when measured in *Xenopus laevis* oocytes, the DAT uptake velocity increased when the membrane was hyperpolarized and decreased when the membrane was depolarized (21). Although serotonin transport is reportedly electroneutral, an increase in uptake with membrane hyperpolarization has also been observed for the SERT from *Drosophila* heterologously expressed in oocytes (28). Under physiological conditions following an action potential, transient depolarization of the plasma membrane during neurotransmitter release may reduce re-uptake to allow for sufficient interaction of ligands with post-synaptic receptors (29).

Importantly, the brain expression pattern of neurotransmitter transporters provides insight into the tight control of synaptic transmission and the systems that they regulate in the CNS. Expression of the glutamate transporters, or excitatory amino acid transporters (EAATs), such as GLT-1 (EAAT2) and GLAST-1 (EAAT1), has been identified on astroglial cells which surround excitatory synapses (10,30). Other members (EAAT3 and EAAT4) have been observed outside the postsynaptic density on the cell bodies and dendrites where they function to prevent spill-over of glutamate into neighboring synapses (30). EAAT5 is primarily expressed in the retina where it plays a central role in the regulation of glutamatergic signaling and, therefore, visual processing (31). Because glutamate stimulation of postsynaptic AMPA and NMDA receptors can lead to a large Ca^{2+} influx, glutamate transporters are critical regulatory components to prevent excitotoxic cell death. Indeed, these transporters maintain exquisite control of the extracellular glutamate concentration, approximately 100 times less than the EC_{50} of the NMDA receptor (10).

In general, NSS are concentrated on the plasma membrane of presynaptic terminals which synthesize the cognate neurotransmitter, although expression in dendrites and along the

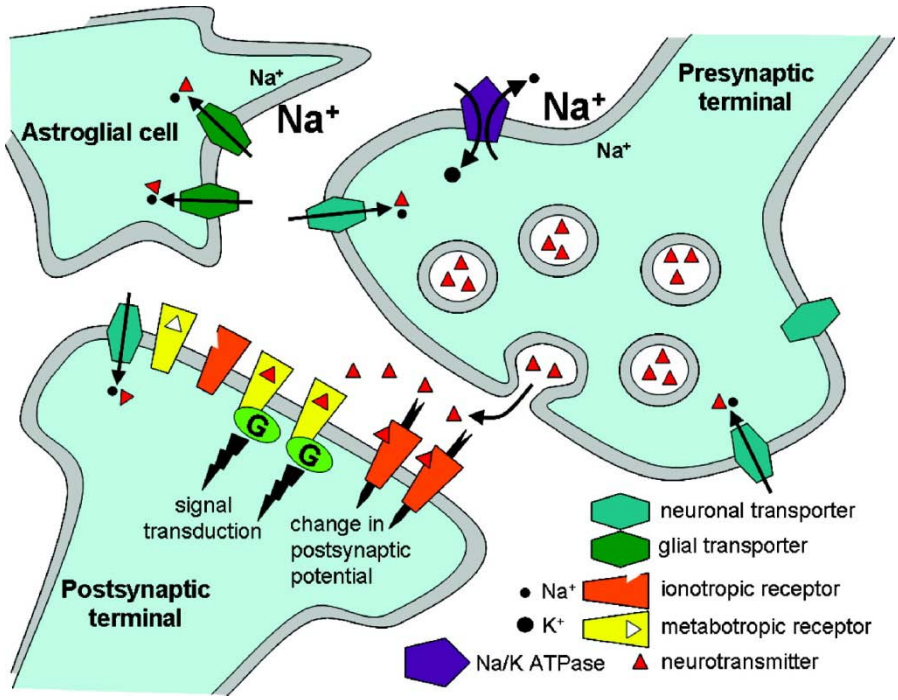

Figure 1. Role and location of neurotransmitter transporters in the synapse. Using the Na^+ gradient established by the Na^+/K^+ ATPase, these transporters catalyze neurotransmitter re-uptake, terminating synaptic transmission. Adopted from Ref 23.

cell soma has been also observed (29). At the synapse, these transporters tend to cluster outside of the active zone in perisynaptic regions along axons (Figure 1). Substantial innervation by dopaminergic and serotonergic neurons have been observed in midbrain regions including the striatum and nucleus accumbens (32-34), brain regions associated with motor control, learning and behavior. Therefore, the DAT and SERT possess critical roles in modulating complex physiological processes such as reward, motivation and locomotion. The regulatory importance of the DAT is highlighted in experiments with mice that lack the DAT gene. Indeed these mice demonstrated hyperlocomotion, which was correlated with an extended lifetime (approximately 100 times longer) of dopamine in the synapse (35). The persistence of dopamine in the synapse also triggered a downregulation of both pre- and postsynaptic receptors, a likely result of excessive receptor stimulation. Since presynaptic autoreceptors control dopamine synthesis and

release (36), a marked decrease in tissue dopamine content was also observed. Similarly, SERT- and NET-deficient mice also demonstrate decreased tissue neurotransmitter content and expression of associated receptors and significantly reduced neurotransmitter re-uptake (37-39), reinforcing the role of these transporters in neurotransmitter and receptor regulation.

Role of NSS in drugs of abuse

Besides controlling fundamental neurochemical signaling events, the NSS are also the sites of illicit drug action. The meperidine analog, 1-methyl-4-phenyl-4-propionoxy-piperidine (MPPP), is a synthetic opioid which produces similar analgesic effects to heroin and morphine (40). In the 1980s, drug addicts began intravenous injections of MPPP, which was unknowingly contaminated with a by-product, 1-methyl-4-phenyl-1,2,5,6-tetrahydropyridine (MPTP), formed during synthesis of the opioid. MPTP is a hydrophobic molecule that can easily pass through the blood-brain barrier. Once taken up by glia, MPTP is rapidly oxidized to the potent neurotoxin 1-methyl-4-phenylpyridinium (MPP^+) by the monoamine oxidase B enzyme (inhibition of this oxidase prevents production of the toxin) (40). MPP^+ inhibits mitochondrial oxidative phosphorylation by interacting with complex I of the electron transport chain leading to ATP depletion and a buildup of reactive oxygen species, triggering apoptotic cell death. MPP^+ specifically targets dopaminergic neurons of the substantia nigra, leading to an identical pattern of cell death observed in Parkinson's disease. Indeed, administration of MPTP resulted in a permanent parkinsonian-like state characterized by immobility and rigidity, which could be treated by therapeutic doses of L-dopa, the precursor of dopamine (41). Various studies have shown that the DAT facilitates entry of MPP^+ into dopaminergic neurons (42). Blockade of the DAT with an antagonist protects these cells from MPP^+ toxicity (40). Furthermore, mice that overexpress the DAT gene are more sensitive to MPP^+, an opposite effect to that observed in DAT-deficient mice (40).

Although MPP^+-induced toxicity may be considered the unintentional result of drug abuse, evidence overwhelmingly supports the notion that the rewarding effects of illicit

psychostimulants, such as cocaine and amphetamine, are mediated directly by NSS as well. Despite fundamentally different modes of interaction, both cocaine and amphetamine increase the extracellular concentration of neurotransmitter by inhibition of NSS, facilitating extended ligand-receptor interactions which are thought to contribute to the reward potential of these psychostimulants, including acute euphoria (43,44). Furthermore, both cocaine and amphetamine induce alterations in transporter trafficking at the plasma membrane, consistent with a dynamic mode of transporter regulation by psychostimulants (45). Certainly changes in trafficking and, therefore, cell surface expression effect overall transport activity by modulating neurotransmitter uptake capacity.

Cocaine is an alkaloid stimulant derived from the coca plant indigenous to South America. According to the 2009 World Drug Report released by the United Nations Office on Drugs and Crime, North America remains the largest world-wide cocaine consumer with estimates of up to 700 metric tons of cocaine having been smuggled into the United States in 2007 (46). Cocaine abuse has been linked to an extensive array of neurological and psychiatric disorders, including reduced cognitive function, psychosis and comorbidity with schizophrenia (44). Depression often occurs following a cocaine binge (47). Although amphetamine or related precursors have been found in several plant species, the drug can be manufactured synthetically (48). The amphetamine derivative methamphetamine can be easily obtained from a one-step reduction of ephedrine or pseudoephedrine, compounds that have been used as nasal decongestants in some over-the-counter drugs (48). Similar to cocaine, a 2008 global assessment indicated that North America remains one of the largest consumers of amphetamine-type substances (49). The stimulant activity of amphetamine has led to an effective treatment of narcolepsy (48). Amphetamine is also used paradoxically in the treatment of attention deficit disorder(50). However, cognitive impairment, hallucinations and psychosis indistinguishable from schizophrenia have been linked to amphetamine abuse (51). These negative effects of illicit drug use ultimately leads to deleterious socioeconomic burdens, such as altered work productivity

and an increased financial weight for proper medical treatment (52).

Cocaine has been shown to interact with the SERT and NET, but studies with genetically modified mice have implicated the DAT as the primary target of cocaine (35). Cocaine behaves as a classical uptake blocker by competitively inhibiting dopamine binding and transport by the DAT (53), resulting in increased dopaminergic neurotransmission. In wild type mice, cocaine administration leads to increased locomotor activity (35), which correlates with movement disorders observed in humans (44). As stated previously, DAT-deficient mice demonstrated a hyperlocomotion phenotype, yet these mice were unresponsive to high doses of cocaine (35). These observations were consistent with a cocaine-induced change in movement activity mediated by the DAT. Interestingly, these DAT-deficient mice exhibit two paradoxical behaviors: 1.) they self-administer cocaine and 2.) demonstrate cocaine-induced conditioned place preference, both of which are classical methods of determining if a drug-exposed animal displays sensitivity to the drug (54,55). These observations suggest that DAT-deficient mice still experience the rewarding effects of cocaine and that the DAT alone does not completely mediate these effects.

Indeed, cocaine was found to bind the SERT in mice lacking the DAT (54), suggesting that serotonergic circuits may be involved in the positive reinforcement of cocaine effects. In support of this, cocaine-induced conditioned place preference is abolished in mice lacking both DAT and SERT (56). Therefore, the neurophysiological effects of cocaine may be topologically diffuse requiring multiple neural pathways. However, the dopaminergic system is likely the chief mediator of cocaine reward since cocaine still increases extracellular dopamine in the nucleus accumbens of DAT-deficient mice (57). The mechanism of increased extracellular dopamine of DAT-deficient mice appears to be dependent on enhanced serotonin sensitivity in the ventral tegmental area, which is not observed in wild type mice (57). While these observations are consistent with the polygenic nature of cocaine reward, they suggest that reward pathways may be modified in genetically altered mice. One study sought to circumvent this potentially

confounding issue by introducing mutations in the DAT that significantly reduced cocaine sensitivity yet retained transport activity (58). These mice that possessed a cocaine-insensitive DAT did not display anatomical changes or altered DAT expression levels compared to wild type mice. Whereas cocaine was found to increase the extracellular dopamine concentration of both wild type and DAT-deficient mice, cocaine did not elevate the dopamine concentration in cocaine-insensitive mice (58). Furthermore, these mice did not develop conditioned place preference for cocaine, but did demonstrate cocaine-dependent *hypolocomotion*. Since cocaine induces hyperlocomotion in wild type animals (35), the authors suggested that, in the absence of cocaine inhibition of the DAT, cocaine may interact with other members of the NSS family (including the SERT) to reduce locomotion (58). Consistent with this hypothesis, cocaine has been found to decrease locomotion in *C. elegans*, a response that required both serotonin and the SERT (59). The results with mice possessing a cocaine-insensitive DAT clearly demonstrate that the cocaine reward pathway is mediated by the dopaminergic system and requires blockade of the DAT.

In contrast to cocaine, voltage-clamp electrophysiology has demonstrated that the presence of extracellular amphetamine or amphetamine-like stimulants (i.e. methamphetamine) elicits a transport-related inward current similar to dopamine mediated by the DAT in *Xenopus laevis* oocytes or HEK-293 cells (8,21,60,61). In addition, this amphetamine-induced current could be blocked with cocaine (8). Biochemical and electrophysiological measurements have clearly shown that apparent amphetamine transport is saturable and dependent on ion gradients (8,62). Collectively, both electrophysiology and biochemical flux assays indicate that amphetamine is a DAT substrate. Therefore, competition of amphetamine with dopamine for binding and transport by the DAT is a likely means of inhibiting dopamine re-uptake. Other experiments have indicated that amphetamine also induces neurotransmitter *release*, or efflux, via the cognate transporters, thereby providing an additional mechanism of increased extracellular neurotransmitter concentrations (35,63-65). For instance, dopamine was readily released from

striatal slices of wild type mice following incubation with amphetamine (35). In contrast, amphetamine-induced dopamine release was absent in DAT-deficient mice, demonstrating that DAT is a required component for enhancing dopaminergic signaling via amphetamine stimulation (35). The exact mechanism by which amphetamine induces a transporter-mediated neurotransmitter efflux is a matter of controversy. Indeed multiple models of reverse transport of the DAT have been proposed, but these models are not necessarily mutually exclusive.

One model envisions the counter transport of dopamine from the cytoplasm with the uptake of extracellular amphetamine. This model, known as facilitated exchange diffusion, predicts that the transport of amphetamine would increase the accessibility of intracellular dopamine binding sites, thereby increasing the probability of intracellular catecholamine binding and subsequent reverse transport (48,66). The model also predicts that, under normal circumstances in the absence of amphetamine, extracellular dopamine could also induce efflux of cytoplasmic dopamine. However, the low concentration of intracellular Na^+ under these conditions decreases the probability of dopamine binding to the intracellular binding sites so that the rate of dopamine uptake is much larger than dopamine release. Indeed, V_{max} for outward transport is less than 20% of V_{max} for inward transport (67). Because amphetamine transport is Na^+ dependent, amphetamine may not only increase the access to intracellular dopamine binding sites, but also significantly increase the local concentration of intracellular Na^+ so as to promote high affinity binding of cytoplasmic dopamine. An amphetamine-dependent increase in cytoplasmic Na^+ concentration has been found to stimulate reverse transport (68).

In contrast to this model, amphetamine does not have to be actively transported to elicit dopamine release. A particular study showed that addition of either dopamine or amphetamine directly to the cytosol, i.e. in the absence of DAT-mediated transport, of the giant dopamine neuron from a pond snail induces dopamine efflux through the DAT (69). This observation suggests that facilitated exchange diffusion cannot explain all aspects of amphetamine-driven dopamine efflux. In 2005, Kahlig and colleagues reported that, under controlled intracellular Na^+

concentrations, amphetamine causes reverse dopamine transport by a slow, transporter-like mode and a fast (millisecond), channel-like mode (70). Although the slow process is consistent with the facilitated exchange diffusion model, the channel-like mode released a "burst" of dopamine similar to that observed with normal vesicular release during an action potential. Even though dopamine has also been shown to elicit efflux (67,71), the channel-like mode of the DAT is inhibited in the presence of dopamine or cocaine, suggesting that dopamine-induced efflux proceeds through the transporter-like mode of the DAT (70). The intrinsic difference between the DAT substrates to induce different modes of dopamine release is not known, but may be related to altered intracellular signaling events and protein-protein interactions discussed later in the chapter.

The effects of amphetamine on the activity of the DAT may be further exacerbated by the intracellular action of amphetamine on vesicular stores of dopamine. Dopamine and other catecholamines are actively removed from the cytosol into acidic storage compartments by the vesicular monoamine transporters (VMATs) (3). The VMATs utilize an outwardly-directed proton gradient to concentrate monoamines into the vesicles up to 100,000 fold relative to the cytosol (48). Two modes of amphetamine interaction with these vesicular pools have been shown to increase cytosolic neurotransmitter concentrations. The membrane-permeable nature of amphetamine allows it to penetrate these synaptic vesicles. Once inside the acidic compartment, the weak base potential of amphetamine collapses the pH gradient required for monoamine transport (72). The presence of amphetamine has been shown to decrease the quantal size vesicular dopamine release in PC12 cells by more than 50%, consistent with a decreased number of stored dopamine molecules (69). However, the stereospecificity of the amphetamine effect at the vesicles suggests a more direct interaction with specific vesicular components, such as the VMATs. Indeed, the *S(+)* –isomer of amphetamine is more effective at releasing monoamine stores than the *R(-)* –isomer, and the *S(+)* –isomer binds preferentially to the VMAT (73). This may suggest that amphetamine is a substrate for VMAT and may induce exchange diffusion,

ultimately increasing the concentration of cytosolic neurotransmitter concentrations and the efflux potential.

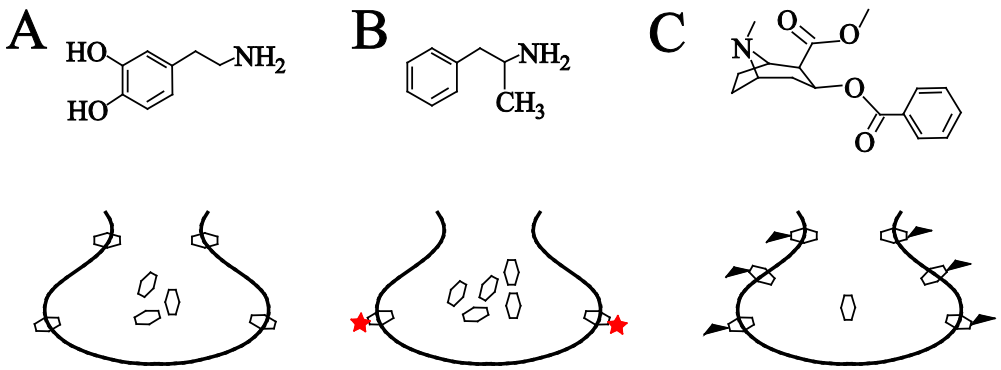

Figure 2. Illicit drug regulation of cell surface expression. (**A**) Normal physiological expression of the DAT. (**B**) Amphetamine causes acute internalization of the DAT, decreasing transport capacity. (**C**) Cocaine, a potent uptake blocker, elicits an upregulation of surface expression. The illustration was inspired from Ref 75.

The normal constitutive internalization and recycling of transporters to the plasma membrane are also altered in the presence of either cocaine or amphetamine (Figure 2). Cocaine has been found to increase the number of functional DATs at the cell membrane. For instance, after incubation with cocaine and subsequent washout, dopamine uptake (V_{max}) increased without a change in K_m (74). These changes correlated with an increase in cell surface expression of the DAT measured by biotinylation, which facilitated an increased uptake. In contrast to cocaine, amphetamine has been shown to have the opposite effect on members of NSS, i.e. a decrease in cell surface expression. A decrease in V_{max} has been observed for both DAT and SERT, consistent with a decrease in the number of functional transporters at the cell surface (61,75,76). A combination of electrophysiology and confocal microscopy has shown that amphetamine-induced internalization of functional DATs is likely to be a clathrin-dependent mechanism that is inhibited by DAT blockers such as cocaine (77). Analysis of a transport deficient DAT mutant indicates

that this process of transporter redistribution appears to be dependent on the increase of the cytosolic amphetamine (78). The means by which these psychostimulants mediate such a dynamic mode of transporter regulation is not entirely clear, but may be tied to extensive autoreceptor stimulation and/or intracellular signaling events and protein-protein interactions addressed in subsequent sections of this chapter.

Pharmacological inhibitors

The neuropsychological effects of cocaine and amphetamine abuse briefly mentioned above, including induced depression, indicates that dysfunction of the associated neurotransmitter systems may underlie the development of severe psychiatric disorders. Indeed, symptoms of major depression such as alterations in mood, appetite, sleep behaviors and suicidal thoughts appear to be linked to dopaminergic, serotonergic and noradrenergic circuits (79). Positron emission tomography of individuals with major depression (not drug induced) has indicated a reduced number of DAT and SERT binding sites (80,81). Coinciding with this observation is a decrease in both serotonin and tryptophan (the serotonin precursor) concentrations, suggesting vast physiological changes associated with major depression (82). SERT knockout mice demonstrate increased anxiety and stress under basal conditions (83).

It is now accepted that both environmental and genetic factors contribute to the development of major depression. In contrast to SERT knockout mice, NET deficient mice have been shown to be resistant to depressive-like behaviors as a result of chronic physical stressors, perhaps through enhanced serotonergic signaling mediated by norepinephrine stimulation of α_1-adrenoreceptors (84). Interestingly, this particular study suggested that noradrenergic pathways are connected to changes in downstream biochemical events such as the regulated expression of brain neurotrophins. Under chronic stress conditions, a downregulation of neurotrophins occur and may be linked to the onset of stress-induced depression. The propensity for genetic factors to influence depressive symptoms is highlighted by functional polymorphisms of the human SERT gene that reduce transcriptional efficiency and increase susceptibility to depression (85).

In addition, the neural connections made between the midbrain and other brain regions often result in the onset of other psychosomatic symptoms. For instance, these neurons project from the midbrain by frontostriatal circuits to the medial prefrontal cortex, the region of advanced cognitive processes such as decision making, where they converge with noradrenergic projections arising from the locus coeruleus of the brain stem (81,86). Patients with major depression or other disorders, such as Huntington's disease (characterized by atrophy of the striatum), demonstrate deficits in executive functions such as attention and planning (81). Furthermore, due to the strong correlation of cognitive impairment with reduced blood flow in the medial prefrontal cortex, low blood perfusion has been suggested to be a hallmark of individuals with major depression (81).

Perhaps the most convincing evidence of the involvement of dopamine, norepinephrine and serotonin in the pathophysiology of major depression is the pharmacology of antidepressants. Similar to NET knockout mice, wild type mice treated with antidepressants prevent depressive-like behaviors and blocked the downregulation of neurotrophic factors (84). Although the modes of action of some antidepressants are not known, several classes of antidepressant drugs have been developed that target specific proteins, including tricyclic antidepressants (TCAs), selective serotonin re-uptake inhibitors (SSRIs) and monoamine oxidase inhibitors (MAOIs). Free cytosolic monoamine transmitters are either transported by VMATs into synaptic vesicles (as described previously) or metabolized by a monoamine oxidase (82). The net effect of MAOIs is an increased concentration of cytosolic serotonin and a shift in the flux of serotonin toward vesicular repackaging. TCAs, such as clomipramine, imipramine and desipramine, act by competitively binding with nanomolar affinity to NSS (87), thereby increasing synaptic neurotransmitter concentrations and postsynaptic receptor stimulation. Interestingly, administration of TCAs to depressed individuals was found to increase blood perfusion in the medial prefrontal cortex, an area in which the NET is fundamental to removing both norepinephrine and dopamine from the synaptic cleft (81,86). However, potent side effects of both MAOIs and TCAs including sedation and orthostatic hypotension provided a driving force

for the development of novel efficacious drugs, such as the SSRIs (79,88,89).

Whereas TCAs are indiscriminate towards inhibition of transporters, the SSRIs such as fluoxetine—marketed as Prozac—more specifically target the SERT, but will bind to the DAT and NET with lower affinity (90). Unfortunately, these inhibitors take several weeks *in vivo* to produce an antidepressant effect, which may be related to the process of serotonin autoreceptor desensitization (83). That is, autoreceptor stimulation provides negative feedback towards inhibiting further neurotransmitter release. The autoreceptor inhibitory effect was found to be attenuated after 14 days of SSRI treatment. This suggests that an adaptive response facilitates the mechanism of SSRI antidepressant action. Furthermore, a significant fraction (~30%) of depressed individuals do not respond to SSRIs and those that do respond deal with multiple side effects such as nausea and sexual dysfunction (79). Due to these observations, one approach may be to employ the synergistic activity of a combination of a specific transport inhibitor and autoreceptor antagonist to facilitate therapeutic inhibition on a shorter temporal scale (79). The promiscuity of SSRIs at higher dosages is also a clear indicator that more work is required to develop faster acting, highly specific drugs to combat major depression and associated debilitating symptoms. Indeed, an SSRI can become a higher affinity inhibitor of the NET with changes to one or two functional groups (91).

To accomplish this task, a fundamental understanding of transporter structure and the relationship of structure to functional activity is required. A detailed structural analysis provides essential information regarding the organization of the polypeptide chain within the context of a lipid bilayer and the orientation of specific components, such as loops, N- and C-termini. How are these components utilized in the functional cycle? A number of studies suggest that posttranslational modifications and protein-protein interactions that involve loop segments or both N- and C-termini are critical for transporter activity and membrane targeting. Furthermore, where are the ligand binding sites relative to inhibitor binding sites? What are the molecular determinates of substrate and inhibitor binding specificity? How does the binding of inhibitors

impact the structure of the transporter? The answers to these questions and others are crucial to the development of models that capture the structure/function relationship as well as to the rational design of specific, highly efficacious inhibitors (91). As discussed below, it is clear that the structure of these transporters not only plays a pivotal role in NSS membrane targeting and transport efficiency, but also regulates efflux and facilitates autoreceptor interaction.

Molecular structure and organization

The GABA transporter from rat brain was the first NSS family member to be cloned (92). The primary sequence suggested a protein of 599 amino acids. Subsequent cloning of the NET, DAT and SERT revealed proteins of similar lengths (617, 620 and 630 amino acids, respectively) (93-95). BLAST analysis of the human GAT primary sequence against those of the NET, SERT and DAT reveals a substantial amount of sequence conservation (42-45% identity). Sequence identity approaches 50% between the SERT and DAT proteins. In particular, the highest degree of conservation occurs in the transmembrane (TM) region, but the most divergence is observed at the variable length N- and C-termini (5). Hydrophobicity analysis has predicted that these polytopic membrane proteins possess 12 TM segments with cytoplasmic N- and C-termini (94). For example, the hydropathy profile of the human DAT primary sequence generated from the Kyte-Doolittle method (96) is plotted in Figure 3A, suggesting the presence of 12 membrane-spanning segments. It has been shown by von Heijne that the distribution of positively charged residues also impacts the topological orientation of the polypeptide chain in the bilayer (97). The results from another topology predicting program that incorporates hydrophobicity, charge bias and other variables, the transmembrane hidden Markov model (TMHMM) (98), is also shown in Figure 3B that illustrates the probable location of TM segments, loop regions and orientation. In addition to the TM segments, a large extracellular loop is predicted between TM3 and TM4 that contains a variable number of *N*-glycosylation sites. Given significant sequence similarity, all NSS are predicted to share a similar topology in which the TM segments form α-helices as

illustrated by the model in Figure 3C.

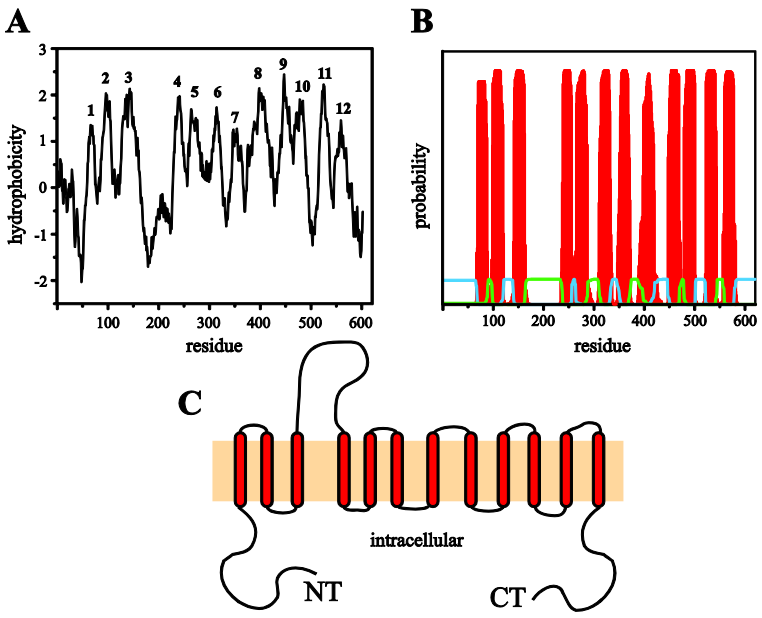

Figure 3. Topology of NSS. Kyte-Doolittle (**A**) and TMHMM (**B**) sequence analysis of the human DAT suggests 12 membrane spanning regions. Predicted transmembrane segments (red) are separated by extracellular (green line) and intracellular (blue line) loops shown in (**B**). Thus, NSS family members are expected to display a membrane topology similar to that shown in (**C**).

Experimental validation of this predicted model is necessary for proper assignment of functionally relevant residues. In the absence of crystallographic evidence, indirect methods have been used to investigate the topological organization at low resolution. All data collected to date support a 12 TM topology with intracellular termini. Immunofluorescence of the NET was observed for polyclonal antibodies of the N- and C-termini only in permeabilized COS-7 cells expressing the NET, consistent with a cytoplasmic location for these termini (99). Using monoclonal DAT antibodies, immunogold electron microscopy indicated that the N-terminus was found in the cytoplasm (100). Bennett and Kanner found that all three naturally occurring *N*-glycosylation sites in the GAT are utilized in the predicted loop between TM3 and TM4, which

argues for an extracellular location (101). Similarly, limited trypsin proteolysis and photolabeled fragments suggested that the *N*-glycosylation sites of the DAT are located between TM3 and TM4 (102). Furthermore, enzymatic treatment of the glycosylated DAT with *N*-glycanase and neuraminidase indicated that N-linked oligosaccharides and sialic acids are attached to these sites.

Despite this agreement, the specific location of some loops and transmembrane segments has been controversial. Two groups investigating the topology of either the GAT or GlyT (glycine transporter) using introduced *N*-glycosylation sites suggested that the topology of the first one third of the protein is different from theoretical predictions (101,103). Based on glycosylation of the first predicted intracellular loop (IL) and lack of glycosylation of the first predicted extracellular loop (EL), alternative models were proposed. In this model, EL1 was placed intracellularly and IL1 was placed extracellularly and the first predicted TM segment does not completely cross the membrane. In addition, TM3 either transverses the membrane twice or forces a string of hydrophobic amino acids into the extracellular milieu. However, the introduction of new glycosylation sites may significantly alter the natural structure of the transporters. Consistent with this notion, the insertion mutations in IL1 of either the GlyT or the GAT greatly reduced or eliminated functional activity. Furthermore, it was suggested that the lack of glycosylation in EL1 in the GlyT may be due to steric factors.

A number of studies contradict this alternative model and support the original topological model. Small cysteine-modifying reagents have been used to increase the sensitivity of measurements designed to probe potentially restricted areas without significant structural perturbation. For example highly conserved cysteine residues in the DAT displayed reactivity with small polar derivatives of methanethiosulfonate (MTS) (104). The endogenous Cys-90 found in the first predicted extracellular loop demonstrated fast reactivity similar to the extracellular loop residue Cys-306 between TM5 and TM6 in both membrane preparations and intact cells. In contrast with the glycosylation studies mentioned above, similar results have been obtained at the site analogous to Cys-90 in the GAT (105). Moreover, the reactivity of the conserved Cys-135,

predicted to be found in IL1, was reduced in cells compared with membranes (104). These results did not agree with the alternative topology proposed for the GAT and GlyT based on inserted glycosylation sites. In addition, reactivity studies with the SERT indicated that Cys-109 predicted to be in EL1 could be biotinylated with MTS derivatives, although alanine mutagenesis prevented biotinylation (106). Collectively, these data suggest that the topology of both the DAT and SERT, and likely all NSS, agree with the original model of TM organization.

Impact of structural elements on NSS regulation

Specific sites within structural elements of the NSS appear to influence the regulated trafficking of transporter to the plasma membrane, as well as impact functional activity. Although the DAT possesses 13 cysteine residues, a pair of cysteines (Cys-180 and Cys-189) in the large extracellular loop between TM3 and TM4 impacts plasma membrane expression (107). Mutation of these cysteines to alanine prevented the DAT from reaching the membrane surface, eliminating all functional activity. These two highly conserved residues map to Cys-200 and Cys-209 in the SERT. Mutagenesis studies of these two cysteines increased the K_m and decreased the V_{max} (75-85% relative to wild type), reflecting a substantial reduction transport capacity (106). By comparison, mutation of another cysteine in EL1 did not alter transport activity. The altered activity of the EL2 mutants was found to be due to reduced cell surface expression and a lower intrinsic activity of the mutant SERT. Interestingly, mutation of Cys-200 to serine increased the reactivity of SERT to MTS reagents, which is reversed in the double mutant C200S/C209S (106). These observations suggested that these two cysteine residues form a disulfide bond in EL2, and may play a role in the Na^+-dependent activity of SERT transport. The conservation of these cysteines in other transporters implicates a role of disulfide bond formation in the DAT and NET as well.

The attachment of sugar moieties to proteins have been shown to affect protein folding, targeting, and functional activity (108). The *N*-glycosylation sites found in the NSS appear to have a pivotal role on the overall activity of the transporters. Studies with the GlyT, DAT and

SERT emphasize the effect of enzymatically removing oligosaccharides or preventing the posttranslational modification via site directed mutagenesis. Approximately 30% of the molecular mass of the GlyT can be attributed to sugar chains, which may be the result of modification of all four asparagine sites in EL2 (109). Mutagenesis of all four sites results in a 65% decrease in transport activity characterized by a decrease in V_{max}, although K_m appeared unchanged. A combination of cell surface biotinylation and immunofluorescence suggested that the reduction in transport velocity can be attributed to a decrease in cell surface expression (110). Therefore, glycosylation appears to be required for efficient targeting of the GlyT, although not absolutely required for function. Interestingly, a previous study of the GlyT reconstituted into proteoliposomes demonstrated a ~75% decrease in transport after a five hour incubation with peptide-*N*-glycosidase F, but no changes were observed with other glycosylation enzymes (109). Although the experiments could not identify if sugar modification altered the structure of the protein or if the sugar moiety interacted with the binding site, this result seems to suggest that glycosylation may impact intrinsic functional activity and not just plasma membrane expression.

A similar observation with the SERT has been reported when insect cells were treated enzymatically to remove the endogenous sugars or in a Asn/Gln mutant that eliminates modification at both glycosylation sites (111). Addition of tunicamycin to Sf9 cells expressing wild type SERT decreased the total ligand binding without changing the K_D. In addition, site directed mutagenesis of both glycosylation sites did not change the K_D relative to wild type, but a decrease in ligand binding mirrored a decrease in total protein expression at the membrane. Transport kinetics also reflected a net decrease in transport velocity without a change in the apparent dissociation constant. In case of the DAT, cell surface biotinylation and confocal microscopy indicated a reduced surface expression of unglycosylated DAT resulting in a reduced V_{max}, but also reduced total protein content (112). More immunofluorescence was also found in the cytosol of mutant DAT than at the plasma membrane, which was correlated with enhanced internalization. Collectively, *N*-glycosylation is not an absolute requirement for either catalytic

activity or plasma membrane expression since unglycosylated forms of the NSS are present to some degree at the membrane and transport substrate. In fact, removal of one glycosylation site in the SERT reduces plasma membrane expression, but not to the same extent as removal of both sites (111). Therefore, the emerging theme is that catalytic activity is impaired relative to fully glycosylated wild type, likely due to a reduced stability at the membrane surface.

Activity at the N-terminus of these transporters may also play a role in transporter regulation through second messengers. The N-terminus of NSS possesses several consensus phosphorylation sites for different protein kinases, including PKA, PKC and Ca^{2+}/calmodulin-dependent protein kinase (113). Pharmacological stimulation of DAT activity through activation of adenylate cyclase has been shown to be reduced to basal levels by the presence of a specific PKA inhibitor (114). In this study, PKA stimulated an increase in uptake velocity without altering the affinity for substrate, and led to the hypothesis that an increase of DAT density at the plasma membrane may mediate these affects. However, it was not clear from this study if PKA stimulation of the DAT was directly due to DAT phosphorylation. Although PKA activation increased the phosphorylation of the SERT, it has been shown that the DAT phosphorylation state is not affected by PKA (113).

In contrast, phosphorylation of the DAT N-terminus has been shown to be PKC dependent. Foster and colleagues recently demonstrated through peptide mapping and epitope-specific immunoprecipitation that the N-terminus of DAT is phosphorylated by PKC at serine residues in the rat striatum (115). Basal phosphorylation was increased in a dose-dependent manner with treatment of PKC activators. This effect was also blocked in the presence of PKC inhibitors. In contrast to PKA, activation of PKC reduces transport V_{max}, although K_m is unaffected, and therefore may have an opposite effect on cell surface expression (113). Indeed, PKC activation also leads to a decrease in uptake velocity of the SERT, but biotinylation/immunoblot analysis suggested that the reduction in V_{max} was due to a redistribution of SERT away from the cell surface (116). Daniels and Amara have shown that the PKC-driven

process of DAT internalization is mediated by clathrin and the GTPase dynamin (117). However, site directed mutagenesis of the consensus PKC phosphorylation sites which prevented PKC phosphorylation did not inhibit PKC-induced internalization (118), suggesting that N-terminal phosphorylation is not required for transporter trafficking and that other mechanism(s) are employed.

It has been suggested that the phosphorylation-dependent regulation of the DAT may be coupled with D_2 pre-synaptic autoreceptor activity (113). Activation of these dopamine autoreceptors has been shown to inhibit PKC activity (119). Thus, the de-activation of the PKC pathway would have stimulatory effect on dopamine transport. Under normal physiological conditions, these pre-synaptic receptors are activated by dopamine in the synapse followed by vesicular release to inhibit further synthesis and release of neurotransmitter (36). The application of a D_2 autoreceptor agonist or antagonist has been shown to either increase or reduce, respectively, DAT activity (29). The mechanism of D_2 autoreceptor regulation has been proposed to involve either changes in membrane polarization or $G_{i/o}$ protein-coupled pathways (21,120). Inwardly rectifying K^+ channels, which hyperpolarize the neuron, are coupled to D_2 autoreceptors (120), which may lead to an increase in DAT activity (see page 4). However, under voltage clamp conditions, dopamine stimulation of the D_2 autoreceptor increased DAT activity by ~70%, which is inconsistent with a voltage-dependent process (120). Instead, the increase in transporter uptake velocity was attributed to an increase in DAT cell surface expression which was sensitive to pertussis toxin treatment, implicating a role for G protein activation and second messenger signaling. These results have been confirmed using a fluorescent MPP^+ analog, ASP^+, as a DAT substrate together with a D_2 autoreceptor agonist (121,122). Furthermore, flow cytometry was used to show that D_2 autoreceptor activation increases DAT surface expression.

The relationship of the D_2 autoreceptor with the DAT was explored further by co-immunoprecipitation and *in vitro* binding assays elegantly demonstrating that the DAT N-terminus directly interacted with the D_2 autoreceptor (123). This physical interaction facilitated

the increased surface expression of the DAT (~20%) and disruption of the interaction resulted in hyperlocomotion in mice similar to the DAT knockout. The D_2 autoreceptor regulation of the DAT may provide a mechanism whereby cocaine increases DAT surface expression. Addition of a D_2 receptor antagonist prevented cocaine-induced DAT up-regulation (29). As a classic uptake blocker, cocaine would not only enhance post-synaptic receptor stimulation, but also D_2 autoreceptor stimulation which leads to an increase in cell surface expression and an increase in transport capacity (see page 12).

The neurotransmitter stimulation of pre-synaptic receptors appears to extend beyond the D_2 autoreceptor. Indeed, D_3 autoreceptors have been shown to modulate dopamine uptake. Because of this observation, autoreceptor regulation of the DAT is confounded by the effects of the mutual response of different pre-synaptic autoreceptors. This requires experimentation in the absence of one or the other autoreceptor to directly determine the specific modulating effects of an individual receptor. Recently, Zapata and colleagues examined the effect of a D_2/D_3 receptor agonist in the absence of intrinsic D_2 receptors and found that D_3 receptor stimulation increased the uptake of the DAT substrate ASP^+ (124). This effect was sensitive to pertussis toxin, again implicating a G protein pathway that proceeded through the MAPK and PI3K pathway. Furthermore, stimulation of the D_3 autoreceptor led to an increase in DAT surface expression. The similarity of these results with those of the D_2 autoreceptors described above may suggest that the observations accompanying supposed D_2 autoreceptor stimulation actually result from D_3 autoreceptor activation. In fact, the D_2 autoreceptor studies used dopamine as a substrate and the effect of D_3 stimulation was not investigated (120). Furthermore, the observation that the D_2 receptor directly interacts with the DAT N-terminus to facilitate increased uptake velocity is fundamentally different from that observed with the D_3 receptor. Indeed, the DAT N-terminus is not required for D_3 receptor modulation of the DAT transport activity (124).

The N-terminus of the NSS is also the site of other protein-protein interactions that alters functional activity. The soluble N-ethylmaleimide-sensitive factor attachment protein receptor

(SNARE) syntaxin 1A has been shown to interact with the N-terminus of the GAT, SERT and NET (125-127). Importantly, the binding of syntaxin to the DAT N-terminus is a critical component of amphetamine-induced dopamine efflux (128). Interestingly, this interaction is facilitated by Ca^{2+}/calmodulin kinase II (CaMKII) activity, an observation also reported for the SERT (129). In fact, it has been shown that CaMKII directly binds to the DAT C-terminus which facilitates N-terminal phosphorylation of serines in order for amphetamine to induce reverse transport of the DAT (130). Mutation of the DAT C-terminus or the N-terminal serine residues significantly impaired dopamine efflux. N-terminal phosphorylation was suggested to shift the DAT from a "reluctant" state to a "willing" state for dopamine efflux (131), indicating that phosphorylation may alter the conformation of the DAT. The effect of CaMKII suggests that increased intracellular Ca^{2+} concentrations play a role in amphetamine action. Indeed, amphetamine treatment led to an increase in cytoplasmic Ca^{2+} concentrations and efflux was dependent on this change (132). Because amphetamine transport increases the intracellular Na^{+} concentration, the associated membrane depolarization may open voltage gated Ca^{2+} channels leading to an influx of Ca^{2+} and subsequent activation of CaMKII.

The C-terminus is not only important in amphetamine-induced efflux, but is also a vital component of export from the endoplasmic reticulum (ER). Fluorescence microscopy and cell surface biotinylation experiments have suggested that tafficking to the plasma membrane is impaired in a DAT mutant in which the last five C-terminal residues were deleted (133). In more rigorous experiments, site directed mutagenesis of three critical residues in the C-terminus resulted in significant retention in the ER, including mutation of a highly conserved Gly residue that completely abrogated plasma membrane expression (134). Specific residues in the C-terminus of the GAT appear to influence ER export to the cell surface (135). Thus, the data suggests that an intact C-terminus is required for export from the ER and targeting to the plasma membrane. Interestingly, when wild type DAT is co-expressed with trafficking-deficient DAT mutants, plasma membrane expression is still impaired (133). This observation suggests that these

transporters may form oligomeric structures during biogenesis, which may be maintained during export to the membrane.

Oligomeric architecture of NSS

The propensity of NSS to form oligomeric structures has been investigated by both biochemical and spectroscopic approaches. Expression of two SERT constructs each containing a different epitope tag have subsequently been co-immunoprecipitated using an antibody for one construct (136). Although both constructs were functionally active, reactivity with a Cys-sensitive MTS reagent de-activated only one of the constructs, suggesting the presence of at least a SERT dimer. This oligomeric association was observed at the plasma membrane as well as in cytosolic compartments. In support of these results, fluorescence resonance energy transfer (FRET), which measures distance-dependent interaction between fluorophores, was observed in the plasma membrane of cells co-expressing functional SERTs or GATs fused with either cyan or yellow fluorescent protein (137,138). In contrast, no FRET was observed in cells expressing only a single construct.

The nature of the FRET experiment in cells does not allow for unambiguous determination of interfaces due to the large range of distances FRET can be observed (typically <100Å), as well as the large size of the fused domains. Furthermore, the interpretation of FRET is complicated by the expression of the acceptor construct, which may lead to errors in assessing direct interaction between donor/acceptor pairs (139). Due to transporter overexpression, it is unlikely that FRET observed between the constructs is the result of non-interacting monomers over a large distance (<100Å), although it is theoretically possible that overexpression leads to non-specific FRET (138). Ideally, calculation of the FRET efficiency, which displays r^{-6} sensitivity (where r is the distance), in dilute solution would be used to determine a unique distance between the fluorophores, assuming the relative orientation of the fluorophores is known (140). This would require a homogeneous purification of the transporter to remove other associated proteins and non-specific interactions that may confound results, assuming that the

purification process does not disrupt the interface or native structure of individual monomers (136). However, the structural components that form the interface(s) may be approximated, albeit at low resolution, by assessing FRET under conditions that may alter the oligomeric state of the transporter.

For example, the primary sequence of the GAT suggested the possibility of a Leu heptad repeat in TM2, possibly forming a hydrophobic "Leu zipper" similar to that observed by dimeric soluble proteins (138). Site directed mutagenesis of this repeat resulted in a loss of FRET and reduced cell surface expression. Because the mutations only modestly affected the kinetics of transport, the transporter was not likely to be grossly misfolded. The data suggested that the GAT naturally forms at least a dimer at the interface of TM2. By measuring donor photobleaching lifetimes between CFP and YFP, Just et al determined that the C-termini of oligomeric SERT were closer together than the N-termini, suggesting that the C-terminal domain may form part of an interface between SERT monomers (141). This is consistent with the data discussed above for the DAT in which an intact C-terminus is required for export from the ER. Furthermore, a peptide fragment consisting of TM11 and TM12 demonstrated a strong association with itself and, when expressed in the presence of full-length transporter, prevented cell surface expression (141). The data implied that an oligomeric interface was formed between TM11, TM12 and the C-terminus of SERT monomers. Although the SERT does not have the same potential to form a perfect "Leu zipper", the association of a peptide fragment constructed of TM1 and TM2 suggested the formation of an interface near the N-terminus similar to that observed with TM2 of the GAT (141). Collectively, the FRET analysis suggested the presence of two interfaces arising from structural components at the N- and C-termini of the SERT.

Besides FRET, cysteine crosslinking experiments have suggested possible locations for symmetric interfaces in an oligomeric assembly. A dimerization motif GXXXG, originally identified in glycophorin A, was found in TM6 of the DAT (142). Treatment with copper phenanthroline induced crosslinking at Cys-306, which was prevented by site directed alanine

mutagenesis. Co-immunoprecipitation of differently epitope-tagged, crosslinked DAT suggested that the DAT forms at least a dimer. In contrast, an interface was not observed at TM6 in the SERT although it possesses this same motif (141). Subsequent crosslinking analysis of DAT with $CuSO_4$ indicated that TM4 may also reside at a dimer interface distinct from TM6, indicating that DAT forms higher order oligomers at the plasma membrane (143). Recently, a combination of cysteine crosslinking and FRET microscopy was used to show that the GlyT forms a dimer at the plasma membrane and that mutation of a Trp residue at the interface results in intracellular retention of the transporter (144).

Although it is difficult to interpret these results in the absence of atomic resolution structures, taken together the observations clearly indicate that these transporters possess a propensity for oligomer formation even during biogenesis at the ER and that oligomer formation plays a role in plasma membrane targeting. The apparent role of an intact C-terminus in ER egress and the finding that the C-termini are likely to be close together in the oligomer suggest the possibility that export signals are employed in membrane targeting. PICK1, a protein containing a PDZ domain which may be important in plasma membrane targeting, interacts with the DAT C-terminus (145,146). Deletion of five amino acids in the C-terminus of the DAT removed a PDZ interaction domain and resulted in cytoplasmic retention (133). Oligomerization may also hide selective retention signals, such as in the case of the NR-1 subunit of the NMDA receptor (147). The interface formed by the C-terminus may also bring ER export signals together, as proposed for the GAT, which would recruit proteins involved in COPII-dependent vesicle budding from the ER (147). It is also likely that other structural elements are required to promote oligomeric assembly and subsequent ER export. Sialylated N-glycans have been shown to promote oligomeric interactions of the SERT and impact functional activity (148).

Recently, it has been proposed that the oligomeric structure of these transporters may facilitate amphetamine-induced efflux (149). A major pitfall of the facilitated exchange diffusion model (described on page 10) is that any substrate, including the biogenic monoamines, is

predicted to induce efflux, creating the potential for a futile transport cycle (67). That is, the increase in local Na^+ concentration would increase the potential that substrates would be "trapped" in an exchange state resulting in no net flux, yet this phenomenon has not been observed *in vivo*. Furthermore, Zn^{2+} binding noncompetitively inhibits dopamine transport, but stimulates amphetamine-induced dopamine efflux (150), an observation difficult to reconcile with a coupled inward/outward substrate transport mechanism. In an oligomeric complex, amphetamine transport by one monomeric unit would trigger the release of cytosolic substrate through the other unit. This mechanism may be consistent with the observed "burst" of dopamine released by the DAT in a channel mode following treatment with amphetamine (70). This mechanism has also been used to explain the observation that the SERT-specific para-chloroamphetamine induced GABA efflux in a SERT-GAT concatemer (149).

The mechanism of transport

From the preceding section, it is clear that structural elements of the NSS are critical components to the overall functionality and regulation of the transporters. However, it is not clear how structural elements are coordinated in a transport mechanism. These transporters form oligomeric complexes as indicated above, but it is not known if or how these interactions affect crosstalk or the activity of pharmacological ligands on individual monomers. Besides membrane targeting, oligomeric interactions may provide a means by which the density of transporters at the synapse can be achieved through ordered arrays leading to efficient spatial and temporal control of synaptic signaling (23). At an even more fundamental level, the absence of three dimensional structural information precludes clear mechanistic treatment of how the structure of transporters facilitate ion/substrate coupling. In addition, the presence of thermodynamically uncoupled currents (see page 3) adds an additional level of difficulty in determining a unique mechanism of transporter functionality. As will be described in the subsequent section, attempting to merge limited structural information with an enormous pool of functional data into a uniform

mechanism is a daunting task. Nevertheless, two models of transporter function have been proposed, single file diffusion and alternating access, which capture specific aspects of known activity. Although it cannot explain all aspects of transport activity, most functional and indirect structural data are interpreted in the context of the alternating access mechanism. However, it must be emphasized that only a superficial treatment of these models should be considered until high resolution tertiary and quaternary structural information is obtained.

Single file diffusion

The movement of ions and substrate into the cell via the NSS has been observed through both biochemical flux assays and measurements of transporter-mediated currents (8,15). The origin of the electrical current is presumably associated with the charge flux of the transported species. Assuming that strict coupling between ions and substrate gives rise to stoichiometric transport, one can estimate the size of the electrical current expected for each transport cycle. However, the size of the observed currents can be several times larger than calculated (151). This is clearly the case in the SERT in which transport is predicted to be electroneutral (no net current flow), but the charge:serotonin ratio is approximately eight on average (20). Increasing the substrate concentration also increases the conductance, suggesting that more ions flow through the transporter per substrate (152). These observations and others led to the proposal that the NSS proteins have the propensity to function as channels.

A generalized single file diffusion model mechanism borrows from the theory of ion channel activity (12,153). In this mechanism, ions and substrate traverse a pore opened to both the cytoplasm and extracellular solution in which ion/substrate interactions within the pore result in coupling. The inwardly-directed Na^+ gradient is primarily responsible for "pushing" substrate into the cytoplasm against a substrate gradient. One version of this model developed by Su and colleagues focused on the coupling interactions attributed to attraction and repulsion of ions and substrates hopping at specific rates between distinct binding sites within the transporter lumen (154). This theoretical treatment could recapitulate some experimental observations (such as the

increase in charge:serotonin flux ratio with increasing membrane polarization), but could not explain blunt channel activity. A slightly different model based on the Hodgkin and Keynes model of K^+ channels proposed that stochastic diffusion of ions and substrate can account for coupling as well as channel-like activity (153).

Some simple observations of the SERT activity can be readily explained by this model. If ions and substrate were strictly coupled in a fixed stoichiometry and the ion concentration gradient maintained, an increase in extracellular substrate concentration would predict a proportional increase in cytoplasmic concentration at equilibrium. However, this was not observed with the SERT at extracellular substrate concentrations above 3μM, suggesting that ions and substrate are not strictly coupled (18). In fact, a time-dependent decrease in the uptake rate was observed with increasing intracellular serotonin concentrations. It was suggested that a channel mode of the SERT would suffice to efficiently remove serotonin from the synapse following an action potential due to the transient inwardly-directed substrate gradient. It was posited that strict ion/substrate coupling would occur only when the driving force supplied by the ion gradients would be utilized to move substrate against its concentration gradient.

Alternating access

Regardless of the intriguing transport-associated currents, these currents are much smaller than those generated by ion channels (67) and channel-like states have been predicted to be brief (~1ms), low probability events (17,19). The dominant transporter mode has been hypothesized to reflect alternating access of a centralized ion/substrate binding compartment formed by the presence of physical "gates" (16). Coupling is realized by the direct interaction of ion and substrate at the binding site. Furthermore, the coordinated movement of the gates during distinct steps of transport maintains the coupled interaction by alternately exposing the binding site to either the extracellular or intracellular milieu. Channel-like behavior may be attributed to aberrations of the gating mechanism such that both gates are briefly opened simultaneously allowing indiscriminant flux of ions/substrate through the transporter (25). Thus, the fundamental

difference between the single file diffusion model and the alternating access model are the conformational changes in the structure of the transporter that is required of the latter mechanism.

A simplistic version of this model was originally proposed by Jardetzky, described as a pump, in which three structural criteria were met: a substrate permeable cavity, the ability of the pump to interconvert between two configurations, and a binding site within the cavity in which the affinity for the substrate is different between the two configurations (155). The original proposal was given in the context of an ion pump moving Na^+ up the concentration gradient with energy supplied by a phosphorylation event that triggered a conformational change in structure. In this case, the process of gating is implied by the chemical-induced change in the configuration of the pump which alters the exposure of the binding site. This model has since been extended to describe the mechanism of secondary active transporters with explicit gating machinery (23). As shown in Figure 4, a thermodynamic cycle of four intermediate states can describe the process of substrate translocation with energy supplied by an ion gradient.

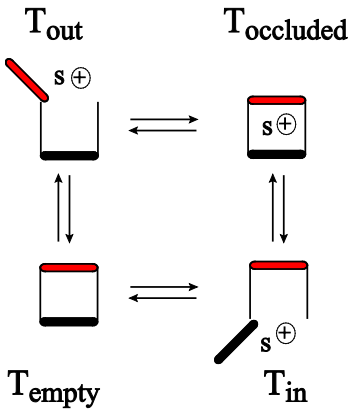

Figure 4. Thermodynamic cycle of ion-coupled transport. Substrates bind in an outward-facing conformation (T_{out}) and proceed through a doubly-occluded conformation ($T_{occluded}$) to achieve the inward-facing, substrate-releasing state (T_{in}). Transporter re-facing to Tout requires an doubly-occluded state in the absence of substrate (T_{empty}). In the SERT, the T_{empty} may be actually be a K^+-bound state.

In the initial conformation, the intracellular gate is closed while the extracellular gate is open to receive ion and substrate. The energy of ion/substrate binding at the centralized location triggers the closure of the extracellular gate and the subsequent opening of the intracellular gate. If the intracellular concentration of ion is lower than the K_D for ion binding, the ion will release into the cytoplasm. Since substrate binding and transport is contingent upon coupling to the ion, the substrate will also release into the cytoplasm due to a change in binding site affinity. Following release, the intracellular gate closes and the pump returns to the initial conformation for subsequent cycles. Jardetzky demonstrated that this process of substrate release will occur even against a concentration gradient provided the chemical energy that drives the pump is available.

The transition between the intermediate states may account for the slow turnover rates observed for the transporters relative to ion channels (23). For instance, the turnover rate for the DAT is on the order of one to two seconds per cycle, necessitating high concentrations of transporter at the plasma membrane for efficient signal termination according to this mechanism (23). In particular, the rate of structural transitions is different between the intermediates. Recently, Erreger et al demonstrated that the reorientation of the DAT from the inward-facing conformation to the outward-facing conformation is the rate-limiting step (8). However, reorientation of the SERT can be potentiated by the presence of intracellular K^+, suggesting that the outwardly-directed K^+ gradient influences the structure of the transporter (16). The resulting increase in rate of serotonin transport is consistent with the exchange or countertransport of K^+ during the SERT cycle, an observation that cannot be adequately explained by the single file diffusion model. Furthermore, this model links the effects of other ligands or modulators to the conformational state of the transporter.

The leucine transporter (LeuT) as a prokaryotic model of NSS

As previously stated, the practical application of these models to the transport of substrate is limited without high resolution structural information. The single file diffusion model of K^+

channels was substantiated by crystal structures of various ion channels from both prokaryotes and eukaryotes (156,157). In the absence of such structural information for the NSS, the form of the cavity, the binding site and gating machinery leaves mere speculation of how these models can be applied to the transport mechanism. At this time, native structure determination is inhibited by the lack of heterologous expression systems yielding sufficient quantities (mg) of material for crystallographic analysis (158). The size of these transporters also precludes structural analysis by current protocols of nuclear magnetic resonance spectroscopy (159). Even if the expression systems were available, there is no guarantee that the membrane proteins would be functional (158).

Due to the conspicuous absence of these methodologies, the scientific community is forced to rely on biochemical approaches yielding insufficient mechanistic details with low structural resolution. Measurements of transport activity following site directed mutagenesis, cysteine crosslinking or cysteine reactivity with MTS reagents can only supply a premise for structural changes in the system. Such experiments have been used to imply that cocaine binding stabilizes the outward-facing conformation, thus preventing the conformational changes required for transport (160). The substituted cysteine accessibility method, which employs site directed cysteine mutagenesis to assess the sensitivity of transport in the presence of covalent modifiers (MTS reagents), has suggested that the putative extracellular regions of TM7 and TM8 in the DAT undergo conformational changes in the presence of substrates or inhibitors (161). Cysteine reactivity studies with MTSET identified specific residues in TM3 that may be involved with substrate permeation and gating in both the SERT and NET (162). Other studies have generated chimeras of transporters to investigate the mechanism of substrate specificity. Chimeras of SERT and NET have suggested that EL2 and EL4 play a role in conformational changes, but do not affect substrate and inhibitor binding specificity (163,164). Many other studies can be mentioned and have been reviewed (16,165). Whereas these results cannot efficiently and explicitly map the structure of these transporters, the data are important for the generation of testable hypotheses.

One avenue whereby structural information can be obtained more easily is through the analysis of evolutionarily related prokaryotic membrane proteins. These homologs can be readily overexpressed and functionally purified. The utility of this approach is exemplified by crystal structures of the KcsA K^+ channel, the *E. coli* lactose permease and the structure of a glutamate transporter homolog (156,166,167). These structures not only provide a context for the interpretation of both structural and functional data, but they also facilitate the development of highly specific hypotheses regarding their mechanisms at atomic resolution. Subsequent structural analysis in the presence or absence of ligands and/or inhibitors provides essential details into the modes of interaction and specificity. This approach has recently been applied to a bacterial homolog of NSS.

The structure of LeuT

Crystallographic and functional analysis of a leucine transporter (LeuT) from Aquifex aeolicus, a thermophilic bacterium found near underwater volcanoes and hot springs, has revealed a tractable structural model for the NSS family (168). The primary sequence of LeuT displays 20-25% sequence identity to eukaryotic members of the NSS family, although conservative substitutions approximate a 45% similarity (169). Even though the sequence identity is rather low, protein segments that are thought to be involved with forming the ion/substrate binding sites in the eukaryotic proteins are conserved in LeuT (5). The structure of LeuT, solved in β-octyl glucoside detergent (OG), reveals a novel fold of 12 TM α-helices, the first ten of which are related by a pseudo two-fold symmetry and forms the protein core (Figure 5). The presence of 12 TM segments is different from the vast majority of prokaryotic homologs in this family, but similar to that predicted for the NSS (170). The co-transported substrates Na^+ and Leu (2 Na^+:1 Leu) are centrally bound in a site devoid of water. Extensive hydrogen bonding and hydrophobic interactions with the Leu substrate are provided by unwound regions within TM1 and TM6 with additional contributions from residues in surrounding helices. The bound Na^+ and Leu are closely associated in space and the carboxylate moiety of the Leu participates in the direct coordination

of one of the Na^+ (designated Na1). LeuT crystallizes as a dimer with an interface formed by TM9 and TM12. In comparison with the predicted topology of the NSS, long N- and C-terminal tails are notably absent and EL2 appears truncated (identified in Figure 5) relative to EL2 of NSS.

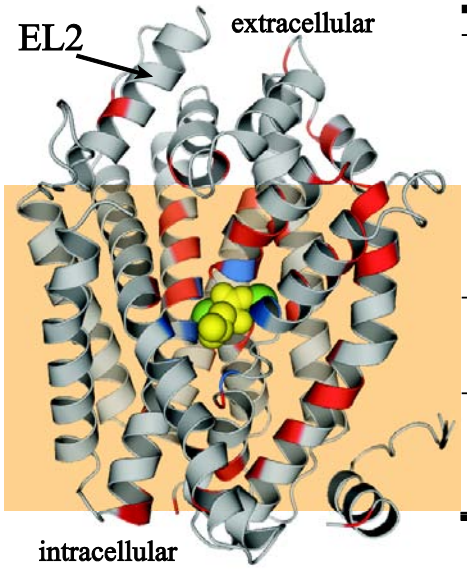

Co-substrate	LeuT Residue	NSS Residue
Leu	Ala22*	Ala
	Leu25	Leu
	Gly26	Gly or Ala
	Val104	Ile, Leu or Val
	Tyr108	Tyr
	Phe252	Phe or Cys
	Phe253	Phe or Tyr
	Ser256	Ala or Gly
	Phe259	Phe, Trp or Leu
	Ile359	Leu, Thr or Gly
	Ser355*	Thr or Ser
Na1	Ala22*	Ala
	Asn27	Asn
	Asn286	Asn
	Thr254	Ser
Na2	Gly20	Gly
	Val23	Val or Ile
	Ala351	Leu
	Thr354	Asp or Gly
	Ser355*	Thr or Ser

*Participates in Leu and Na^+ binding

Figure 5. Location of conserved residues in the LeuT structure. The view is captured along the membrane plane (transparent orange box). Positions highlighted in red are strictly conserved, while those in blue represent sites of conservative mutations. Leu and Na^+ are depicted in yellow and green space filling models. The table identifies sites that participate in Leu and Na^+ binding. LeuT PDB code 2A65 is shown. TM10-12 have been removed for clarity.

LeuT is functionally dependent on Na^+ since substitution with K^+ did not support transport (168). In contrast to NSS, LeuT is not dependent on the presence of Cl^-. Prokaryotic transporters like LeuT share a highly conserved acidic residue (Asp or Glu) near the Na1 binding site that is a highly conserved Ser residue in the Cl^--dependent eukaryotic transporters. Introduction of an acidic residue at this position renders SERT, DAT and rat GABA transporters Cl^--independent and neutralization of the Asp/Glu in LeuT and the tyrosine transporter Tyt1 renders binding and/or transport Cl^-dependent (171,172). Identified by two separate groups, this

Cl^- binding site is approximately 5Å away from Na1, supporting an interaction energy of -11 kcal/mol and suggests how Na^+ and substrate could interact with Cl^- at the binding site (171).

Proposed transport mechanisms of LeuT

How does the crystal structure of LeuT inform the mechanism of Na^+-coupled transport?

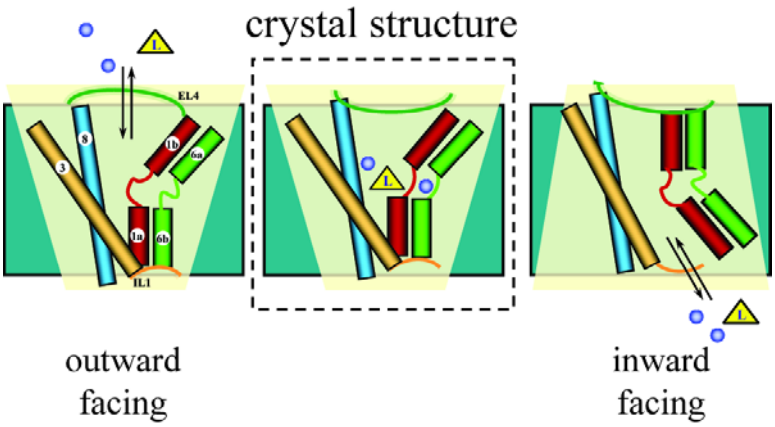

Figure 6. Proposed alternating access mechanism of LeuT based on the initial crystal structure. The transition between outward-facing and inward-facing states is facilitated by the intrinsic flexibility of TM1 and TM6. Adopted from Ref 168.

First, the centralized binding site is occluded from both the cytoplasmic and extracellular sides. Thus, there is no clear entry way for ions and substrate to permeate to the binding site, or for them to exit out the other side. The structure appears to support the alternating access model (168) in that it is likely occupying the intermediate state between the outward-facing and inward-facing conformations characterized by closed extracellular and intracellular gates (Figure 6). Binding site occlusion from the extracellular side is primarily achieved by the helical hairpin turn of EL4, as well as F253 in TM6, D404 and R30 in TM10 and TM1, respectively. The two charged residues, D404 and R30, are located near a vestibule and are predicted to serve as an ionic extracellular gate. The pathway leading from the binding site to the cytoplasm is much more

extensive and compact.

Subsequent crystal structures revealed that LeuT is rather promiscuous, binding several other amino acids including Ala, Val and Met. In these structures (173), the packing of the helices and loops were identical to the Leu-bound structure (Figure 7A). Interestingly, crystal structures

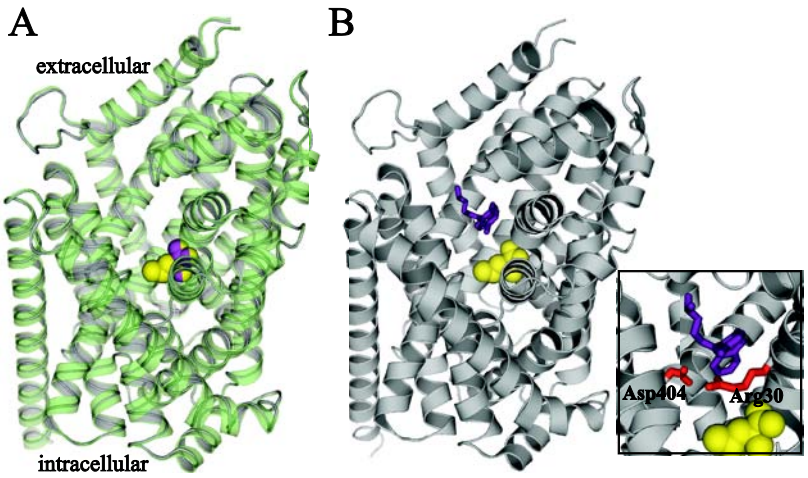

Figure 7. LeuT forms similar crystal structures with different substrates or in the presence of TCA inhibitors. (**A**) The Ala crystal structure (transparent green helix, PDB 3F48) is nearly identical (<0.15Å rmsd) to the Leu-bound LeuT structure (gray loop). Leu (yellow) and Ala (magenta) occupy a similar space at the primary binding site. (**B**) A TCA, clomipramine (purple stick, PDB 2Q6H), binds in a vestibule ~10Å above the Leu binding site. The ionic pair, Asp404 and Arg30 (inset) postulated to form the extracellular gate, forms a direct interaction in the TCA-bound structure. In the original LeuT structure, this interaction is mediate by a single water molecule.

of LeuT with bound TCAs (169,174) or SSRIs (91) in the extracellular vestibule also reported a nearly identical structure with Na^+ and Leu also bound in the central binding site (Figure 7B). Alignment of the original LeuT structure with the TCA clomipramine-bound structure using the molecular visualization tool Pymol revealed an rmsd of less than 0.1Å for all atoms. One subtle difference was identified involving the ionic interaction between D404 and R30. In the original structure, this interaction was bridged by a water molecule (168). In contrast, this water is missing

in the TCA-bound structure (174). Combined with noncompetitive inhibition kinetics, the authors suggested that the TCAs stabilized the occluded conformation, by sterically restricting conformational movement and by "locking" the ionic extracellular gate. However, it is not clear how this TCA binding site relates to that found in the NSS, since the mechanism of TCA inhibition in the NSS is competitive, suggesting a binding site that overlaps with the native substrate binding site (87,89). Mutagenesis studies of the SERT based on this TCA binding site in LeuT has suggested that the inhibitory site is conserved in the SERT (169); yet, these affects may be mediated indirectly.

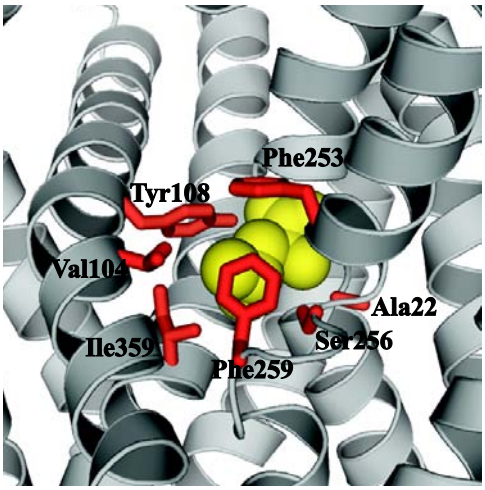

Figure 8. Stabilizing interactions of the primary binding site. Side and main chain atoms contribute to forming the substrate binding site. Note the interactions provided by the discontinuous helix of TM6. PDB code 2A65 is shown.

The geometric organization of the binding site not only provides for specific interactions, but also insight into how the transporter may expose the binding sites. TM1 and TM6 reveal a break in the α-helical pattern of the polypeptide chain at the binding site (Figure 8). This appears to confer specific functions (168). Residue side chains as well as backbone atoms contribute to

the formation of the binding site. Furthermore, the discontinuity of the helices exposes the intrinsic dipole moment which contributes to the coordination of charges. Lastly, the loss of periodicity may confer flexibility at the binding site to allow alternating exposure to the extracellular or intracellular media. The pattern of discontinuous helices in LeuT also appears in other transport proteins, including the glutamate transporter and the ClC H^+/Cl^- exchanger, in similar topological arrangement or as helical re-entry loops involved with binding of substrates (175).

While the crystal structure of LeuT provides a structural context for functional activity, it must be emphasized that more structural analysis is required to elucidate all aspects of transporter functionality. That is, there are questions that still remain to be answered. Foremost, the doubly-occluded nature of the structure demands investigation into what structural changes occur to accomplish Na^+-coupled transport. Yet another, what is the structural basis of functional inhibition by other compounds, such as cocaine? A number of intensive efforts have been undertaken to integrate the structural information of LeuT with the structure/function data of the NSS. For example, the alignment of LeuT with the SERT sequence suggested that residues along TM5 near the cytoplasm may form part of the intracellular permeation pathway (160). The reactivity pattern of substituted cysteines with MTSEA in the presence of either substrates or inhibitors seems to substantiate this hypothesis. Based on the LeuT crystal structure alone, this is not an obvious result due to the densely packed nature of the intracellular domain (168). A number of studies have used the LeuT structure as a basis to fold the sequence of the NSS to generate homology models (176-180). These computational models can help to align the molecular details of prior and novel indirect structural measurements of the NSS, as well as conjure new hypotheses. A recent study featuring computational modeling and functional analysis of the DAT implicates a conserved intracellular interaction network that may control cytoplasmic gating (181). Another study using a molecular model of the DAT found that the binding site for cocaine overlaps with the dopamine binding site, which was found to be consistent with previous

mutagenesis studies in the DAT (181,182).

Subsequent reports of other prokaryotic Na^+-coupled transporters crystallized in different conformations suggested that structural information regarding the mechanism of transport could be gathered from analysis of the unique arrangement of structural elements coupled to the conditions of crystallization. This approach, which attempts to align these different structures with the thermodynamic cycle shown in Figure 9, appears to have some merit as these transporters are dependent on Na^+ and possess a similar topological organization to LeuT (183).

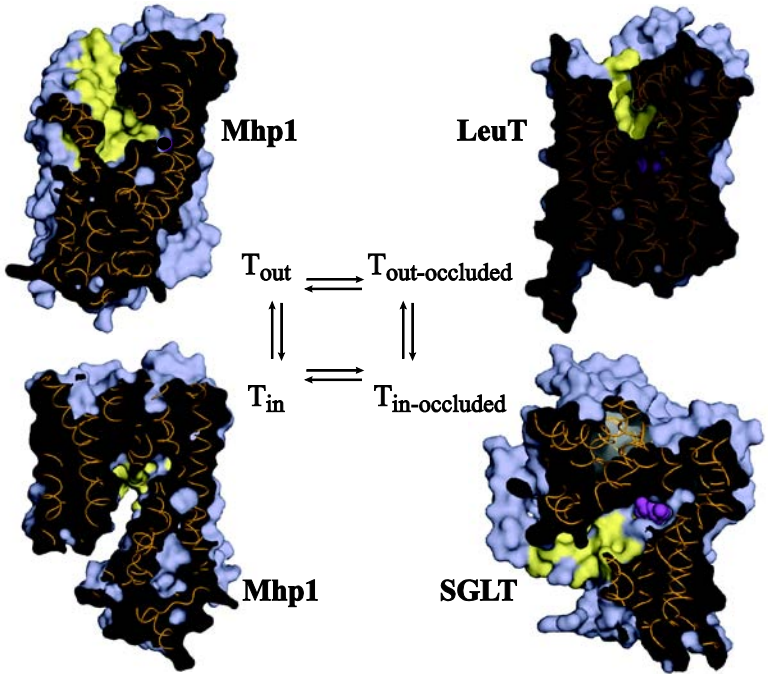

Figure 9. Thermodynamic cycle of transport based on available crystal structures. The structure of Mhp1 (PDB 2JLN), which was suggested to be in an outward-facing state, is an example of the T_{out} configuration. The original LeuT structure (PDB 2A65) has been suggested to be in an outward-facing occluded state ($T_{out\text{-}occluded}$), whereas the structure of vSGLT (PDB 3DH4) may represent an inward-facing occluded ($T_{in\text{-}occluded}$) conformation. The crystal structure (PDB 2X79) of an inward-facing Mhp1 with an empty binding site may represent the T_{in} state. The figure was inspired from Ref 183.

Three crystal structures of the NCS1 benzyl-hydantoin transporter, Mhp1, have been reported in

different conformations (184,185). Although the specific details of substrate occlusion are different in Mph1 (mainly the inward bending of TM10 toward the binding site), in the presence of substrate it resembles a doubly-occluded structure similar to LeuT (185). In the absence of substrate, the Mph1 adopts a more outward-facing configuration facilitated by the outward movement of TM10. Recently, an inward-facing conformation of Mhp1 was reported with an empty binding site, illustrating much larger structural changes from the occluded intermediate (184). Relative to the occluded conformation, this cytoplasmic open state is facilitated by movement of a four-helix bundle (TMs 3, 4, 8 and 9). The Na^+/galactose transporter vSGLT adopts a more inward-facing conformation, yet substrate remains bound and occluded (Figure 9) (186). This model emphasizes the presence of residues and/or structural elements forming gates at the extracellular and intracellular sides of the binding site and that the doubly-occluded structure is an obligatory intermediate in the conformational cycle. Obviously, the most complete conformational cycle is represented by the structures of Mhp1. However, to combine the crystal structures of multiple unrelated transporters assumes that the structures represent native conformations, the transport mechanism is uniform and that individual transporter idiosyncrasies do not affect the details of the overall transport process. This is not necessarily the case.

Ideally, efforts to identify the structural intermediates of LeuT are advantageous to the elucidation of specific properties of transport in the family of NSS. Although crystallographic analysis of LeuT with other amino acids revealed a similar structure, Trp will also displace Leu, but leads to a significant expansion of the extracellular vestibule (Figure 10) (173). Trp was also found to inhibit transport, leading the authors to suggest that Trp stabilizes an outward-facing conformation. The structure was solved in the presence of 50mM Trp, which is three orders of magnitude above the K_i (~25μM). The high Trp concentration may have contributed to what appears to be non-specific binding. Four Trp molecules were resolved in the structure but only two were bound in close proximity to the Leu binding site. Nevertheless, it is difficult to interpret the relationship of this inhibited structure in the context of a functional cycle of transport.

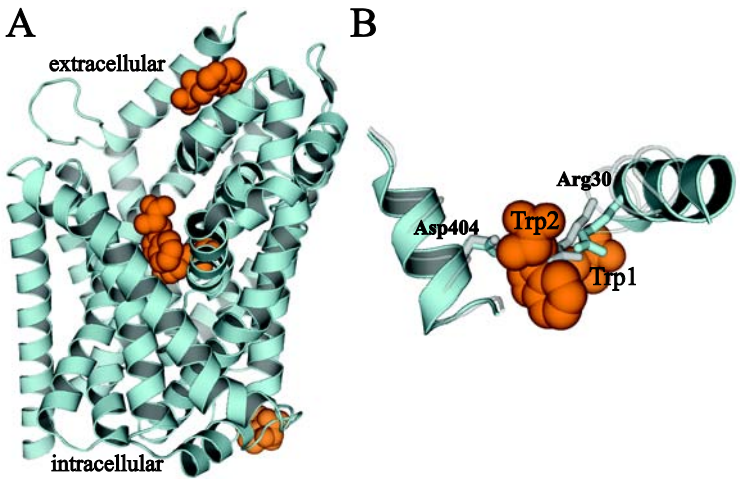

Figure 10. Crystal structure of LeuT in the presence of 50mM Trp. (**A**) Leu is competitively displaced by Trp in the primary binding site. (**B**) A second Trp molecule disrupts the interaction between Asp404 and Arg 30. PDB code 3F3A is shown.

In order to generate a LeuT model of the inward-facing conformation, Forrest et al exploited the internal pseudosymmetry of the inverted topological repeats formed by the first 10 TM segments (187). By computationally tilting a four-helix bundle composed of TM1, 2, 6 and 7, they were able to essentially swap the conformation of the repeats revealing a potential pathway for substrate exit into the cytoplasm. This model was used to predict cytoplasmic exposure of specific residues in the SERT upon substrate binding (Figure 11). Thus, this "rocker switch" type model predicts two prominent conformational intermediates, outward- and inward-facing, and the transition between these two states may not necessarily depend on the formation of a doubly-occluded intermediate. Fundamental to the generation of this model is the assumption that the original LeuT structure essentially represents an outward-facing conformation. Presumably, this assumption is based on the presence of an extracellular vestibule and a binding site this is occluded by only a few residues, whereas no vestibule is visually present on the cytoplasmic side of the binding site (168). Although some differences were identified, the inward-facing structure of Mhp1 suggests that similar rigid body movement may be associated with isomerization from

an outward-facing intermediate (184).

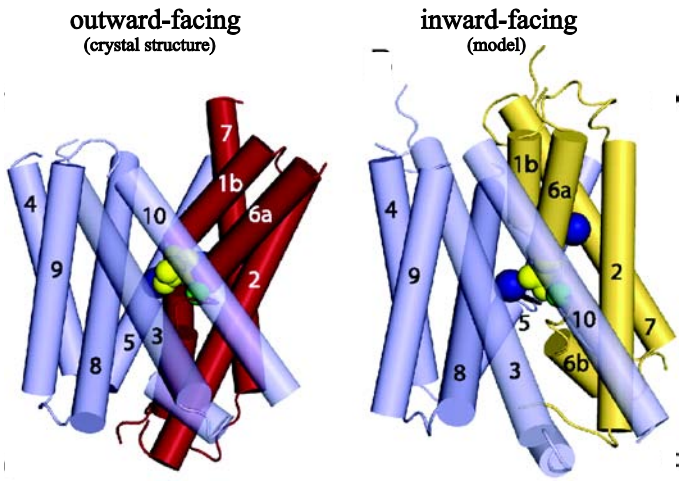

Figure 11. The rocking bundle mechanism. Inward tilting of a four helix bundle is proposed to close the extracellular permeation pathway and establish a conformation open to the cytoplasm. The model exploits the pseudo-two fold symmetry of internal structural repeats formed by TM1-5 and TM6-10. The figure was adopted from Ref 187.

A more detailed functional model of the transport cycle of LeuT was recently investigated by a combination of steered molecular dynamics (SMD) simulations and radiolabeled flux assays (Figure 12) (188). By "pulling" the Leu substrate out of the primary binding site (denoted the S1 site) toward the extracellular milieu, the SMD calculations identified a potential second substrate binding site (denoted the S2 site) in the extracellular vestibule similar to the location of the TCA and SSRI binding site. Subsequent functional analysis in both *n*-dodecyl-β-D-maltopyranoside (DDM) detergent and proteoliposomes indicated that Leu can bind with nM affinity to both sites simultaneously (2Leu:1LeuT, stoichiometry). Furthermore, mutation of residues involved in the formation of the S2 site or the presence of a TCA inhibitor eliminated Na^+-coupled transport. The authors postulated a mechanism whereby substrate binding to the S2 site allosterically triggers the cytoplasmic release of Na^+ and substrate in the S1 site.

Hence the formation of the inward-facing conformation may be contingent on substrate occupation of the S2 site. Furthermore, the presence of the TCA inhibitor appears not only to stabilize the occluded conformation, but also functions as a "symport uncoupler" by preventing substrate binding to the S2 site.

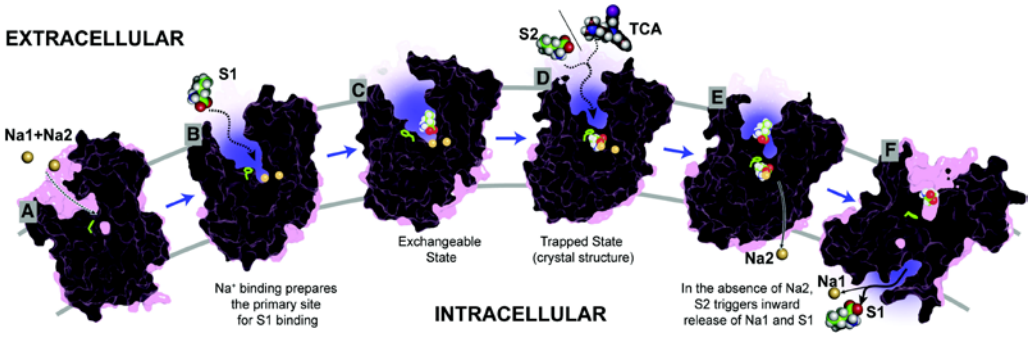

Figure 12. A functional model of transport. Based on steered molecular dynamics, Na^+ binding facilitates opening of LeuT so that Leu can bind in the primary (S1) site. From radiolabel ligand binding experiments, Leu binding in the S2 site triggers release of Na1 and Leu in the S1 site, a mechanism disrupted by TCAs (or OG or SSRIs) binding in the S2 site. Adopted from Ref 188.

Significance of further LeuT investigations

The foundation of a functional transport mechanism relies on the identification of multiple intermediate states. However, all crystal structures of LeuT, except one (Trp-bound), adopt a similar conformation (91,168,169,173,174). Prompted by the observation that LeuT can only bind one Leu when purified in OG detergent in contrast to that purified in DDM detergent, Quick and colleagues recently determined by X-ray crystallography that a molecule of OG occupies the extracellular vestibule similar to a TCA inhibitor (189). Functional analysis also confirmed that OG inhibits Na^+-coupled transport similar to the TCAs. In contrast to all published functional data obtained from LeuT purified in DDM micelles, all crystal structures were obtained in OG detergent. Indeed, re-examination of the electron density map of the original LeuT structure revealed a residual density consistent with the presence of OG (189). The apparent

disparity led the authors to conclude that the current library of LeuT crystal structures represent inhibited intermediates. Therefore, models of conformational changes based on these structures as described above are fundamentally flawed since these models assume that the original LeuT structure represented a legitimate, uninhibited intermediate in the functional cycle.

This critical observation demands further examination of the LeuT structure and its relationship to a functional cycle. Furthermore, how different intermediate states are connected through dynamic fluctuations in structure is an important consideration for the proper characterization of Na^+-coupled transport. This is most appropriately described by Karpowich and Wang in their editorial comments on the inward-facing crystal structure of the Na^+/galactose transporter (190):

> *Isolation of secondary transporters in specific conformational states remains a major technical obstacle for structural studies. However, with structural information for some conformational states in hand, spectroscopic techniques can provide precise information about the nature and magnitude of the conformational states during the transport cycle.*

Using a spectroscopic approach, experiments can be designed to identify the structural characteristics of intermediate states as well as capture the dynamics associated with specific protein conformations. These dynamic properties cannot be observed properly in the confines of the crystal lattice, which may even lead to structural distortions (191,192). The body of work presented in this manuscript describes the investigation of the LeuT conformational cycle by electron paramagnetic resonance (EPR) spectroscopy, a technique highly sensitive to both local and global conformational rearrangements in protein structure. Chapter 2 features a formal introduction to EPR spectroscopy and the application of the technique to protein structure and mechanism. Subsequent chapters report the results of the analysis, outlining the structural transitions of LeuT that occur during the first two steps of the transport cycle in the region of the extracellular vestibule and in the context of both DDM micelles and proteoliposomes. Furthermore, the results clearly demonstrate the differential effect of inhibitors on the structure of LeuT relative to natural substrates.

CHAPTER II

ELECTRON PARAMAGNETIC RESONANCE SPECTROSCOPY

Origin of the EPR signal

The spectroscopic basis of the EPR experiment is contingent on the transition of electron spin states between discrete energy levels induced by the oscillating magnetic dipole component of microwave radiation. The process is quantum mechanically similar to nuclear magnetic resonance (NMR) which observes transitions between energy states of nuclei. As will be discussed below, the fundamental requirement for observing these transitions in EPR is having an unpaired electron (193). Detection of these signals furthermore requires an external magnetic field. Free radical species and transition metals that possess an unpaired electron, such as Cu^{2+} and Mn^{2+}, demonstrate unique EPR signals. In a biological context, the incorporation of stable free radicals, such as a nitroxide spin label, is often necessary to introduce an unpaired electron. The sensitivity of the free electron to the molecular environment allows the spectroscopist to interpret EPR spectra as reporting specific interactions that may include neighboring nuclei and molecular structure. The following description briefly elaborates on the processes that give rise to electronic transitions, as well as those that influence the lineshape of absorption signals.

Electron spin state transitions in a magnetic field

The physical property of charge in addition to quantized spin angular momentum confers the electron with a permanent magnetic moment. As illustrated below, this magnetic moment is the basis for the behavior of an electron in an external magnetic field (H_o) and, therefore, the spectroscopic investigation of electron spin dynamics. The energy of interaction between the electron and H_o along the z-direction can be described by the Hamiltonian

$$\mathcal{H} = -\mu_z H_o \qquad (1)$$

in which μ_z is the electron magnetic moment. This mathematical statement can be rewritten to

$$\mathcal{H} = gBH_oS_Z \quad (2)$$

which emphasizes the direct dependence of the interaction energy on the electron spin quantum operator, S_z. In Equation 2, g is the dimensionless electron g factor and B is the electron Bohr magneton, both of which are known constants. For the electron, the S_z operator yields spin eigenvalues (M_S) that are ±½. From the Pauli Exclusion Principle, no two electrons can possess the same value of M_S if occupying the same orbital. Thus, if an electron is paired with another electron, the spin angular momentum is canceled and cannot contribute to the magnetic moment (193,194). Therefore, paired electron spins are said to be diamagnetic or EPR "silent". For unpaired electrons, the values of M_s lead to Zeeman interaction energies of either -½gBH$_o$ (α state) or ½gBH$_o$ (β state) according to Equation 2. In an ensemble of unpaired electrons, the spins will either occupy the α (lower energy) state or the β (higher energy) state. Those spins which occupy the α state are said to be parallel to (or align with) the magnetic field, whereas those in the β state are antiparallel. The difference in energy (ΔE) between these two states is given by

$$\Delta E = gBH_o = h\nu \quad (3)$$

where h is the Planck constant and ν is the frequency of electromagnetic radiation. Importantly, this equation indicates that these two energy states are degenerate outside of a magnetic field. That is, there is no measurable difference between the two energy states in the absence of H$_o$. In addition, the separation between the two states will increase proportionally to the strength of the magnetic field. Furthermore, when the magnetic moment of an impinging oscillating field of electromagnetic radiation ($h\nu$) matches the separation of the energy levels, known as the resonance condition, the spins from one state will absorb this energy leading to a transition to the other state (193,194). A diagram depicting this behavior of electron spins in a magnetic field is shown in Figure 13.

This stimulated transition can be accomplished in one of two ways. As in a NMR experiment, the frequency of electromagnetic radiation to induce a transition can be interrogated

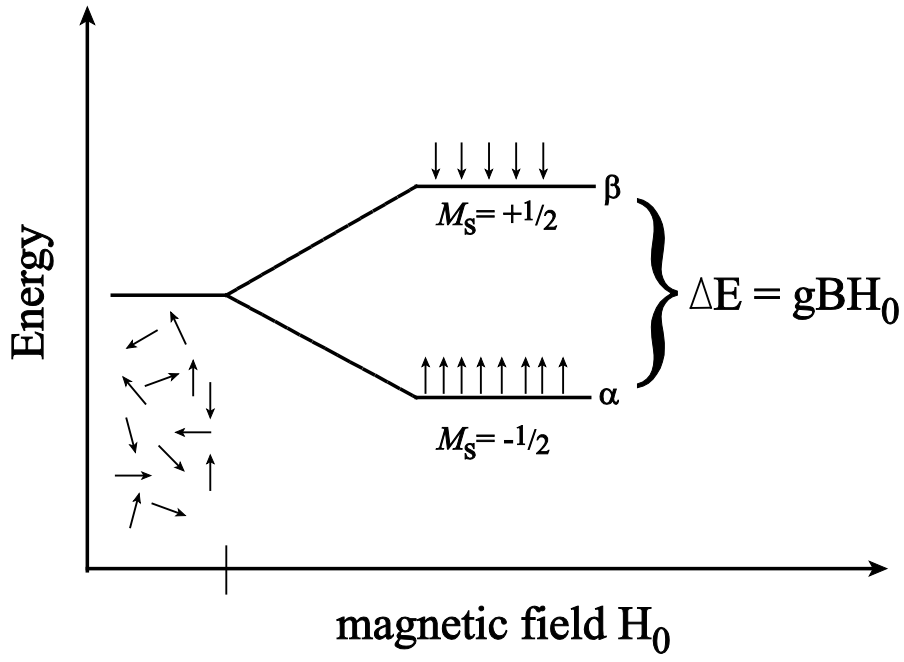

Figure 13. Behavior of an electron spin ensemble in a magnetic field. In the absence of a magnetic field, electron spins will orient randomly (bottom left) and their energies are similar. When a field is applied, the spins will align with (α) or against (β) the field, resolving energetic differences between spin states. The α state is only slightly more populated than the β state.

at a constant magnetic field strength (159). Alternatively, an EPR experiment typically holds the frequency of radiation constant while scanning the magnetic field (193). From the resonance condition described in Equation 3 above, the electronic transition will occur with an electromagnetic radiation frequency of 9.5 GHz at a magnetic field strength of 0.34 Tesla (or 3400 Gauss). This frequency, known as X-band, corresponds to the microwave region of the electromagnetic spectrum and is the predominate regime applied in EPR spectroscopy (193).

The stimulated transitions have an equal probability of resulting from an electron moving from the α state to the β state, or from the β state to the α state. This elicits the fundamental question of how an absorption signal is detected. At thermal equilibrium, relaxation processes (that will be discussed in detail in a subsequent section) dictate that an excess of spins occupy the α state (Figure 13). The population of spins in each energy level can be described by the

Boltzmann distribution in which the spin population ratio of the states is a temperature-dependent exponential function of ΔE

$$\frac{N_\alpha}{N_\beta} = e^{(\Delta E/kT)} \quad (4)$$

where N_α and N_β represent the populations of state α and state β, *k* is the Boltzmann constant and T is the absolute temperature (193,194). Using this expression, it can be calculated that N_α/N_β for electron spins is ~1.0046 at a temperature of 293K and a 1 Tesla magnetic field, indicating that the lower energy α state is only slightly more populated than the higher energy β state. Therefore a *net* excitation of spins from the α state to the β state results in the appearance of a single absorption line. Equation 4 establishes the sensitivity of the EPR measurement as only those spins that contribute to the population difference between the states give rise to the signal. However, Equation 4 also indicates that the signal intensity, which is directly proportional to the induced polarization of spins, can be increased by either lowering the temperature or increasing the magnetic field strength, or a combination of both.

Hyperfine interactions

The preceding discussion focused on the interaction of a "naked" electron in a magnetic field that could be sufficiently described by the Hamiltonian in Equation 2. However, some atomic nuclei also possess a permanent magnetic moment arising from nuclear spins with nonzero angular momentum. The presence of two (or more) particles with magnetic moments gives rise to specific interplays between spins that alter the energetic interaction of the electron with the magnetic field (193,194). In the case of nitroxide spin labels, the unpaired electron is located in a π-like orbital between the nitrogen and oxygen bond, predominately residing near the nitrogen nucleus. The spin quantum operator, I_z for the ^{14}N nucleus results in eigenvalues (M_I) of ±1 and 0, leading to three spin states characterized by nuclear Zeeman interaction energies $\pm 1 g_n B_n H_o$ and $0 g_n B_n H_o$ (i.e., the associated interaction energy for the M_I=0 state is zero). Here, the subscript *n* refers to the nuclear g factor and nuclear Bohr magneton. These spin states couple

to the spin states of the free electron introducing hyperfine interactions into the spin Hamiltonian and re-defines the resonance condition. To a first approximation (193,194), the complete spin Hamiltonian is:

$$\mathcal{H} = gBH_oS_z - g_nB_nH_oI_z + A_oS_zI_z \qquad (5)$$

In this equation, A_o is the isotropic hyperfine coupling constant which defines the interaction energy between the unpaired electron and the ^{14}N nucleus. The result of Equation 5 is that the energy levels sampled by the electron are further split, which gives rise to the approximate energy level diagram depicted in Figure 14.

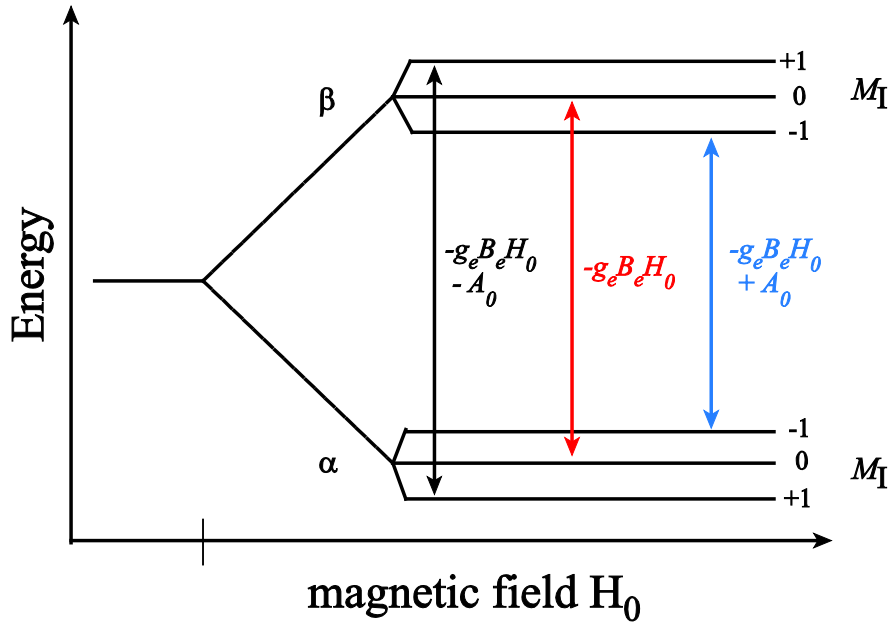

Figure 14. Resonance condition including hyperfine interactions. The presence of a permanent magnetic moment from the ^{14}N of a nitroxide spin label increases the number of available spin states. Quantum selection rules dictate three electronic transitions, as shown with the associated energies, resulting in three absorption lines in the EPR spectrum.

From the diagram above, it is apparent that the electron can occupy one of six spin states as opposed to two spin states of the "naked" electron: three in the α state (M_S = -½, M_I = ±1, 0)

and three in the β state (M_S = ½, M_I = ±1, 0). Likewise, this leads to six potential electronic transitions. However, the conservation of angular momentum during the interaction of microwave radiation with the electron demands selection rules for induced transitions, $\Delta M_S = \pm 1$ and $\Delta M_I = 0$, which means that sufficient energy leading to absorption can only change the spin state of the electron and not the nucleus (193,194). Therefore, there are only three quantum mechanically "allowed" transitions, as illustrated in Figure 14 with the associated energies derived from Equation 5. These transitions correspond to three absorption lines of equal intensity separated by the hyperfine coupling constant A_o in the EPR spectrum.

The orientation dependence of the g and A tensors

In the preceding treatment, it has been assumed that the g factor in the spin Hamiltonian of Equation 5 takes on the unique value of the free electron g factor (2.0023) and the hyperfine coupling constant arises from purely isotropic interactions with the ^{14}N nucleus. In many cases, the g factor does not take on this value resulting in a shift in the resonance position. In a nitroxide spin label, an additional component to the electron magnetic moment arises from the coupling interaction between the electron spin angular momentum and orbital angular momentum. This interaction must be considered for unpaired electrons that occupy non-spherical orbitals where the electron and nuclear g factors and A_o are not purely isotropic (193). The spin-orbit interaction is facilitated by a local magnetic field induced by the interaction of the orbital angular momentum with the external magnetic field, which alters the overall field experienced by the electron such that

$$H_{eff} = H_o + H_{local} \qquad (6)$$

where H_{eff} represents the effective magnetic field at the electron. The presence of local magnetic fields (H_{local}) affect the electron Zeeman energies analogous to that observed in NMR with the appearance of chemical shift for atomic nuclei in non-identical chemical environments (159). Therefore, deviations in both the g factor and A_o can be expected. It is helpful to consider a

coordinate axis system that describes H_{eff} relative to the electron (Figure 15). In this system, the z-axis is taken along the direction of the localized electron and θ/φ are the angles between the H_{eff} vector and z-axis and x-axis, respectively (193).

Both the g factor and A_o are best represented as symmetric tensors that demonstrate the relationship between the magnetic field vector and the electron spin vector and between the electron spin vector and the nuclear spin vector that includes components from all directions along the Cartesian system set up in Figure 15. For instance, the principle value g_{xx} of the g tensor

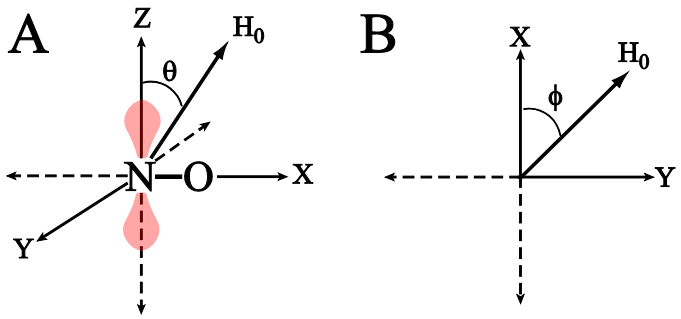

Figure 15. Coordinate axis defined for the nitroxide. The z-axis direction is taken along the unpaired electron (colored orbitals). The H_o vector is defined relative to the z axis (**A**) and x-y plane (**B**) by angles θ and φ, respectively.

describes the g factor of the electron along the x-axis of the magnetic field. In a purely isotropic system, the principle values of these tensors (i.e., the diagonal of the matrix) are identical: $g_{xx} = g_{yy} = g_{zz}$ and $A_{xx} = A_{yy} = A_{zz}$. However, in a nitroxide spin label these values are different (anisotropic), emphasizing the dependence of these values on the orientation of the nitroxide in a magnetic field (193). As a result, an orientation-dependent function of the observed g factor and A_o can be shown to be

$$g_{eff} = g_{xx}sin^2\theta cos^2\varphi + g_{yy}sin^2\theta sin^2\varphi + g_{zz}cos^2\theta \quad (7)$$

$$A_{eff} = [A_{xx}^2 sin^2\theta cos^2\varphi + A_{yy}^2 sin^2\theta sin^2\varphi + A_{zz}^2 cos^2\theta]^{1/2} \quad (8)$$

where g_{eff} and A_{eff} represents the effective g factor and hyperfine coupling constant. Therefore, the observed EPR spectrum is a function of the orientation of the nitroxide spin label in the magnetic field.

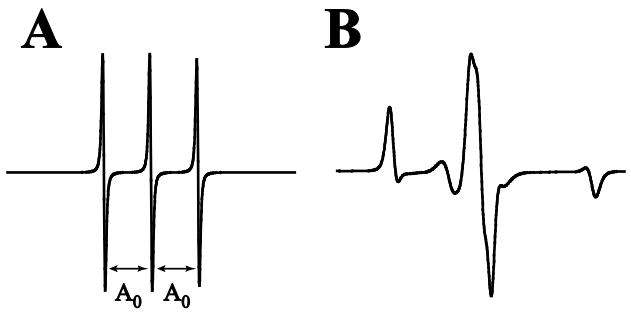

Figure 16. First derivative EPR spectra of motional extremes. (**A**) The fast motion limit due to rapid reorientation of a nitroxide in solution. (**B**) The EPR spectrum approaching the "rigid" limit resolving components along all directions in the magnetic field. Both spectra were simulated using standard g and A tensor values in the program MatLab.

In an ensemble of randomly oriented (and static) spin labels, such as in a crystalline powder, the absorption of microwaves while scanning the magnetic field will yield an EPR spectrum that is the *sum* of all possible orientations (194). Because the nitroxide is held motionless, this EPR spectrum represents the "rigid" limit or no motion EPR spectrum (Figure 16B). However, in dilute solution the principle values of both the g and A_o tensors are *time-averaged* due to rapid reorientation of the label relative to the magnetic field. In this case, g_{eff} and A_{eff} is equal to

$$g = \frac{g_x + g_y + g_z}{3} \quad (9)$$

$$A_o = \frac{A_x + A_y + A_z}{3} \quad (10)$$

which yields three evenly-spaced narrow lines centered about the average g factor that is orientation independent (194). This EPR spectrum is classified as the "fast motion" limit (Figure

16A). Importantly, this indicates that the *rate* of reorientation influences the EPR spectrum. As will be seen later in this chapter, spectra that sample a range of lineshapes are informative about the local molecular structure that may restrict the reorientation rate of the spin label.

Relaxation processes and lineshape

As previously stated, the slightly larger population of spins occupying the lower energy α state at equilibrium is the basis for net absorption of microwave radiation (193,194). However, the electron spin states are energetically equivalent in the absence of a magnetic field. This elicits the question of how the net polarization is achieved once an ensemble of electron spins is placed in a magnetic field. In a bulk ensemble of electron spins, some spins will occupy the α state and some will occupy the β state collectively contributing to a bulk magnetic moment vector, M. In the absence of a magnetic field, the degeneracy of both spin states drives M to zero (i.e., M is proportional to the population difference of spin states). However, an applied uniform magnetic field along the z-direction results in a time-dependent shift in M due to an alteration of the population of spin states and is described by the Bloch equation:

$$\frac{dM_Z}{dt} = \frac{M_o - M_z}{T_1} \qquad (11)$$

In Equation 11, M_z is the initial bulk magnetization along the z-direction in the absence of a magnetic field and M_o is the bulk magnetization at thermal equilibrium achieved after a time T_1 in the presence of an applied magnetic field (193,194). After the time T_1, the population of spin states is described by the Boltzmann distribution and the *net* magnetization vector aligns with the direction of the applied magnetic field. Therefore, T_1 describes how fast M aligns with the magnetic field direction.

The processes involved in the T_1 mechanism induce an exponential decay of non-radiative energy transfer from excited spin states to the surroundings (lattice), which is known as spin-lattice relaxation or longitudinal relaxation (193,194). The value of T_1 reflects the degree of coupling between all electron spins (or nuclei) in the field to the surrounding environment. The

shorter the T_1 time, the stronger the coupling that leads to faster relaxation. This pathway, which for instance exchanges excited spin states into molecular rotations and vibrations within the lattice (193), is also a critical component of achieving a ground energy state following microwave absorption. In the absence of spin-lattice relaxation, the populations of the spin states would equalize when excited by microwaves. The resulting saturation of spin states eliminates the net polarization required for absorption; thus, the EPR signal disappears. However, if T_1 is sufficiently long, population saturation can still be achieved by high microwave powers which enhance $\alpha \rightarrow \beta$ transitions (193). This is the fundamental basis of power saturation experiments that will be discussed later in this chapter.

Equation 11 defines the interdependence between the net magnetization in a magnetic field to the spin-lattice relaxation. Therefore, thermodynamic equilibrium characterized by the Boltzmann distribution of spin states cannot be obtained in the absence of relaxation. That is, the bulk magnetization will decay to zero in the absence of relaxation processes even in the presence of a magnetic field. If T_1 were not present, the change in M_z with respect to time would be zero (193). However, M is a vector quantity and is fully described by components along the x and y-axis (M_x and M_y). In addition, M also possesses a bulk angular momentum originating from the ensemble of electron spin angular momenta. Thus, the applied magnetic field exerts a torque on the bulk spins causing M to precess about the magnetic field direction like a gyroscope (Figure 17) (159,193,194). In contrast to M_z in the absence of relaxation, this precession is defined by time-dependent changes in the M_x and M_y magnetization components and the frequency of precession is referred to as the Larmor frequency. The following Bloch equations describe the behavior of the transverse components M_x and M_y in the presence of relaxation:

$$\frac{dM_x}{d_t} = \gamma H_o M_y - \frac{M_x}{T_2} \quad (12)$$

$$\frac{dM_y}{d_t} = -\gamma H_o M_x - \frac{M_y}{T_2} \quad (13)$$

where γ is the electron gyromagnetic ratio ($=2\pi gB/h$). Whereas relaxation induces a T_1-dependent transition of $M_z \rightarrow M_o$ (Equation 11), relaxation causes the M_x and M_y components to go to zero. However, this relaxation process is different from T_1 due to different mechanisms characterized by a T_2 relaxation time (159,193). The T_2 time describes the rate of signal decay in the transverse (x-y) plane.

Unlike T_1 relaxation, the T_2, or transverse, relaxation mechanism does not alter the population of spin states because it does not operate on the M_z component of the bulk magnetic

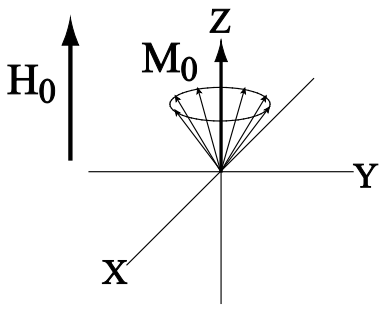

Figure 17. Precession of electron spins in a magnet. An external magnetic field interacts with the bulk angular momentum from a spin ensemble causing the spins to rotate about the magnetic field direction. The precession of spins causes the x and y components of the vector M to cancel, leaving only the z component. The net magnetization (M_o) along the z-axis results from having a greater population of spins in the lower energy α state aligned with the direction of H_o.

moment. Typically, T_2 relaxation is referred to as spin-spin relaxation, which qualitatively describes either dipolar interaction or collision with neighboring spins (159,193). These interactions facilitate mutual spin "flips" or reorientation of the spin magnetic moments, which transfers energy to the individual spins and not the lattice. Therefore, there is no net exchange of energy to the lattice. Both relaxation mechanisms contribute to the observed EPR lineshape.

Continuous irradiation of microwaves, such as in continuous wave (CW) EPR, along the axis perpendicular to the magnetic field H_o generates a steady-state magnetization behavior in the

spin ensemble. The solution to the Bloch equations, which takes into account the perturbing interaction of the oscillating microwave field, reveals an absorption line that has the form of a Lorentzian function (193,194). The full width at half height of the lineshape is inversely proportional to $1/T_2$. Therefore, faster T_2 times lead to broader lineshapes. However, the T_1 relaxation pathway prevents infinitely narrow absorption lines by establishing finite lifetimes for excited states. Both relaxation mechanisms are critical to signal generation as only a portion of the ensemble of spins contributes to the absorption of microwaves per unit of time. Outside of these processes, few technical applications can be employed to enhance the EPR signal. Among these, decreasing the absolute temperature or increasing the magnetic field strength has already been mentioned. In the absence of narrowband microwave signal detectors, a common EPR scheme to enhance sensitivity employs magnetic field modulation in combination with phase-sensitive detection which effectively filters out noise (193). The result of this detection scheme is an EPR lineshape that is the first derivative of the absorption signal.

Strategy of site directed spin labeling

A chief focus in structural biology is the identification of the molecular determinants governing the construction of complex assemblies, ligand/inhibitor interactions and enzymatic reactions. A fundamental understanding of how these and other elements are linked together to drive critical biological processes demands focused investigation to probe the structure/function relationship. Obtaining a picture, preferably one at atomic resolution, often represents a milestone in this endeavor. Yet the challenge is to not only define the spatial relationship of structural elements, but to elucidate their relative contributions to a functional process. Importantly, the experimental means by which molecular machinery are interrogated sets boundaries on the answers to an ever-deepening well of relevant questions. For instance, at its very best x-ray crystallography can define molecular architecture under a given set of conditions. However, this structural "snapshot" can only stimulate hypotheses regarding a mechanism of action.

The information gap between a protein of known structure and a mechanism is the dynamic fluctuations in the structure that facilitate functional activity. Structural dynamics may lead to the formation of stable intermediate states related to a conformational cycle. One approach to address this issue is to crystallize the protein in a different set of conditions that putatively favor a different conformational intermediate. Whereas the identification of the exact conditions may be an experimental bottleneck, some dynamic features may remain unresolved due to a non-unique spatial position of loop regions or by constraining crystal lattice forces. Trapping specific conformations with inhibitors may yield an altered conformation, but it is difficult to interpret this data in the context of a functional cycle.

Spectroscopic techniques are a viable alternative to deciphering the role of both structure and dynamics in protein activity. Specifically, EPR spectroscopy offers many advantages over more popular techniques such as crystallography and NMR spectroscopy. Crystallography typically demands high protein concentrations (mg quantities) and conditions conducive for the formation of an ordered crystal lattice (192). These conditions most likely will not resemble the normal biological medium sampled by the protein. Although NMR is sensitive to dynamic processes, the ability to observe sharp resonance lines decreases with increasing molecular size due to slower rotational correlation times and enhanced T_2 relaxation rates (159). However, sophisticated pulse sequences and magnetic resonance techniques, such as transverse relaxation optimized spectroscopy (TROSY) and paramagnetic relaxation enhancement, provide a means of determining structural restraints of macromolecules approximating 100 kDa. This is illustrated by the recent solution NMR structure of diacylglycerol kinase (195). In EPR, proteins of arbitrary size can be investigated in more native-like environments with structural resolution at the level of the backbone fold (196,197). In addition, EPR does not demand large sample preparations, requiring as little as ~100 pmol of labeled protein. As mentioned in the previous section, the fundamental requirement of EPR spectroscopy is having an unpaired electron. The presence of unpaired electrons in a biological system represent a potent redox hazard in the cell (superoxide,

for instance). Thus, free radicals are a transient species in a healthy biological system. Nitroxide spin labels are stable free radicals that are commonly introduced into a protein sequence and used to report specific parameters that characterize the microenvironment of the spin label side chain (198-200). Changes in these parameters are often correlated to the intrinsic protein dynamics related to functional activity. The following discussion highlights methods in EPR used to extract fine structural detail.

Incorporation of nitroxide radicals

Most commonly, a site for introduction of a nitroxide spin label in a protein sequence is created by site directed cysteine mutagenesis (200). The sulfur moiety of the cysteine is subsequently used as the site of nitroxide attachment with a sulfhydryl-specific spin label probe. This reaction scheme is often achieved by methanethiosulfonate derivatives as depicted in Figure 18. In theory, spin labels can be incorporated at any site along a peptide chain using this method, although labeling sites with restricted access (buried sites) may require modifications of the protocol. This procedure typically requires initial mutations to remove native cysteine residues to control for label placement (200). Recently, Fleissner and colleagues described a method of incorporating a genetically encoded unnatural amino acid which is subsequently reacted with hydroxylamine reagent to generate the nitroxide moiety (201). This would seem to eliminate the need of cysteine mutagenesis and potentially expand the application of EPR to those molecules that possess cysteine residues required for function. Experimentally, labels are introduced one at a time in a protein sequence. As a result, the EPR method is labor intensive requiring many spin labeled mutants to fully characterize structure and dynamics. Although most EPR methods call for only a single site for incorporation, it is appropriate under certain circumstances to incorporate a second site to measure the strength of dipolar coupling between labels (discussed in a subsequent section). Because site directed spin labeling requires the incorporation of extrinsic labels, it is important to ascertain the structural and functional integrity of mutant proteins. This analysis should occur at two stages: following mutagenesis and after subsequent nitroxide

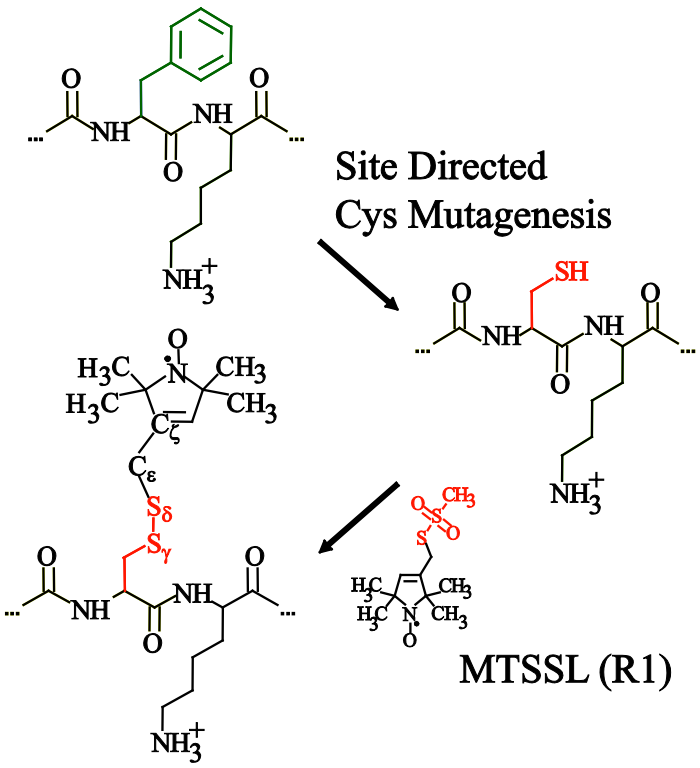

Figure 18. Site-directed spin labeling. Targeted Cys mutagenesis introduces a sulfhydryl moiety for the attachment of a nitroxide spin label, R1. This procedure requires the conversion of native Cys residues to non-reactive residues.

modification. Assessing the activity of the protein in this manner deconvolutes the specific contribution of cysteine mutagenesis and/or labeling to alterations in function. Nevertheless, a systematic study of T4 lysozyme structure and function after labeling indicated that core locations or sites directly involved in function significantly alter the activity (202). Furthermore, labeling of core residues was found to be the most perturbing as measured by thermal denaturation studies. However the induced thermodynamic perturbations were at the level of those found for natural amino acid substitutions. Protein surface sites not directly related to the binding site of T4L tolerated the spin label with little thermodynamic and functional perturbation. Another consideration is the labeling efficiency which may influence the interpretation of both structural and functional data. As will be discussed, labeling efficiency is a crucial element in the

interpretation of broadened EPR spectra due to dipolar coupled spin labels. Furthermore, the correlation between labeling efficiency and functional activity may provide insight into the perturbing effects of spin labeling.

EPR parameters: spin label mobility

The applicability of the nitroxide probe to the determination of local structure originates with the sensitivity of the spin label to its orientation in a magnetic field. In brief, a sweep of the magnetic field under constant microwave irradiation will induce absorption at three resonance positions determined by the electron g factor and is reported in the first derivative lineshape of the EPR signal. The intrinsic anisotropy of the g and A_o tensors allows for a range of lineshapes to be observed with boundaries characterized by two motional extremes. Hence the rate of motion of the nitroxide in the magnetic field impacts the observed lineshape. This is illustrated in Figure 19 for an array of rotational correlation times (τ_c), assuming isotropic rotational diffusion along all the principle axes of the magnetic field frame of reference (i.e. the nitroxide tumbles in all directions without preference). The fast motion limit is achieved when $\tau_c \cong 0.01$ ns. As τ_c increases, the rotation of the nitroxide decreases and the time averaging of the g and A_o tensors is reduced which broadens the EPR spectrum (bottom right spectrum of Figure 19).

This principle of nitroxide motional averaging is generally applicable to spin labels that are attached to a polypeptide chain. However, the motional degrees of freedom are complicated by the modification. An attached spin label no longer tumbles freely in solution as it is now coupled to the motion of the protein. Therefore, the EPR lineshape is reflective of the available degrees of motional freedom of the attached spin label as well as the dynamic properties of the tumbling macromolecule (203). Specifically, the overall tumbling rate of the protein, local dynamic fluctuations of the backbone to which the nitroxide is attached and the intrinsic rotation of the spin label about the bonds that tether the probe to the protein contribute to the spin label dynamics observed in the EPR lineshape. For large macromolecules (>50 kDa), such as

membrane proteins, the overall rate of protein tumbling is too slow ($\tau_c \cong 10^{-8}$ s or slower depending on solution viscosity) to have an effect on the EPR spectrum (10^{-11}-10^{-9} s timescale, Figure 19) (196,202). Therefore, the motion of the spin label side chain is largely dictated by bond rotations and backbone dynamics. Separation of these two variables requires a full simulation of the EPR lineshape (203,204).

Figure 19. The EPR lineshape depends on the spin label rate of rotation. Slower reorienation rates of a nitroxide causes broadening of the resonance lines, which increases the breadth of the EPR spectrum. Lineshapes were simulated using standard g and A tensor values in the program MatLab. Special thanks to Dr. Richard Stein for help with generating the simulations.

The spin label R1 in Figure 18 is the most commonly used in EPR studies of proteins due to the high reaction selectivity for cysteine sulfhydryls and its relatively small size (on the order of a Trp side chain) (200). A detailed analysis of this particular nitroxide side chain suggested that intrinsic spin label rotation is largely limited to C_ε—C_ζ and the C_ε—S_δ bonds (202). Rotation about the disulfide linkage is restricted by a sufficiently large energy barrier ($\geq$ 7 kcal/mol). Also,

rotation about the S_γ—C_β is negated by interaction of the S_γ atom with the C_α hydrogen, which was subsequently supported by crystallographic analysis of spin labeled T4 lysozyme. Importantly, these observations suggest that the chemical structure of the nitroxide side chain will impact the EPR lineshape. Mchaourab et al demonstrated several cases where the lineshape is modulated by different side chain structures that alter specific interactions with the backbone and nearest neighbor residues (205).

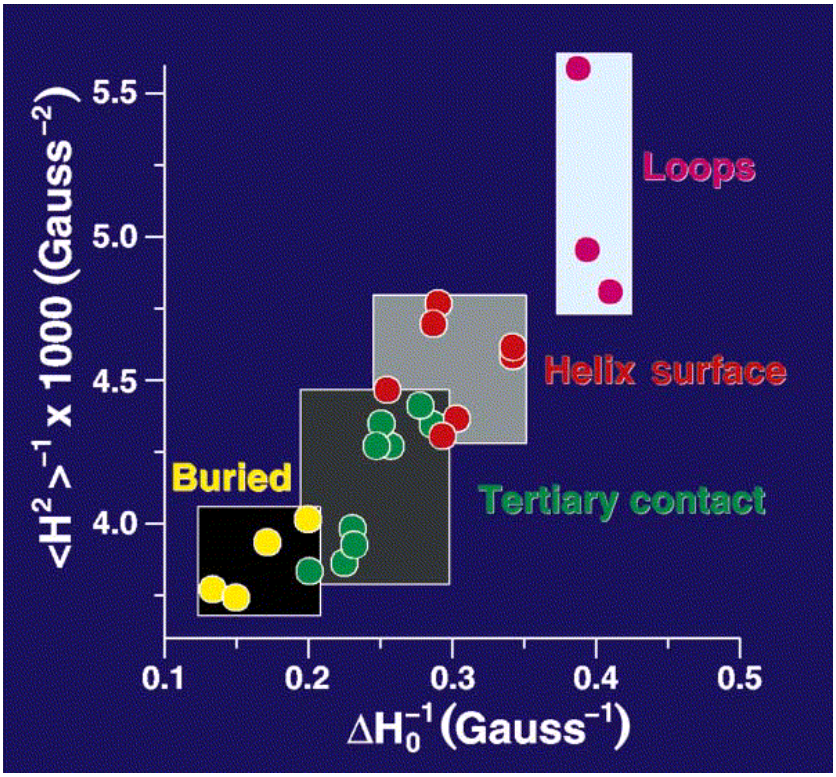

Figure 20. Correlation of spin label mobility with site of attachment. Spin labels attached to the backbone of flexible loops (pink dots) demonstrate high mobility characterized by a narrow central line and second moment. In the other extreme, buried spin labels (yellow dots) exhibit slow motion as described by larger values of both parameters. Intermediate values typically reflect contact interactions (green dots). The figure was adopted from Ref 196.

Besides the structure of the side chain, Mchaourab and coworkers showed that spin label dynamics are contingent on the local molecular structure of the protein (202). In studies using the R1 spin label and T4 lysozyme as a model, attachment to different structural elements led to distinct lineshapes. The results suggested that a phenomenological analysis of the EPR central line width (ΔH) or the spectral second moment ($\langle H^2 \rangle$, represents the breadth of the spectrum) could qualitatively differentiate between spin labels attached to buried, surface or loop sites as well as those in tertiary interaction with structural elements. These terms established a general correspondence between the local structure of the protein and the "mobility" of the spin label. As the mobility (which refers to the collective motions of the label) of the probe increases, both the ΔH and the $\langle H^2 \rangle$ decreases as reflected by an increase in signal amplitude and narrowing of the three resonance lines. Plotting the inverse $\langle H^2 \rangle$ as a function of the inverse ΔH demonstrated a linear increase in spin label mobility from buried to loop sites (Figure 20) (202). The mobility of the spin label can thus be used to report structural characteristics of the immediate surroundings. Furthermore, the exquisite sensitivity of the probe to the environment allows detection of conformational changes that may be associated with function through changes in lineshape.

EPR parameters: spin label solvent accessibility

The placement of a spin label in a protein not only leads to a "fingerprint" of the local structure manifested in the EPR spectrum, but may also result in differential accessibility of the spin label to solvent (197,200). This adds a new dimension to the spectroscopic analysis and effectively increases the structural resolution of the EPR technique. Recently, a pulsed EPR method has been utilized to determine the accessibility of a nitroxide probe to water within a membrane protein (206). This method relies on proton modulation of the time-dependent echo decay of the EPR signal to estimate the number of water molecules in close (3-6Å) vicinity. However, the most common method of determining spin label solvent accessibility is by measurement of the collision frequency of the spin label with a diffusing paramagnetic reagent

using a conventional CW-EPR method (207). This method is based on Heisenberg exchange where a bimolecular reaction between two unpaired electron species results in a swapping of spin orientations. That is, if an unpaired electron possessing the β state energy (e_β^1) collides with another unpaired electron in the α (e_α^2) state, the electron spin exchange process dictates that (e_β^1)→ (e_α^1) and (e_α^2)→ (e_β^2).

The protocol yields a dimensionless parameter, Π, which is directly proportional to the Heisenberg exchange rate (W_{ex}). This exchange rate is also directly proportional to the concentration of the collisional reagent and a rate constant which is coupled to the diffusion rate of the paramagnetic species:

$$\Pi = \alpha W_{ex} = k_{ex} C_r \sim D_r \qquad (14)$$

where α is a proportionality constant, k_{ex} is the exchange rate constant, C_r and D_r is the concentration and diffusion rate constant of the paramagnetic collisional reagent, respectively (207). Equation 14 indicates that in the absence of diffusion W_{ex} cannot be measured and, therefore, Π is undetermined. Ideally then, the collisional reagent should be a small, water soluble compound with a high diffusion rate to ensure a strong exchange interaction (207). Both Ni(II)ethylenediamine diacetic acid (NiEDDA) and molecular oxygen (O_2) possess these properties and are commonly used collisional reagents. Because W_{ex} is related to changes in T_1, experiments that exploit the coupling of the spin label to the surrounding environment (lattice) will provide insight to the exchange interaction. In practice, Π is usually determined from power saturation of the EPR signal (207). Because nitroxides have slow relaxation times ($T_1 \approx 1\mu s$), increasing the microwave power will lead to saturation of the α/β spin states (i.e. the spin populations are equalized) and the EPR signal will disappear (Figure 21). The chosen collisional reagent will possess a fast T_1 time relative to the spin label and, upon collision, an excited nitroxide electron will transfer its energy to the fast-relaxing compound. The net effect of this process is that T_1 for the nitroxide appears to get shorter and saturation of the EPR signal is impaired. Plotting the central line amplitude of the EPR spectrum as a function of the square root

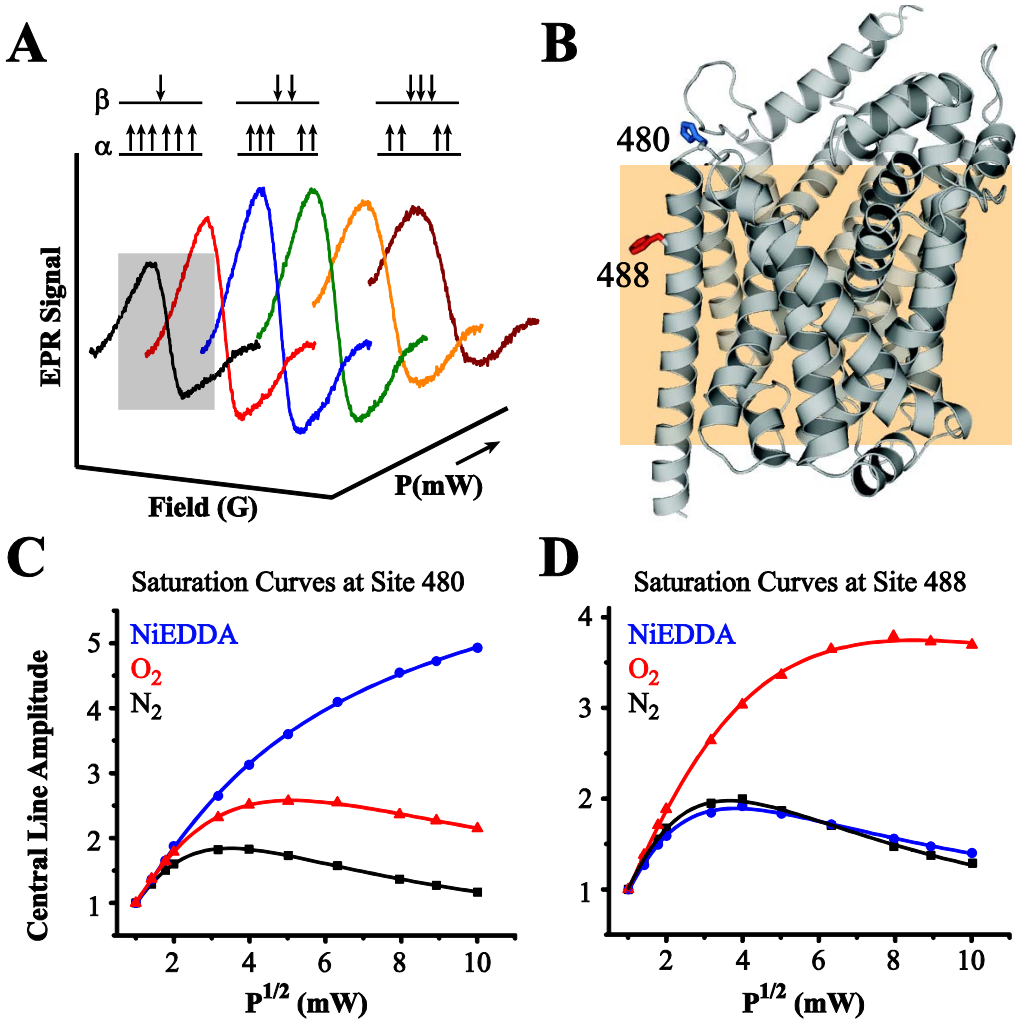

Figure 21. Correlation of power saturation curves with spin label environment. (**A**) Increasing the microwave power increases the transitions from the α state to the β state, which increases the signal amplitude (gray box). In the absence of relaxing agents, high microwave powers will equalize the spin states resulting in a power-dependent *decrease* in signal intensity (also shown in N_2 controls in (**C-D**). (**B**) The differential solubility of fast-relaxing paramagnetic reagents (NiEDDA and O_2) allows the unique determination of spin label environment. (**C**) The high NiEDDA accessibility at site 480 in LeuT relative to O_2 and N_2 control determined from power saturation curves suggests a water exposed position of the spin label. (**D**) In contrast, the high O_2 accessibility at site 488 indicates that the spin label samples the lipid phase. An approximate membrane-water interface for LeuT is outlined by an orange box in (**B**). Power saturation curves are fit using a non-linear least squares algorithm as described in the *Experimental Methods* of Appendix B. The LeuT PDB code 2A65 is shown in (**B**).

of the microwave power results in a saturation curve which describes the EPR signal behavior in absence and presence of a fast-relaxing reagent.

The power saturation curve is described by the parameter $P_{1/2}$, which is obtained from a non-linear least squares fit of the data. $P_{1/2}$ is the microwave power required to achieve half of the unsaturated EPR signal amplitude and this number is used to calculate the value of Π (207). The value of $P_{1/2}$ is determined in the absence and presence of a fast-relaxing species, which are then used to determine $\Delta P_{1/2}$. Furthermore, three factors influence $P_{1/2}$: the T_1 time (see above), the T_2 (spin-spin relaxation) time and a variable (Λ) that describes the efficiency of the EPR resonator (207). Essentially, Λ describes the variability of instrument response and can be properly accounted for by determining the $P_{1/2}$ of a known standard. W_{ex} is also related to changes in the T_2 time and, because T_2 impacts the EPR signal line width, the presence of a fast-relaxing agent can lead to Lorentzian line broadening (208). As shown in Equation 15, isolation of the T_1 component of the power saturation curve is achieved by dividing $\Delta P_{1/2}$ by the peak-to-peak central line width (ΔH_{pp}) of the EPR spectrum to remove contributions of T_2 relaxation. This value is subsequently normalized by a standard to remove instrument bias (207).

$$\Pi = \frac{\left[\frac{\Delta P_{\frac{1}{2}}}{\Delta H_{pp}}\right]}{\left[\frac{P_{\frac{1}{2}}}{\Delta H_{pp}}\right]_{ref}} \qquad (15)$$

In general, there is a direct correlation between the mobility and accessibility of the spin label. That is, high spin label accessibility is often degenerate with high spin label mobility, such as observed in exposed loop regions. Importantly, the absolute value of Π, as shown in Equation 14, is a function of the concentration of the collisional reagent. Therefore, the structural interpretation of the accessibility values from multiple sites can only be realized from experiments using identical concentrations of the collisional reagent.

A power of the accessibility measurement lies within its ability to identify secondary structural elements. If a structural element is asymmetrically solvated, the pattern of accessibilities revealed by a nitroxide scan along that element will be consistent with the periodicity (3.6 for α-helices; 2.0 for β-sheets) and phase of the polypeptide chain reflecting the three dimensional organization (197). Furthermore, the topological organization of membrane proteins can be investigated due to the differential solubility of NiEDDA and O_2 in the lipid bilayer (209). A concentration gradient of O_2 exists toward the center of the bilayer, while the concentration of NiEDDA in the lipid phase is very low. Hence, the pattern of NiEDDA and O_2 accessibilities will reveal the location of transmembrane segments as well as any solvent exposed connecting loops (Figure 21). In addition, the concentration gradient of O_2 in the bilayer allows for the detection of tilt angles of transmembrane segments. Changes in the pattern of accessibilities have been correlated with structural dynamics (210,211). Other techniques based on chemical reactivity have also been shown to be informative about dynamic changes in protein structure, albeit with lower resolution. The information Π divulges about conformational changes initially may be considered analogous to that obtained by MTS reactivity experiments with native or engineered cysteines. "Accessibilities" from these experiments typically are inferred indirectly by changes in the MTS-induced protein inactivation rate in the presence of ligands (160,187). In contrast, spin label accessibility is determined directly because the value of $P_{1/2}$ is a direct consequence of a physical interaction with a diffusing reagent usually without compromising structural or functional integrity.

EPR parameters: distance-dependent dipolar coupling

The preceding discussion highlighted two spectroscopic parameters that define the local structural environment of the spin label. The sensitivity of these parameters confers the ability to measure distinct conformational changes within a protein, effectively discerning differences between specific environments. In addition to these site specific measurements, global structural constraints can be generated by measuring the energetic interaction between two spin labels. In

contrast to crystallography, distance-dependent spin-spin coupling establishes the spatial relationship of structural elements in solution. The value of this information is highlighted by recent computational studies demonstrating significant improvement of structural models generated by the *de novo* folding algorithm Rosetta by reducing the conformational search space (212). Furthermore, the information obtained from spin label mobility, solvent accessibility and dipolar coupling will uniquely define the three dimensional structure at the level of the backbone fold that can be directly compared to crystal structures (210,213).

Spin-spin interaction occurs at two levels distinguished by the specific coupling mechanism and each of these two mechanisms dominate in different distance regimes. As a result of the presence of two electron spins, the effective spin Hamiltonian must be modified to reflect changes in the energetic transitions.

$$\mathcal{H} = \beta H_o \cdot g^1 \cdot S^1 + \beta H_o \cdot g^2 \cdot S^2 - \omega_n (I_z^1 + I_z^2) + \gamma I^1 \cdot A^1 \cdot S^1$$
$$+\gamma I^2 \cdot A^2 \cdot S^2 + S^1 \cdot D \cdot S^2 + J S^1 \cdot S^2 \qquad (16)$$

In Equation 16, ω_n is the Larmor frequency of the nitrogen nucleus, γ is the electron gyromagnetic ratio, D is the dipolar coupling tensor and J is a spin-spin exchange factor (193). The numerical superscripts designate the two electron spins. Spin-spin interaction via scalar J coupling occurs through chemical bonds, as probed in NMR spectroscopy, or through very close spatial interactions facilitated by orbital overlaps, such as in Heisenberg exchange described above (159,193). However, J coupling decreases exponentially with increasing distance and contributes little to the overall interaction beyond ~8Å (214,215). For spin labels, the length of the tether (~7Å) linking the nitroxide to the protein backbone precludes through-bond interactions. In the absence of direct orbital interaction, J coupling is generally disregarded.

The dipolar interaction term of Equation 16 represents through-space spin coupling between probes that can be measured from 8-70Å. In the absence of both dipolar and J coupling, Equation 16 reduces to a Hamiltonian that describes the sum of two non-interacting spins. The

energy of the dipolar interaction is inversely proportional to the cube of the distance (r^3) and is dependent on θ which describes the angle between the external magnetic field and a line that joins the two spins (193,200,214). Equation 17 states the energetic relationship between two interacting dipoles (μ) and the distance between them.

$$E = \frac{\mu_1 \mu_2}{r^3}(3cos^2\theta - 1) \quad (17)$$

The sum of all orientations of both spin labels from parallel (θ=0°) to perpendicular (θ=90°) between the two dipole moments results in a composite Pake pattern in which the frequency of separation between the two peaks is proportional to r^{-3}. A sum of Pake patterns is typically used as a broadening function in the analysis of EPR spectra demonstrating dipolar coupling (Figure 22 and described below) (215). The dipolar interaction between nuclei is averaged to zero by isotropic motion in solution NMR, and is effectively removed by spinning the sample at the "magic angle" of 54.7° in solid state NMR (159). The angular dependence creates an inherent anisotropy of the dipole-dipole interaction. For freely moving spin labels, on a protein surface for instance, an isotropic distribution of θ is generally assumed which leads to simple models of analysis (215).

When the dipolar interaction is sufficiently strong (<20Å), spin-spin coupling significantly alters the EPR lineshape by broadening the spectrum (Figure 23). As a result the strength of the interaction can be assessed qualitatively from the degree of line broadening or measured directly by a variety of lineshape analysis techniques. If the two spin labels adopt a unique orientation, a full simulation of the EPR lineshape can extract the distance information (216). However, this is not normally the case. Approximations of the spin-spin distance can be made if the protein tumbles sufficiently slowly so as not to reduce contribution of the dipolar coupling to the EPR spectrum through rotational averaging of the interspin vector (196,217). Furthermore, approximations by Fourier convolution/de-convolution analysis of the spectral lineshapes assume that the dipolar interaction spectrum is a convolution of a non-interacting

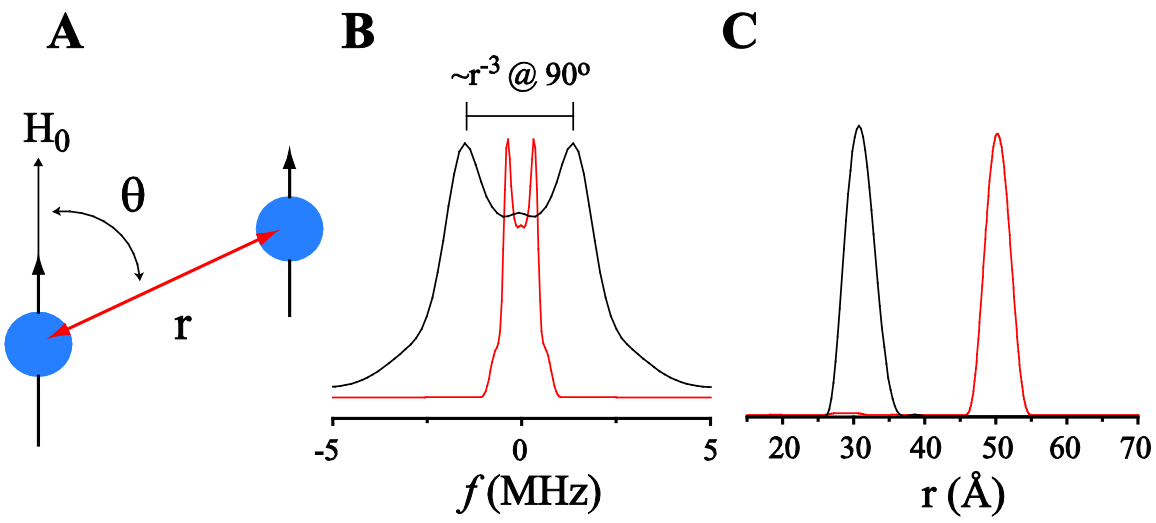

Figure 22. Relationship between the angular-dependent dipolar interaction and the distance. (**A**) The energetic interaction between two magnetic dipoles is dependent on the distance r and angle θ. (**B**) The frequency of separation between the two peaks of the Pake pattern is inversely proportional to the distance at θ = 90°. The Pake patterns in (**B**) give rise to the distance distributions in (**C**). The broader, black-line Pake in (**B**) is associated with a shorter distance, indicating a stronger dipolar interaction.

spectrum (obtained from the spectral sum of corresponding single mutants) with a Pake broadening function (215,218). The inherent flexibility of the nitroxide, and dynamics from the protein backbone, generally leads to a distribution of distances, which is plotted as a probability of a distance (P(r)) as a function of a given distance (r), as opposed to a singular distance. However, a "tether-in-a-cone" model has been developed that simulates the EPR spectrum of nitroxides and is beneficial for deciphering distance distributions that include specific label orientations from nitroxides that demonstrate a more ordered (slower τ_c) lineshape (216). Both of these approaches impose a Gaussian model upon the resulting distance distributions.

For distances above 20Å, the line broadening due to dipolar interactions (3-5 Gauss) can no longer be resolved because of the intrinsic width of the EPR lineshape (6-8 Gauss) (214). Yet spin-spin coupling can be probed with pulse EPR methods to extract distance information. This technique relies on the time-dependent spin echo decay in the transverse plane of the magnetic

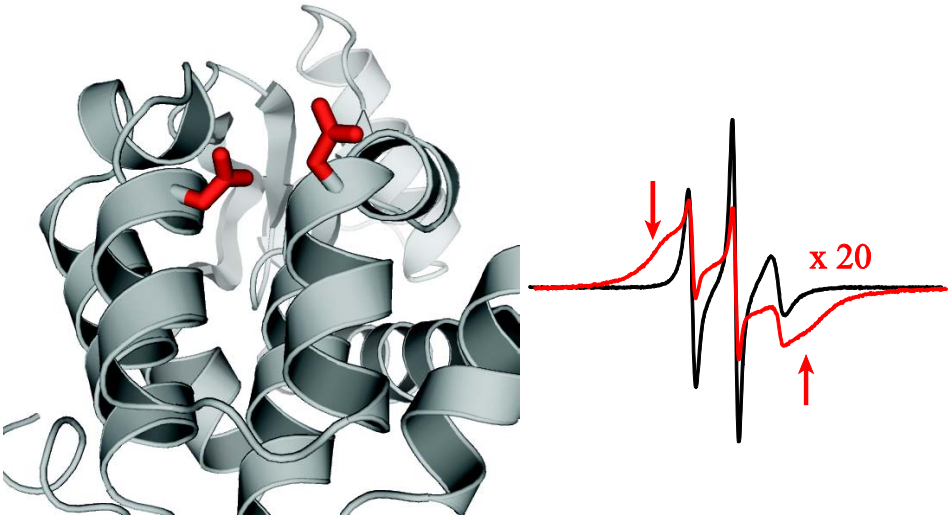

Figure 23. Dipolar broadening of the EPR spectrum. Spin-spin interaction will broaden the EPR spectrum (red trace) if two spin labels are within 20Å of each other (arrows). The amount of broadening depends on the distance between the probes. The red trace has been multiplied by a factor of 20 to emphasize the outer intensities arising from the dipolar interaction relative to the sum of non-interacting spin labels (black trace). Data adopted from Ref 208.

field following a series of microwave pulses designed to selectively excite two separate populations of spin labels (219). Double electron electron resonance (DEER) spectroscopy follows a four-pulse protocol shown in Figure 24A and the **observe** and **pump** pulses are qualitatively defined in Figure 24B. Recall that the magnetic moment of electron spins results in a bulk magnetization along the direction (traditionally taken along the z-axis) of the external magnetic field and these spins rotate about the field characterized by the Larmor precession frequency. To observe dipolar coupling requires perturbation of these spins at thermal equilibrium. This is achieved by a $\pi/2$ (90°) pulse of microwaves along the x-axis at a specific frequency to tip the bulk magnetization of the **observe** spins in the x-y plane. The decay of this magnetization back to thermal equilibrium (spin alignment along the z-direction) will contain the information regarding dipolar coupling and is a function of T_1 (alignment along the z-axis) and T_2 (decay along x-y plane) relaxation. Following the $\pi/2$ pulse, the excited spins are briefly coherent along the x-axis; however, each spin experiences a slightly different magnetic field depending on

their coupling interactions which results in a slightly different precession frequency subsequently resulting in dephasing of the spins in the x-y plane (i.e. the spins fan out in either direction in the transverse plane away from each other). The spin echo, which contains the dipolar information, is formed by a π (180°) pulse which has the net effect of reversing the direction of the dephasing in the x-y plane (i.e. spins are moving *toward* each other instead of *away* from each other). The point at which the spins are transiently coherent corresponds to the peak of the first spin echo. However, we do not observe this echo.

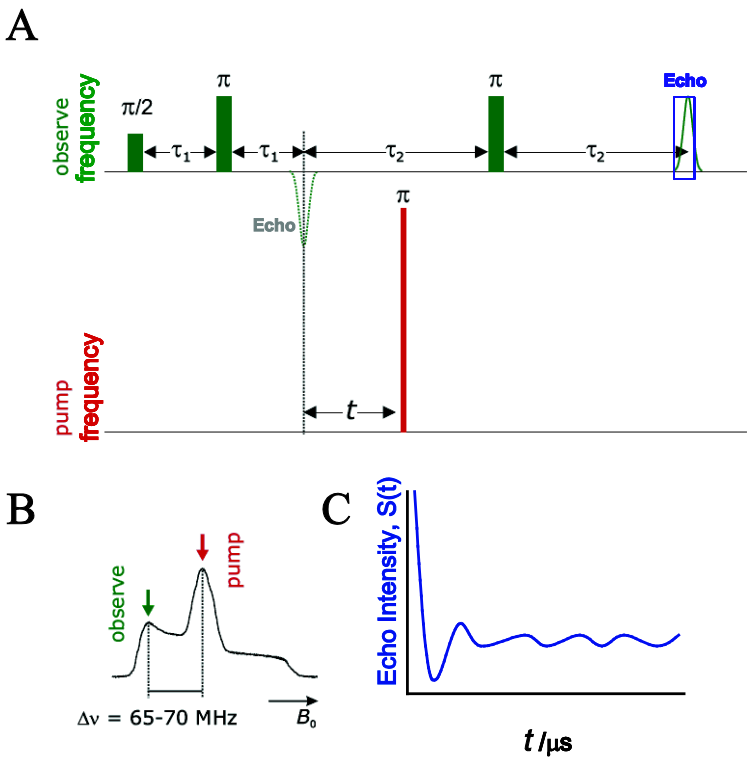

Figure 24. DEER pulse protocol and spin echo decay. (**A**) Standard four-pulse protocol for DEER spectroscopy. (**B**) The EPR absorption signal illustrating the positions of the pump and observe pulses. The pump pulse specifically excites an ensemble of spins that absorbs radiation at the central part of the spectrum. The effect of the pump pulse on the dipolar interaction is observed by the time-dependent behavior of the spin echo formed by a low field ensemble of spins (**C**).

After the **observe** spin π pulse, a π pulse of microwaves is applied corresponding to the frequency of the **pump** spins (Figure 24). This has the effect of flipping the bulk magnetization of this spin ensemble (initially along +z-axis) in the -z direction, and this effect alters the magnetic field experienced by the observe spins that are dipolar coupled and, therefore, their behavior as they return back to thermal equilibrium. A final π pulse at the **observe** spin frequency re-focuses the perturbed spins into the observed spin echo. In the experiment, the position of the **pump** π pulse is moved incrementally defined by τ to determine how this pulse modulates the final observe spin echo. The data from the experiment is collected by plotting the amplitude of the observe spin echo as a function of τ. If the interaction is sufficiently strong, oscillations will appear in the DEER signal. The frequency (or frequencies) that characterize this time-dependent decay is related by r^{-3}. The rate of signal decay to baseline is related to the width of the distance distribution. Importantly, the phase memory time, T_m, for the observe spins following perturbation limits the length of detection in the experiment. T_m is primarily a function of T_2 relaxation and can be extended by decreasing the absolute temperature. Because T_m is short for large proteins, a complete characterization of the echo decay requires lowering the temperature substantially, typically near liquid N_2 temperatures (~80 K). Obviously at these temperatures the sample is frozen and the resulting distance distributions are considered to be a static representation of isotropically averaged distances between the probes (215,220).

To extract distance information, the DEER signal can be Fourier transformed into the frequency domain to obtain the corresponding dipolar (Pake) spectrum. However, the DEER signal can be directly analyzed by fitting routines, such as through a parameterized Gaussian model. In the absence of parameterization, it must be noted that obtaining distance distributions from the DEER signal is inherently complicated because the Fredholm relation (Equation 18) connecting the distance distribution P(r) to the experimental data V(t) is an ill-posed problem:

$$\int K(r,t)P(r)dr = V(t) \qquad (18)$$

where K(r,t) is the ensemble average of dipolar coupling. This means that a unique solution to the equation is not mathematically attainable. Tikhonov regularization, which directly simulates the time-domain data, has been shown to be a suitable method for *approximating* a unique solution to the Fredholm equation (221). This method is contingent on identifying an appropriate regularization parameter which stabilizes the Fredholm equation and balances the uniqueness of the fit with the smoothness of the distance distributions. Therefore, critical to the analysis are data sets that possess a good signal to noise ratio, else the regularization will introduce artificial peaks in the distance distribution.

The information obtained from measuring the distance-dependent dipolar coupling may be considered complementary to fluorescence resonance energy transfer in which the FRET efficiency demonstrates an r^6 distance dependence. With the major caveat from both techniques that the distance measured is between probe centers and not the C_α or C_β carbons, there are several advantages to the EPR technique. First, FRET is complicated in application due to problems with light scattering, especially in the context of lipid phases (215). Second, EPR only requires labeling at two sites with the same probe. Traditional FRET experiments require two different labels, a donor and an acceptor, whose optical properties are properly tuned for sufficient overlap of the donor emission and acceptor absorbance envelopes. Labeling efficiency of the acceptor probe is the major source of error in FRET because low acceptor labeling will lead to a decreased energy transfer efficiency which would translate to an artificially longer distance (139). To circumvent labeling problems, homotransfer FRET, which occurs between identical fluorophores, has been shown to be an accurate alternative (222). Similar to heterotransfer FRET, CW-EPR analysis of broadened lineshapes can be complicated by insufficient labeling. Because broadened lineshapes yield lower absolute intensities, the presence of singly-labeled sites can dominate the EPR spectrum through the larger amplitude lines. Because of this, lineshape analysis procedures must include additional parameters to account for the presence of non-interacting spins. In contrast, DEER spectroscopy is only sensitive to those

spins which are dipolar coupled and proteins that are underlabeled do not contribute to the intramolecular time-dependent echo decay.

Thirdly, FRET reports a single distance that assumes an average dipole orientation of the two probes (139). This can lead to substantial deviations in the accuracy of the FRET measurement (140). Although distance distributions, especially broad ones, from the EPR experiments emphasize the intrinsic difficulty of identifying a unique distance between probes, these distributions may be informative as to the dynamic nature of a particular conformational intermediate, a concept that is apparently well justified as discussed in the subsequent section. However, the local dynamics of the probe may also contribute to the width of the distribution depending on their relative orientation to each other (213,223). A qualitative assessment of changes in spin label dynamics with a given condition through changes in the EPR spectrum may indicate possible contributions to the width of the distribution. In some cases, it may be required to determine all possible rotameric configurations of the spin label to separate the contribution of probe dynamics from backbone fluctuations (224). In the following section, a brief summary of EPR applications to specific membrane proteins establish the power of the technique to define the nature, magnitude and direction of conformational changes in protein structure.

Practical application of EPR spectroscopy to a primary active membrane transporter

EPR spectroscopy has been applied to a variety of protein systems to investigate outstanding questions regarding molecular structure and mechanism. Specifically, this method has been particularly insightful toward the structural dynamic basis of membrane protein functionality. Notable examples include studies of the photoactivation of bacteriorhodopsin, conformational changes in K^+ channel homologs and structural transitions in the sugar transport mechanism of *E. coli* lactose permease (LacY) (191,225,226). An extensive experimental dataset including spin label mobility, solvent accessibility and DEER analysis has characterized the structure of MsbA in various intermediate states. MsbA is an *E. coli* membrane transporter that couples the movement of lipid A to ATP hydrolysis and belongs to a subgroup of ABC (ATP

binding cassette) transporters, which include human P-glycoprotein (210). Investigation of the structure and mechanism of membrane proteins in this class by multiple laboratories is driven in part their implicated role in multi-drug resistance.

Crystal structures of MsbA, which functions as a homodimer, have previously suggested the existence of different conformational states putatively associated with a thermodynamic cycle of substrate transport (227). In the absence of nucleotide, apo MsbA has been found to crystallize in a cytoplasmic open and closed conformation, suggesting large domain movements in the cytoplasm. In the presence of nucleotide, extensive interactions between the cytoplasmic nucleotide binding domains (NBD), the intracellular domains (ICD) and transmembrane domains (TMD) from each monomer closed off cytoplasmic access to the V-shaped cavity formed in the open apo structure. These movements also facilitated increased access from the extracellular side suggesting that this conformation represented an outward-facing state.

The first EPR analysis of MsbA by Dong and colleagues investigated the solution structure in four biochemical intermediate states (210). Extensive mapping of the spin label mobility and solvent accessibility along helix 2, 5 and 6 that span the ICD and TMD revealed the topological location and orientation of these segments in proteoliposomes (Figure 25). In the apo state, the pattern of NiEDDA accessibilities along the ICD suggested a predominately open conformation toward the cytoplasm. The addition of either AMP-PNP (a non-hydrolyzable ATP analog), ADP-Vi or ATP-Vi (stabilization of the high energy post-hydrolysis transition state) revealed similar changes in the EPR parameters consistent with a reversal of the transporter orientation from inward-facing to outward-facing. The similarity of the results with the nucleotide binding studies suggested that ATP binding provides the power stroke for cytoplasmic closure.

The spin label mobility and accessibility analysis was extended to other helices in the TMD and connecting loops (211). Together with the previous findings, the EPR studies established that nucleotide-dependent conformational changes take place to facilitate alternating access of the putative substrate binding chamber. However, the magnitude of these changes had

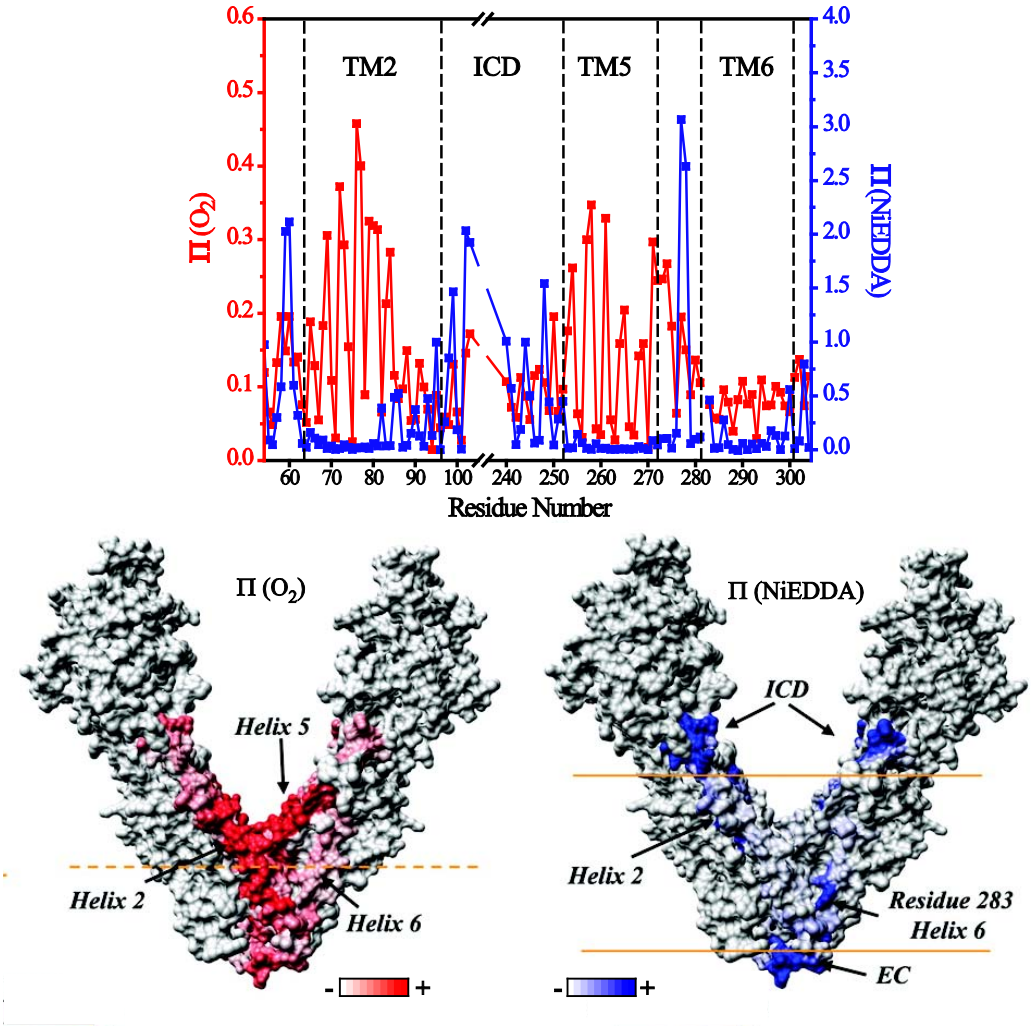

Figure 25. Accessibility of Apo-MsbA. The pattern NiEDDA and O2 accessibility across three TM segments and the ICD domain (top panel) illustrates the topological arrangement of these helices in proteoliposomes. Mapping of solvent accessibility onto the open Apo crystal structure identifies boundaries of the membrane-water interface. Figure adopted from Ref 210.

not been investigated. DEER spectroscopy of MsbA, as well as homotransfer FRET, has suggested that large conformational motions occur upon ATP binding to bring the NBDs and ICDs together from the apo state (213,223). Striking evidence of these distance changes are illustrated for certain sites such as 121 at the N-terminus of helix 3. Here, the distance change is at least 30Å, since in the apo state 121 is separated by 50Å and upon ATP binding are close enough (≤15Å) to exhibit strong dipolar coupling in the EPR lineshape (Figure 26B).

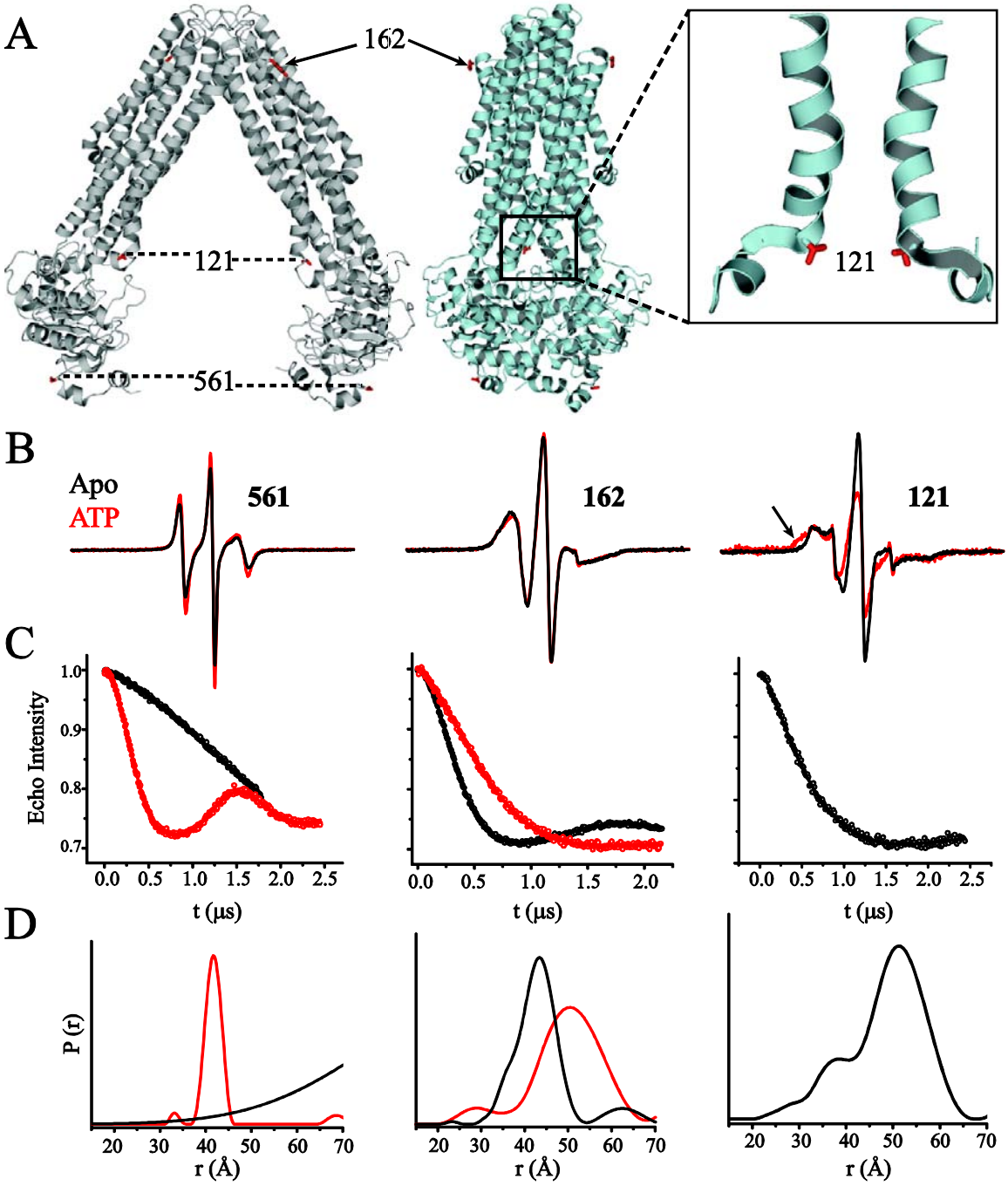

Figure 26. Mapping of conformational changes by spin label dipolar coupling. (**A**) Crystal structure of open Apo-MsbA (gray) and the closed, ATP bound state (cyan) highlighting the location of specific sites interrogated by EPR distance analysis. (**B**) EPR spectra of spin labels at these positions in both states. (**C**) The Tikhonov fits of the time-dependent spin echo decays and resulting distance distributions (**D**) for both states. Positions 561 and 162 show opposite changes distance between states, consistent with rigid body movement of helices in an alternating access mechanism. Symmetry-related spin labels at site 121 in the ICD is separated by ~50Å in the Apo state (**D**), but is close enough for dipolar broadening of the EPR spectrum in the ATP-bound state (**B**). Data adopted from Ref 223.

Furthermore, substrate binding studies with lipopolysaccharide (LPS) suggested that distances between these domains increased with LPS binding and that subsequent ATP binding could mostly reverse this effect and establish an ATP-bound configuration. Importantly, closing the chamber with ATP binding prior to LPS addition prevented substrate effects on the apo state structure and argues for a direct, functional interaction of LPS with MsbA.

One of the more interesting spectroscopic observations stemming from these studies is the sensitivity of the distance-dependent dipolar coupling to backbone dynamics. Site 561 is located in the cytoplasmic NBDs and analysis of spin-spin dipolar coupling indicates that these two symmetry-related sites are separated by a distance longer (>70Å) than is resolvable by DEER methods. ATP binding brings these two sites within 40Å of each other (Figure 26). A salient feature of the two states is the widths of the distance distributions. In the apo state, a broad envelope of distances is reported, whereas a very narrow distribution is found in the nucleotide-bound state. The changes in the distributions are directly related to the fast signal decay of the apo state, which precludes a modulation of the time domain signal leading to a broad distance distribution. Because the spin label mobility is not sensitive to changes between these two states, the distributions likely reflect changes in the degree of order in the backbone (223). Therefore, the apo state reflects a high degree of conformational flexibility and the binding of ATP establishes a unique conformation. Interestingly, dynamics of the spin label at site 162 on the extracellular side is also not sensitive to ATP-induced distance changes. However, the changes in the distance distribution are opposite to those observed at 561 (Figure 26). Collectively, these results indicate that the shape of the distance distributions is due to backbone fluctuations.

The extensive analysis of MsbA establishes a precedent for monitoring conformational changes in membrane transport proteins with EPR spectroscopy. In combination with all three methods, site-specific changes in the local environment of the spin label can be correlated with global changes in structure. Chapters 3 and 4 illustrate how this approach can define the structural basis of ion-coupled transport using the leucine transporter, LeuT, as a model.

CHAPTER III

NA^+/LEU-DEPENDENT CONFORMATIONAL CHANGES IN THE LEUCINE TRANSPORTER

Rationale

The crystal structure of the Na^+-dependent leucine transporter, LeuT, revealed an occluded, centralized binding site containing two Na^+ and one Leu (168). From this structure alone, it is not clear what structural changes occur to accommodate ion/substrate permeation to the binding site. Although both Na^+ atoms are bound close to the Leu substrate, and Leu participates in coordination of Na1, it is not known if Na^+ binding elicits conformational changes that facilitate substrate binding. Furthermore, the fact that all crystal structures of LeuT are likely to be in functionally inhibited conformations precludes a mechanistic interpretation of the structural dynamics that may occur to support ion/substrate coupling (189). However, this structure may be exploited as a high resolution molecular map to guide a spectroscopic analysis of LeuT function. In the work presented here, spin labels were introduced into the sequence of LeuT corresponding to sites located in the extracellular region in order to determine the structural features of conformational intermediates sampled by LeuT under conditions that mimic distinct steps of a transport cycle.

The specific sites of nitroxide incorporation were based initially on the results of steered molecular dynamics simulations (188). In these simulations, the Leu molecule was "pulled" out of the primary (S1) binding site toward the extracellular milieu to identify an extracellular permeation pathway. During the computation, Leu made preferential binding contacts in a vestibule (the S2 site) ~10Å above the S1 site. Based on these results, spin labels were introduced at or near this site in transmembrane and extracellular loop segments to monitor changes in local dynamics and solvent accessibility in three biochemically-induced intermediates: 1. Apo (absence

of Na^+/Leu), 2. NaCl alone and 3. Na^+/Leu. In addition, the magnitude and direction of global conformational changes in these states were investigated through distance-dependent dipolar coupling between two strategically placed spin probes at surface locations. The structural characteristics of these intermediates were assessed in both *n*-dodecyl-β-D-maltopyranoside (DDM) detergent micelles and proteoliposomes, the solvent environments employed for all prior and current functional studies. In a collaborative effort, these studies combined with functional analysis (Jonathan A Javitch and Matthias Quick, Columbia University) and molecular dynamics simulations (Harel Weinstein and Lei Shi) identify the structural dynamics of LeuT enabling substrate permeation to internal binding sites and the subsequent formation of an occluded intermediate.

Functional analysis

To assess the impact of site directed cysteine mutagenesis and spin labeling, all mutants were subjected to a [^{3}H]-Leu binding assay and/or [^{3}H]-Ala uptake assay. Although more thoroughly described in the *Experimental Methods* (see Appendix B), direct [^{3}H]-Leu binding was evaluated for Ni^{2+} affinity purified LeuT mutants in DDM micelles by the scintillation proximity assay (SPA) (228). In this assay, the N-terminal His_{10}-tag binds to a Cu^{2+} chelate scintillation bead which releases light upon radiolabeled ligand binding to LeuT. Specific Na^+-dependent binding for cysteine mutants before and after labeling with 1-oxyl-2,2,5,5-tetramethylpyrroline-3-methyl methanethiosulfonate (MTSSL) were compared to the specific binding activity of wild type LeuT, which is devoid of endogenous cysteines.

The functional analysis of the mutants for EPR studies is summarized in Figure 27, Figure 28 and Table 1. The binding parameters of sites labeled with a (*) in Figure 27 are found in Table 1. According to Figure 27, the vast majority of single cysteine mutants demonstrate at least 50% binding of 100nM [^{3}H]-Leu relative to wild type and the presence of the spin label does not change the binding profile. It is likely that the variation in the amount of Leu bound in

the mutants reflects a shift in the K_D^{Leu}. To illustrate this point, wild type LeuT binds two Leu and exhibits an EC_{50}^{Leu}= 70nM according to Table 1. Although the G249C mutant reports wild type Leu binding stoichiometry, the EC_{50}^{Leu} is approximately nine fold greater than wild type, consistent with a decrease in binding affinity. This is also indicated for the double mutants in Figure 28 where all display wild type stoichiometry but vary in the total amount of Leu bound according to the pattern of changes in the EC_{50}^{Leu}.

Only two sites in Figure 27, L29 in TM1 and D404 in TM10, show significantly lower (~10%) total Leu binding relative to wild type when the native residue was changed to cysteine. L29 is a buried residue near the S1 site and, therefore, mutation may perturb the local helix packing and indirectly effect binding at the S1 site (168). Mutation at L29 may also disrupt the ionic interaction between neighboring R30 and D404. The Asp at site 404 is a highly conserved and critical residue shown to form a salt bridge with R30 which has been proposed to serve as part of the extracellular gate (5,168). Therefore, it is not unexpected that mutation of this residue drastically influences binding behavior. Subsequent spin labeling at these sites does not change the binding profile.

There are also a few sites that show decreased Leu binding when the spin label is attached (P137C and D138C in EL2; G307C and A311C in EL4). The cysteine mutation at P137 and D138 decreases binding relative to wild type, but the amount of binding exceeds 50% of the total. Given the peripheral location of these positions in the crystal structure, it is difficult to envision the source of additional perturbation due to spin labeling. It is also quite interesting that spin labeling at the C-terminal residue positions 145-150 in EL2 potentiates substrate binding. This may suggest a slight repacking of the loop against other structural elements that may increase access to either the S1 or S2 site. Mutation and labeling at sites 307 and 311 are likely to disturb the tight packing of the helix-turn-helix from TM7 to EL4. Figure 29 illustrates the location of

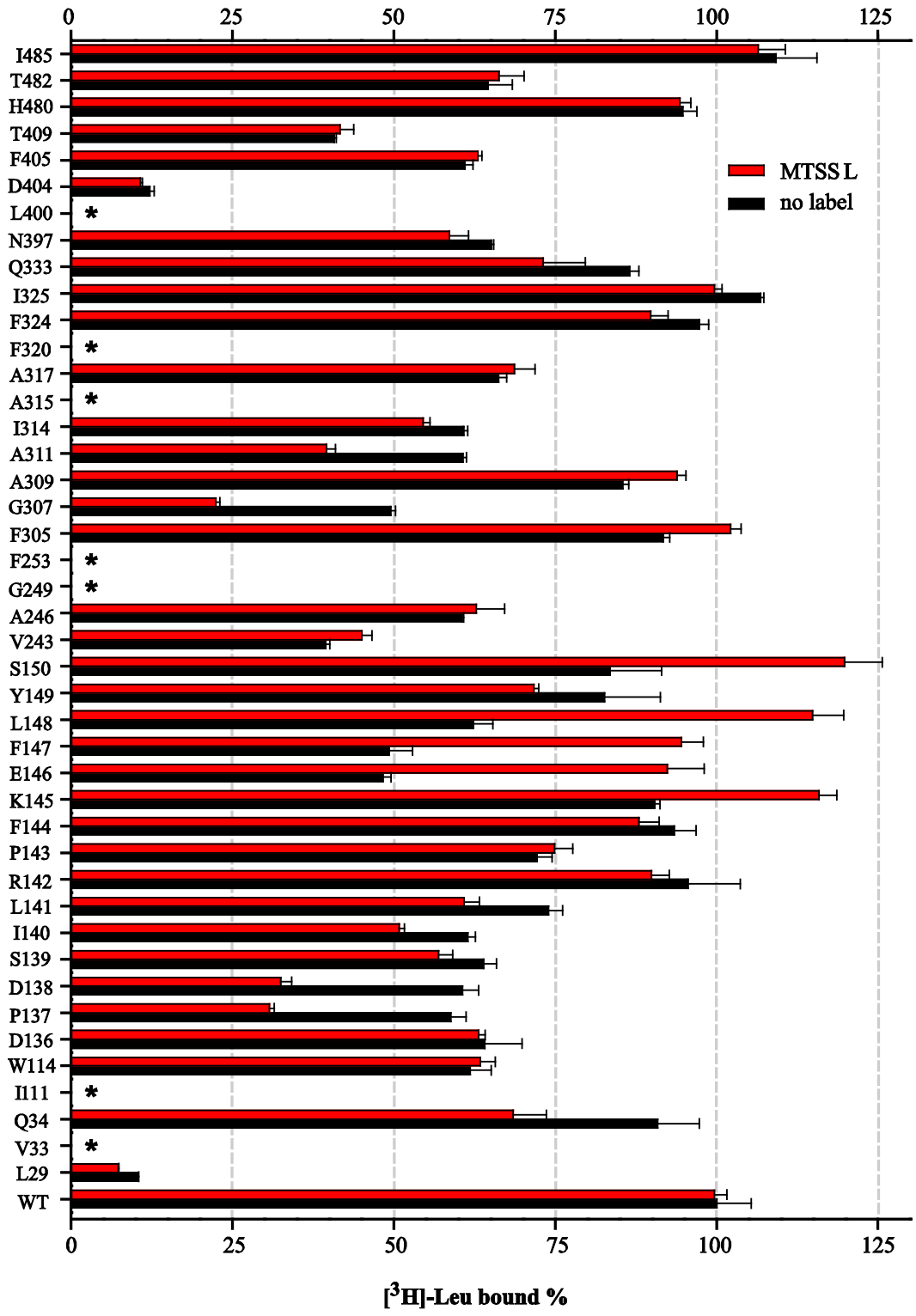

Figure 27. [^{3}H]-Leu binding analysis of LeuT single Cys mutants determined from SPA in the presence (red bar) and absence of spin label. Data are shown as the mean ± SEM.

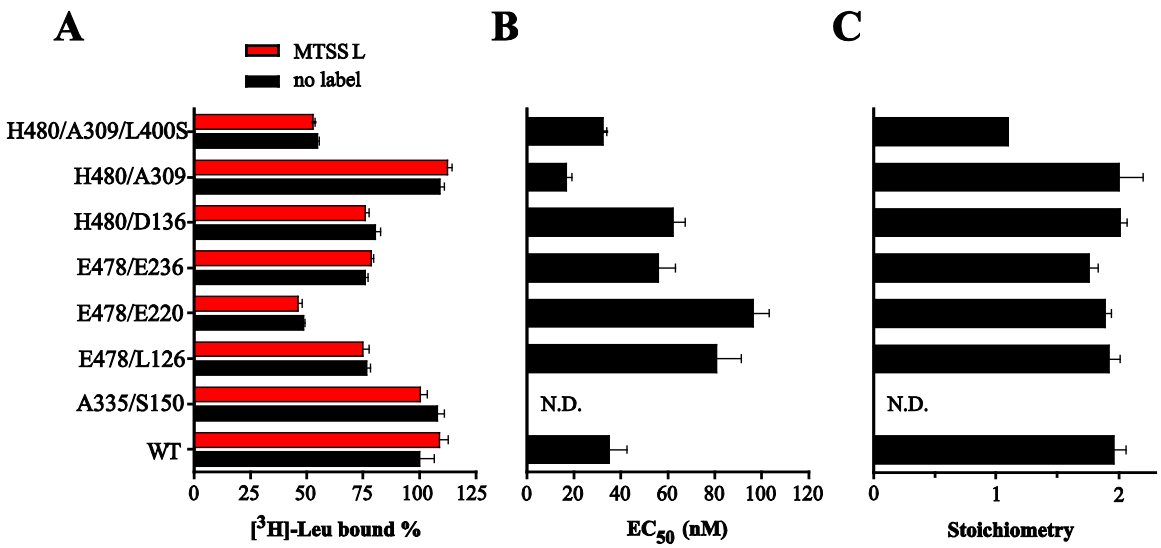

Figure 28. [^{3}H]-Leu binding analysis of select LeuT double Cys mutants determined from SPA analysis in the presence and absence of spin label. Data are reported as mean ± S.E.M. The total amount of 100nM Leu bound (**A**) varies with the EC50 (**B**). All double mutants possess wild type stoichiometry (**C**). The triple mutant, H480C/A309C/L400S eliminates binding to the S2 site, as described in the text.

Table 1: Binding parameters of purified LeuT mutants determined from SPA analysis. Data are reported as mean ± S.E.M. See *Experimental Methods* in Appendix B for protocol.

Mutant	**LeuT- Unlabeled**		**LeuT- MTSSL**	
	EC_{50} (nM)	Leu-to-LeuT stoichiometry	EC_{50} (nM)	Leu-to-LeuT stoichiometry
LeuT-V33C	616 ± 46 (n=3)	1.83 ± 0.10	690 ± 8 (n=3)	1.80 ± 0.02
LeuT-I111C	105 ± 18(188)	1.00 ± 0.10	116 ± 4 (n=3)	1.00 ± 0.03
LeuT-L400C	68 ± 11(188)	0.90 ± 0.01	69 ± 6 (n=2)	0.96 ± 0.03
LeuT-A315C	105 ± 1 (n=2)	1.99 ± 0.02	101 ± 1 (n=2)	1.99 ± 0.01
LeuT-F320C	28 ± 2 (n=4)	1.96 ± 0.06	31 ± 3 (n=2)	1.98 ± 0.01
LeuT-F253C	101± 5 (n=4)	0.98 ± 0.06	83 ± 9 (n=2)	1.02 ± 0.06
LeuT-G249C	647 ± 33 (n=2)	1.92 ± 0.02	552 ± 7 (n=2)	1.80 ± 0.13
LeuT-WT	70 ± 7(188)	1.80 ± 0.10	N/A	N/A

these particular sites where mutation and/or labeling reduces Leu binding in the SPA. Nevertheless, all spin labeled mutants were informative with site specific changes in EPR parameters according to the conditions tested.

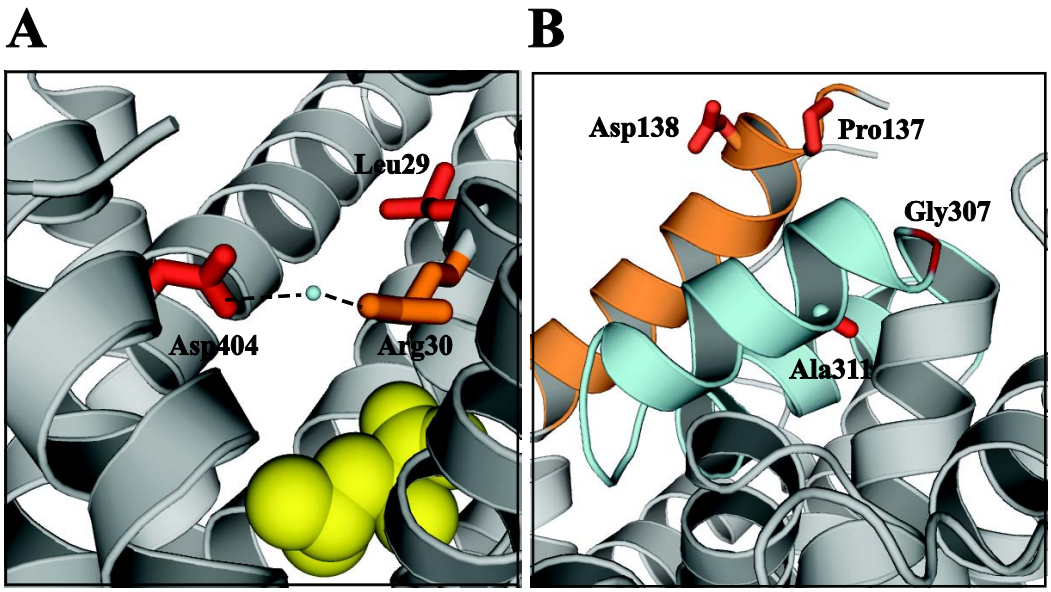

Figure 29. Location of positions that significantly alter Leu binding. (**A**) Mutation of Asp404 or the buried site Leu29 significantly decreases Leu binding. Asp404 participates in a salt bridge with Arg30 mediated by a water molecule (blue sphere). (**B**) Sites in EL2 and EL4 that decrease Leu binding after labeling with MTSSL.

Na^+ binding induces a dynamic outward-facing conformation

Although the LeuT crystal structure clearly shows a Leu molecule bound in the S1 site, Leu was never added during the purification or to the crystallization soup (168,188). Therefore, the Leu bound in the S1 site must have come from the expression medium which survived the purification process reflecting the intrinsic high affinity of the transporter for Leu. As indicated by the *Experimental Methods*, after LeuT mutants were expressed in E. coli and the membrane fraction isolated, the membranes were subjected to extensive washing in Na^+ free buffer to

remove endogenously bound Leu. According to a previous study, this preparative procedure doubled the amount of Leu binding relative to unwashed membranes as measured by the SPA, which is consistent with the two binding site model (188). Following Ni^{2+} affinity purification, the mutants were gel filtered and subsequently desalted in a Na^+ free buffer. This protocol effectively removes both Na^+ and residual Leu from the transporter to generate the Apo state in DDM micelles. EPR spectra of single and double mutants were collected in DDM. However, for analysis of spin label mobility and solvent accessibility in proteoliposomes, all LeuT mutants were initially reconstituted in the Apo state and the other biochemical intermediates were formed by the addition of either Na^+ or Na^+/Leu to the liposome preparation. Double electron electron resonance spectroscopy between doubly labeled mutants was performed mostly in DDM.

Oligomeric structure of LeuT in solution

Although doubly labeled mutants were designed to investigate intramolecular dipolar couplings, an important consideration for the DEER analysis is the oligomeric structure of LeuT in solution. In the crystal structure of LeuT, a dimeric interface is formed by TM9 and TM12 (168). If LeuT forms a dimer in solution, the DEER signal will be a composite of both intramolecular and intermolecular dipolar couplings. To investigate the propensity of LeuT to form a dimer at this interface in solution, spin labels were placed along TM12 and analyzed by conventional CW-EPR and pulse EPR for evidence of spin-spin interaction. Based on the organization of this helix in the crystal, strong dipolar coupling will be manifested by extensive spectral line broadening between symmetry-related spin labels. However, this is not observed in either DDM or proteoliposomes regardless of the biochemical conditions (Figure 30). Likewise, DEER spectroscopy of the singly labeled TM12 mutants display a weak signal consistent with background decay. Furthermore, the high mobility lineshapes of those sites predicted to be in tertiary contact also suggests that this dimer interface does not exist in DDM micelles or proteoliposomes (Supplemental Figure 1). Therefore, the distances measured between sites in the extracellular vestibule exclusively arise from the intramolecular dipolar interactions.

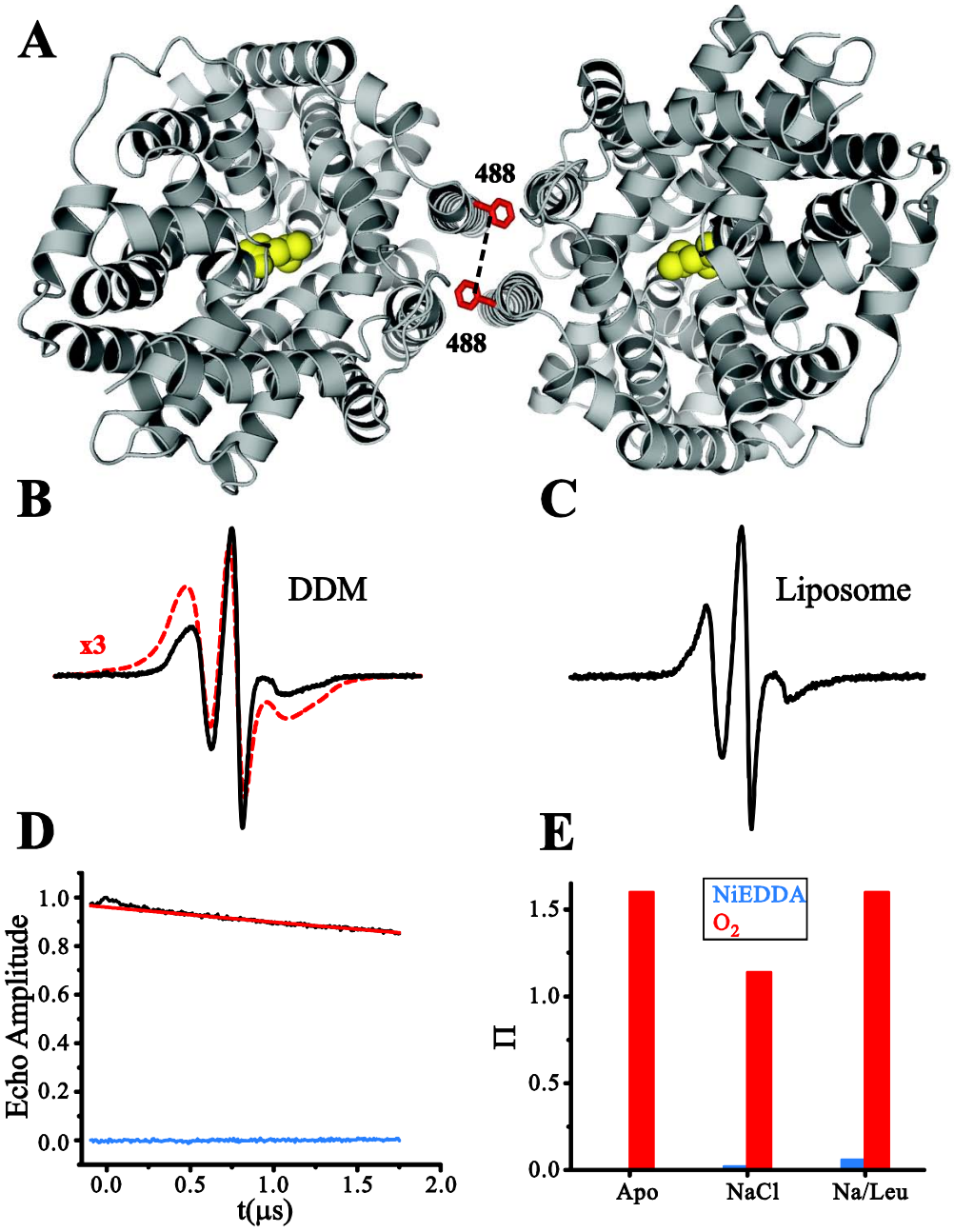

Figure 30. LeuT is a monomer in solution. (**A**) Crystallographic dimer interface highlighting the close proximity (10Å) of position 488 in symmetry related monomers. (**B-C**) EPR spectra at site 488 in DDM and proteoliposomes do not demonstrate the expected spin-spin interaction. The dashed red trace in (**B**) is a simulation of the EPR spectrum expected for two spin labels separated by 10Å. The red trace has been multiplied by 3 to emphasize the outer intensities arising from dipolar coupling. (**D**). The time-dependent echo decay (black line) does not show evidence of long-range interactions. The red and blue lines in (**D**) are the baseline and imaginary component, respectively. Besides lineshape and DEER analysis, the high O_2 accessibility suggests that the spin label at site 488 is exposed to the lipid environment and not packed against protein as in the crystal structure.

Na^+ binding alters the conformation of EL4

DEER spectroscopy was used to map the global structural features of all three intermediates by measuring distances between spin label pairs placed in the loops that surround the extracellular vestibule. Specifically, a spin label was placed in EL6 (sites 478 and 480) and in either EL2 (sites 126 and 136), EL4 (site 309) or EL3 (sites 220 and 236) as shown in Figure 31. Other spin label pairs either investigated the tertiary fold of EL2 (126/150) or the spatial relationship between EL2 and EL4 (A309C/S139C and A335/S139C). In general, most of the distance distributions are either heterogeneous possessing multiple, unresolved peaks or broad, asymmetric envelopes consistent with a large range of distances sampled in the Apo state (Figure 31). The broad, Gaussian-like appearance of some distributions are the result of featureless signal decays that quickly approach a baseline (Supplemental Figure 2 and 3). Depending on the position of the probe, these distributions may reflect rapid spin label reorientation in the magnetic field, dynamic backbone fluctuations or a combination thereof. However, the addition of Na^+ or Na^+/Leu either induce shifts in the average distance and/or alter the width of the distributions. Furthermore, the CW-EPR spectra of the double mutants do not change substantially, suggesting that apparent changes in the distance distributions likely reveal backbone movements (Figure 31).

For instance, H480C/A309C, which probes the distance between EL6 and EL4, demonstrates a prominent peak in the distribution at ~25Å and other lower probability populations sampling longer distances (30-40Å) in the Apo intermediate. The addition of Na^+ induces a right shift in the average distance between the spin labels and increases the width of the distribution. In addition, the overall shape of the distribution changes as well, revealing two unresolved distance populations (arrows in Figure 31A2). Multi-Gaussian analysis of the distance distribution identifies two separate populations with equal intensities centered about 28.5 (±3.1)Å and 36.7 (±3.8)Å , whereas ~2/3 of the spin populations occupy a distance of 25.8 (±2.6)Å in the Apo intermediate (Table 2, Supplemental Figure 4).The lack of significant changes in the spin label mobility argues that the Na^+-induced distance distribution originates with dynamic

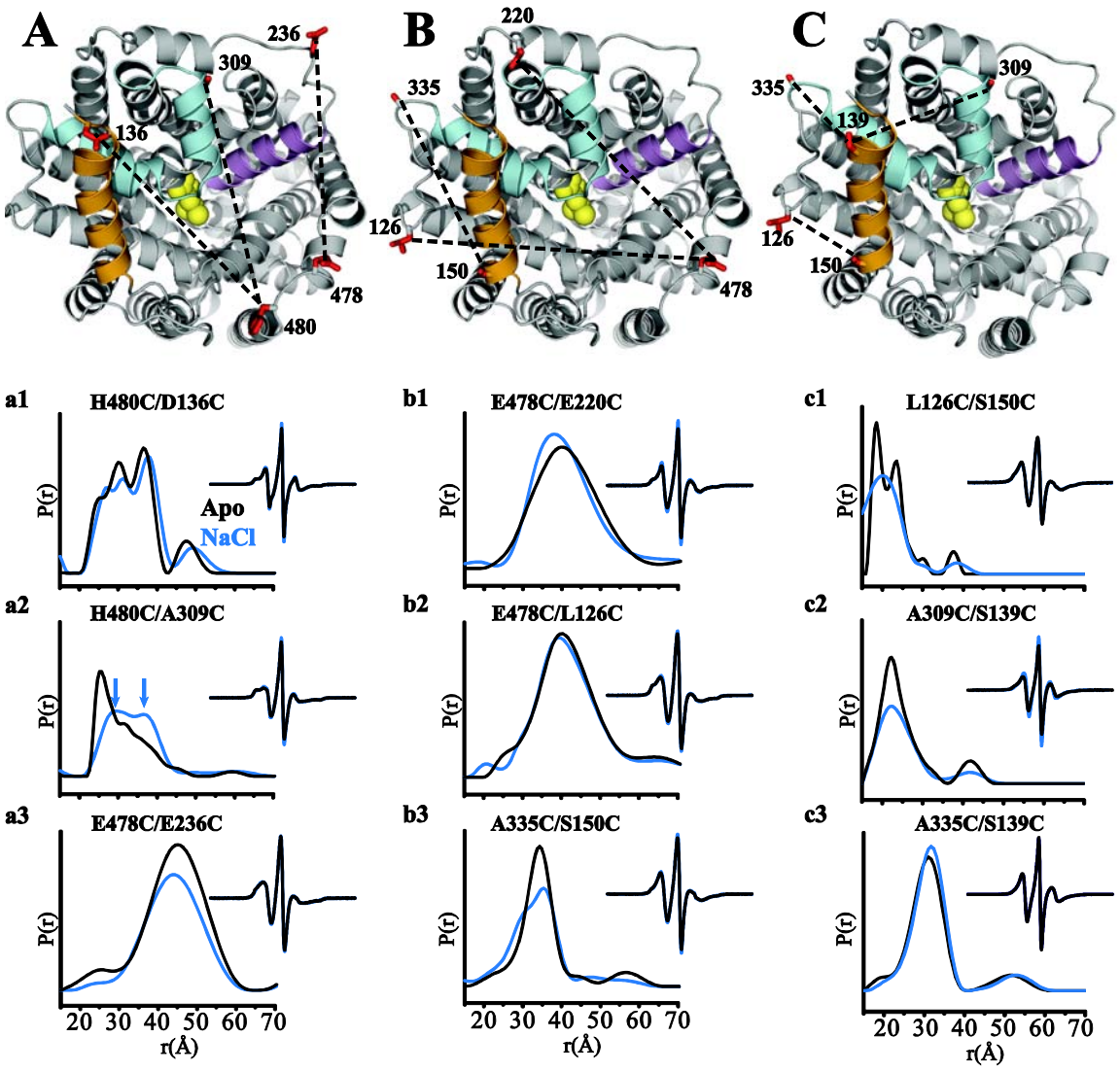

Figure 31. Global structural rearrangements upon Na^+ binding. Distance analysis of dipolar coupled spin labels shows that Na^+ binding leads to increased dynamic behavior of LeuT in specific regions (**A2**, **B3** and **C1**). Also, EL4 (**A2**) has a role in establishing an outward-facing state. No changes in spin label mobility suggest that changes in the distance distributions reflect backbone movements. Multi-Gaussian analysis of the distance distributions to model the changes in the average distance and distribution widths are shown in Table 2.

backbone movements between two conformers. Importantly, the distance distribution for E478C/E220C does not change in the presence of Na^+, suggesting that EL6 (E478-H480) is relatively static (Figure 31B1). Therefore, dynamic backbone fluctuations of EL4 probably give rise to the distance distribution of H480C/A309C in the Na^+ intermediate.

The overall right shift in the distance distribution of H480C/A309C suggests an increase in the average distance between EL6 and EL4. A comparison of the distributions for the Apo and Na^+ states indicates that Na^+ binding enriches the populations of spins sampling longer distances in the Apo intermediate. Thus, the shape of the distance distribution in the Apo state may reflect an equilibrium between closed and open conformers. This pattern of distance changes suggests that the binding of Na^+ increases the population of transporters occupying a more open configuration. Furthermore, similar distance changes are observed in proteoliposomes, confirming these structural transitions in a more native-like environment (Supplemental Figure 5). Negligible changes in the average distance are observed for the other spin label pairs in the presence of Na^+ (Figure 31, Table 2), suggesting some conformational degeneracy in EL2 and EL3. Although the DEER analysis is not exhaustive with this limited set of dipolar coupled spins, the results suggest that movement of EL4 is central in the structural transition to the outward-facing state. In addition, this movement likely leads to exposure of both substrate binding sites since EL4 contributes to the occlusion of the extracellular permeation pathway. This interpretation is supported by the site-specific changes in spin label mobility and solvent accessibility discussed below.

Dynamic behavior of EL2

Although backbone movement of EL4 appears critical to the formation of an open state, dynamic features of EL2 also emerge from the analysis of both the Apo and Na^+ intermediates. Multi-component distance distributions are observed in one or both of these states in the analysis of H480C/D136C (EL6/EL2), A335C/S150C (EL4/EL2) and L126C/S150C (EL2/EL2) shown in Figure 31. Three dominant populations are observed in the distance distribution of H480C/D136C

Table 2. Model Parameters from Multi-Gaussian Fits of Distance Distributions

Mutant	State	Gaussian 1			Gaussian 2			Gaussian 3		
		Amp	r(Å)	σ	Amp	r(Å)	σ	Amp	r(Å)	σ
H480C/A309C	Apo	0.63	25.8	2.6	0.37	32.5	5.4			
	NaCl	0.50	28.5	3.1	0.50	36.7	3.8			
	Na/Leu	0.67	24.4	1.3	0.33	29.1	3.6			
H480C/D136C	Apo	0.20	24.3	1.6	0.38	30.0	2.9	0.42	36.9	2.2
	NaCl	0.28	26.3	2.3	0.30	31.4	2.2	0.42	37.8	2.6
	Na/Leu	0.11	30.0	1.6	0.86	31.8	4.3	0.03	37.1	0.9
E478C/E236C	Apo	1.0	45.0	7.0						
	NaCl	1.0	44.0	7.0						
	Na/Leu	1.0	41.9	8.0						
E478C/E220C	Apo	1.0	40.8	8.1						
	NaCl	1.0	39.5	7.2						
	Na/Leu	1.0	39.8	7.4						
E478C/L126C	Apo	1.0	41.0	7.5						
	NaCl	1.0	40.8	7.4						
	Na/Leu	1.0	42.9	7.8						
A335C/S150C	Apo	0.12	30.0	1.0	0.88	34.3	2.9			
	NaCl	0.44	29.6	3.8	0.56	36.2	3.0			
	Na/Leu	0.32	28.7	3.4	0.68	34.2	2.7			
L126C/S150C	Apo	0.57	18.5	0.1	0.43	22.9	2.3			
	NaCl	0.96	19.6	4.3	0.04	38.4	2.0			
	Na/Leu	0.56	17.8	1.4	0.44	22.4	2.3			
A309C/S139C	Apo	1.0	22.6	3.4						
	NaCl	1.0	23.9	4.1						
	Na/Leu	1.0	23.6	3.4						
A335C/S139C	Apo	1.0	30.8	3.6						
	NaCl	1.0	31.4	3.5						
	Na/Leu	1.0	30.1	3.7						

in the Apo and Na^+ intermediates, which may be related to backbone movements in EL2 along the N-terminus (discussed later in more detail). Interestingly, one distance component is observed in the Apo state of A335C/S150C (Table 2), which probes the distance between the extreme C-terminus of EL4 and the C-terminus of EL2. However, Na^+ binding elicits the formation of a second population, consistent with increased dynamics along the C-terminus of EL2 even though the average distance does not change much. In accordance with this observation, the signal

modulation observed in the Apo state of the L126C/S150C pair, which fingerprints the tertiary fold of EL2, is dampened in the Na^+ state, leading to a broadening of the distance distribution and a concomitant loss of distinct features in the Apo state (Figure 31C1). This pair is also close enough in space to see evidence of dipolar coupling in the EPR lineshape. However, the EPR spectra does not change under any biochemical condition, suggesting that the DEER analysis resolves a contribution of EL2 backbone dynamics induced by Na^+ that is not apparent in the EPR lineshape. Regardless of these changes in dynamics, the spatial relationship between the N- and C-termini of EL4 and EL2 appears conserved based on the distance distributions of A335/S139C and A309C/S139C which show no significant changes in distance.

Na^+ binding increases dynamics and accessibility of the extracellular permeation pathway

The pattern of distance changes suggests that areas in the vicinity of EL4, i.e. the extracellular vestibule, may experience changes in local dynamics and solvent accessibility with the addition of Na^+. Most sites located within the extracellular vestibule demonstrate restricted spin label motions in the Apo intermediate, indicative of a tightly packed structural organization. However, Na^+ addition titrates a mobile component into the EPR lineshape. Figure 32A shows the EPR spectra in the Apo and Na^+ states for a set of representative sites positioned in different areas of the vestibule. The increase in spin label mobility suggests that the extensive packing interactions of the Apo state are relaxed upon Na^+ binding. These lineshapes are consistent with increased local dynamics, which mirrors the observations in the DEER analysis described above. The lineshape change at the S2-site mutant I111C is particularly informative on the nature of Na^+-induced changes in local packing. Monitoring the change in EPR lineshape in DDM micelles as a function of [Na^+] reveals an $EC_{50}^{Na} \approx 15$mM (Figure 33A-B), similar to that obtained for Na^+ stimulated [^{3}H]-Leu binding (19mM), suggesting that the changes in lineshape are solely due to Na^+ binding.

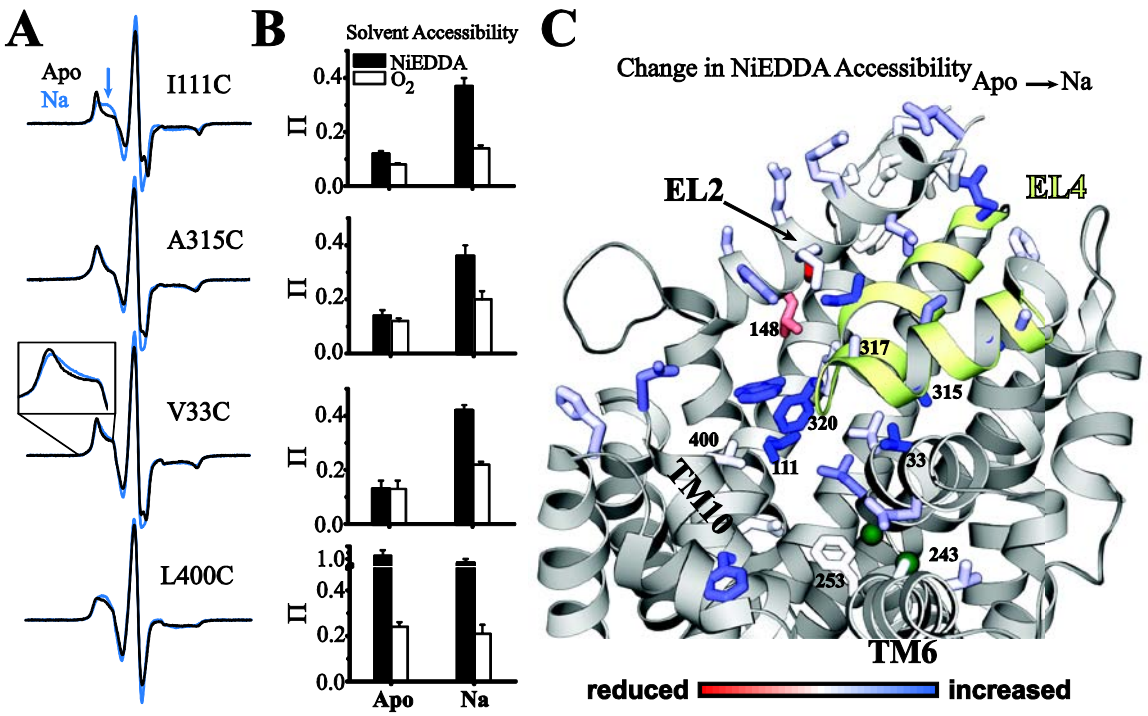

Figure 32. Na^+ binding induces changes in the local spin label environment within the extracellular vestibule. Increased spin label mobility (**A**) correlates with higher accessibility (**B**), suggesting that increased water penetration is facilitated by looser packing in the extracellular vestibule. (**C**) Mapping the changes in NiEDDA accessibility onto the structure of LeuT highlights increased access to the permeation pathway. The LeuT PDB code 2A65 is shown in (**C**).

In support of this observation, K^+ does not elicit the same change in the spectrum (Figure 33C). This is consistent with the functional dependence on Na^+ and the lack of transport activity in the presence of K^+. Consistent with the detergent EPR lineshape, the presence of the ionophore gramicidin that destroys Na^+ gradients across lipid bilayers does not change the EPR spectrum of Na^+-bound I111C, suggesting that a Na^+ *gradient* is not required to produce this conformational change (Figure 33D).

Interestingly, not all sites report extensive tertiary interactions in the absence of Na^+. Indeed, the spin label mobility at L400C, another S2 site mutant, in the Apo state is consistent with a higher rate of rotation relative to other sites in the vestibule, suggesting a much less tightly

packed local environment. This result parallels the pattern of solvent accessibility for this site, in which the accessibility to 50mM NiEDDA at L400C is 7-fold greater than for I111C (Figure 32B) even though these sites reside at a similar depth in protein and their side chains project into the extracellular vestibule. Although the addition of Na^+ increases the spin label mobility at L400C, the NiEDDA accessibility remains statistically unchanged. In contrast, I111C increases more than 3-fold in the presence of Na^+, suggesting that an increase in water penetration accompanies looser packing within specific region(s) of the vestibule.

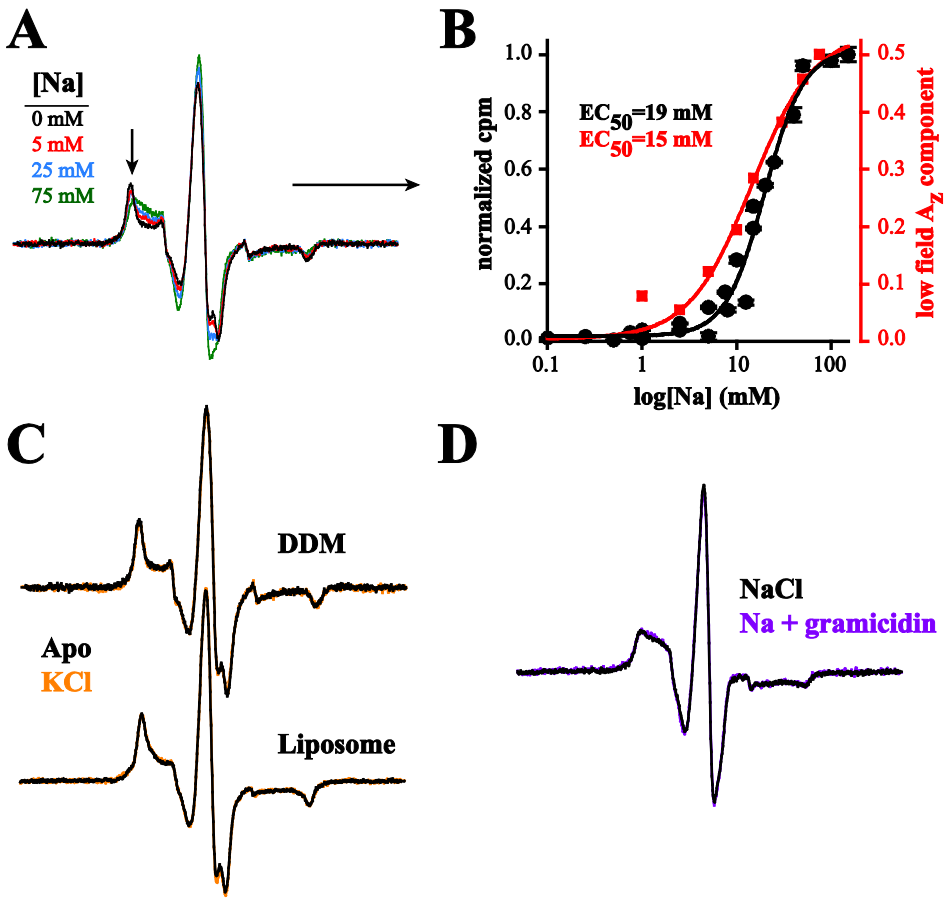

Figure 33. Characterization of ion-dependent changes. (**A**) $[Na^+]$-dependent changes in the EPR spectrum of I111C reveals a similar EC_{50}^{Na} as Na^+-stimulated Leu binding (**B**). (**C**) K^+ does not change the EPR spectrum of I111C relative to the Apo state. (**D**) Gramicidin does not change the Na^+-induced EPR spectrum of I111C in proteoliposomes, suggesting that a Na^+ gradient is not required for the conformational change.

Mapping the Na^+-induced changes in NiEDDA accessibility of 41 sites in the extracellular region onto the LeuT crystal structure reveals an increase in water penetration within the vestibule and outlines the permeation pathway to the S1 substrate binding site (Figure 32C). Changes in oxygen accessibility, shown in Supplemental Figure 6, support the pattern of NiEDDA accessibility changes in Figure 32C. Specifically, those sites that appear to have restricted access to solvent in the crystal structure demonstrate increased NiEDDA accessibility in the presence of Na^+. This is emphasized for buried sites in EL4, such as A315C. The highly restricted dynamics of the spin label suggests that the side chain of A315 projects into a buried environment, yet a concomitant increase in spin label mobility and accessibility is observed in the Na^+ intermediate. V33C in TM1 projects into the nearby environment of A315C and shows a similar change in both EPR parameters (Figure 32A-B). Notably, surface sites show larger absolute values of accessibility, which are attributed to larger local concentrations and diffusion rates of NiEDDA (Table 3) than within the vestibule (207). These surface sites, such as those in EL4 (e.g. A309C, 314C and A317C) and most sites in EL2, do not show significant changes (within experimental error, i.e. <20%) in accessibility with Na^+ binding. Similar to these sites, spin labels in TM10 and TM6 show limited Na^+-dependent changes in accessibility.

The pattern of accessibility changes shown in Figure 32 in conjunction with spin label mobility and the DEER analysis illuminate two structural aspects of LeuT. First, the analysis reveals structural features of the Apo state from the perspective of the extracellular region. The Apo state, which has not yet been crystallized, may represent a transient intermediate in the thermodynamic cycle of the alternating access model following intracellular release of ion and substrate. According to Erreger et al, this structural transition is the rate limiting step for dopamine transport (8). The low values of solvent accessibility and restricted spin label motion suggest that specific structural regions are buried by the conformation of EL4 in the Apo state, which is described by the prominent short distance component of the H480C/A309C (EL6/EL4) distance distribution. However, those areas that reside outside of EL4 contact, such as TM10 and

Table 3: NiEDDA accessibility of MTSSL-labeled LeuT single Cys mutants. Values are reported with confidence intervals for a single experiment. **(*) i**ndicates the mean ± S.D. obtained from three independently determined Π values. Values for O_2 accessibility are reported in Supplemental Table 1.

Position		Π (Apo)	Π (NaCl)	Π (Na/Leu)
TM1	25	0.11 ± 0.01	0.14 ± 0.02	0.14 ± 0.01
	29	0.09 ± 0.02	0.09 ± 0.01	0.06 ± 0.02
	33*	0.13 ± 0.03	0.42 ± 0.02	0.17 ± 0.01
	34	1.08 ± 0.07	1.15 ± 0.06	1.13 ± 0.07
TM3	111*	0.12 ± 0.01	0.37 ± 0.03	0.23 ± 0.01
	114	0.12 ± 0.02	0.16 ± 0.02	0.11 ± 0.03
EL2	136	7.39 ± 0.30	8.03 ± 0.35	8.38 ± 0.38
	137	2.80 ± 0.09	2.40 ± 0.07	2.51 ± 0.11
	138	4.71 ± 0.18	3.73 ± 0.26	4.85 ± 0.14
	139	6.38 ± 0.33	6.06 ± 0.34	5.84 ± 0.40
	140	1.05 ± 0.05	0.83 ± 0.05	0.50 ± 0.03
	141	1.68 ± 0.07	1.78 ± 0.05	1.66 ± 0.07
	142	7.02 ± 0.26	6.77 ± 0.26	6.58 ± 0.31
	143	3.00 ± 0.08	2.54 ± 0.09	2.81 ± 0.13
	144	0.28 ± 0.02	0.22 ± 0.01	0.31 ± 0.02
	145	1.18 ± 0.06	1.09 ± 0.06	1.10 ± 0.07
	146	4.15 ± 0.22	4.03 ± 0.18	3.79 ± 0.18
	147	0.49 ± 0.12	0.22 ± 0.03	1.73 ± 0.11
	148	0.56 ± 0.07	0.35 ± 0.06	0.49 ± 0.10
	149	0.86 ± 0.02	0.96 ± 0.04	0.94 ± 0.04
	150	5.40 ± 0.23	5.33 ± 0.22	5.24 ± 0.31
TM6	243	0.46 ± 0.05	0.44 ± 0.06	0.29 ± 0.07
	246	0.43 ± 0.02	0.38 ± 0.02	0.63 ± 0.03
	249	0.13 ± 0.01	0.18 ± 0.01	0.23 ± 0.04
	253*	0.14 ± 0.01	0.11 ± 0.01	0.12 ± 0.02
EL4	305	2.05 ± 0.09	1.85 ± 0.06	2.12 ± 0.09
	307	0.04 ± 0.01	0.04 ± 0.01	0.06 ± 0.01
	309	7.11 ± 0.34	7.27 ± 0.38	6.98 ± 0.28
	311	0.21 ± 0.01	0.35 ± 0.03	0.24 ± 0.02
	314	2.38 ± 0.08	2.73 ± 0.11	2.55 ± 0.07
	315*	0.14 ± 0.02	0.36 ± 0.04	0.09 ± 0.01
	317	3.15 ± 0.16	3.19 ± 0.19	3.86 ± 0.31
	320*	0.21 ± 0.02	0.29 ± 0.01	0.21 ± 0.02
	324	0.11 ± 0.02	0.10 ± 0.03	0.17 ± 0.02
	325	0.61 ± 0.06	0.83 ± 0.10	0.58 ± 0.08
	333	2.79 ± 0.12	3.54 ± 0.16	3.57 ± 0.16
TM10	397	1.35 ± 0.15	1.57 ± 0.12	1.27 ± 0.08
	400*	0.85 ± 0.09	0.74 ± 0.06	0.19 ± 0.04
	404	0.20 ± 0.03	0.17 ± 0.02	0.12 ± 0.02
	405	1.05 ± 0.04	1.32 ± 0.05	0.62 ± 0.04
EL6	480	4.16 ± 0.15	4.16 ± 0.16	4.06 ± 0.22

TM6, are exposed to the extracellular milieu and therefore do not demonstrate large changes in solvent accessibility in the presence of Na^+. The distance distribution of E478C/E236C (EL6/EL3) in the Apo and Na^+ states may also support this interpretation. E236 is four residues away from the N-terminus of TM6, and changes in distance between E478C/E236C may echo movement of TM6. A role for TM6 in the dynamics of transport was initially proposed based on the discontinuity of the TM segment at the S1 binding site, which may confer intrinsic flexibility (168). Notably, the presence of Na^+ does not change this distance distribution, suggesting the lack of conformational changes in this area and rationalizing the lack of changes in the solvent accessibility profile of TM6.

Lastly, and perhaps most importantly, distinct changes in the local environment of the vestibule correlate with movement of EL4 captured by the DEER analysis. A movement of EL4 also rationalizes the attenuation of NiEDDA accessibility at sites 147 and 148 in EL2 in the presence of Na^+. Indeed, an increase in dipolar coupling between spin labels fingerprinting the spatial relationship of EL2 and EL4 indicates an effective decrease in distance between the two loops in this region (Figure 34, Supplemental Figure 7). Collectively, this dataset strongly suggests a pivotal role of EL4 in generating an outward-facing conformation that exposes the extracellular permeation pathway and internal binding sites to solvent and substrate.

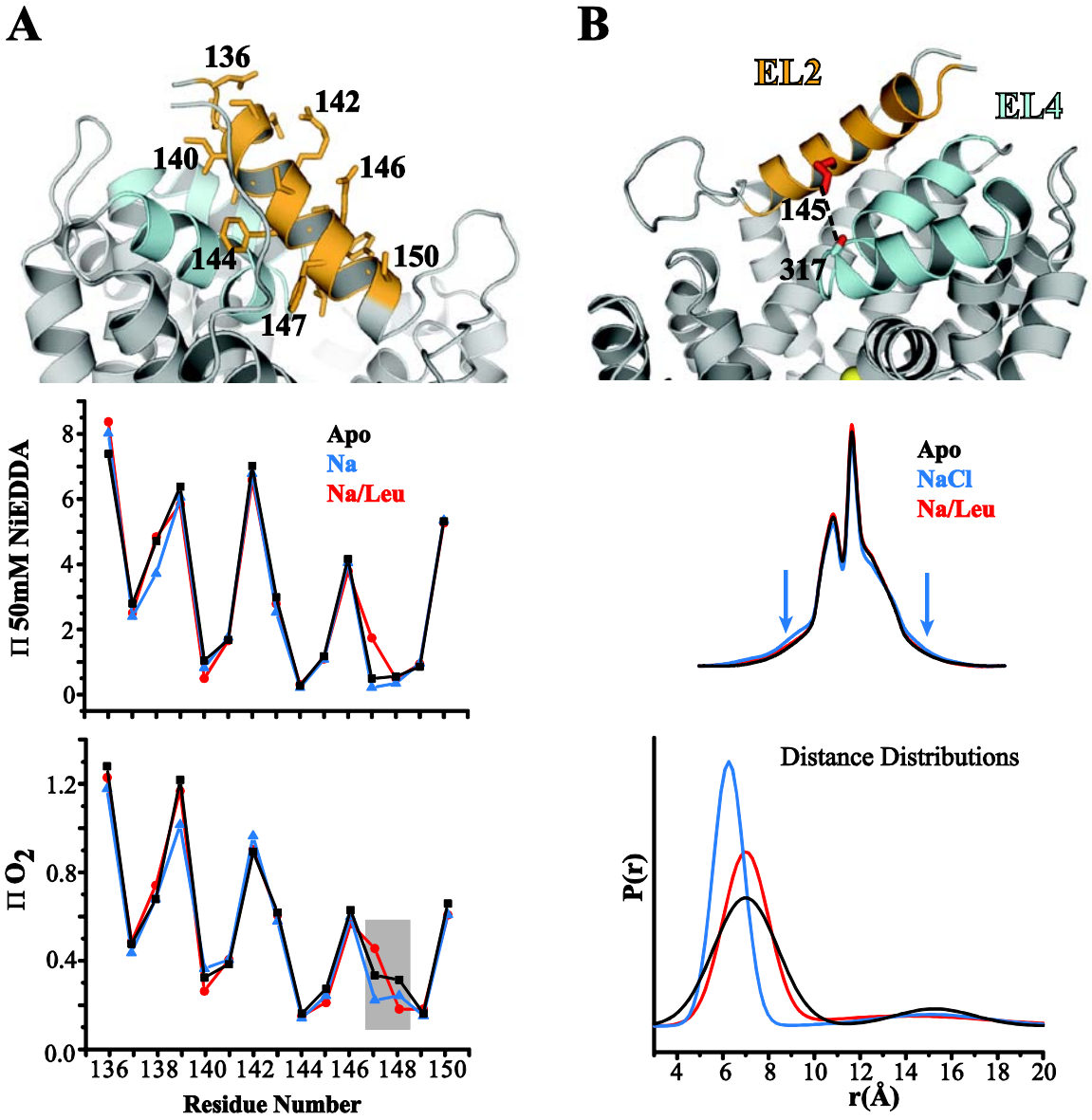

Figure 34. Relative movement between EL2 and EL4. (**A**)The pattern of accessibilities to both NiEDDA and O_2 suggests that EL2 is a tilted α-helix, consistent with the crystal structure. (**B**) The Na^+-dependent increase in dipolar interaction between spin labels at positions 317 (EL4) and 145 (EL2) is consistent with a decrease in distance between the two loops. The attenuation of spin label accessibility at positions 147 and 148 (gray box) is consistent with movement of EL4 toward EL2 upon Na^+ binding. The distance distributions in (**B**) were obtained from non-linear least squares analysis of the EPR spectrum assuming a two Gaussian model. The EPR spectra have been integrated to emphasize the ion/substrate-dependent changes in broadening.

Leu binding and the formation of an occluded intermediate

Leu binding establishes a globally occluded conformation

DEER analysis also suggests that distinct conformational changes occur upon Leu binding to the Na^+ intermediate. Figure 35 reports the DEER signal and resulting distance distributions of all three intermediates. Specifically, changes in the average distance between spin labels as well as an increase in structural order are observed in the presence of Leu. Both of these changes are manifested in the distance distribution of H480C/A309C in which the broad, two-component Na^+ intermediate becomes a narrow, single component with a significant shift to smaller distances (Figure 35A2). The narrower distribution of the Na^+/Leu state is due to the appearance of oscillations in the time-dependent echo decay of the DEER signal (Supplemental Figure 2). The lack of changes in spin label dynamics again indicates that this movement is due to a change in the backbone conformation of EL4. Thus binding of Leu appears to reverse the effect of Na^+ to the Apo intermediate. Yet the magnitude of the left shift in the distribution and the changes in width distinguish the Na^+/Leu state from both the Na^+ and Apo intermediates. Indeed the average distance between the spin labels is shorter than in either the Na^+ *or* Apo conformations. The formation of a dominate single component indicates that the structural flexibility of the Na^+ intermediate is exchanged for a more rigid, structurally homogeneous conformation upon Leu binding (Table 2).

A similar change in the shape of distance distributions occurs in the presence of Leu across other LeuT structural elements, suggesting an overall decrease in transporter dynamics. For instance, the multi-component distance distributions of H480C/D136C and A335C/S150C coalesce into a single population (Figure 35A1 and B3, Table 2). The distance distribution of H480C/D136C in the Apo and Na^+ states can be reasonably estimated by simulating theoretical conformations of the spin label at both H480C and D136C (dashed trace) using an unpublished spin label rotamer library developed by Gunnar Jeschke, possibly indicating that the distributions

reflect only movement of the spin label (Figure 35A1). It must be noted that this rotamer library was developed *in silico* and needs to be validated under experimental conditions. The EPR spectrum of H480C/D136C is degenerate in all conditions, suggesting that the sampled spin label

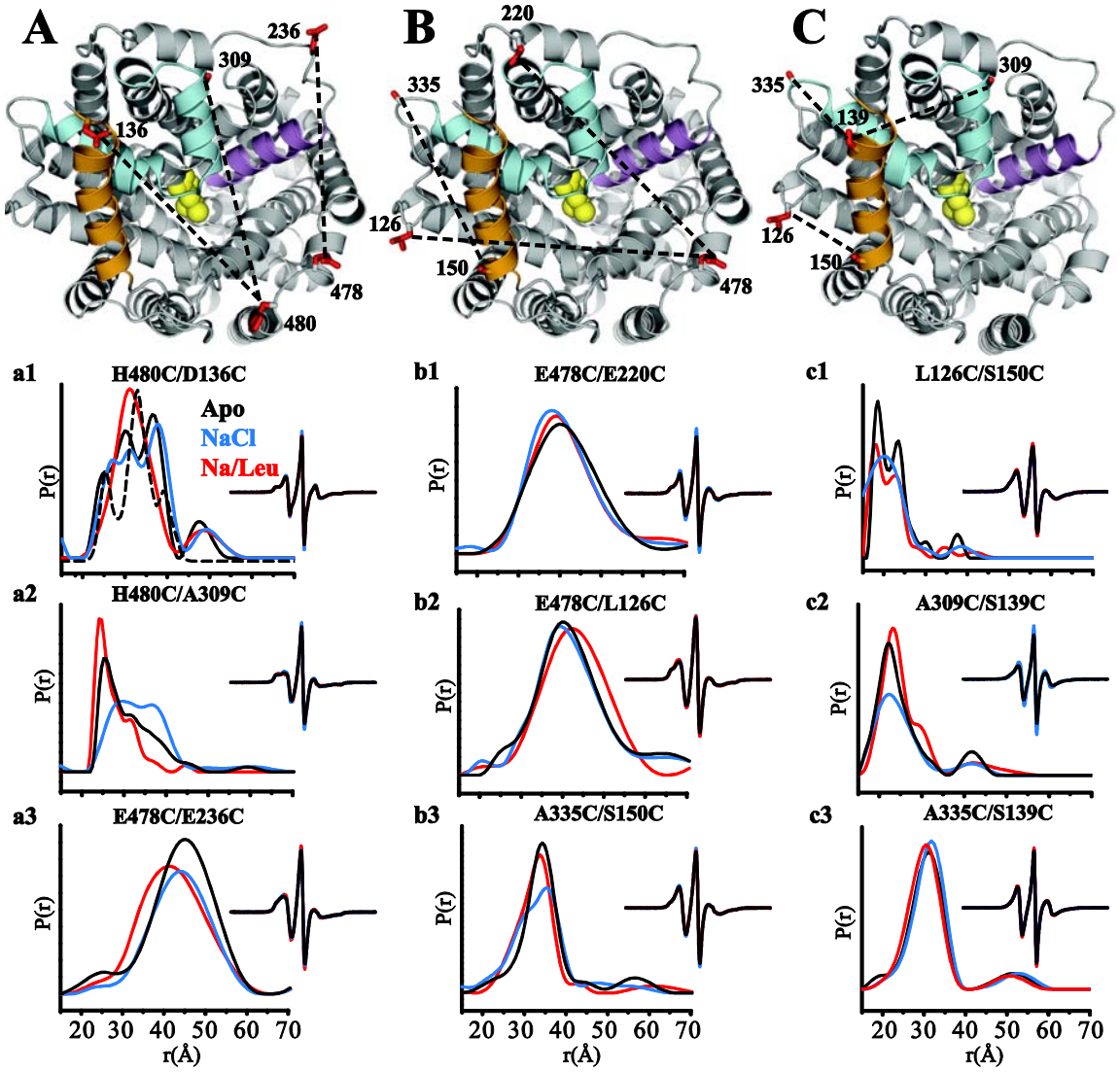

Figure 35. Leu binding establishes an occluded state. Changes in the distance and associated distributions suggests that Leu binding leads to a closed and more rigid structure relative to the Na^+ intermediate. This is emphasized in the (**A**) panels, which also shows that a decrease in distance between EL4 and EL6 (**A2**). Little change in the average distance is observed outside of the extracellular vestibule in all states.

conformations possess similar mobilities. However, the formation of a single component induced by Leu binding may suggest that sampling of these predicted rotameric conformations is associated closely with the backbone dynamics of EL2. That is, the binding of Leu establishes a unique conformation of EL2 which selectively enhances a specific rotamer population of the spin label. As shown in Figure 35, not all spin label pairs demonstrate narrowing of the distance distribution. For instance, E478C/E236C does not show a decrease in the width of the distribution. This is likely due to the structural nature of the polypeptide chain, i.e. E236C resides in an unstructured loop (168). Therefore, the width of the distribution is tied to the dynamic motion of this loop. Regardless, a Leu-dependent decrease in the average distance between the spin labels in this double mutant is consistent with the formation of a globally occluded conformation that is distinct from the Apo and Na^+ intermediates.

Leu binding decreases dynamics and accessibility of the extracellular permeation pathway

The Leu-dependent changes in the distance distributions correlate with changes in local dynamics and solvent accessibility within the vestibule. Typically, a reduction in spin label mobility accompanies Leu binding at sites within the vestibule. In particular, the transition to an occluded state is highlighted for L400C where large amplitude motion of the spin label is substantially reduced in the Leu-bound form as illustrated in Figure 36A. Coinciding with decreased spin label dynamics is a significant decrease in spin label accessibility (Figure 36B). The changes in solvent accessibility upon Leu binding relative to the Na^+ intermediate are mapped onto the crystal structure in Figure 36C. In contrast to the Na^+ state, these results indicate that Leu binding effectively reverses the accessibility of the vestibule and establishes a tightly packed conformation. Furthermore, the blueprint of Leu-dependent accessibility suggests that these changes are facilitated, in part, by movement of EL4. In addition, the decrease in solvent accessibility at sites within TM10 also suggest an inward movement of this helix toward the

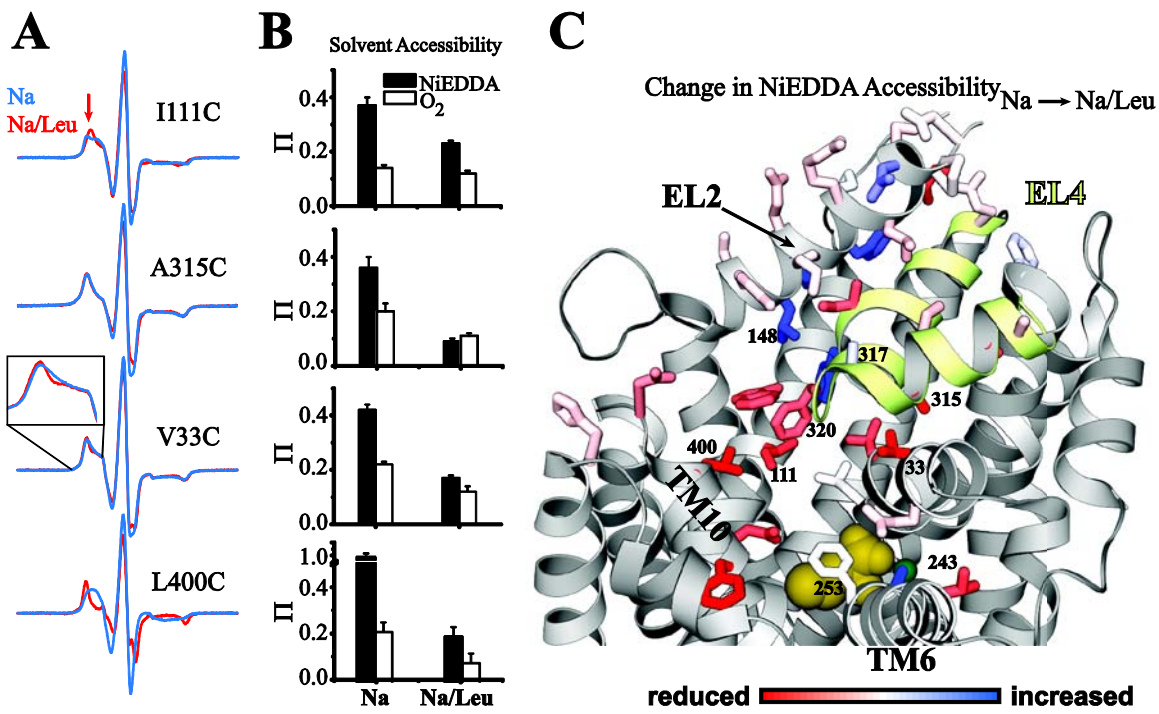

Figure 36. Leu binding decreases accessibility and increases order within the extracellular permeation pathway. A decrease in spin label mobility (**A**) correlates with a decrease in solvent accessibility within the vestibule (**B**). The pattern of accessibility changes (**C**) indicates that movement of EL4 modulates access to the permeation pathway. The LeuT PDB code 2A65 is shown.

vestibule. In support of this, a similar pattern of substrate-dependent EPR lineshape changes emerge at sites in TM10 that describe the local environment from the vestibule toward the S1 site. Although this movement of TM10 is not apparent from the crystal structure, it may be reminiscent of the substrate-dependent inward movement of TM10 in the NCS1 benzyl-hydantoin transporter, Mhp1 (185). An overlay of both structures illustrates where TM10 in LeuT may bend toward the extracellular vestibule (Figure 37). Gly residues have been suggested to confer flexibility to transmembrane segments in K^+ channels (192), and helix bending is most likely facilitated by a Gly at position 371 in Mhp1 (185). Likewise, Gly408 in TM10 of LeuT may provide similar flexibility. Therefore, the N-terminus of TM10 may play a role in blocking access of the extracellular permeation pathway to the solvent.

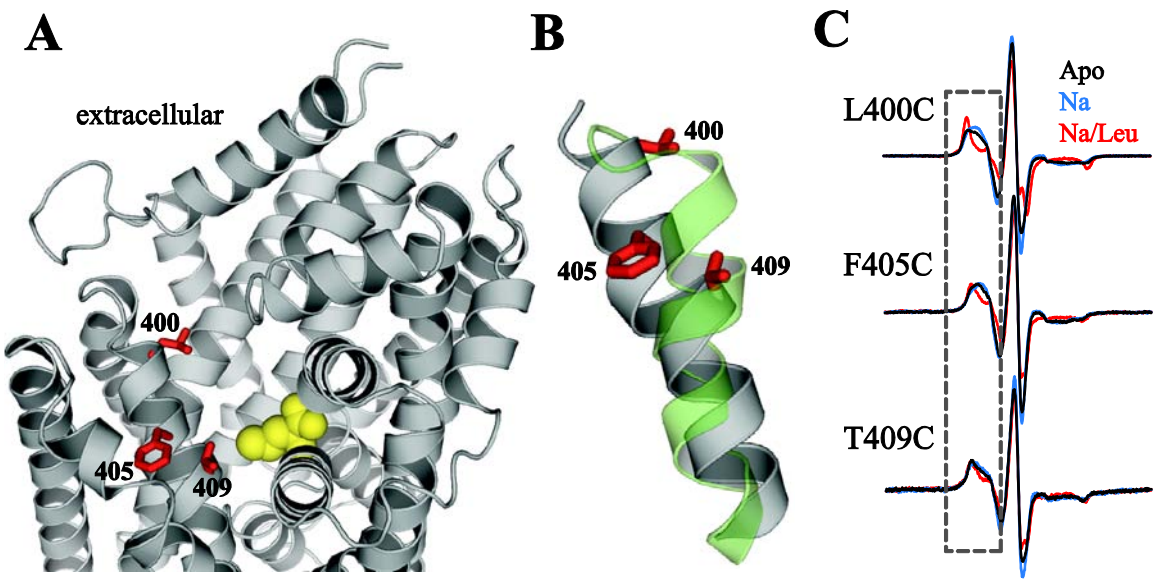

Figure 37. TM10 may bend toward the vestibule in the Na^+/Leu intermediate. (**A**) LeuT crystal structure highlighting the location of N-terminal TM10 residues relative to the Leu binding site. The combination of decreased spin label mobility (**C**, gray dashed box) and solvent accessibility (Figure 10) suggests a Leu-dependent conformational change of TM10, similar to substrate-bound Mhp1 (PDB 2JLO) (**B**).

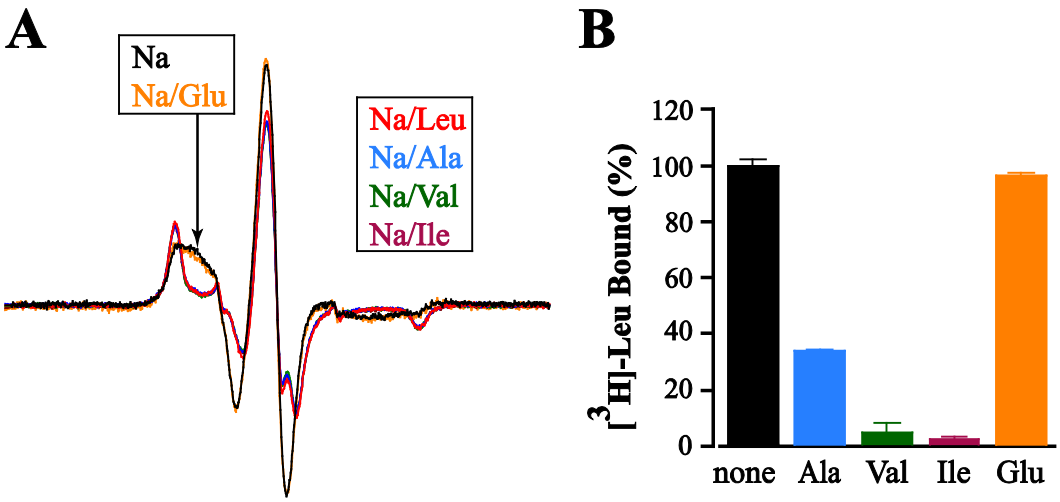

Figure 38. Promiscuity of LeuT. The Leu-dependent change in lineshape at L400C occurs with other known LeuT substrates. (**B**) The substrates that alter the EPR spectrum in (**A**) compete with Leu for binding to LeuT.

Binding studies have shown that LeuT is rather promiscuous by binding a variety of amino acids. Specifically, these studies suggested that Ala, Val, Ile and other neutral amino acids are substrates of LeuT (173). Furthermore, crystallographic analysis of some of these complexes suggests that these substrates displace Leu in the S1 site and the overall architecture of LeuT is nearly identical to the Leu-bound LeuT structure. This may also suggest that similar conformational changes occur in LeuT when binding to these substrates. In support of this, the EPR spectrum of Ala-, Val- and Ile-bound LeuT at L400C is superimposable with the Leu-bound spectrum (Figure 38). In contrast, Glu does not induce these lineshape changes, indicating that Glu is not a substrate for LeuT.

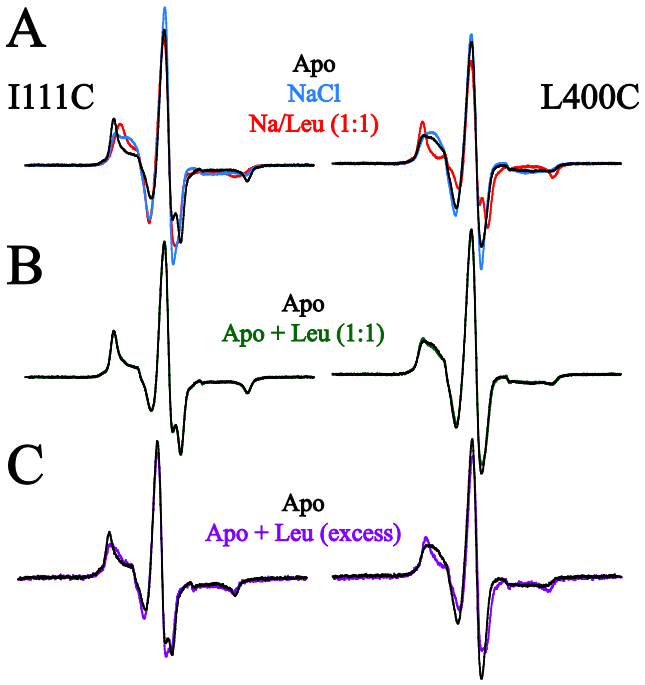

Figure 39. Na^+-dependence of Leu binding. (**A**) Overlay of Na^+/Leu-dependent changes in the EPR spectrum at I111C and L400C. (**B**) In the absence of Na^+, stoichiometric Leu binding is not observed. (**C**) In contrast, some substrate binding is observed in the absence of Na^+ if the [Leu] is large enough (mM) relative to the [LeuT], suggesting that Na^+ binding enhances the binding affinity of Leu to LeuT.

Importantly, the changes in EPR lineshape induced by Leu are dependent on the presence of Na^+. As previously stated, L400C and I111C are critical residues in the extracellular vestibule that form part of the S2 site and mutation of these residues disrupts substrate binding there. Correspondingly, the molar stoichiometry of these mutants is 1:1 (Leu-to-LeuT), as indicated by binding analysis (Table 1). In the Apo state, the addition of a stoichiometric amount of Leu does not alter the EPR spectrum, suggesting that Leu does not bind in these conditions (Figure 39).

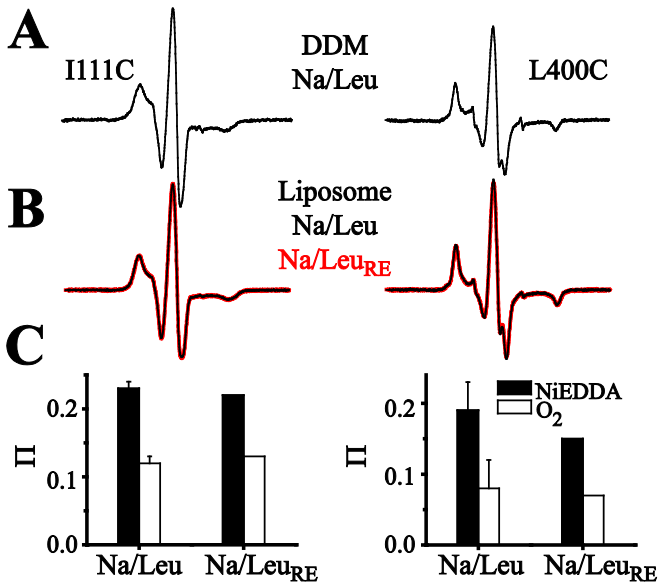

Figure 40. A Na^+ gradient is not required for Leu binding. (**A**) Changes in the EPR lineshapes of I111C and L400C in DDM micelles are similar to those changes in proteoliposomes (**B**). The thick red trace in (**B**) is the resulting EPR spectrum following reconstitution of LeuT in the presence of Na^+ and Leu. The black line is the EPR spectrum resulting from the external addition of Na^+ and Leu to reconstituted Apo-LeuT. (**C**) Accordingly, solvent accessibilities at these two sites show similar behaviors to that described in (**B**).

Furthermore, the presence of K^+ also does not support Leu-dependent changes in the EPR lineshape (Supplemental Figure 8). These results may reflect a Na^+-dependent decrease in the K_D^{Leu}. Indeed, the EPR lineshapes show evidence of some binding in the absence of Na^+ at Leu

concentrations in vast excess (mM) of the LeuT concentration (μM) (Figure 39C). A Na^+-dependent increase in substrate binding affinity has been observed for the benzyl-hydantoin transporter (185). Importantly, similar changes in EPR lineshape in both DDM micelles and proteoliposomes suggest that a directional Na^+ *gradient* is not required to support the Leu-dependent conformational changes (Supplemental Figures 9-16). Indeed, no differences in EPR lineshapes or solvent accessibilities were observed for I111C or L400C when these mutants were reconstituted in the presence of both Na^+ and Leu (i.e. identical concentrations of Na^+/Leu on both sides of the proteoliposome) as shown in Figure 40.

Leu binding dehydrates the S1 site

Spin labels near the binding site (e.g. L25C, L29C and F253C) report low accessibilities and restricted motion in all states, although the spin label at L29C shows changes in mobility (Table 3, Supplemental Figure 9). According to the crystal structure, F253 occludes the extracellular side of the S1 site and participates in direct interaction with the Leu substrate (168). Even though site-directed cysteine mutagenesis of F253 only slightly perturbs the binding affinity relative to wild type, the mutation reduces the molar stoichiometry to 1:1, Leu-to-LeuT (Table 1). Furthermore, the mutation also abolishes transport activity, consistent with disruption of the proposed symport mechanism (Figure 41B) (188). Binding studies show that the tricyclic antidepressant (TCA) clomipramine (CMI), a potent inhibitor of uptake, reduces the total amount of Leu binding to wild type LeuT by ~50%, consistent with CMI blocking Leu binding to the S2 site in the extracellular vestibule (Figure 41C). Notably, CMI binding nearly abolished all binding to the F253C mutant (Figure 41C). This observation suggests that Leu binds only to the S2 site in this mutant.

The spin label accessibility of F253C to 50mM NiEDDA averaged 0.12±0.01 (n=3) over all conditions tested, suggesting steric restriction of NiEDDA (which is ~13 times larger than water) and/or the lack of significant diffusion of paramagnetic reagents at the S1 site (Figure

41D)(207). This result suggests that water activity may be underdetermined and therefore prevents a structural interpretation of changes in water penetration near the binding site. However

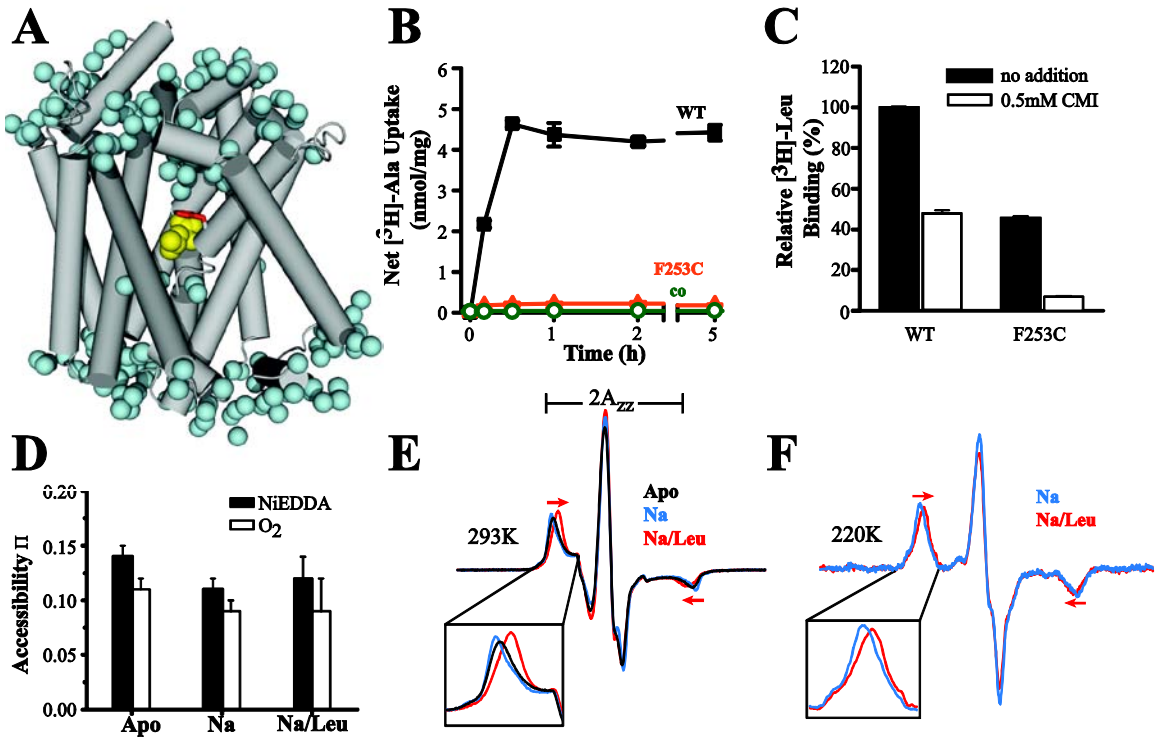

Figure 41. Evidence of water exclusion at the S1 site upon Leu binding. Mutation of F253C (**A**) eliminates transport activity and reduces binding (**B**). The presence of CMI eliminates nearly all Leu binding (**C**), suggesting that Leu only binds to the S2 site in the extracellular vestibule in this mutant. (**D**) The spin label solvent accessibilities are low in all states, consistent with a buried location in the crystal structure (**A**). Leu binding causes a decrease in spectral breadth ($2A_{zz}$) at room temperature (**E**) and 220K (**F**), consistent with a dehydrated S1 binding site as observed in the crystal structure (**A**).

the breadth ($2A_{zz}$) of the EPR spectrum is different in all three conditions (Figure 41E). This observation can be attributed to either subtle changes in mobility or changes in the polarity of the environment of the spin label. In low dielectric environments, the splitting of hyperfine extrema ($2A_{zz}$) decreases (229). Relative to the Apo state, the addition of Na^+ increases the value of $2A_{zz}$,

consistent with increased hydration of the S1 site (Figure 41E). In contrast, Leu reduces the spectral breadth by 8 Gauss, which implies that water is excluded from the area of the binding site. To eliminate any contribution of spin label dynamics to the changes in the EPR spectrum, the experiment was repeated at low temperature (220 K). At this temperature, motional averaging is "frozen" and any changes to $2A_{zz}$ will be a function of the local dielectric. Indeed, the breadth of the EPR spectrum decreases at this low temperature with Leu binding (Figure 41F). Thus, the decrease in solvent accessibility within the extracellular vestibule is characterized also by dehydration at the primary binding site, consistent with the absence of water molecules near the S1 site in the crystal structure (Figure 41A). The shedding of water is likely to facilitate highly specific interactions of Leu within the S1 site. Importantly, these results appear to highlight the connection between the S1 and S2 sites since substrate binding in the extracellular vestibule triggers a reduction in water activity at the primary binding site.

Leu-dependent conformational changes: correlation with the binding sites

Collectively, the data reveal that Leu binding induces a conformational change that reduces access to the extracellular permeation pathway—a result opposite to that of Na^+ binding to the Apo intermediate. In combination with the functional analysis (Table 1), it appears that binding to the S1 site alone is sufficient to drive formation of the Na^+/Leu state. Since L400C eliminates binding to the S2 site (188), the structural rearrangement captured by the mobility and accessibility analysis of spin labeled L400C is a function of Leu binding to the S1 site. In fact, titration of L400C with Leu shows that the maximal change in the EPR lineshape occurs at a molar ratio of 1:1, Leu-to-LeuT (Figure 42B). However, qualitatively similar results are obtained from mutants that possess wild type binding stoichiometry, such as V33C and A315C (Figure 36, Table 1), suggesting that binding to the S2 site may not contribute to changes in the local spin label environment. However, global conformational changes also seem to demonstrate the same behavior. Leu titration of H478C/E236C and H480C/A309C, both of which bind two Leu per LeuT, indicates that the Leu-induced change in spin label distance is saturated at a 1:1

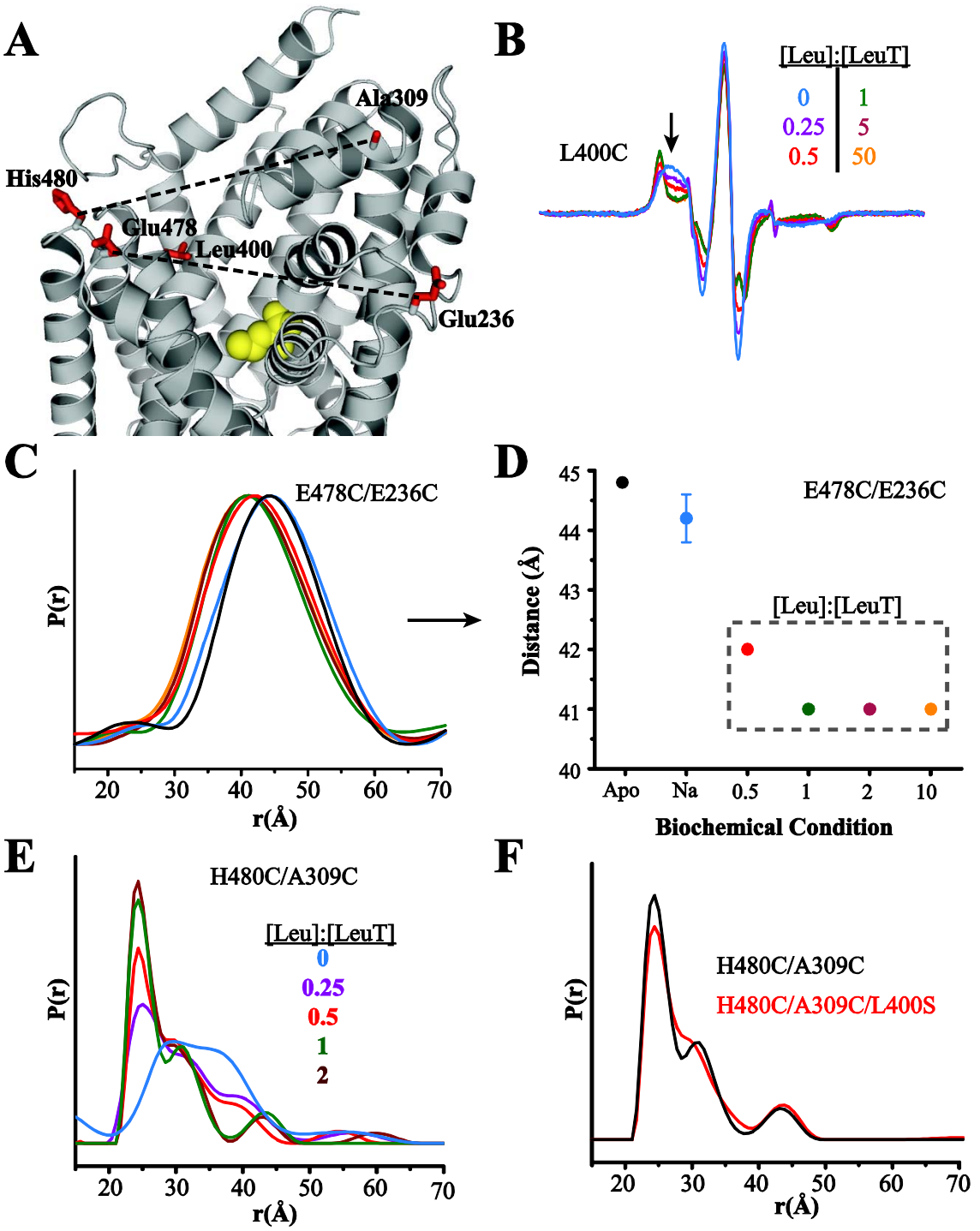

Figure 42. Leu binding in the S1 site drives conformational changes. (**A**) Position of spin labeled sites used to investigate the correlation of Leu-dependent conformational changes with binding stoichiometry. The Leu titration of L400C (**B**) and global distance changes (**C-E**) indicate that substrate binding to the S1 site alone will drive occlusion of the extracellular permeation pathway. (**F**) This is further supported by superimposable distance distributions of H480C/A309C with an S2 site disrupting mutation (L400S).

stoichiometric ratio (Figure 42C-E, Supplemental Figure 17). In addition, incorporation of an S2-disrupting background mutation, L400S, into the H480C/A309C construct did not alter the distance distribution (Figure 42F).

In light of these results, it is interesting to consider the unique spectroscopic signatures reported by the F253C mutant that binds Leu only to the S2 site as demonstrated by functional analysis. This data seems to imply that binding to the S2 site will also trigger conformational changes that reduce water penetration, which may suggest that binding to either the S1 *or* S2 site produces a similar Na^+/Leu intermediate. Alternatively, the concentration of both LeuT and Leu used in the EPR experiments may be above the K_D^{Leu} for the perturbed S1 site. This would imply that the decrease in spectral breadth is due to binding in the S1, and not necessarily the S2, site. From the perspective of the SPA binding analysis applied here, specific interactions are masked by high backgrounds at protein and substrate concentrations employed for EPR spectroscopy. In addition, it is not possible to perform EPR experiments in the sub-micromolar regime. Therefore, complete overlap with the binding and EPR data cannot be achieved with confidence.

Although not conclusive, two lines of EPR evidence discussed here may suggest that binding at either the S1 or S2 site produces a similar Leu-bound intermediate. First, a background mutation, L400S was introduced into the F253C construct. The SPA reveals no Leu binding to the double mutant (data not shown), consistent with disruption of both substrate binding sites. However, EPR studies show lineshape changes consistent with some substrate binding. Relative to the F253C mutant, the F253C/L400S double mutant shows attenuated Leu and Ala binding at all tested concentrations of LeuT (3, 5, 20 and 50μM) as indicated by the change in spectral breadth (Figure 43A-C). This result is suggestive of an attenuated Leu-induced conformational change driven by binding to the S2 site. An important caveat to this experiment is the appearance of a mobile component in the spectrum (arrow, Figure 43). This component is observed also in the Apo and Na^+ states (Figure 43D), suggesting that the additional L400S mutation may have altered the protein conformation or packing interactions. Second, the result of a TCA inhibitor

binding study is consistent with attenuated Leu binding in the S2 site. This experiment and the result is described in the following section.

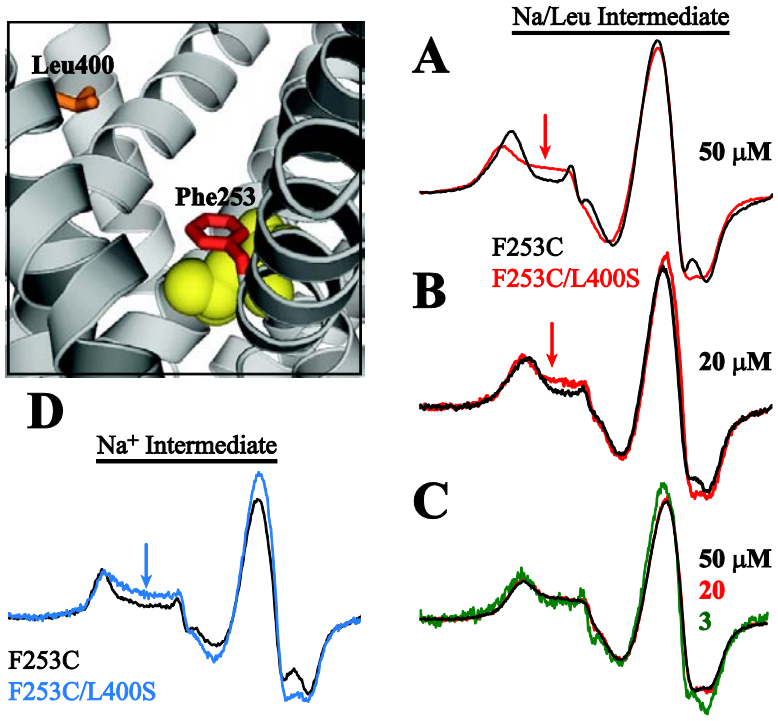

Figure 43. Mutation of an S2-site residue disrupts S1 site dehydration. Leu binding, as measured by a decrease in $2A_{zz}$, appears attenuated by the L400S background mutation (**A**-**B**), suggesting that reduced binding is the result of a disturbed S2 site. (**C**) This result is also observed a low [LeuT]. However, the presence of a mobile component in the EPR spectrum of the double mutant (arrows, **A**, **B** and **D**) suggests that the additional background mutation may alter the packing interactions of LeuT.

Inhibitors induce distinct conformations of LeuT

Clomipramine and octyl-glucoside alter the structure of the Na^+/Leu intermediate

The observation that octyl-glucoside (OG), the detergent used in all crystallization studies, inhibits Na^+-coupled substrate symport by binding in the extracellular vestibule has led to

the conclusion that all structures represent inhibited conformations (189). This proposal is supported by other inhibitor binding experiments that show TCAs and selective serotonin reuptake inhibitors (SSRIs) occupy a similar location in the vestibule to generate nearly identical crystal structures (91,169,174). Therefore, a significant disparity exists between these structures

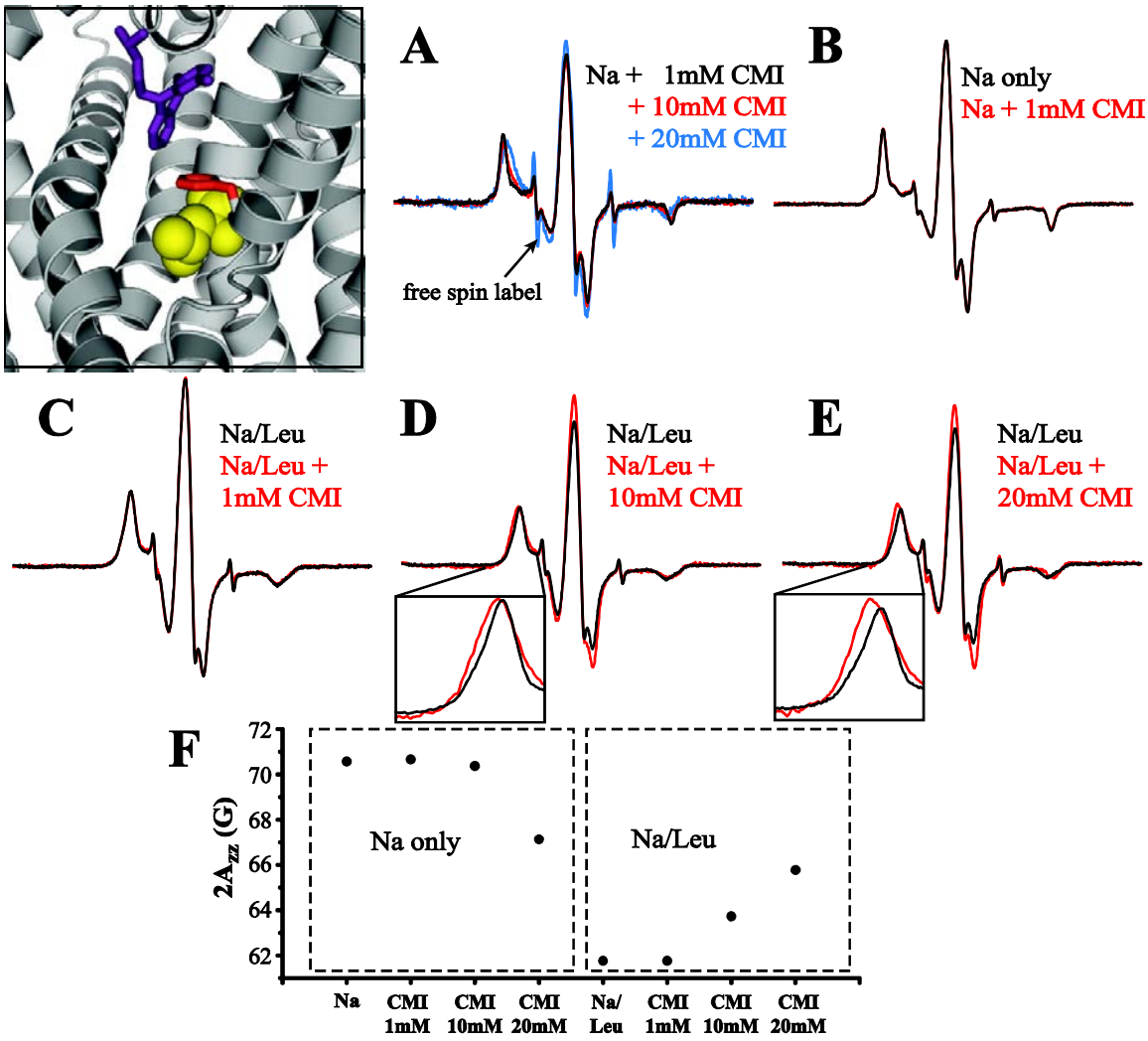

Figure 44. A tricyclic antidepressant impairs Leu binding. (**A**) [CMI]-dependent changes in the EPR spectrum of F253C in the presence of Na+ alone. (**B**) 1mM CMI does not alter the lineshape of F253C relative to the Na+ state or prevent stoichiometric Leu binding (**C**). However, both 10mM (**D**) and 20mM CMI (**E**) impairs Leu binding as shown by an attenuation of the decrease in spectral breadth (**F**).

of LeuT and the functionally relevant Na^+/Leu intermediate. The apparent sensitivity of the F253C mutant to binding in the S2 site provides an avenue to differentiate the effect of inhibitors relative to native substrates. As shown previously, the presence of CMI blocks most Leu binding activity of the F253C mutant (Figure 41C). Interestingly, a [CMI]-dependent change in the EPR lineshape is observed at this position in the presence of Na^+. At 1mM, the EPR spectrum of 20μM LeuT-F253C remains essentially unaltered relative to the Na^+ intermediate (Figure 44A-B). However, at higher concentrations (10 and 20mM), the low and high field resonance lines increase in width. At 20mM CMI, a slight decrease in the $2A_{zz}$ value is observed, but does not approach the value of the Leu-bound form (Figure 44A,F). At this high concentration of CMI, a white precipitate is formed, suggesting protein aggregation, and a significant amount of free spin label is seen in the spectrum. Also, Leu binding is substantially reduced as measured by a change in the value of $2A_{zz}$ (Figure 44E-F). In contrast, no precipitation is observed at 10mM CMI, the concentration used for previous crystallization trials, and the spectral breadth does not change relative to the Na^+ state. Yet in the presence of both 20μM Leu (1:1, Leu-to-LeuT) and 10mM CMI, the EPR spectrum shows a modest increase in $2A_{zz}$, suggesting impaired Leu binding (Figure 44D). This result implies that binding of CMI to LeuT prevents dehydration of the S1 site and is also consistent with the functional analysis suggesting that Leu binds only to the S2 site in the F253C mutant.

From a global perspective, the presence of 1mM CMI induces a small but reproducible decrease in the distance between spin labels in the E478C/E236C mutant relative to the Na^+/Leu state (Figure 45A-B, Supplemental Figure 18). This shift in the distance distribution appears to be due to a specific binding interaction, presumably in the extracellular vestibule, because it does not occur in the absence of Leu (Figure 45C). Given that Na^+/Leu are present in the crystal structure of CMI-bound LeuT, this result may suggest that Leu binding in the S1 site establishes a preferential conformation for TCA binding. Consistent with this notion, 10mM CMI recapitulates the distance change in the presence of Na^+ alone (Figure 45D). This may suggest that the

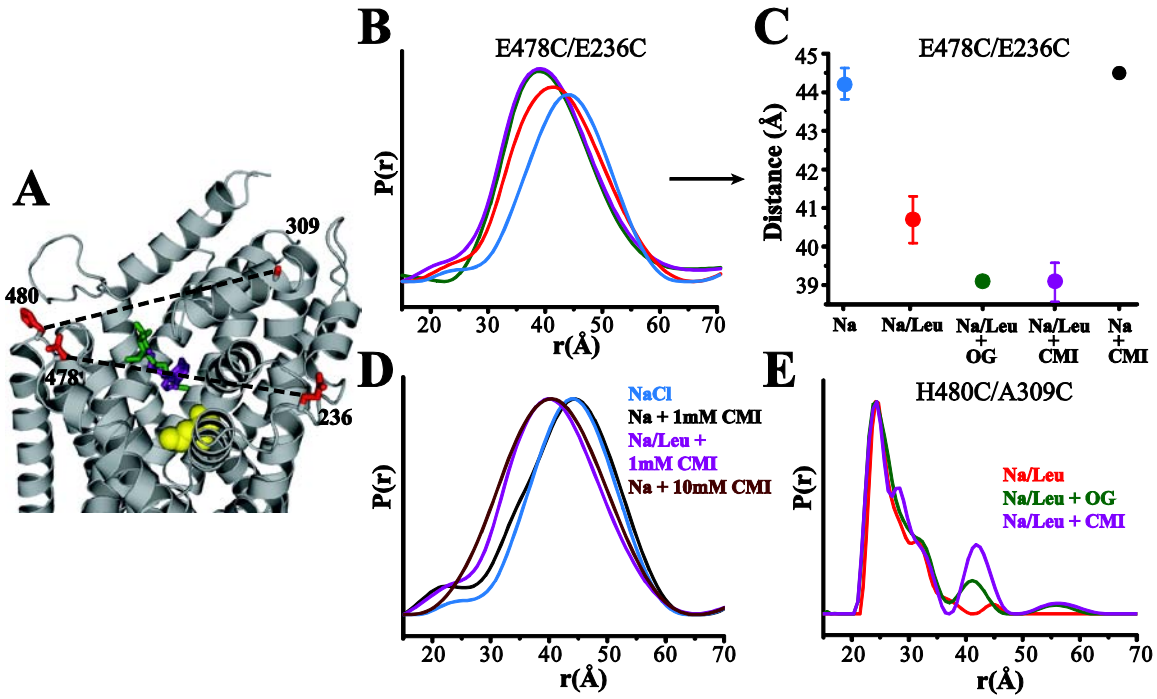

Figure 45. OG and CMI binding induce a distinct global structure. (**A**) LeuT structure highlighting the spin label pairs used to measure global changes in structure upon inhibitor binding. (**B**) CMI and OG induce similar magnitude left shifts in the distance distribution of E478C/E236C. (**C**) Although the 1mM CMI-induced shift was dependent on the presence of Leu, a similar left-shift was observed with 10mM CMI in the absence of Leu (**D**), suggesting that Leu binding in the S1 site may enhance the binding affinity of CMI to the extracellular vestibule. (**E**) The effects of these inhibitors may be localized to specific structural regions since the average distance between spin labels at H480C and A309C did not change in the presence of OG or CMI.

structural change associated with Leu binding in the S1 site enhances the affinity of LeuT for CMI. This may also explain why 10mM CMI is required to observe impaired Leu binding to the F253C mutant described above (since Leu does not bind in the S1 site in this mutant). Interestingly, an identical shift in the distance distribution is observed in the presence of OG, consistent with the observation that this inhibitor binds in a similar location to the TCAs (Figure 45A). Therefore, both OG and CMI induce a similar global conformation of LeuT. However, CMI and OG do not significantly alter the distance distribution of H480C/A309C, suggesting that the conformation of EL4 remains unchanged (Figure 45E). Since E236C is found in EL3 in close proximity to TM6, the data may suggest that these inhibitors produce local structural

rearrangements of EL3, TM6 or both. Importantly, the dataset is limited in scope and other conformational changes may occur that were not captured here. Nevertheless, the changes imply that the Na^+/Leu intermediate is distinct from the inhibitor bound structure.

Tryptophan produces an extreme outward-facing conformation

Of all available crystal structures, LeuT adopts a unique conformation in the presence of the competitive inhibitor Trp (173). Four Trp molecules are found in this structure with two "wedged" into the extracellular permeation pathway and the S1 binding site. As a result, the extracellular vestibule expands to accommodate the bulkier amino acid. This structure has been interpreted as a trapped "open-to-out" conformation characterized in part by outward displacement of EL4 (Figure 46A). Consistent with the crystal structure, the addition of 20mM Trp to the Na^+ intermediate produces a right shift in the average distance relative to both the Na^+ and Na^+/Leu bound conformations (Figure 46B, Supplemental Figure 19A). Trp also induces a right shift in the distance distribution of E478C/E236C relative to the Na^+/Leu state (Supplemental Figure 19B). As shown in Figure 46, two important observations distinguish this inhibited conformation from the outward-facing Na^+ state. First, the Trp-bound distance distribution overlaps the most extended component in the heterogeneous Na^+ ensemble (gray dashed box). This suggests that Trp selectively enhances a specific conformation of LeuT sampled in the equilibrium of Na^+-dependent conformers. Second, the Na^+-induced distance distribution is wider than in the Trp-bound form, indicating that Trp reduces the intrinsic dynamic behavior of EL4. Consistent with a competitive mode of inhibition (173), Leu binding in the S1 site mostly restores the Na^+/Leu distance distribution for H480C/A309C (data not shown).

The Trp-dependent changes in global structure are reflected also in the solvent accessibility of buried sites reported by the Na^+/Leu intermediate. For example, the NiEDDA accessibility of A315C in the presence of Trp is twice as much as the Na^+ state and more than seven-fold larger than the Na^+/Leu state (Figure 46C). Other sites in the extracellular vestibule or those near the binding site also show increased water penetration reported by a right shift in the

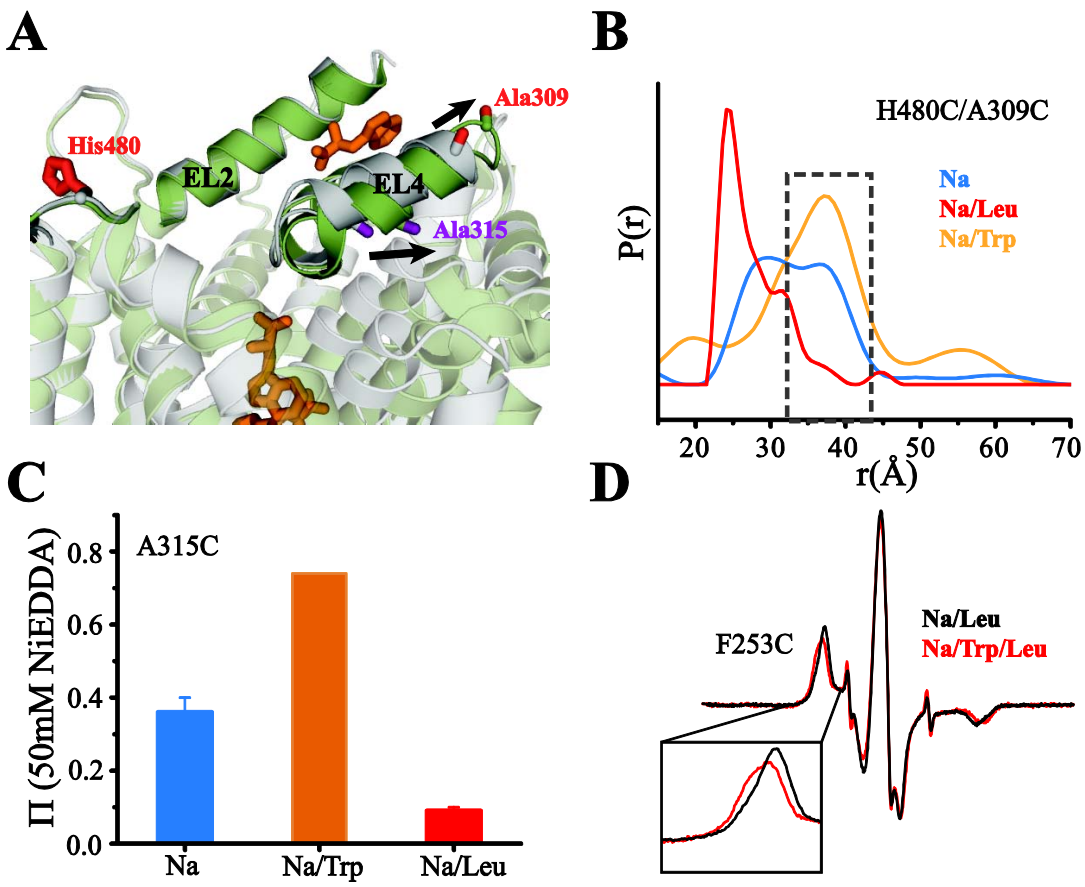

Figure 46. Trp binding creates an extreme outward-facing conformation. (**A**) Expansion of the extracellular vestibule upon Trp binding is partly due to outward movement of EL4 (green structure). (**B**) This outward movement is captured by the H480C/A309C spin labeled pair, illustrating that Trp stabilizes an exaggerated open state relative to the Na^+ intermediate. (**C**) The movement of EL4 also increases access to the vestibule, as shown by A315C. (**D**) Consistent with the role of an inhibitor, the presence of Trp impairs Leu binding as indicated by an attenuated change in spectral breadth of the spin labeled F253C mutant.

power saturation curves (Supplemental Figure 19C-D). Furthermore, dehydration of the S1 site is impaired in the presence of Trp (Figure 46D), consistent with the stabilization of an extreme open conformation. Fundamentally, the structural features of Trp-bound LeuT are distinct from the outward-facing conformation induced by Na^+ binding. Although the Trp-bound state samples a Na^+-induced conformer, the prominent dynamic features of the Na^+-intermediate are missing. A possible origin of this distinguishing feature is revealed in molecular dynamics simulations as

shown in Figure 47. In the Na^+ only configuration, TM6 adopts an outward tilt relative to the Na^+/Leu state that is similar to the Trp-bound crystal structure and consistent with the E478C/E236C distance distribution (Figures 47B-C and Supplemental Figure 19B). However, the simulations also indicate that Trp occupation of the S1 site may prevent configurational changes of specific side chains involved in the generation of the Na^+ and Na^+/Leu intermediate states (Figure 47D).

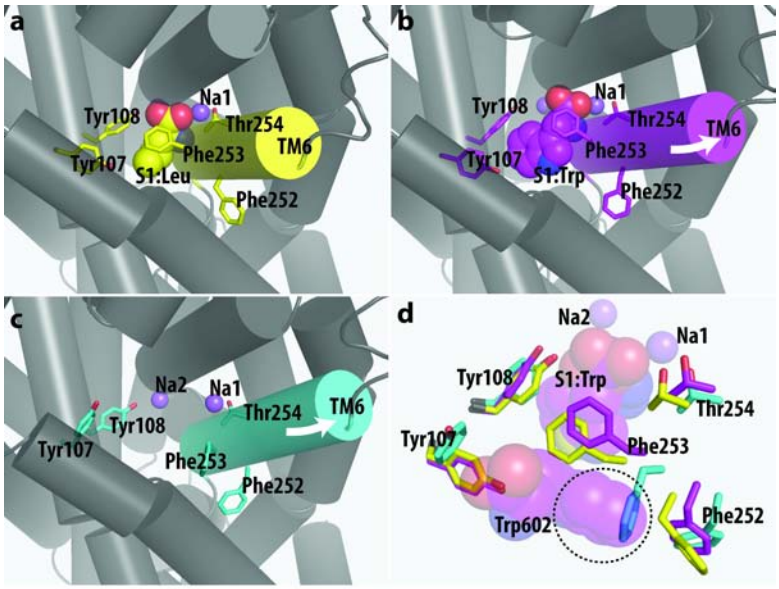

Figure 47. Molecular dynamics simulations reveal side chain rotamer orientations that stabilize the outward-facing conformation. Trp binding produces an outward tilt of TM6 (**B**) relative to the Na^+/Leu state (**A**). A similar movement of TM6 is shown in the Na^+ only configuration (**C**), consistent with the formation of Na^+-dependent outward-facing state. (**D**) Changes in the rotameric conformation of S1 site residues Phe253 and Phe252 may be involved with stabilizing this intermediate state. The presence of Trp in the S1 site occupies a similar space to Phe253 (dotted circle), which may trap LeuT in an outward-facing conformation. Special thanks to Dr. Lei Shi (Cornell University) for producing this figure.

Mechanistic implications for Na^+-coupled substrate transport

The results of the EPR analysis presented above outline the structural features of three intermediates associated with a functional transport cycle. In addition, the presence of either non-competitive or competitive inhibitors alters the structural constraints and effectively differentiates between a functional transporter conformation and its inhibited form in solution. Even though these structural changes are not nearly as large as those seen in other transporters, such as MsbA (223), the results clearly demonstrate significant ion/substrate-dependent conformational movement. The data strongly suggest that Na^+ binding alone provides a thermodynamic driving force to establish an outward-facing state characterized by a novel, dynamic movement of EL4. The Na^+-driven expansion of the extracellular vestibule increases access to the substrate permeation pathway and facilitates substrate binding, consistent with an ordered binding scheme. This contests previous molecular dynamics simulations that suggested limited movements occur allowing only a few water molecules to penetrate in the absence of Leu (230). On the contrary, the large size of NiEDDA relative to water leads to an *underestimation* of the aqueous accessibility of the permeation pathway. Therefore, Na^+ and Leu are not only tightly coupled by direct interaction at the S1 site, but also through structural rearrangements that expose the binding site. Subsequent Leu binding effectively reverses the Na^+-induced conformation leading to restricted access of the permeation pathway. The Na^+/Leu intermediate is predominately formed by inward movement of EL4, highlighting a "lid-like" function of this extracellular loop. However, TM6 and TM10 may contribute to the formation of an occluded state as shown by changes in distance distributions or local environmental parameters.

The results of the EPR lineshape changes observed for the F253C mutant suggest that Leu binding to the S2 site induces a conformational change in LeuT. Furthermore, this data emphasizes the connection between the S1 and S2 binding sites. Mutants that possess wild type binding stoichiometry do not show additional global or local effects with substrate binding to the S2 site. This implies that binding in the S2 site is not required to form an occluded state.

However, small changes, such as side chain re-packing or reorientation, may occur with S2 binding that are beyond the resolution of the EPR technique. In the absence of the activity assays, the complete EPR dataset can be rationalized by a single binding site model, as shown in the crystal structure. The high binding affinity of Leu combined with μM reagent concentrations for EPR may drive binding to the primary site even in the presence of disrupting mutations such as F253C. In this case, attenuated changes in spectral breadth due to CMI binding in the extracellular vestibule could then be attributed to steric restriction of functional transporter dynamics.

However, one important consideration is the limited number of spin labeled positions. That is, conformational changes due to substrate occupation of the S2 site may be detectable with a more thorough nitroxide scan of structural components. Another consideration is that the binding data were collected in the absence of an ion gradient. Since substrate binding in the S2 site has been proposed to allosterically trigger Na^+ symport (188), S2-driven conformational changes may require a Na^+ gradient. Alternatively, the conformational changes produced by binding in the S2 site may be degenerate with those produced by binding in the S1 site alone. Validation of this possibility necessitates experimental conditions that selectively enhance substrate binding to one site or the other.

CHAPTER IV

ION-DEPENDENT CONFORMATIONAL EQUILIBRIA AND SUBSTRATE BINDING

Rationale

Previous studies have shown that neurotransmitter transport is critically dependent on Na^+ as a coupling ion (9,15). Likewise, transport activity in LeuT is Na^+-dependent and it was proposed that the larger K^+ could not fit into the Na^+ binding sites (168). Accordingly, the results presented in the previous chapter indicate that Na^+ binding induces a change in the structure of LeuT to facilitate substrate binding. Interestingly, the smaller Li^+ has been shown to induce uncoupled currents (20), suggesting that this cation may affect the structure of neurotransmitter transporters. Li^+ has been used pharamacologically to treat depression and bipolar affective disorder (82,231), although the mechanism of therapy is not known. Treiser and co-workers found that Li^+ increased serotonin release in the hippocampus, but that uptake was unaffected (232). However, an increased rate of MTSET-driven inactivation and enhanced uncoupled currents relative to Na^+ suggested that Li^+ induced a conformational change in the SERT (233). Investigation of the GAT also has suggested that Li^+ produces a conformation that supports a Li^+ leak current, which is abolished in the presence of Na^+ (234). In addition, Li^+ was found to support GABA transport in the presence of low Na^+ concentrations, which was interpreted that Li^+ can replace Na^+ at one of its binding sites (235). A subsequent study confirmed these findings in the GAT and, based on a similar molecular architecture of LeuT, identified a low affinity Na^+ binding site for which Li^+ can readily substitute (236). Corresponding to the Na2 site in LeuT, Li^+ binding in this site is controlled by an Asp residue that when mutated eliminates the Li^+ leak current *and* Li^+ stimulated transport. These results provided solid evidence that Li^+ can be co-transported provided that Na^+ occupies the other ion binding site. Recent molecular dynamics studies indicated that two different mechanisms are responsible for the robust selectivity of Na^+

over other monovalent ions in LeuT. The selectivity at the Na1 site is primarily a function of the strong electrostatic field produced by the coordinating residues, whereas structural constraints control the selectivity at the Na2 site (237). However, these studies suggested that these sites are only modestly discriminatory for Na^+ over Li^+, and that Li^+ could potentially support substrate binding (238). The work presented in this chapter outlines the structural impact of Li^+ binding to LeuT in the absence of Na^+ or substrate, highlighting a conformational equilibrium between Apo and ion-bound forms. In addition, the results show that Li^+, unlike K^+, will support substrate binding. Preliminary evidence also indicates that substrate binding properties are unique in LiCl solution, potentially uncovering different binding modes.

Li^+-induced conformational changes underscore a conformational equilibrium

Spin labeled sites that demonstrated sensitivity to Na^+ binding were used to investigate the potential for Li^+ to alter the structure of Apo-LeuT. Specifically, spin labels attached to V33C in TM1, I111C in TM3 and A315C in EL4 show spectroscopic changes in EPR parameters that suggest a Li^+-induced structural change. The spin label mobility and solvent accessibility to 50mM NiEDDA was measured in three biochemical states: Apo, LiCl and NaCl. Notably, the spin label at V33C shows a significant (nearly 2-fold) increase in accessibility in the presence of 200mM Li^+ relative to the Apo intermediate (Figure 48B). The Π value in LiCl solution is approximately 65% of that observed in NaCl solution. Although the difference in accessibilities between Apo and Li^+ states at A315C is just outside statistical significance (Table 4), a similar upward trend in the mean Π value is observed in the ion-bound form. In contrast to the changes in accessibility, the EPR lineshapes of V33C and A315C do not change in the presence of Li^+ (Figure 48B-C). Therefore, specific tertiary interactions appear to persist at these positions, even though the collision frequency of the probe with NiEDDA increases.

Relative to A315C, spin labeled I111C demonstrates a smaller, statistically insignificant increase in Π in the presence Li^+ (Figure 48D). However, the EPR spectrum of I111C does show

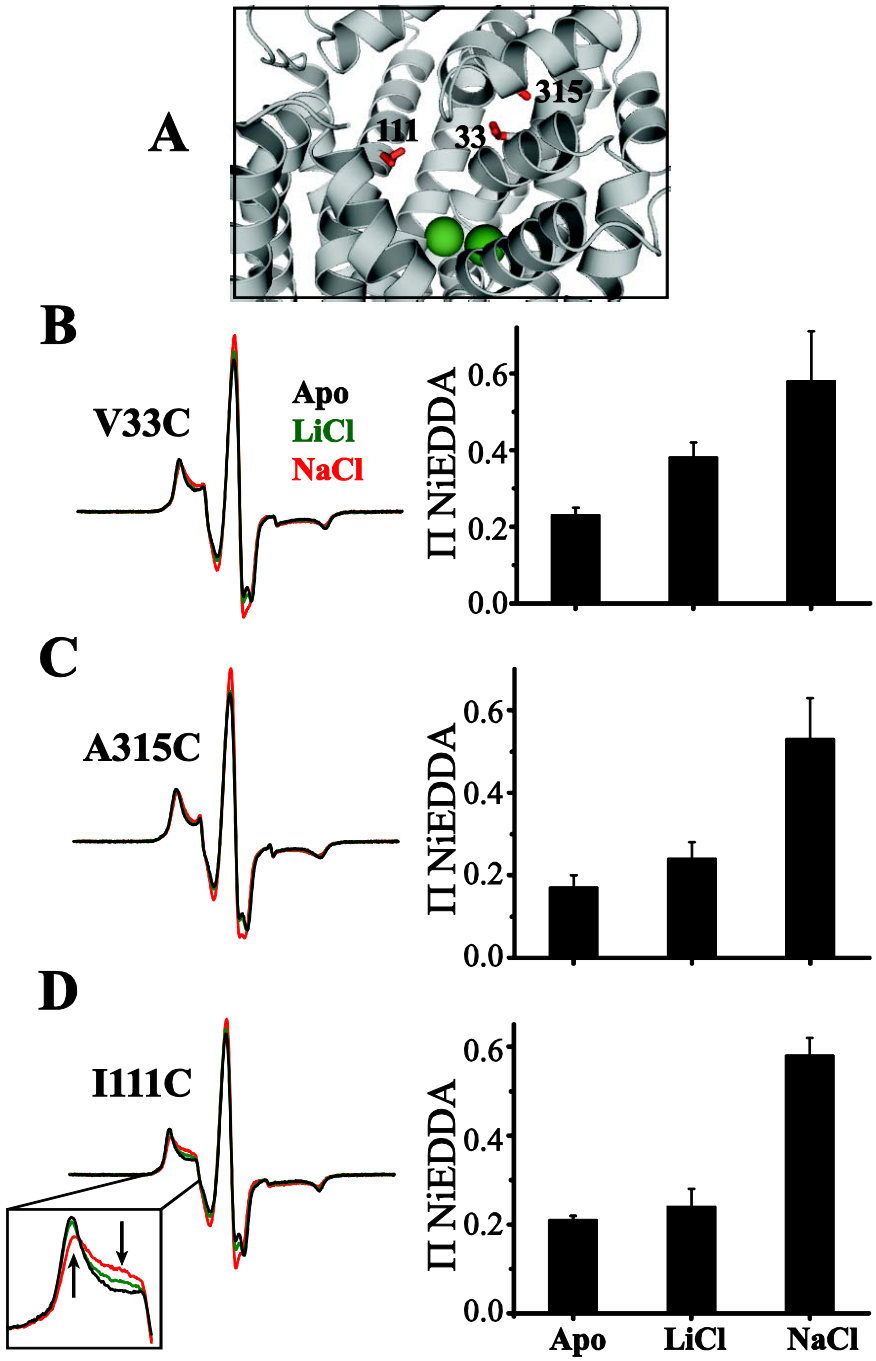

Figure 48. Li^+ alters the local structural environment. (**A**) Location of spin labeled sites in or near the extracellular vestibule relative to the S1 site. (**B-D**) Ion-dependent changes in EPR spectra and solvent accessibility in proteoliposomes. V33C and A315C do not show significant changes in lineshape in the presence of Li^+. However, a significant increase in NiEDDA accessibility is observed for V33C (**B**). In contrast, the lineshape of I111C suggests the presence of at least two motional states (arrows), in which the ion binding enhances the fast motion component (**D**).

Table 4. Ion-dependent changes in solvent accessibility within the extracellular vestibule

Mutant	Π (Apo)		Π (LiCl)		Π (NaCl)	
	NiEDDA	O_2	NiEDDA	O_2	NiEDDA	O_2
V33C	0.23±0.02	0.14±0.02	0.38±0.04	0.23±0.01	0.58±0.13	0.23±0.04
A315C	0.17±0.03	0.16±0.01	0.24±0.04	0.17±0.02	0.53±0.10	0.25±0.01
I111C	0.21±0.01	0.12±0.01	0.24±0.04	0.16±0.01	0.58±0.04	0.28±0.02
F259G/I111C	0.29±0.02	0.12±0.01	0.62±0.00	0.19±0.01	0.72±0.02	0.22±0.01

definitive changes in the three conditions tested. Overall the spin label mobility increases with the presence of either ion, with Na^+ promoting the most change. Close inspection of the changes in EPR spectra suggests that each of the three lineshapes represents the sum of two or more motional components arising from spin labels with different rates of rotation. Indeed, lineshape fitting routines have so far been unsuccessful in identifying the discrete motional properties of the spin label in the Apo state assuming either one or two components with standard g and hyperfine tensor values (Figure 49). Qualitatively, the presence of multiple components is most evident in the Na^+ intermediate where at least two different spin label populations (arrows Figure 48D) are demarcated by an inflection in the low field resonance lineshape. Each of the two populations, which arise from a fast and slow motion component in the EPR spectrum, may reflect two conformational extremes of the spin label. In addition, these extreme components are unresolved (Figure 49B), suggesting the presence of an ensemble of intermediate states as well. Thus, an exchange model that accounts for interconversion between two rotational rates may be necessary to properly fit the spectra. Relative to the Apo state, the presence of either ion increases the population(s) of spin labels sampling higher rotational rates, but to different extents.

Collectively, the dataset described above can be modeled by a conformational equilibrium between the Apo and ion-bound intermediates (Figure 50). In the Apo state, the EPR spectrum of I111C is predominately a single component characterized by a population of spin labels exhibiting highly restricted motion. Although the addition of either Li^+ or Na^+ increases the overall mobility, the slow motion component does not completely disappear. Importantly, Li^+

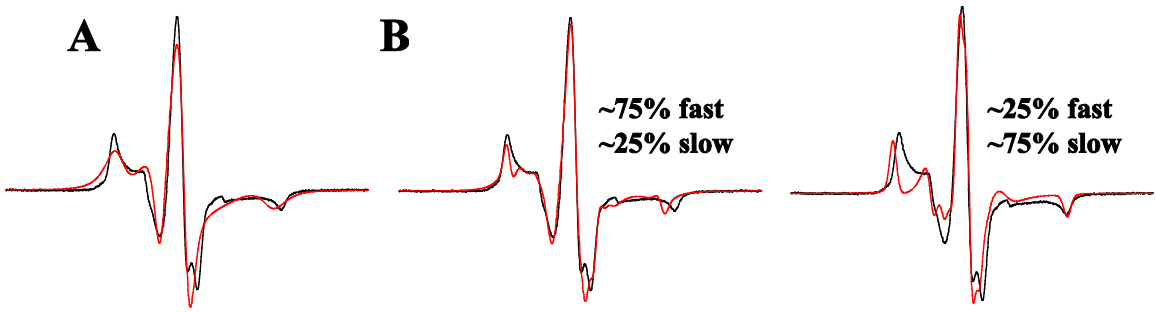

Figure 49. Non-linear least squares fits (red trace) of the EPR spectrum of I111C in the Apo state. (**A**) Single component and (**B**) two component fits using standard g and A tensor values.

elicits a subtle increase in probe mobility in between the Apo and Na^+ states. In applying the results from Chapter 3, this result suggests that Li^+ binding induces a right shift in the equilibrium between a closed and open state toward an outward-facing conformation (Figure 50). The maximal shift toward the open state is achieved by the binding of Na^+. This model also explains the incremental increase in solvent accessibility at V33C and A315C with Li^+ binding. The nature of the power saturation technique captures an average Π value weighted by the populations in the spin ensemble (207).

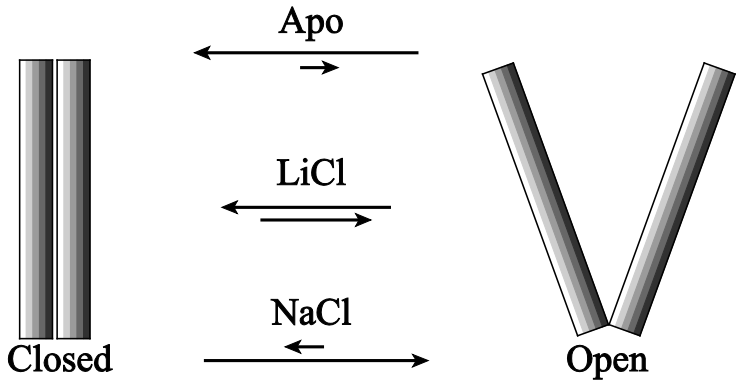

Figure 50. Ions shift the conformational equilibrium toward an outward-facing state. In the Apo state, the transporter predominately resides in a closed conformation. The binding of either Li^+ or Na^+ shifts the equilibrium towards an open state.

Two additional lines of evidence support the presence of an ion-dependent equilibrium shift between open and closed conformers of LeuT. Incorporation of the background mutant F259G into the I111C construct exaggerates the observed changes in both the EPR lineshape and solvent accessibility. As will be discussed later, the F259G mutation disturbs substrate binding at

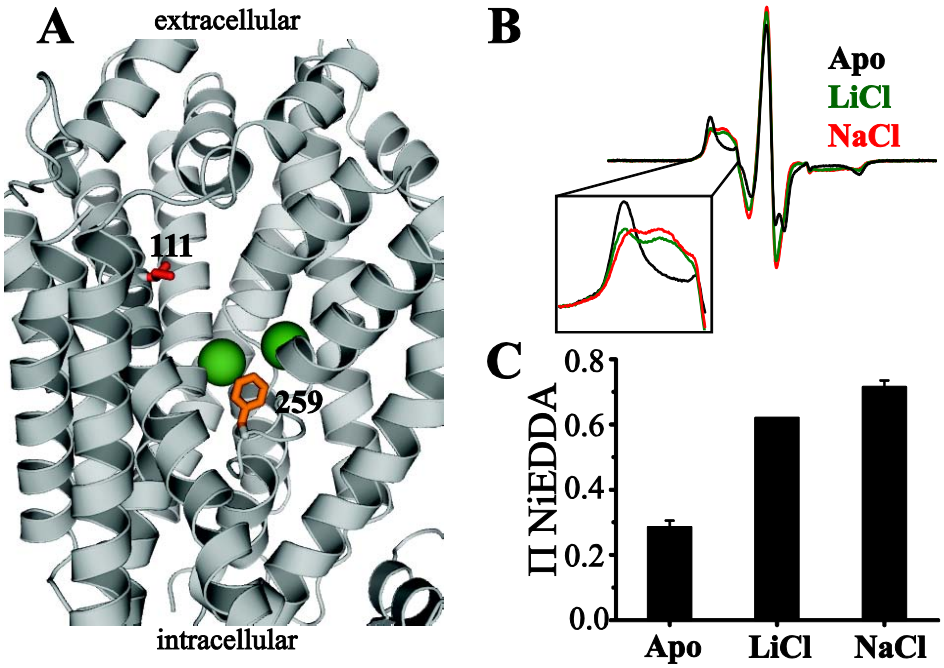

Figure 51. Increased ion sensitivity in the F259G background. Mutation of Phe259 near the ion/substrate binding sites (**A**) increases the mobility of the spin label at I111C relative to the single mutant background (**B**). This effect is also manifested in the NiEDDA accessibility (**C**), suggesting that the F259G mutation creates a bias toward the open state in the conformational equilibrium.

the S1 site. In this background, the spin label at I111C reports changes in lineshape in all three states relative to the I111C mutant alone (Figure 51B). Immediately noticeable is the amplified population(s) of higher mobility spin labels in the ion-bound states and the increase due to Li^+ binding approaches the level due to Na^+ binding. This result is mirrored by similar levels of NiEDDA accessibility (Figure 51C). The low field resonance line of Apo-I111C/F259G also

shows an increase in width in the EPR spectrum and solvent accessibility increases by a small margin. Collectively, these results suggest that the background mutation creates an inherent bias towards an open state in the equilibrium which enhances the sensitivity of LeuT to Li^+ and Na^+ binding. Despite this bias, the immobilized component in the EPR spectra persists in the ion-bound states of this double mutant.

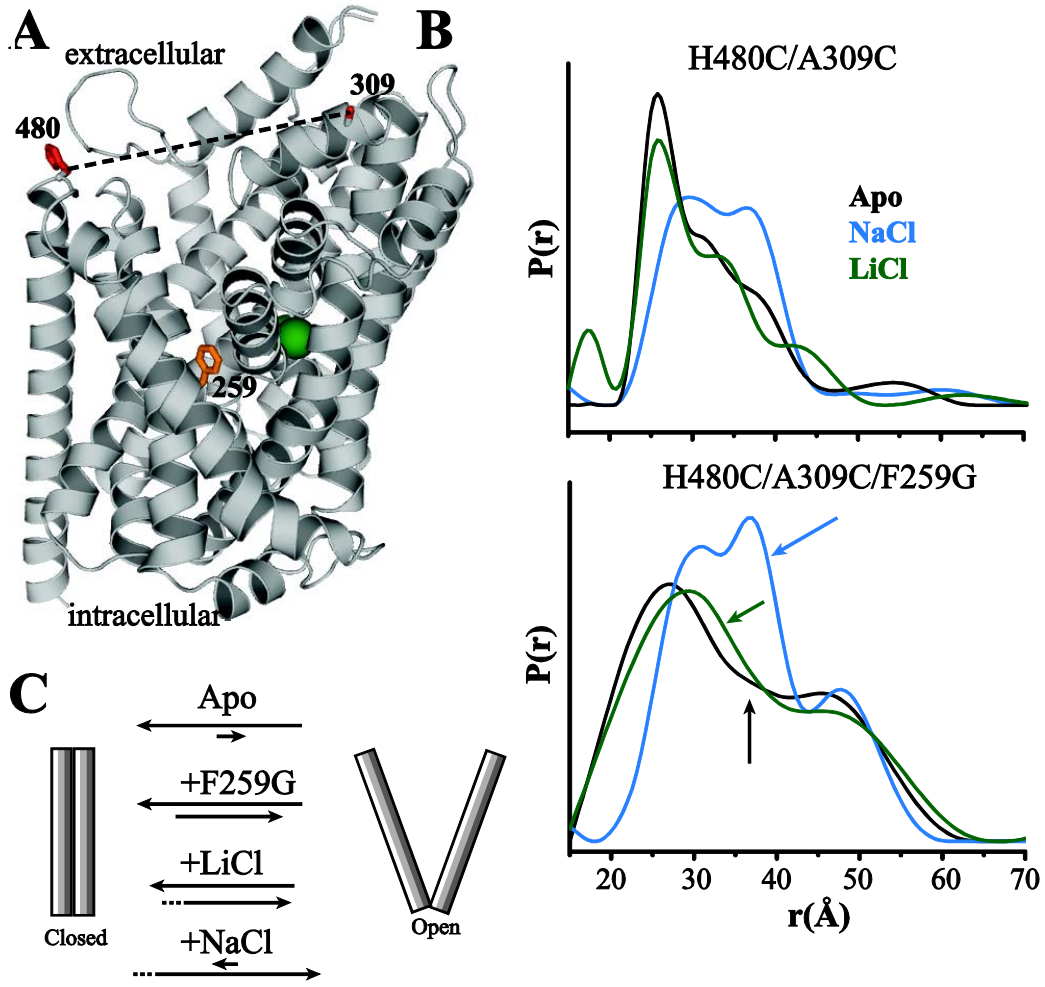

Figure 52. Increased global dynamic behavior in the F259G background. (**A**) Distance measurements were made between EL6 and EL4 to determine the impact of Li^+ binding on global changes in structure. Although the local effect of Li^+ binding is not resolved at a global level with DEER spectroscopy (top panel in **B**), broader distance distributions and ion-dependent enhancements of specific LeuT conformers are observed in the F259G background (arrows). (**C**) These results suggest that the F259G mutation increases the probability of an open conformation in the Apo and ion bound states.

Secondly, these results are directly in line with the shape of the distance distributions of H480C/A309C as described in Chapter 3. The Apo intermediate displayed multiple distance components with a prominent short distance population occupying the vast majority of all interspin distances. Also, Na^+ binding enhanced the lower probability distance populations without completely eliminating the shortest distance component. These data are consistent with a Na^+-driven shift in the conformational equilibrium toward an open state. However, the Li^+-induced structural change is too small to be resolved by global distance analysis (Figure 52B). Yet, the incorporation of the F259G mutation into the H480C/A309C mutant broadens the Apo state distribution and increases the sensitivity of ion binding to be detected by DEER analysis, which is consistent with a mutation-driven shift toward an open state (Figure 52B-C).

Evidence that Li^+ supports substrate binding

The results described above suggest that the presence of Li^+ leads to structural changes in LeuT that may facilitate substrate binding. The experiments described below attempt to spectroscopically characterize Li^+-supported binding of two substrates: Leu and Ala. The major difference between these two substrates is that Ala has a lower binding affinity (at least 15-fold) and larger k_{cat} (5-fold), making Ala a much more informative amino acid to measure transport activity (173). However, crystal structures with Ala are nearly identical to the Leu-bound structures (173). Furthermore, EPR lineshape analysis of L400C (and other sites) indicates that Na^+-dependent Ala binding induces a similar conformational change to Leu binding (Chapter 3).

Li^+ supports Leu binding

Functional analysis suggests that total binding of 100nM [^{3}H]-Leu to wild type LeuT is reduced by ~50% (consistent with 1:1 stoichiometry) and substrate transport is eliminated in the presence of Li^+ (Figure 53A-B). Incorporation of mutants that prevent substrate binding only to

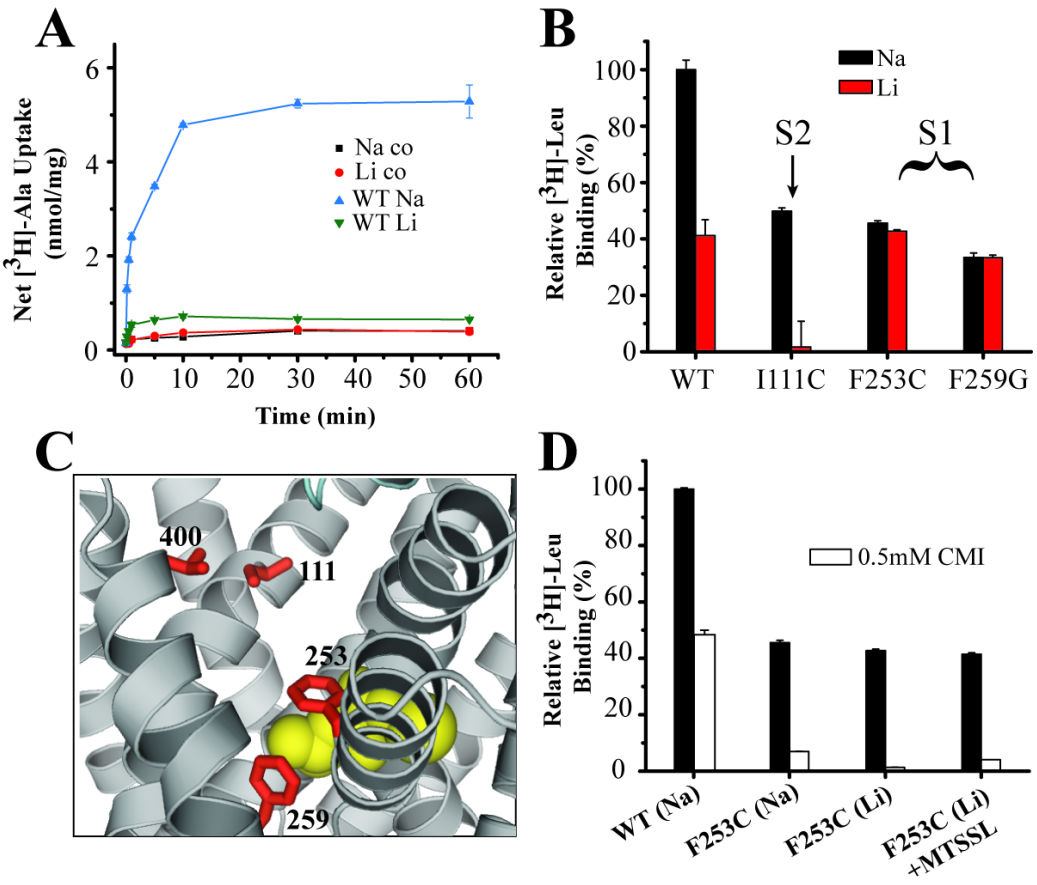

Figure 53. Functional analysis of LeuT in the presence of Li^+. (**A**) Li^+ does not support Ala transport. (**B**) Leu binding is reduced by ~50% in the presence of Li^+ relative to the Na^+ control according to SPA analysis. Mutation of S1 binding site residues (Phe253 and Phe259) does not change the Leu binding profile relative to Na^+. However, mutation of S2 site residues (i.e. I111) eliminates Li^+-dependent binding, suggesting that Li^+ promotes Leu binding to the S2 site. (**C**) Location of binding site residues shown in (**B**) and subsequently used for substrate binding studies by EPR. (**D**) Na^+ and Li^+-dependent Leu binding is eliminated in the presence CMI which binds in the extracellular vestibule and blocks substrate binding to the S2 site.

the S2 site completely abolish Li^+-dependent Leu binding activity (Figure 53B). However, site directed mutagenesis of positions that contribute to the S1 binding site (F253C, F259G) does *not* disrupt Li^+-dependent Leu binding relative to wild type (Figure 53B) and Na^+ controls. Thus, the SPA analysis suggests that Li^+ promotes Leu binding only to the S2 site. Consistent with this observation, the EPR spectrum of S1 site mutant F253C indicates that Li^+ supports binding of Leu to the S2 site similar to Na^+ (Figure 54A-C). Furthermore, Li^+-dependent Leu binding is

reduced in the presence of CMI (Supplemental Figure 20). Global distance analysis as measured by H480C/A309C also indicates that Leu binding drives the formation of an occluded state in the presence of Li^+ (Figure 54D).

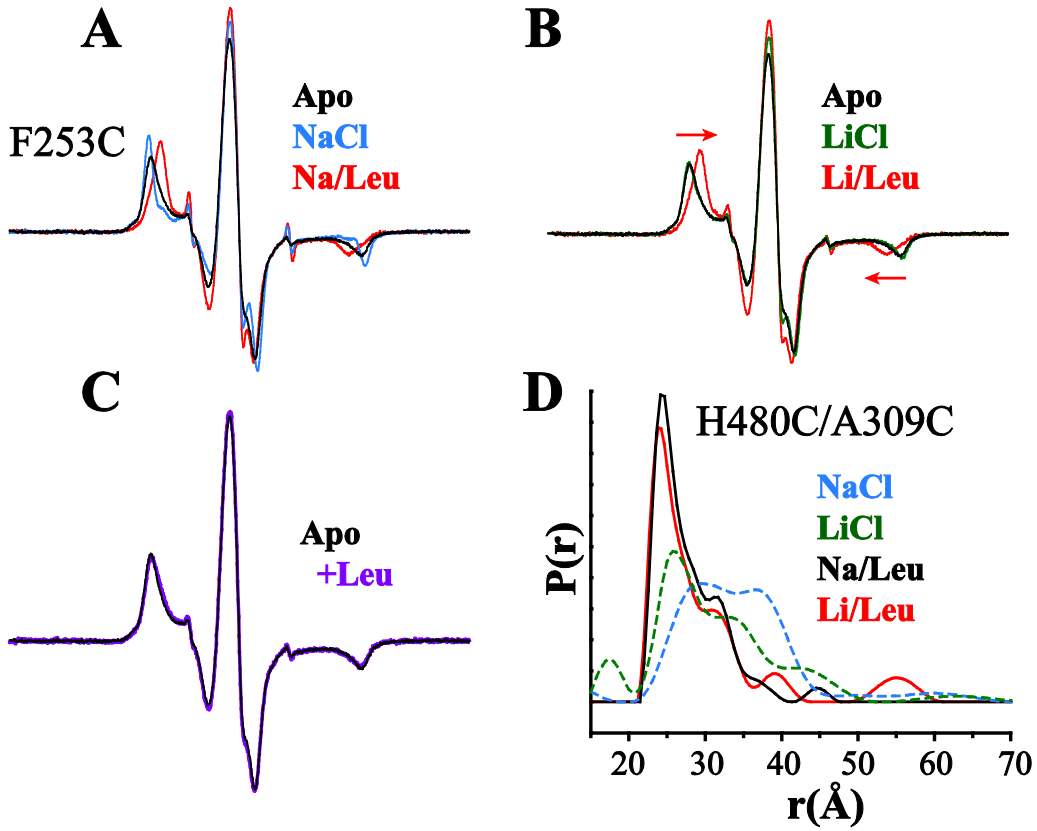

Figure 54. EPR lineshape analysis suggests Li^+ supports Leu binding. (**A**) Spectroscopic changes in EPR lineshape at F253C in the presence of Na^+. (**B**) Although Li^+ does not alter spectral features of the Apo state, a decrease in spectral breadth (arrows) indicates that Leu will bind in the presence of Li^+. (**C**) The Leu-induced changes in the EPR spectrum of (**A**) and (**B**) are dependent on the presence of the ion, since Leu alone does not alter the Apo state spectrum (thick purple trace). (**D**) Leu also establishes a similar globally occluded intermediate in the presence of Li^+.

Unexpectedly, changes in the EPR lineshape at the S2 site mutants L400C and I111C are consistent with Li^+-dependent Leu binding to the S1 site (Figure 55). This result was obtained

with 20μM LeuT and a 1:1 Leu-to-LeuT molar ratio and may suggest that these reagent concentrations are above the K_D^{Leu} of the S1 site in the presence of Li^+. Supporting this possibility is the observation that Li^+ appears to support a 2:1 binding stoichiometry provided the [Leu] is in the μM range (SPA analysis data not shown). However, lower reagent concentrations do not prevent Li^+-dependent binding to the S1 site (Supplemental Figure 21). Even incorporating an S1 site mutant background (F259G) does not prevent Leu binding as measured by changes in lineshape at either L400C or I111C (Figure 55, Supplemental Figure 21). Since the difference between the K_D^{Leu} measured for the S1 and S2 sites is reportedly marginal, it appears that the affinity of Leu is too high to observe differential binding effects of the S1 and S2 sites by EPR.

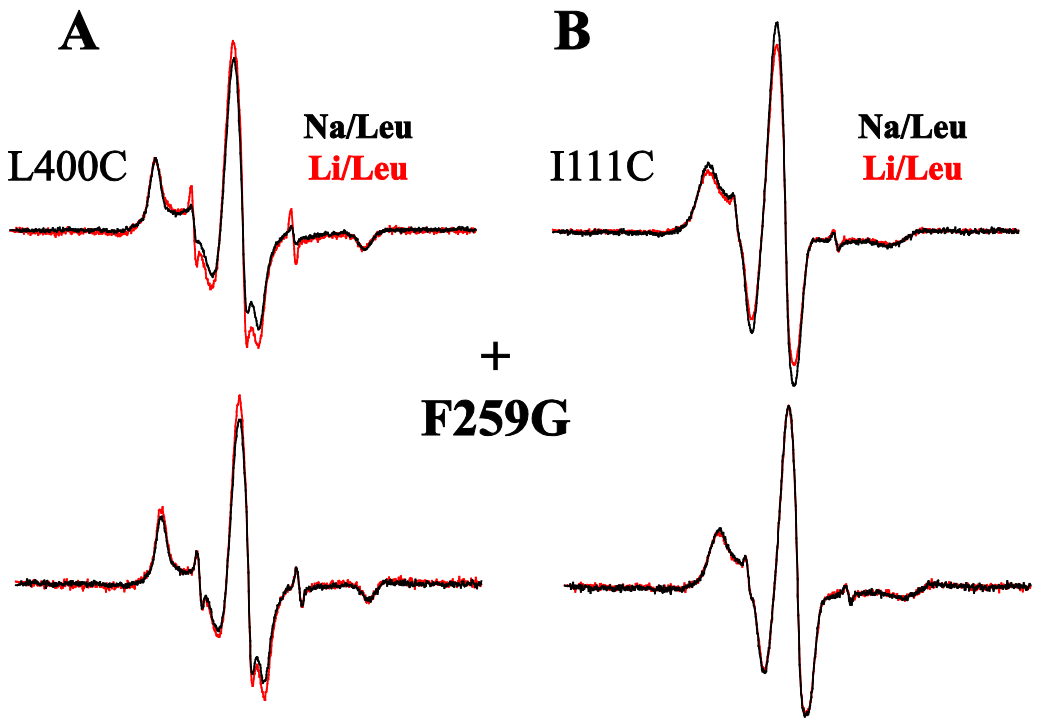

Figure 55. Li^+-dependent Leu binding in S1- and S2-site disrupting backgrounds. Although functional analysis indicates that Leu will not bind to mutant LeuT with a disturbed S2 site, both L400C (**A**) and I111C (**B**) show similar Leu-induced changes in EPR spectra in the presence of either ion. Furthermore, incorporation of the F259G background (an S1 site mutant) does not prevent Leu binding, suggesting that the binding affinity of Leu is too high to correlate spectral changes with substrate occupation of a specific binding site by EPR.

Preliminary characterization of Li^+-dependent Ala binding

The EPR spectrum of 20μM L400C shows that 20μM Ala induces similar changes in the lineshape in the presence of either Li^+ or Na^+ (Figure 56).

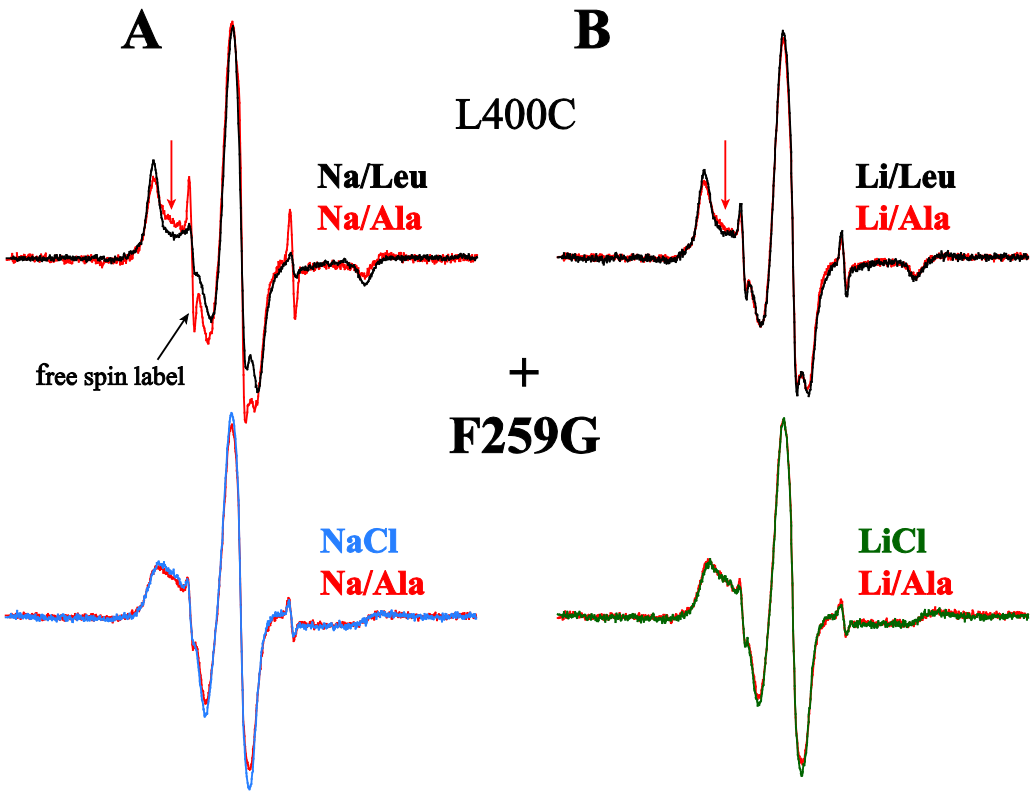

Figure 56. Ion-dependent Ala binding is abolished in the F259G background. The degree of spin label restriction at L400C due to stoichiometric Ala binding is reduced relative to the Leu-bound state (arrows in **A** and **B**), albeit to a lesser extent in LiCl solution (top panel of **B**). However, incorporation of the F259G background mutation eliminates Ala-induced spectral changes relative to the ion-bound state, suggesting that the change in spin label mobility is due to substrate occupation of the S1 site.

However, the degree of restricted spin label motion is less than that with Leu as a substrate at identical concentrations, which may be reflective of the lower intrinsic binding affinity of Ala to LeuT. This interpretation is supported by the observation that 2μM LeuT and Ala reports little

ion-dependent change in EPR lineshape relative to the Apo intermediate, although the spin label mobility is completely restricted in the presence of Leu (Supplemental Figure 21). The tight binding of Leu prevents an estimation of binding affinity by EPR methods using μM reagent concentrations. In contrast, titration of L400C with Ala in the presence of Na^+ shows a monotonic

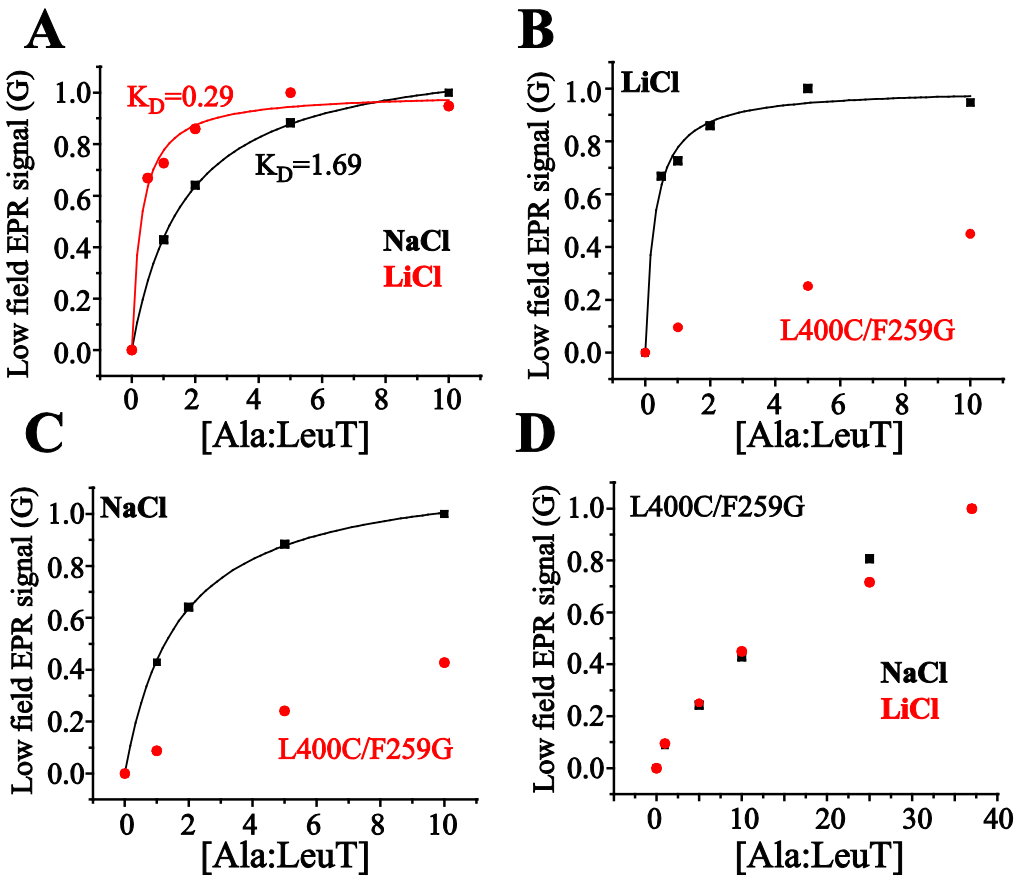

Figure 57. Li^+ alters the binding affinity of Ala. (**A**) The Li^+/Ala titration curve of L400C revealed a left shift relative to Na^+, suggesting a Li^+-dependent increase in Ala binding affinity. (**B-C**) The background mutation, F259G, strongly shifts the binding curve to the right, suggesting a substantial decrease in Ala binding affinity in the double mutant. (**D**) The ion-dependent differences in binding isotherms observed in (**A**) are eliminated in the double mutant.

change in EPR lineshape that saturates at ~5:1 (Ala-to-LeuT) molar ratio (Figure 57A). Non-linear least squares analysis using a single site binding model to fit the data estimates a K_D^{Ala} of

1.7μM. Interestingly, the binding curve is shifted to the left in the presence of Li^+, consistent with an increase in Ala binding affinity relative to Na^+ (Figure 57A). Incorporation of the F259G background mutation abrogates Ala binding at a 1:1 molar ratio regardless of the ion identity (Figure 56). Generation of an Ala binding isotherm (Figure 57B-D) in this double mutant shows two important differences with respect to that reported in Figure 57A. In contrast to L400C, the signal saturates at much higher Ala concentrations, consistent with an overall increase in the K_D^{Ala}. This may suggest that the changes in EPR lineshape of spin labeled L400C are contingent on Ala binding in the S1 site. Secondly, the apparent difference in affinity between the Na^+- and Li^+-dependent curves is no longer observed.

Li^+-dependent Ala binding is also observed with the F253C mutant, which is evident by a decrease in $2A_{zz}$. Maximal changes in the EPR spectrum are seen with a 5:1 molar ratio, which is attenuated in the presence of 10mM CMI (Figure 58B, F). Interestingly, the Na^+/Ala spectrum shows evidence of two components at this molar ratio (Figure 58C-D). An overlay of the Li^+/Ala spectrum suggests that the outermost intensities of the Na^+/Ala spectrum represent a population of unbound LeuT. Increasing the concentration of Ala decreases this spin population and the EPR spectrum converges to a single component at ~50:1 molar ratio (Figure 58E). These observations are consistent with a Li^+-dependent enhancement of Ala binding affinity to the S2 site.

Concluding comments

Overall, the results presented here indicate that the presence of Li^+ will induce a conformational change and that Li^+, unlike K^+, will support substrate binding to LeuT. In combination with structural analysis described in Chapter 3, the Li^+ binding studies highlight a dynamic conformational equilibrium between a predominately closed, Apo state and more open, ion-bound intermediates. Small, but significant changes in local environmental parameters reflect a subtle shift in the equilibrium toward an outward-facing conformation in the presence of Li^+.

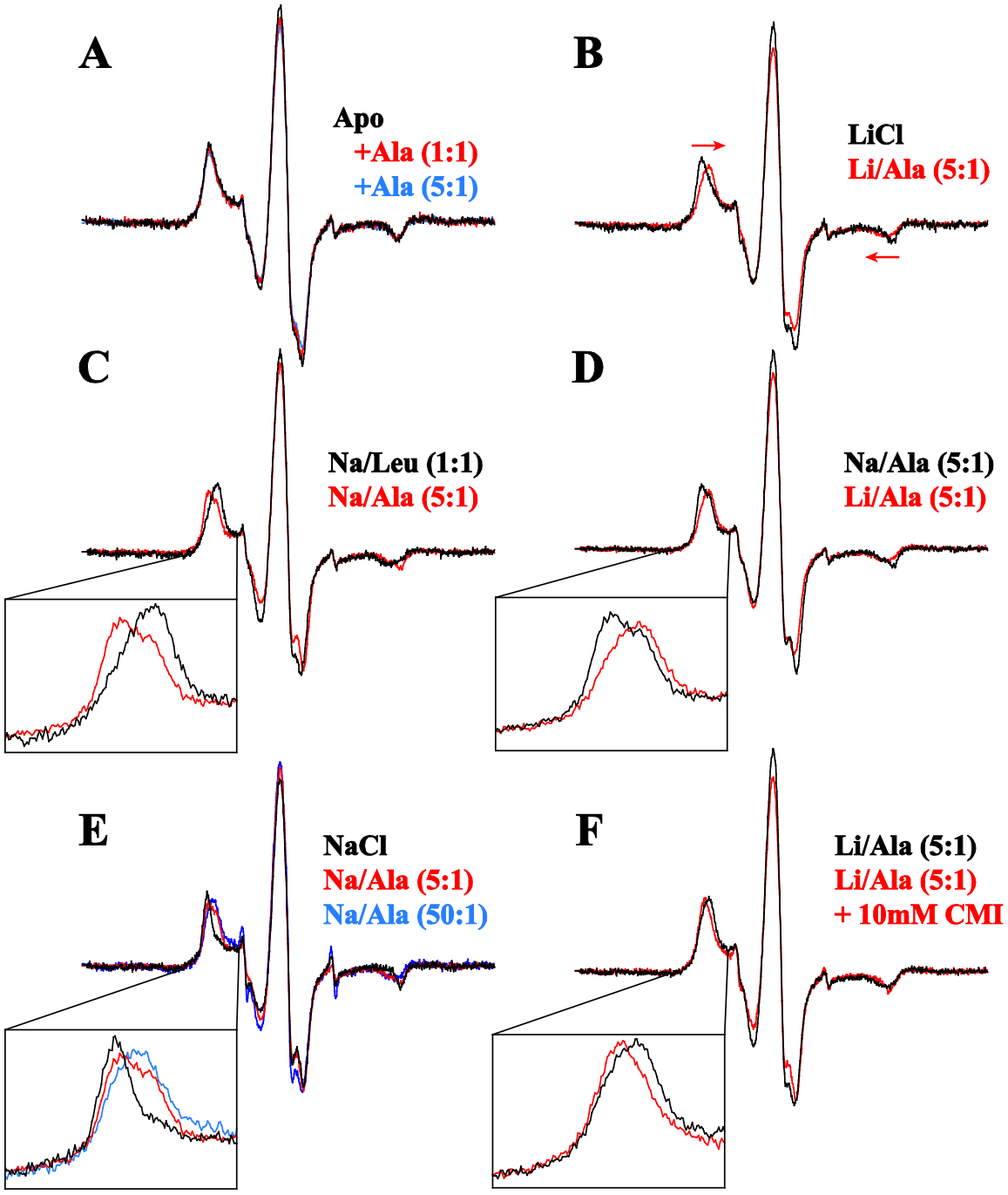

Figure 58. Li^+ enhances Ala binding to an S1 site mutant. Ion-dependent Ala binding to F253C is shown by a decrease in spectral breadth (**A-B**). In contrast to Leu, the spectral change requires ~5-fold more Ala than the equivalent Leu-dependent change. (**C**) The EPR spectrum of Na^+/Ala appears to be two components, suggesting that some LeuT remains unbound when compared to the Leu-bound state or to the Li^+/Ala bound state (**D**). (**E**) ~50-fold molar excess is required to complete Ala binding in the presence of Na^+. (**F**) Li^+-dependent Ala binding is impaired in the presence of CMI. Collectively, the data set is consistent with an enhancement of substrate binding to the S2 site in the presence of Li^+.

However, the finely tuned architecture of the ion binding sites promotes a maximal shift in the equilibrium when these sites are occupied by Na^+.

Similar to Na^+, the Li^+-induced conformational change facilitates binding of either Leu or Ala. The EPR lineshapes and global distance analysis suggest that structural changes induced by Li^+ and substrate are similar to those induced by Na^+ and substrate. According to the SPA analysis, Li^+ selectively enhances Leu binding to the S2 site at nM reagent concentrations. A fundamental discrepancy in the results shown here is the spectroscopic observation of Li^+-dependent Leu binding to the S1 site, even in the presence of S1-disrupting mutations (Figure 55). Most likely, this is attributed to a combination of nM Leu binding affinity and the μM concentrations of reagent used for the EPR analysis. Under these conditions, it is difficult to directly compare the functional and spectroscopic results, and thus provide a unique structure-based interpretation of mechanism.

Interestingly, ion-dependent Ala binding seems to uncover distinctive characteristics of LeuT behavior. Remarkably, the K_D^{Ala} is at least 6-fold less in Li^+ than in Na^+ for the spin labeled L400C mutant (Figure 57). At this time, the origin of this difference in affinity is not clear. In contrast to Leu binding, SPA reveals that Ala will bind to LeuT with a molar stoichiometry of 2:1 (Ala-to-LeuT) at sufficiently high (μM) Ala concentrations in the presence of Li^+, but 1:1 in the presence of Na^+ (data not shown). This unexpected result suggests that the mode of Ala binding is a function of ion identity. Furthermore, it may be interesting to consider that the ion-dependent difference in binding isotherms observed at L400C is a manifestation of differences in binding stoichiometry. Indeed, the F259G/L400C mutation, which presumably disrupts Ala binding to the S1 site, seems to abolish the ion-dependent difference in the binding curves (Figure 57). Alternatively, the difference in L400C binding curves may also be explained by altered interactions of Li^+ and Ala within the binding sites that may be disturbed in the F259G/L400C double mutant. Importantly, the substantial decrease in substrate binding of this double mutant relative to L400C emphasizes the cooperativity between the S1 and S2 sites. Therefore, a

mechanistic interpretation of these results must be tempered by the possibility that point mutations within one binding site may perturb Ala binding to both sites. Crystallization of LeuT in the presence of Li^+/Leu and Li^+/Ala may help to decipher the spectroscopic and functional results.

CHAPTER V

PERSPECTIVES ON FUTURE INVESTIGATIONS

Synopsis

The crystallographic analysis of LeuT provided a single, high resolution snapshot of a ligand-bound Na^+-coupled transporter evolutionarily related to the NSS superfamily. However, the structural dynamic properties that mediate activity could only be speculated in the absence of experiments that resolve transporter behavior in solution. The work presented here describes the first spectroscopic characterization of the conformational changes that couple to ion-dependent substrate binding in LeuT, thereby establishing a dynamic dimension to an emerging model of substrate symport. The global and local EPR analysis provide novel constraints that define the structural features of three biochemical intermediate states putatively associated with the first two steps of a transport cycle. As a result, the experiments explicitly identify structural elements, such as EL4, that participate in conformational rearrangements in close proximity to the extracellular vestibule. Access to the internal binding sites is restricted in the Apo and Na^+/Leu states. The structural transition from an empty, predominately closed state to a more open intermediate proceeds through a shift in a conformational equilibrium in the Apo state that is modulated by the presence of ions. The results clearly show that Na^+ binding establishes an outward-facing conformation relative to the Apo and Na^+/Leu intermediates that exposes the extracellular permeation pathway to solvent. Subsequent Leu binding to the S1 site in the Na^+ state drives the formation of a distinct occluded intermediate. Based on experiments with S1-site mutations, it may be possible to form a similar occluded state by substrate binding in the S2 site. However, this bound configuration is not conducive to symport as defined by the S1/S2 mechanism given that substrate is not bound in the S1 site (188). Since binding of the inhibitors CMI and OG induce a similar change in EPR parameters, the original crystal structure of LeuT (which has bound OG in

the extracellular vestibule) is not likely to represent a functionally relevant form (189). Based on the data described here, a qualitative description of the conformational dynamics that occur in LeuT is summarized in Figure 59.

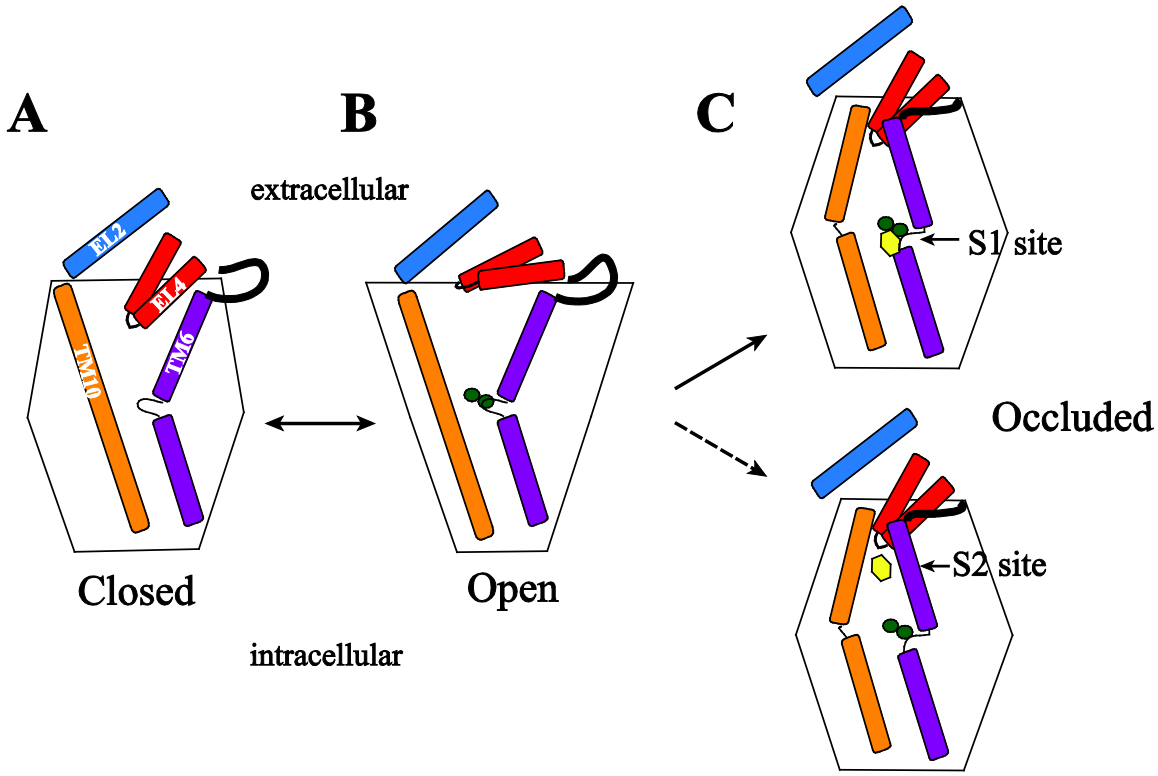

Figure 59. Cartoon model of LeuT functional dynamics. (**A-B**) The transporter exists in a conformational equilibrium characterized by transitions between a closed and open extracellular gate. In the absence of a functional ion, this equilibrium is shifted heavily towards a closed state. Ion binding "stabilizes" the outward-facing state formed in part by the movement of EL4. This outward-facing state is poised to bind substrate. (**C**) The subsequent binding of substrate in the S1 site drives conformational changes in EL4, TM6 and TM10 to occlude the extracellular permeation pathway. Substrate binding in the S2 may also induce similar rearrangements in the extracellular vestibule.

How conserved is this mechanism of structural dynamics of a prokaryotic transporter with the proposed conformational changes of the medically relevant eukaryotic transporters? The high conservation of residues involved in the ion/substrate binding sites suggests a common mode

of interactions and perhaps the dynamic properties as well. The predictive power of the LeuT crystal structure has enabled rational experimental design to investigate structural elements within other members of the NSS superfamily. The results of these experiments strongly suggest that low to medium resolution structural models of the NSS can be built from the high resolution LeuT fold (239). Furthermore, specific regions within these NSS models exhibit state-dependent accessibility changes to MTS reagents. These regions include those that correspond to the LeuT segments that undergo conformational changes as shown in Figure 59. For example, a number of studies using cysteine accessibility experiments indicate that TM6 forms part of the extracellular permeation pathway of the SERT (176,239,240). In addition, accessibility to engineered cysteines is reduced in the presence of serotonin (176,239), consistent with the model presented in Figure 59 of TM6 movement contributing to the formation of a substrate-bound occluded state.

Despite lower sequence identity in the loop regions, EL2 and EL4 are likely conserved among other NSS proteins (5). Prior to the release of the LeuT structure, cysteine scanning mutagenesis and accessibility measurements in the SERT suggested that EL4 was composed of two α-helical segments separated by a short turn with similar topology to that revealed in LeuT (241). Generation of a SERT/NET chimera in which the EL4 sequence from the NET replaced the corresponding sequence in the SERT significantly reduced transport activity, even though plasma membrane expression remained unaltered. This suggested that this loop segment was involved in conformational changes associated with transport (163). Subsequently, altered cysteine accessibility to MTS reagents in the presence of coupling ions and substrate supported the notion that EL4 participates in functional dynamics of the SERT and the GAT (161,241,242). These observations suggest that conformational movement associated with the transport mechanism is most likely conserved among members of the NSS superfamily.

Importantly, the focus of the experiments described in this dissertation is the cation/substrate-dependent changes in the extracellular region. Therefore, the analysis is limited in scope and does not extensively report on structural rearrangements outside of the vestibule. A

complete picture of transporter dynamics requires a spectroscopic investigation of ion/substrate-dependent changes in other regions of LeuT. Four possible areas of focus are described below with their relationship to the current results.

Global analysis of conformational movement

From a global perspective, the non-exhaustive set of pairwise spin label distances suggests that most of the conformational motion occurs within the extracellular vestibule. However, it is not known if the dynamics observed in the loop segments are facilitated by conformational changes of specific transmembrane helices. Two examples can be evoked from the current dataset. The Leu-dependent decrease in distance between spin labels observed with the H478C/E236C mutant suggests that EL6 and the C-terminus of EL3 move toward each other (Figure 35). As described in Chapter 3, this movement may be associated with a rearrangement of TM6, although this possibility has not been explicitly tested. Secondly, the conformational change of EL4 may be related to movement of TM7 that directly precedes this loop. The binding of Na1 in the LeuT crystal structure is facilitated in part by coordination with the Glu290 side chain in TM7 (168). Furthermore, a recent report from Forrest and colleagues suggested that the major conformation change in LeuT to an inward-facing state involves tilting of a four-helix bundle which includes TMs 1, 2, 6 and 7 (187). A series of distance measurements by placing spin labels in TM2, TM6 and TM7 should completely characterize their movement relative to each other as well as to the vestibule (Figure 60). In addition, the peripheral location of TM2 and TM7 may confer sensitivity to ion/substrate-dependent changes in exposure to the lipid phase, which may be detectable in solvent accessibility measurements. Furthermore, conformational changes may be propagated to other lipid exposed transmembrane segments. Figure 60 illustrates potential spin label sites in these helices near the extracellular region that may capture such relative movement through distance analysis.

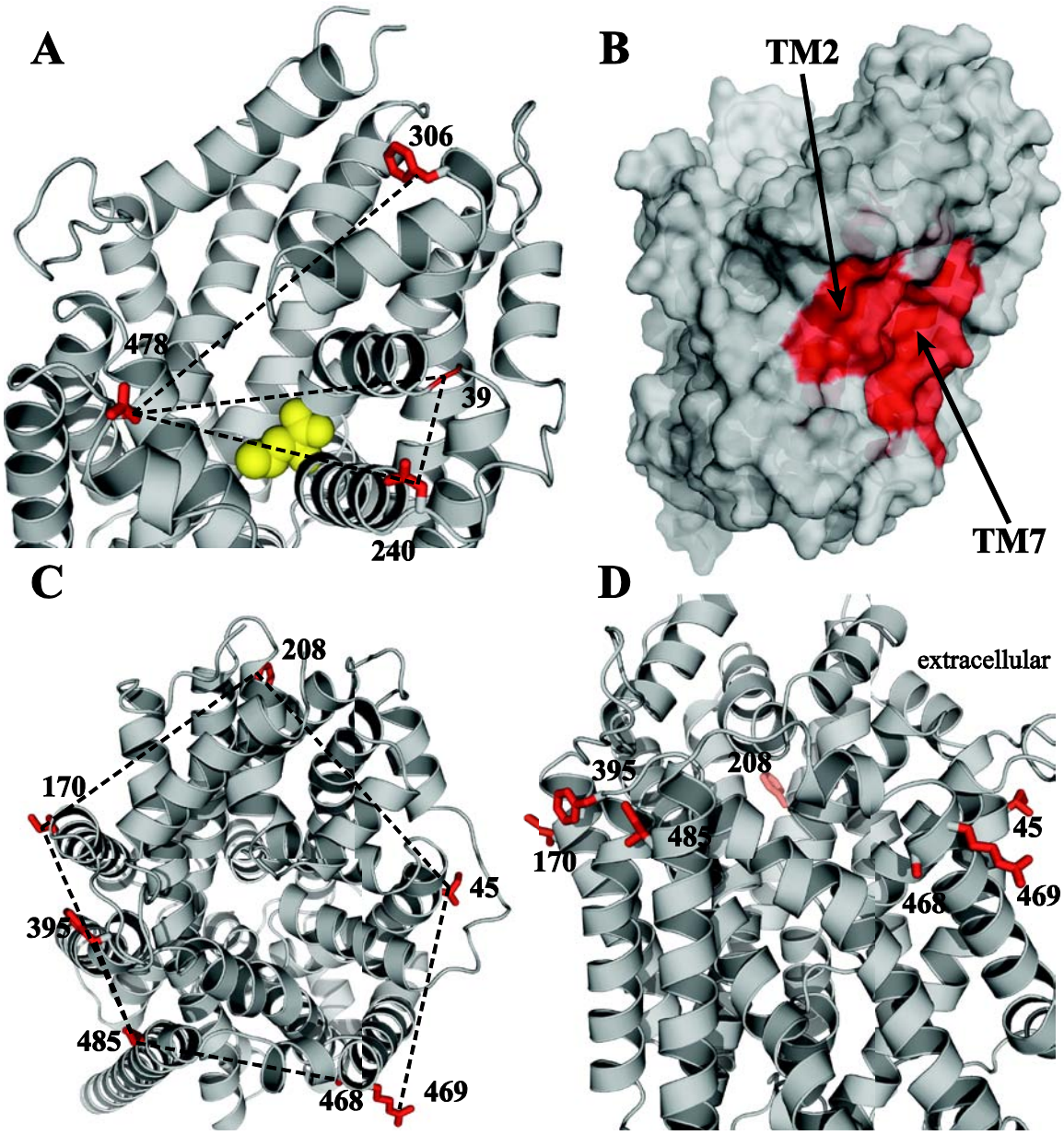

Figure 60. Global and local structural characterization of transmembrane helix movement. (**A**) Explicit movement of TM1 (position 39), TM6 (position 240) and TM7 (position 306) may be assessed by dipolar coupling to EL6 (position 478). Relative movement between TM1 and TM6 may be investigated by spin-spin interaction of 39/240. (**B**) Parts of TM2 and TM7 are exposed to the lipid environment according to the crystal structure. Substrate and/or ion binding could alter the packing arrangement, which can be directly assessed through spin label mobility and solvent accessibility experiments. (**C-D**) Distance analysis of peripheral transmembrane helices may uncover dynamic modes of structural segments outside of the vestibule region.

Structural dynamics of the intracellular region

Isomerization of an outward-facing to an inward-facing conformation is critical to achieve cytoplasmic Na^+/substrate release. Because the spectroscopic analysis presented here is limited to the extracellular region, data interpretation is blind to the conformation of the intracellular permeation pathway (i.e. the intracellular gate). One may anticipate, based on the current results of the extracellular side, that Na^+ induces an opposite effect on the intracellular side. That is, Na^+ binding closes the intracellular gate. Likewise, substrate binding may be expected to elicit an opening of the intracellular gate. In a related bacterial homolog, two intracellular cysteines (based on alignment with LeuT) in the tyrosine transporter Tyt1 displayed altered sensitivity to the sulfhydryl-alkylating reagent NEM depending on solution conditions. In the presence of Na^+, transport inhibition by NEM was reduced, consistent with a decrease in cysteine reactivity. In contrast, in the Apo state or in the presence of Tyr, reactivity with NEM increased and exacerbated its inhibitory effect on transport (170). These results are consistent with an alternating access mechanism in which Na^+ binding decreases accessibility to the cytoplasmic region of Tyt1, whereas Tyr binding increases it. However, complete characterization of the nature and magnitude of the proposed conformational changes has not been measured. In the crystal structure of LeuT, the packing of the intracellular region is much more extensive than the extracellular side (168). This may suggest that more substantial conformational changes must occur for substrate translocation. In the original model of LeuT structural dynamics, TM1 and TM6 play a substantial role in the formation of the inward-facing form mediated by the flexibility of helical discontinuity (168). A nitroxide scan of the intracellular portion of these helices may support this proposal by determining changes in local structural constraints (Figure 61). In the context of the proposed S1/S2 allosteric mechanism, substrate occupation of the S2 site activates cytoplasmic release of Na^+ and substrate in the primary site. Even though the vast majority of the EPR results do not appear to capture the effects of S2 binding in the extracellular region, changes in the pattern of spin label mobility, solvent

accessibility and spin-spin interactions fingerprinting the intracellular fold may be sensitive to substrate binding in the S2 site.

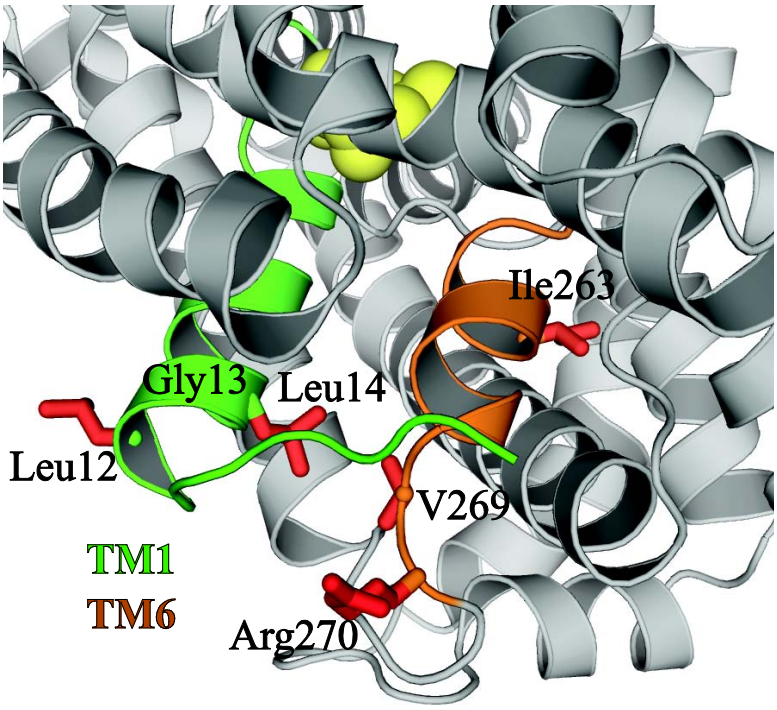

Figure 61. Investigation of the role of TM1 and TM6 in the cytoplasmic gating mechanism. Movement of TM1 and TM6 has been proposed to be essential for the formation of an inward-facing state. The highlighted positions may be informative toward site-specific changes in local structure associated with ion/substrate binding.

Coupling of the extracellular and intracellular gates

The alternating access model mechanism predicts that the empty, centralized binding site is exposed to one side of the membrane and that substrate occupation drives transporter reorientation toward the opposite side of the bilayer. In this mechanism, the opening of one "gate" requires the closing of the other. Therefore, the movement of substrate from one side of the membrane to the other is critically coupled to the dynamics of the gating mechanism.

Specifically, to maintain strict ion/substrate-coupling in a symport mechanism, the intracellular gate must close prior to the opening of the extracellular gate. In doing so, the coordinated movement of both gating processes is likely to prevent indiscriminate flux of ions into the cell. Indeed, ion channels in the NSS may be associated with simultaneous opening of both gates, but are typically low probability events (19). The mechanism by which the dynamics of both gates are coupled to the formation of discrete intermediate states is fundamental to the overall transport process. Based on the data presented here, Na^+ binding may be regarded as a key to open the extracellular gate to establish a binding competent intermediate, but also provides the energy to close the intracellular gate.

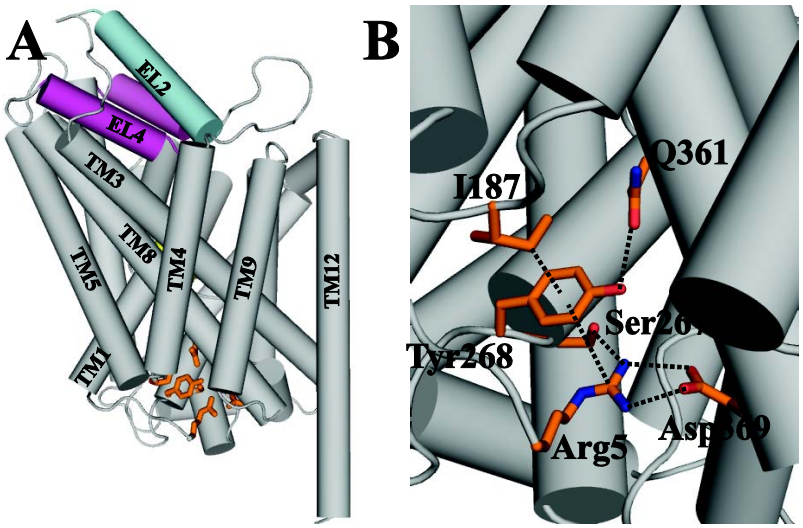

Figure 62. A network of interactions on the intracellular side of LeuT. (**A**) Full side view of the location of the network relative to extracellular loops. (**B**) Tyr268 is a hub for the interaction network. Mutation of this residue increases dynamics of the intracellular and extracellular regions of LeuT. The figure was inspired from Ref 181.

Recent evidence suggests that a conserved network of interactions on the cytoplasmic side of these transporters may play a pivotal role in the formation of the outward-facing

conformation (Figure 62) (181). Similar to the proposed function of a salt bridge between Arg and Asp residues on the extracellular side of LeuT, the ionic interaction between Arg60 and Asp436 in the DAT (Arg5 and Asp369 in LeuT) may form an intracellular latch. Additional cation-π and hydrogen bonding interactions contribute to the stability of the latch. Site directed mutagenesis within the network substantially decreased V_{max} and K_m of transport, although cell surface expression was comparable to the wild type DAT. Molecular dynamics simulations showed that mutation of a tyrosine residue in this network increased structural flexibility by disrupting specific hydrogen bonding interactions. Furthermore, normal mode analysis suggested that a disrupted interaction network will impair dynamic properties of the extracellular region. EPR analysis of spin labeled mutants in the extracellular region of LeuT on the background of point mutants that disrupt this intracellular network may demonstrate the dependence of the outward-facing conformation and substrate binding on the "locking" potential of the intracellular gate. Global structural analysis may be particularly informative in determining the capacity of these cytoplasmic positions to influence the conformation of segments shown to be involved in dynamic fluctuations associated with ion and substrate binding.

Impact of Cl^- binding

Unlike the NSS, LeuT and Tyt1 function independently of Cl^- binding and/or transport (168,170). The discovery of negatively charged residues that partially form the Na1 binding site in LeuT led to the identification of the Cl^- binding site in the SERT, DAT and GAT (171,172). The negatively charged residues, Glu or Asp, functionally replace the role of Cl^- in prokaryotic transporters. Interestingly, site directed mutagenesis of Glu290 in TM7 of LeuT or Asp259 in Tyt1 results in a Cl^--dependent transport activity (Figure 63). Subsequent studies have shown that substrate transport in Tyt1 is stimulated by a outwardly-directed H^+ gradient in the prokaryotic transporters (13). Indeed, V_{max} in proteoliposomes increased ~6-fold when the pH of the external solution and internal solution was 8.5 and 6.5, respectively. These results were shown to be

consistent with H^+ antiport via a protonation/deprotonation cycle of an Asp (or Glu) residue that participates directly in Na^+ binding. However, H^+ antiport is abolished in Tyt1 mutants that are Cl^--dependent. Collectively, the researchers suggested that influx of Cl^- or efflux of H^+ counterbalances the depolarizing Na^+ influx and is essential for maximal activity. The putative

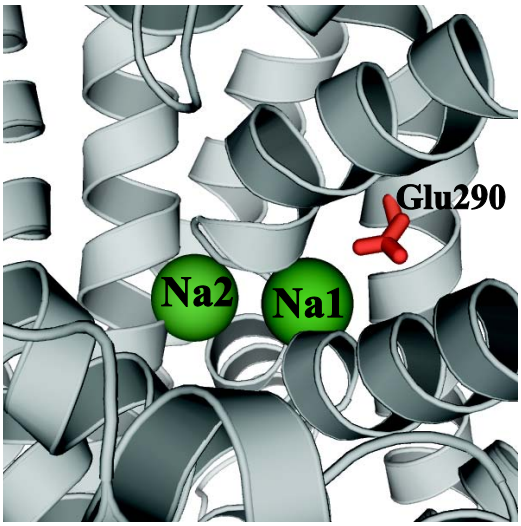

Figure 63. The negatively charged Glu290 contributes to the Na1 binding site. Mutation of Glu290 to Ser confers Cl^- dependence to LeuT transport. Experiments with E290S-LeuT may resolve Cl^--dependent conformational dynamics.

direct interaction of Cl^- with Na^+ may suggest that Cl^- binding impacts the formation of intermediate states. If this is the case, EPR analysis of Cl^--dependent LeuT may demonstrate conformational changes that are functionally related to Cl^- binding, effectively establishing an unambiguous structural role for the anion in the dynamics of symport.

APPENDIX A

SUPPLEMENTAL MATERIAL

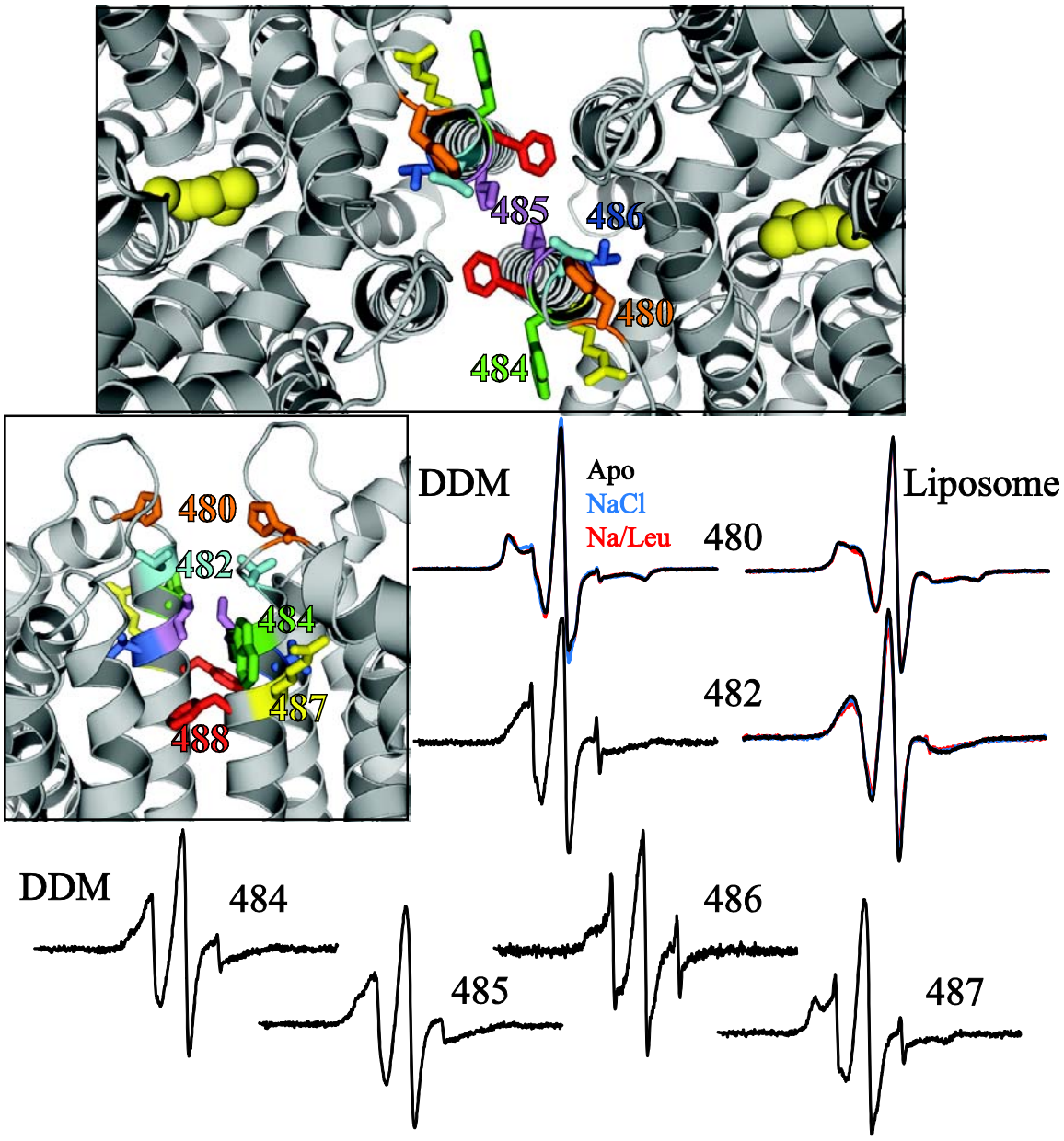

Supplemental Figure 1. EPR analysis of the crystallographic dimer interface. EPR lineshapes do not show the expected spin-spin interaction at positions contributing to the oligomeric state of LeuT. EPR spectra for site 480 and 482 are shown in DDM micelles and proteoliposomes. EPR spectra for sites 484-487 are shown in DDM micelles only. Leu, colored yellow, is shown as a space-filling model at the primary binding site.

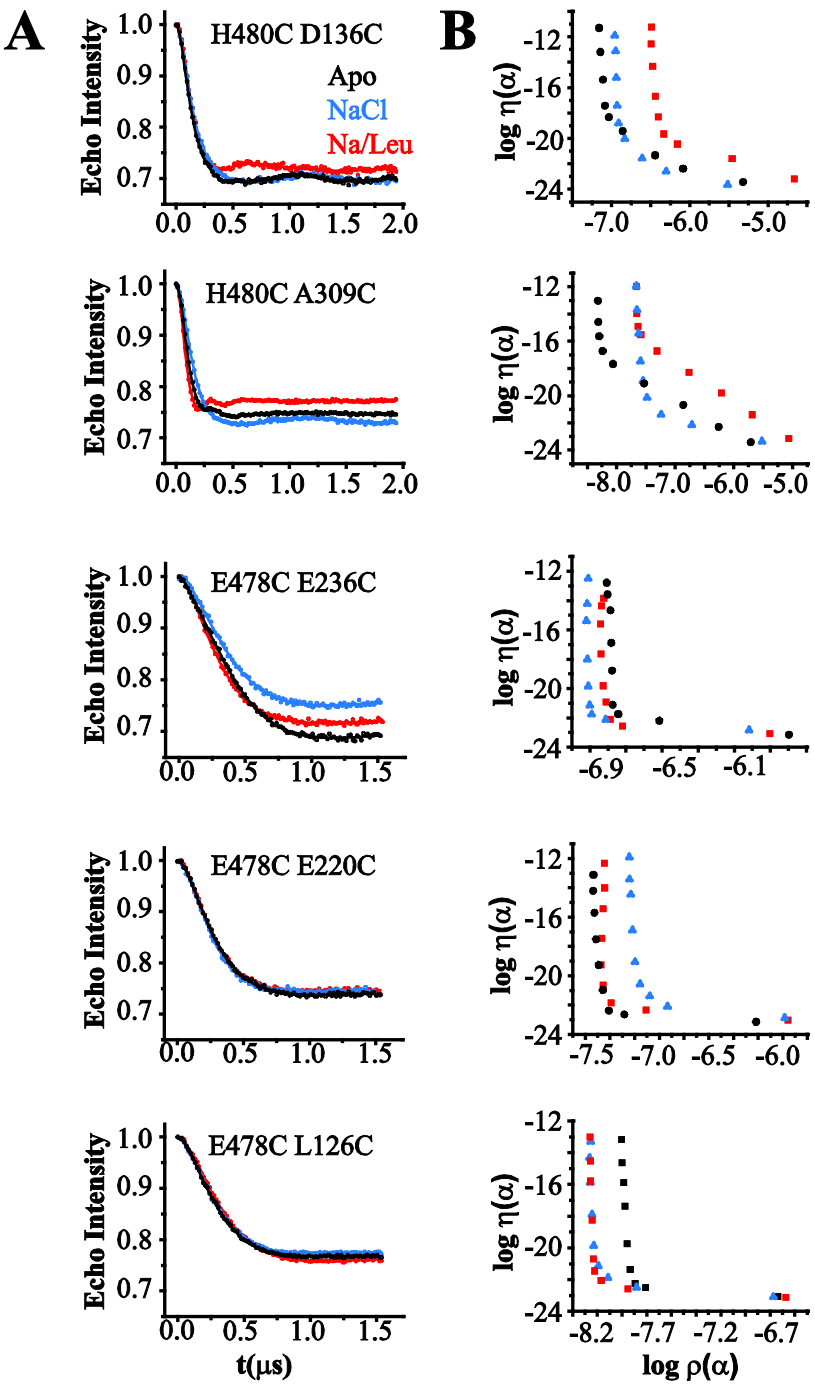

Supplemental Figure 2. DEER analysis of LeuT double mutants. The time-dependent spin echo decays (dots) and the fit (line) from Tikhonov regularization are shown in (A). The optimal regularization paramater (α), and thus the best distance distributions shown in Figures 31 and 35, was determined from the elbow of the L-curves shown in (B).

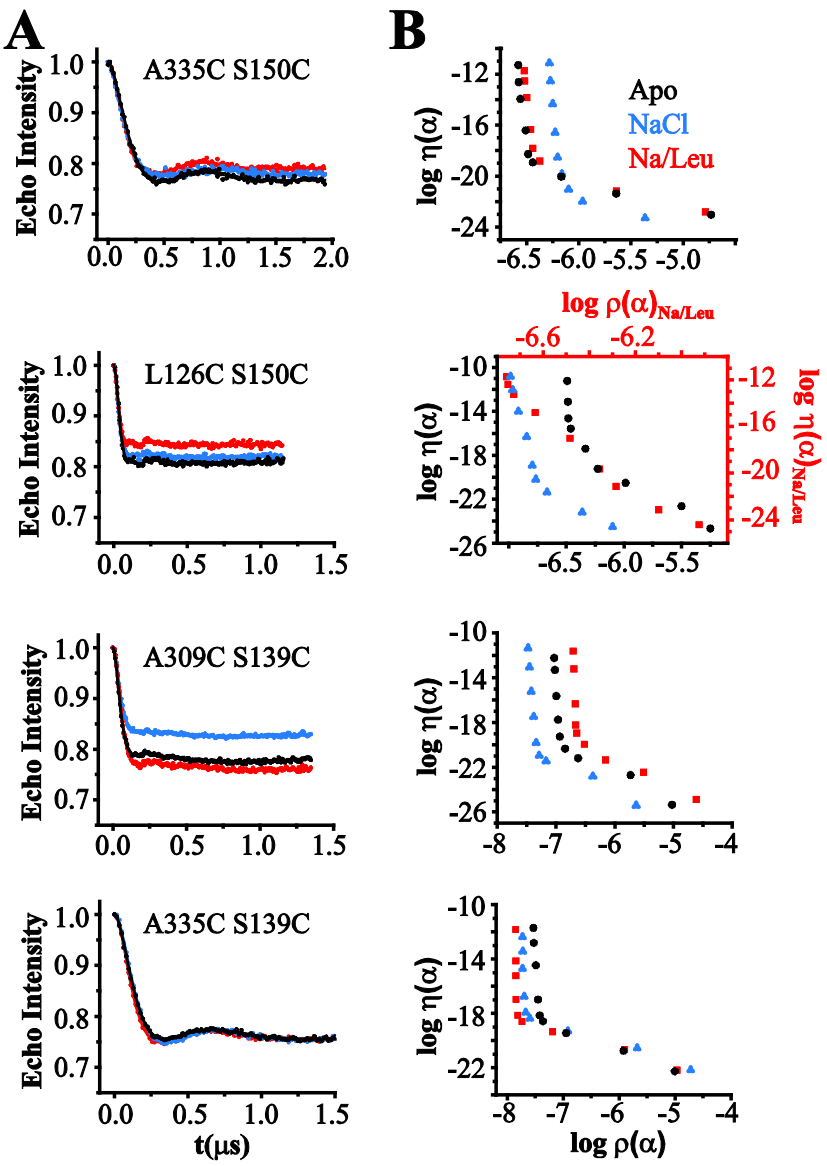

Supplemental Figure 3. DEER analysis of LeuT double mutants continued. Panels in **A** and **B** are the same to that described in legend of Supplemental Figure 2.

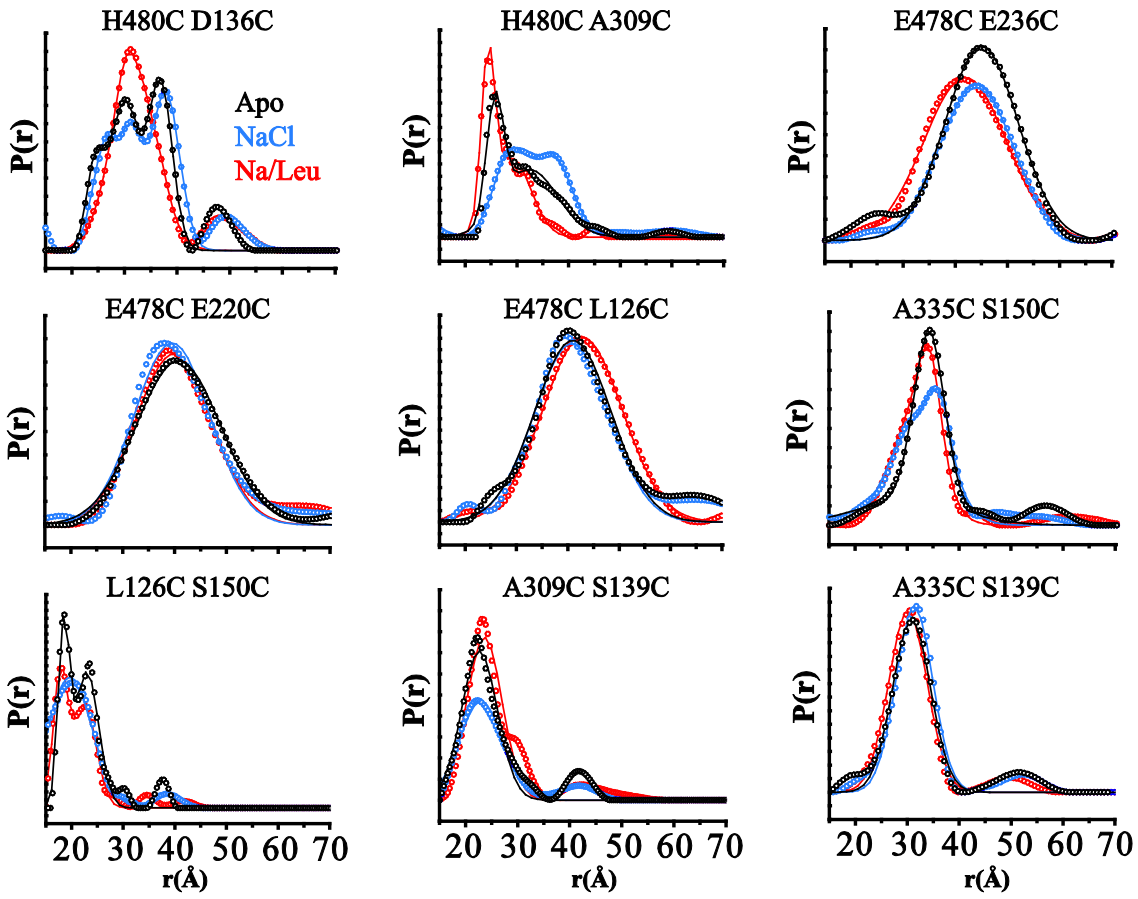

Supplemental Figure 4. Multi-Gaussian fits of distance distributions obtained from Tikhonov regularization. The parameters for each of the fits can be found in Table 2.

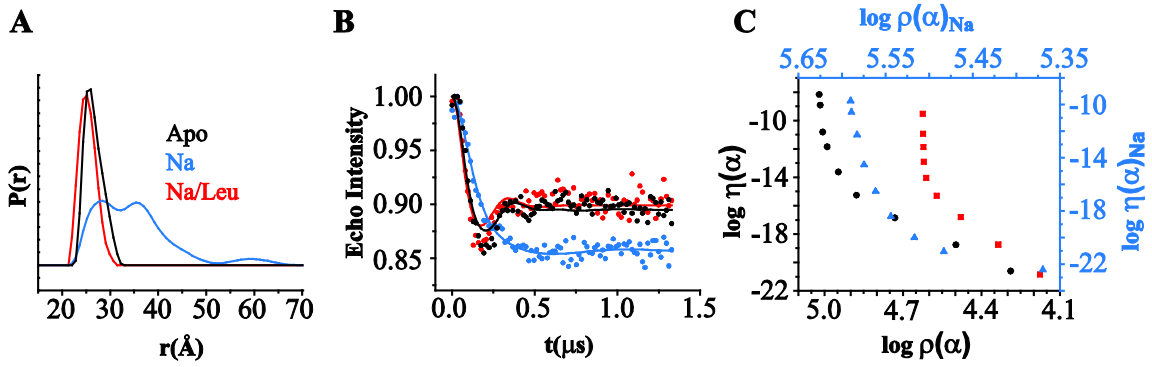

Supplemental Figure 5. DEER analysis of H480C/A309C in proteoliposomes. The distance distributions (**A**) suggest a similar conformational cycle of EL4 to those in DDM micelles. The fit of the time-dependent decay of the DEER signal (**B**) and L-curve analysis (**C**) are described in the legend of Supplemental Figure 2.

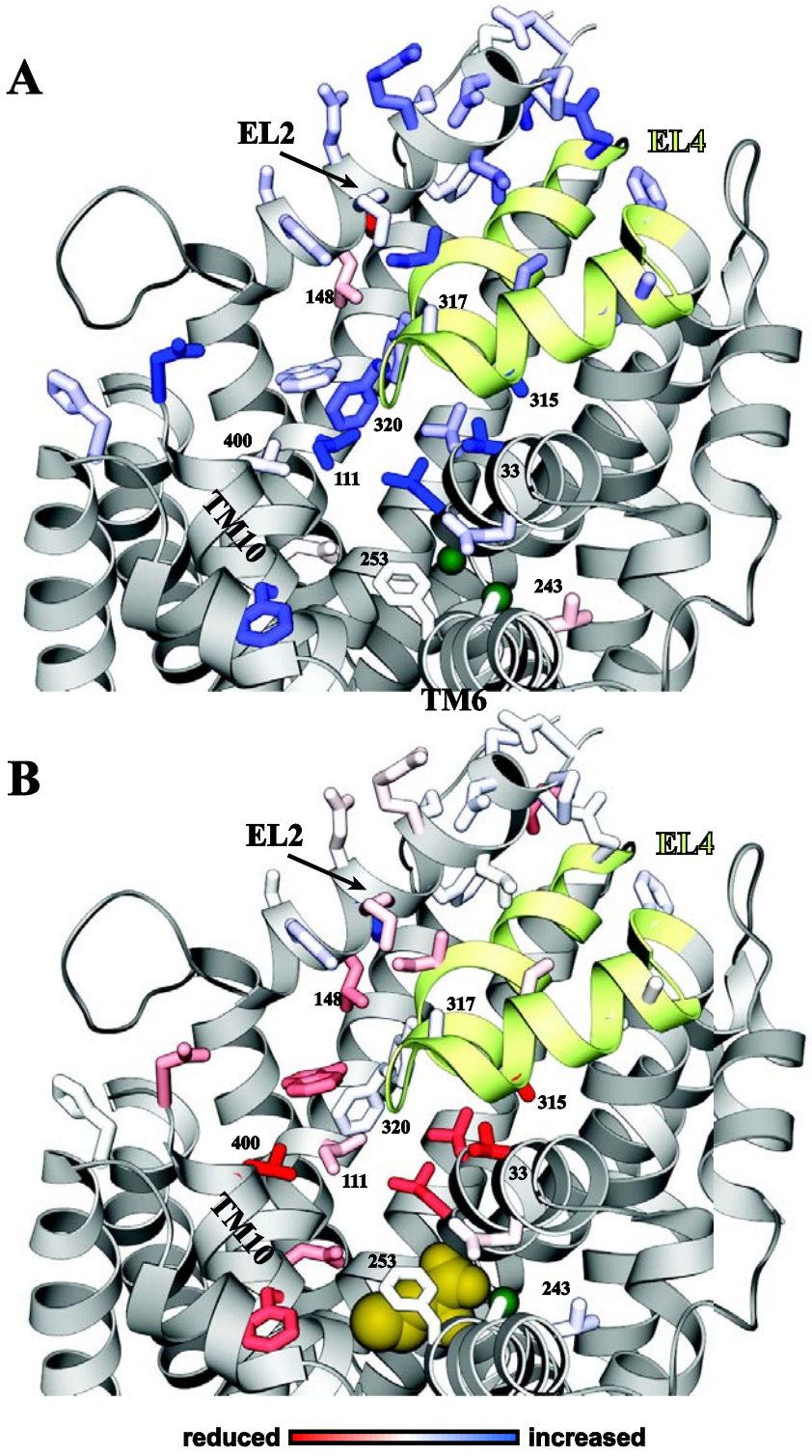

Supplemental Figure 6. Changes in spin label oxygen accessibility mapped on to the crystal structure of LeuT. The pattern of O_2 accessibility in the Na^+-bound (**A**) and Leu-bound states (**B**) support the conclusions made from the pattern of NiEDDA changes shown in Figures 32 and 36.

Supplementary Table 1: O_2 accessibility of LeuT single Cys mutants. Values are reported with confidence intervals for a single experiment. **(*) i**ndicates the mean ± S.D. obtained from three independently determined Π values.

Position		Π (Apo)	Π (NaCl)	Π (Na/Leu)
TM1	25	0.06 ± 0.01	0.08 ± 0.01	0.06 ± 0.01
	29	0.08 ± 0.02	0.08 ± 0.01	0.05 ± 0.01
	33*	0.13 ± 0.03	0.22 ± 0.01	0.12 ± 0.02
	34	0.40 ± 0.03	0.37 ± 0.02	0.36 ± 0.03
TM3	111*	0.08 ± 0.004	0.14 ± 0.01	0.12 ± 0.01
	114	0.12 ± 0.01	0.11 ± 0.02	0.08 ± 0.01
EL2	136	1.27 ± 0.02	1.17 ± 0.02	1.22 ± 0.02
	137	0.48 ± 0.02	0.45 ± 0.02	0.49 ± 0.02
	138	0.68 ± 0.02	0.68 ± 0.03	0.74 ± 0.02
	139	1.21 ± 0.05	1.01 ± 0.03	1.16 ± 0.03
	140	0.33 ± 0.01	0.37 ± 0.02	0.27 ± 0.01
	141	0.39 ± 0.02	0.41 ± 0.01	0.41 ± 0.02
	142	0.89 ± 0.02	0.96 ± 0.04	0.90 ± 0.04
	143	0.62 ± 0.01	0.59 ± 0.02	0.62 ± 0.02
	144	0.17 ± 0.01	0.15 ± 0.02	0.17 ± 0.01
	145	0.28 ± 0.01	0.25 ± 0.01	0.22 ± 0.01
	146	0.63 ± 0.02	0.59 ± 0.02	0.57 ± 0.02
	147	0.34 ± 0.02	0.22 ± 0.02	0.46 ± 0.02
	148	0.32 ± 0.02	0.24 ± 0.03	0.19 ± 0.06
	149	0.17 ± 0.01	0.16 ± 0.01	0.20 ± 0.01
	150	0.66 ± 0.02	0.61 ± 0.03	0.61 ± 0.03
TM6	243	0.33 ± 0.02	0.26 ± 0.03	0.29 ± 0.04
	246	0.14 ± 0.01	0.12 ± 0.01	0.12 ± 0.02
	249	0.10 ± 0.01	0.10 ± 0.01	0.14 ± 0.02
	253*	0.11 ± 0.01	0.09 ± 0.01	0.09 ± 0.03
EL4	305	0.39 ± 0.01	0.38 ± 0.02	0.41 ± 0.01
	307	0.12 ± 0.02	0.13 ± 0.02	0.13 ± 0.01
	309	1.00 ± 0.02	0.99 ± 0.02	0.97 ± 0.04
	311	0.13 ± 0.01	0.13 ± 0.01	0.14 ± 0.01
	314	0.37 ± 0.01	0.38 ± 0.01	0.35 ± 0.01
	315*	0.12 ± 0.01	0.20 ± 0.03	0.11 ± 0.01
	317	0.54 ± 0.03	0.50 ± 0.04	0.58 ± 0.03
	320*	0.10 ± 0.01	0.11 ± 0.01	0.12 ± 0.02
	324	0.14 ± 0.02	0.14 ± 0.02	0.15 ± 0.02
	325	0.25 ± 0.02	0.29 ± 0.02	0.24 ± 0.02
	333	0.49 ± 0.02	0.55 ± 0.02	0.57 ± 0.02
TM10	397	0.23 ± 0.03	0.31 ± 0.03	0.25 ± 0.04
	400*	0.24 ± 0.02	0.21 ± 0.04	0.08 ± 0.04
	404	0.16 ± 0.02	0.14 ± 0.01	0.10 ± 0.01
	405	0.28 ± 0.01	0.29 ± 0.01	0.18 ± 0.02
EL6	480	0.61 ± 0.02	0.56 ± 0.02	0.56 ± 0.03

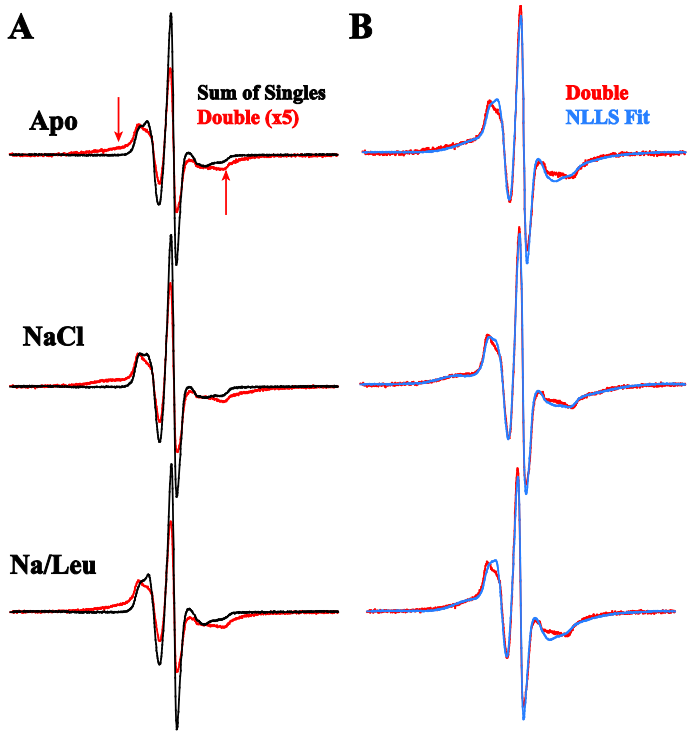

Intermediate	Distance 1 (Å)	% Contribution	Distance 2 (Å)	% Contribution	% Sum of Singles
Apo	7.0±1.4	86.0	15.2±1.7	14.0	19.7
NaCl	6.2±0.7	86.3	15.1±2.5	13.7	23.0
Na/Leu	7.0±1.0	82.7	14.1±3.6	17.3	20.0

Supplemental Figure 7. Distance analysis of A317C/K145C. (**A**) Dipolar coupling is observed in all intermediate states (red line) compared to the spectral sum of singles (black line). However, the presence of Na^+ increases the strength of the interaction, consistent with a decrease in distance. (**B**) Non-linear least squares analysis (blue line) of the spin-spin interaction for each state, assuming a two-Gaussian model. The parameters for the fits are found in the table.

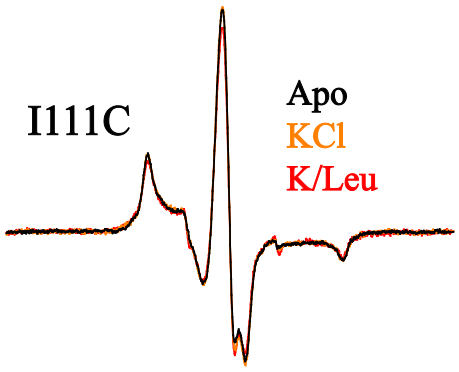

Supplemental Figure 8. K^+ does not support Leu binding in proteoliposomes as indicated by a lack of lineshape changes. Compare these three spectra with those found in Figure 39A for I111C.

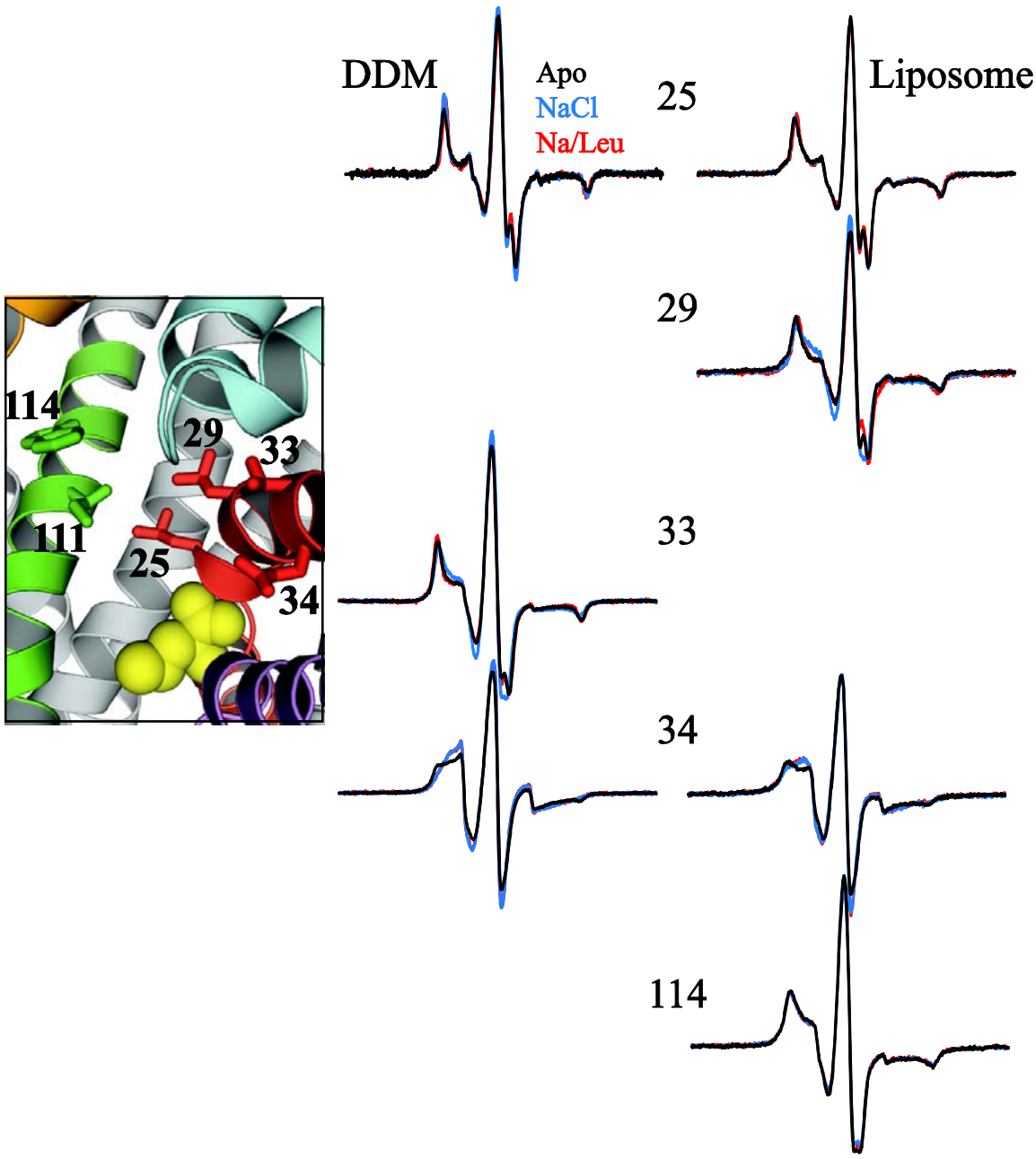

Supplemental Figure 9. EPR spectra of TM1 and TM3 spin labeled mutants in DDM micelles and proteoliposomes. EPR spectra of V33C in proteoliposomes can be found in Figures 32 and 36. Most sites shown in this figure and in Supplemental Figures 10-16 demonstrate similar EPR lineshapes in DDM and liposomes.

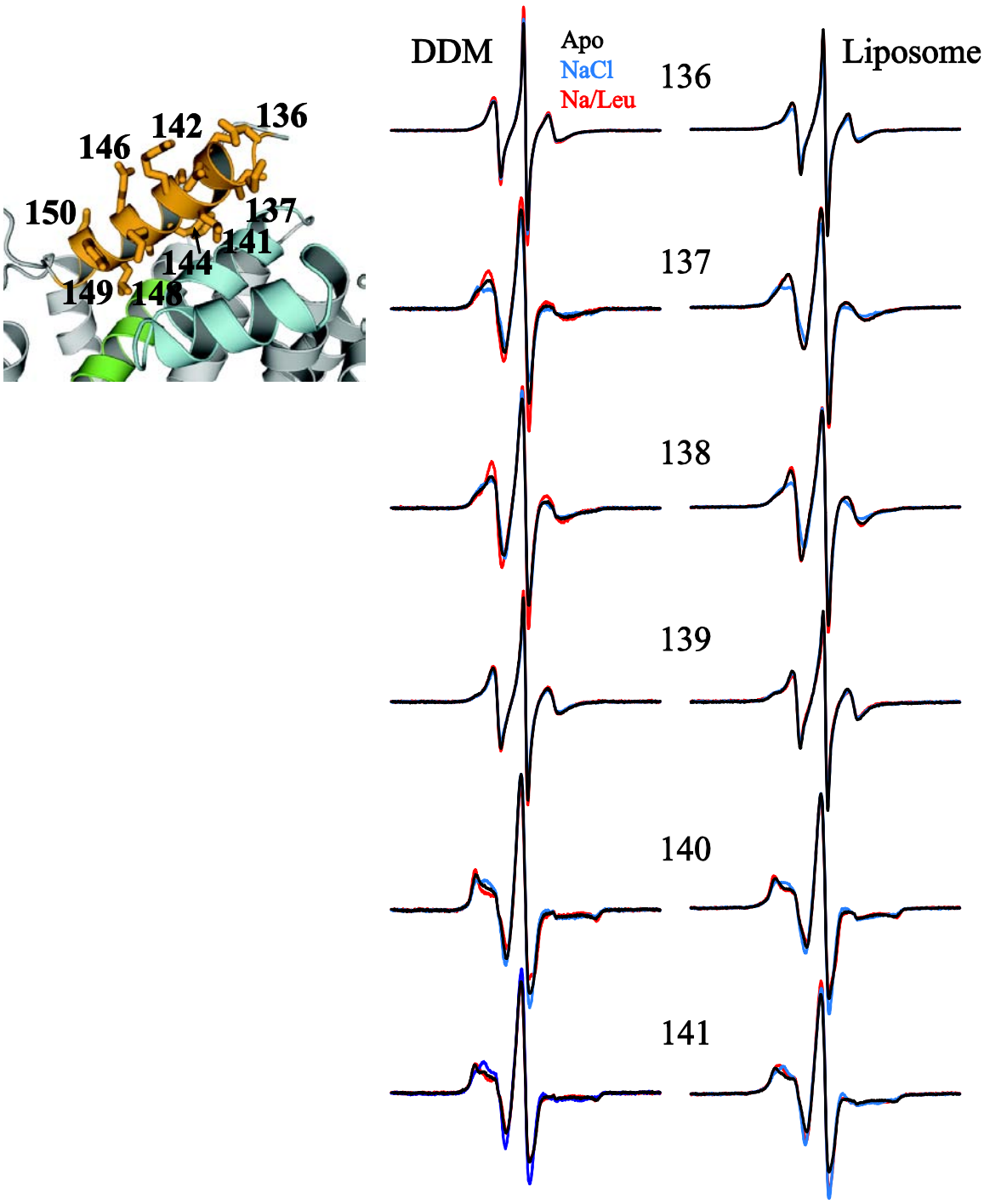

Supplemental Figure 10. EPR lineshapes of EL2 in DDM micelles and proteoliposomes.

Supplemental Figure 11. EPR spectra of EL2 mutants continued.

Supplemental Figure 12. EPR spectra of EL2 mutants continued.

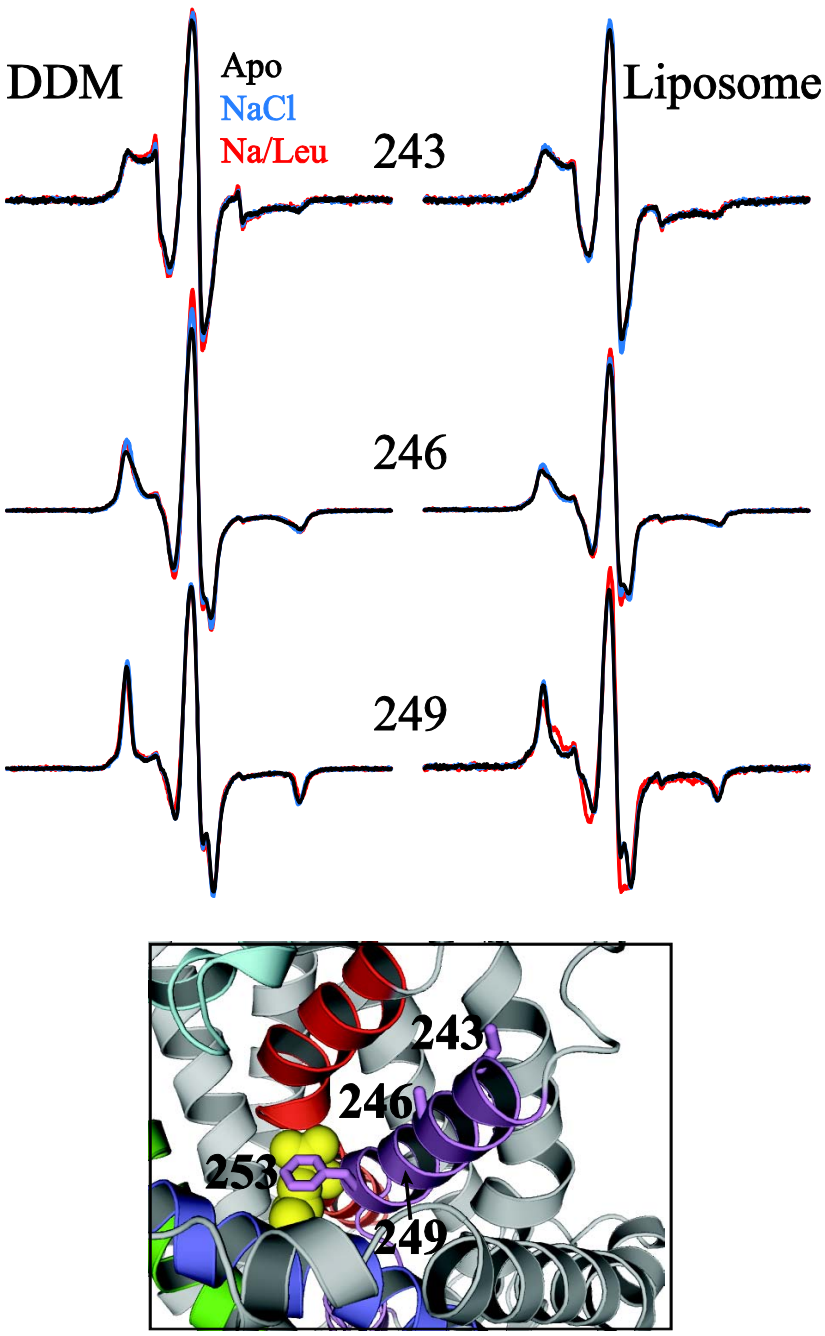

Supplemental Figure 13. EPR spectra of spin labeled TM6 mutants in DDM micelles and proteoliposomes. In the crystallographic model shown below the spectra, the position of G249 is highlighted by an arrow.

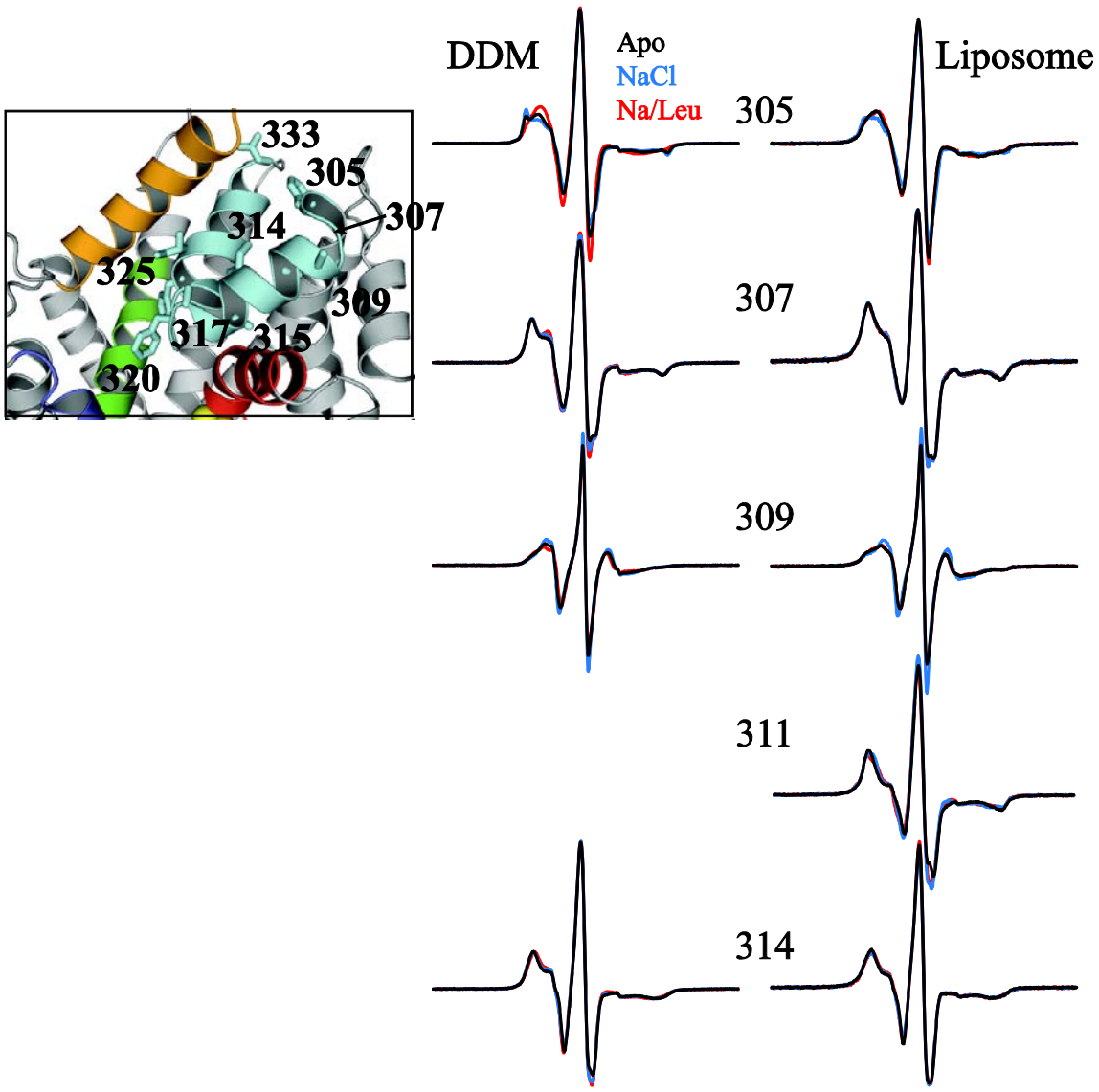

Supplemental Figure 14. EPR spectra of spin labeled EL4 mutants in DDM micelles and proteoliposomes. In the crystallographic model shown beside the spectra, the position of G307 is highlighted by an arrow.

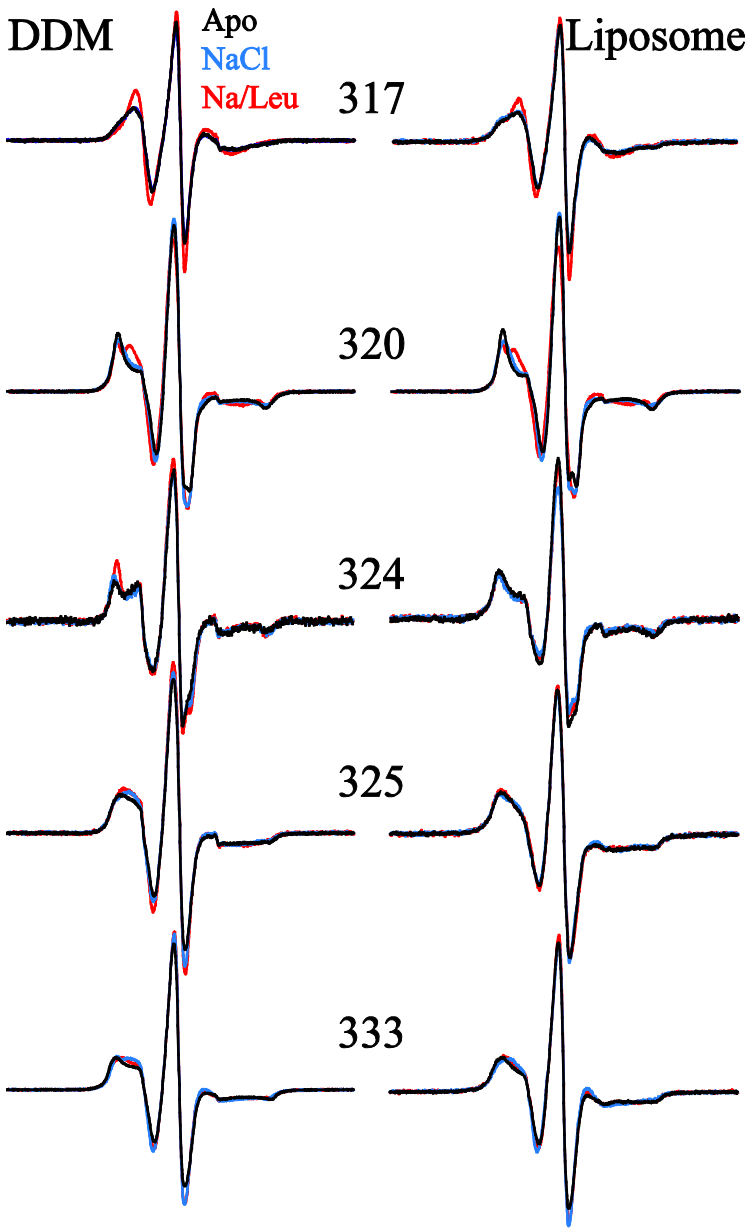

Supplemental Figure 15. EPR spectra of EL4 mutants continued.

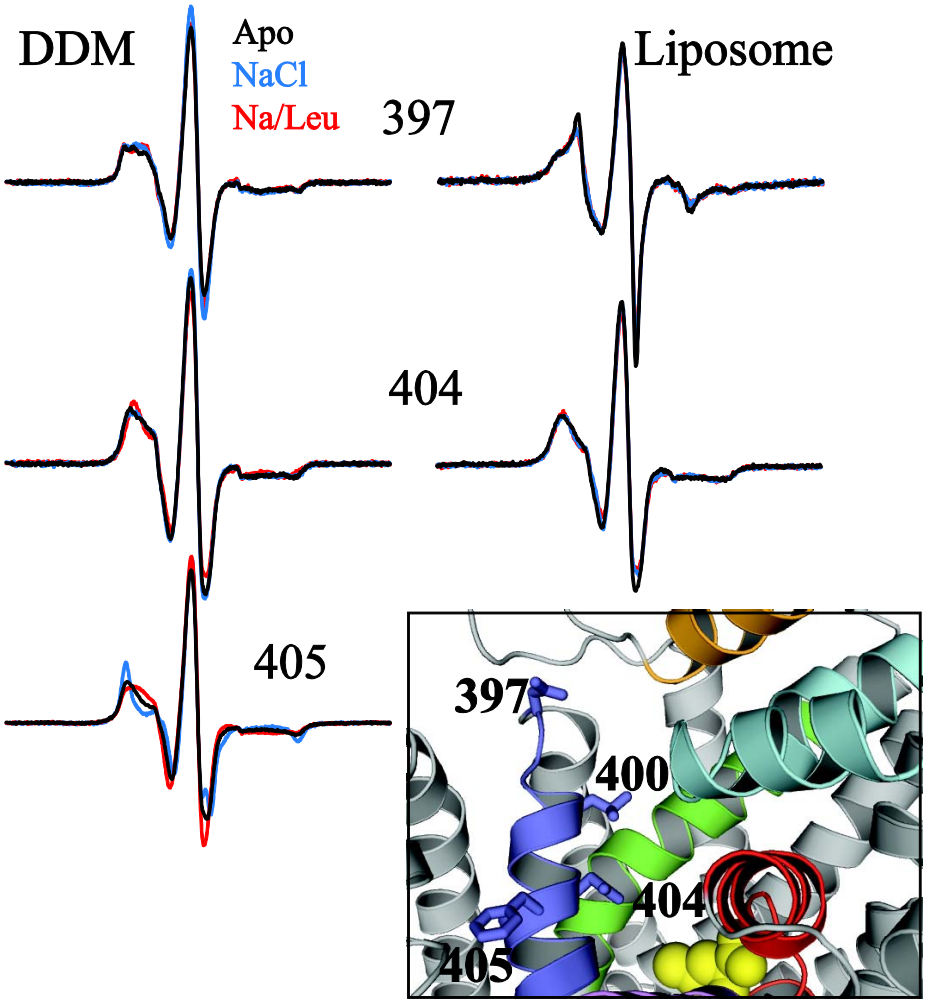

Supplemental Figure 16. EPR spectra of spin labeled TM10 mutants in DDM micelles and proteoliposomes. EPR spectra of F405C in proteoliposomes can be found in Figure 37.

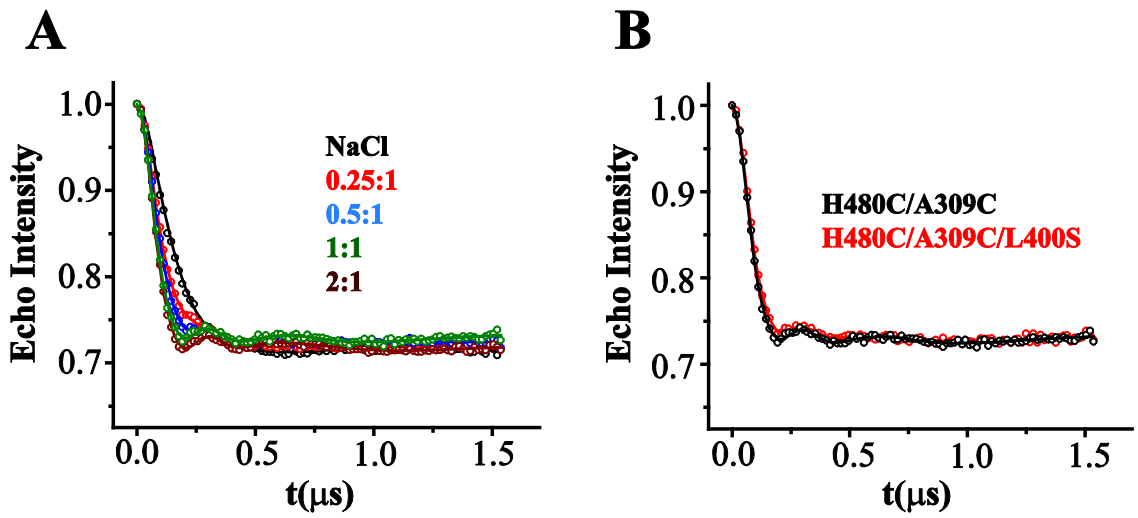

Supplemental Figure 17. Correlation of global structural changes with Leu binding stoichiometry. (**A**) [Leu]-dependent changes in the time domain DEER signal of H480C/A309C. The resulting distance distributions are shown in Figure 42E. (**B**) The spin echo decay in the Leu-bound form for the H480C/A309C pair is similar in the presence and absence of an S2-site disrupting mutation (L400S). The resulting distance distributions is shown in Figure 42F.

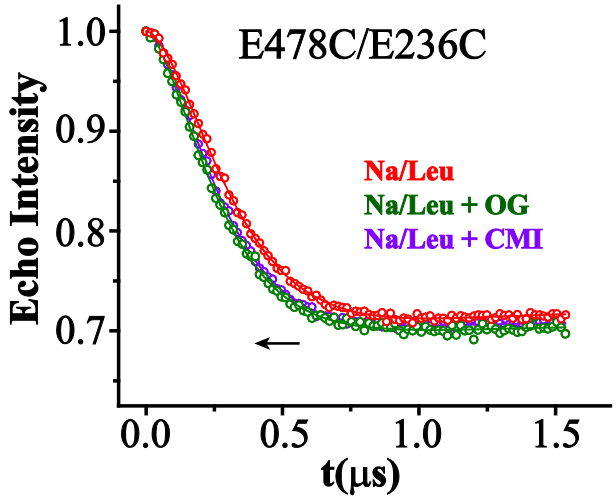

Supplemental Figure 18. Inhibitor-dependent changes in distance measured by E478C/E236C. The time-dependent decay of the DEER signal shifts to the left (arrow) in the presence of either OG or CMI inhibitors, consistent with a decrease in distance between the probes relative to the Na^+/Leu intermediate. The resulting distance distributions are shown in Figure 45B and C.

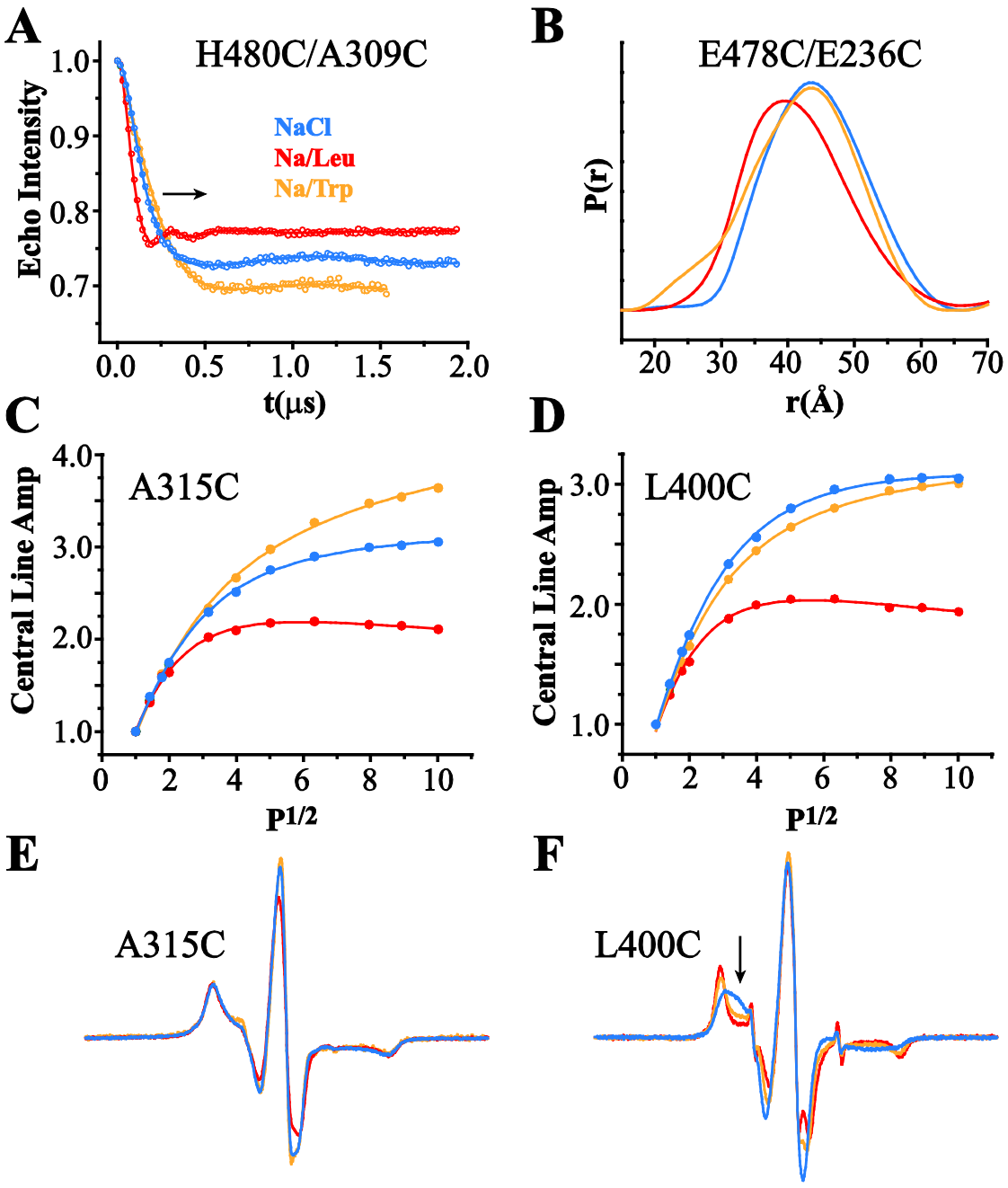

Supplemental Figure 19. Spectroscopic analysis of Trp binding. (**A**) The DEER signal decay shifts to the right (arrow) in the presence of Trp, consistent with an increase in distance relative to both the Na^+ and Na^+/Leu states. The resulting distance distributions are shown in Figure 46B. (**B**) The distance distributions between EL6 and EL3 showing that the position of EL3 (and likely TM6a) in Trp-bound state is similar to the Na^+ only configuration. This behavior was also observed in MD simulations found in Figure 47. (**C** and **D**) Trp binding increases the accessibility of the extracellular vestibule to NiEDDA as evidenced by a right shift in the power saturation curves of A315C and L400C. (**E** and **F**) Although no significant change in the EPR spectra at A315C is observed in presence of Trp, a mobile component (arrow) is observed at L400C, consistent with decreased packing interactions relative to the Leu-bound state.

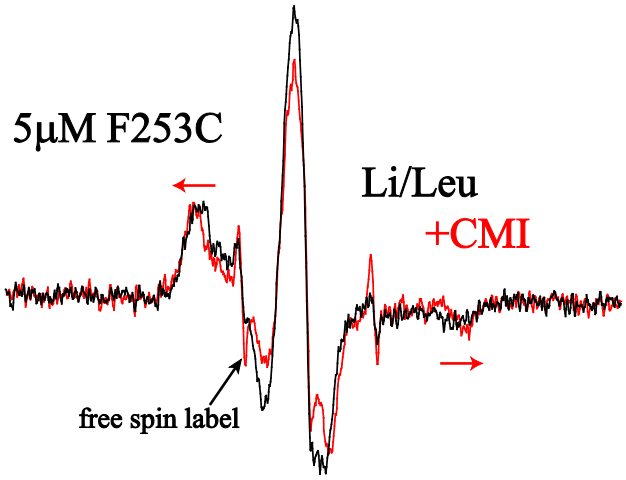

Supplemental Figure 20. Li^+-dependent Leu binding is impaired by CMI.

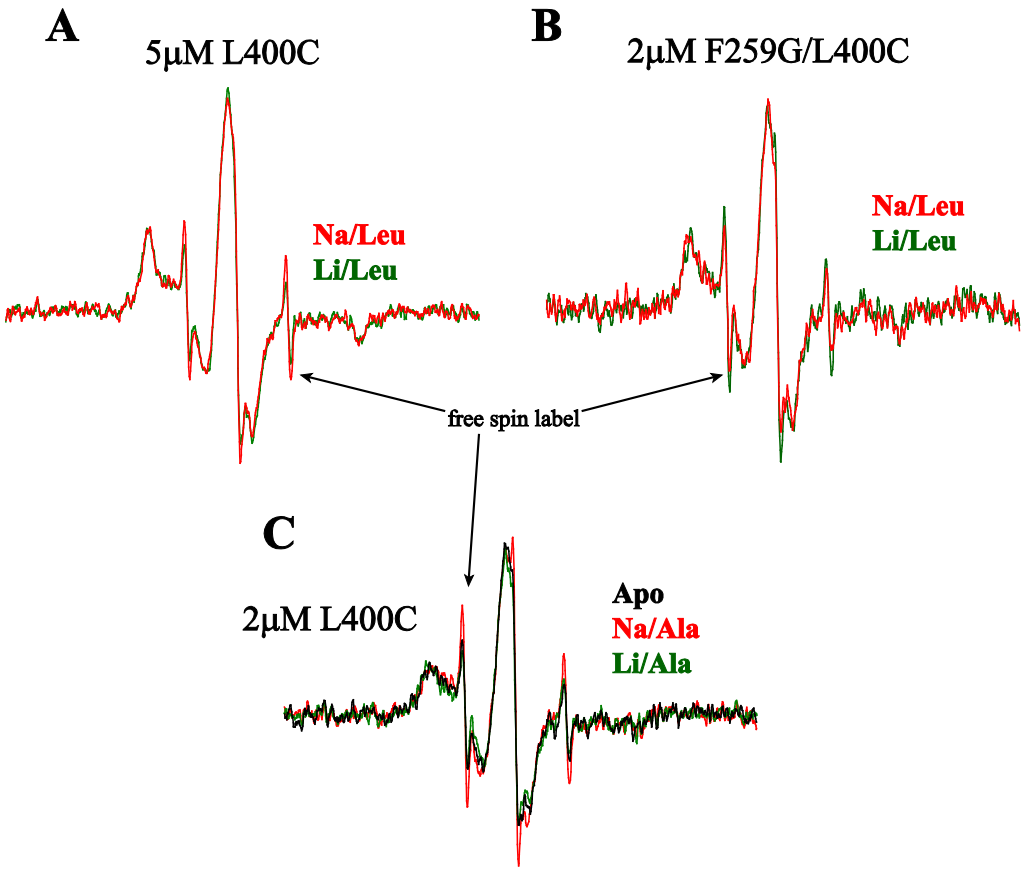

Supplemental Figure 21. Correlation of ion-dependent binding behavior of Leu and Ala with binding site mutations. (**A**) Leu binds to LeuT at low [Leu] and [LeuT] in the presence of either Na^+ or Li^+, even in the presence of an S1-site disrupting mutation (**B**), consistent high affinity Leu binding. (**C**) In contrast, no binding is observed with Ala at low [Ala] and [LeuT], consistent with the lower binding affinity of Ala relative to Leu.

APPENDIX B

EXPERIMENTAL METHODS

Mutagenesis

The synthetic LeuT DNA sequence containing an N-terminal His_{10} tag was inserted into a pQE-derivative expression vector (designed by Matthias Quick at Columbia University, New York) controlled by the T5 promoter. Cysteine residues were introduced, individually or in combination, in recombinant LeuT by the QuikChange site-directed mutagenesis protocol (Agilent Technologies) that uses two complementary oligonucleotides containing the desired mutation and a high fidelity polymerase to synthesize a mutant, double-stranded DNA. The methylated parental DNA template in the PCR reaction was subsequently digested by DPN1 endonuclease. Following digestion, the synthetic DNA product was transformed into *E. coli* XL1-Blue cells and plated on LB agar containing 100 $\mu g \cdot mL^{-1}$ ampicillin. DNA was extracted from colonies (Qiagen) and screened for the LeuT sequence insertion by combining a restriction digest of the product at flanking NcoI and HindIII sites with ensuing 1% (w/v) agarose gel electrophoresis stained with ethidium bromide. DNA samples demonstrating the appropriate molecular weight insertion were sent for sequencing at the Vanderbilt DNA sequencing core to confirm the presence of the desired mutation and the absence of unwanted changes using the following three primers:

5'-3' Upstream (bases 51-71)—AAT AGA TTC AAT TGT GAG CGG

5'-3' Mid-length (bases 651-671)—ATT GGC GTG CCG AAA GGC GAT

3'-5' Reverse Terminator (bases 1832-1812)—TCA CCA CTT TGT ACC ACG TGC

Following sequence analysis, mutants were transformed into *E. coli* BL21(DE3) cells for expression.

Expression and Purification

One colony from the BL21(DE3) transformation was used to inoculate 10 mL of LB broth containing 100 $\mu g \cdot mL^{-1}$ ampicillin, which was grown overnight at 37° C for no more than 15 hrs. All of the seed culture was added to 1 L of minimal media (1 g ammonium sulfate, 4.5 g KP_i monobasic, 10.5 g KP_i dibasic, 0.5 g sodium citrate) supplemented with 1 mM magnesium sulfate, 100 $\mu g \cdot mL^{-1}$ ampicillin, 1 mL of 50x amino acid mixture, 0.5% (v/v) glycerol and 2.5 mg thiamine. Cells were grown for 7 hrs at 37° C (Supplemental Figure 22A) and induced with 1 mM IPTG at 20° C for 16 hrs. Cells harvested by centrifugation were re-suspended in 100 mM KP_i pH 7.5 buffer and lysed by sonication. Cell debris was removed by centrifugation at 9000 rcf for 10 min and the membrane fraction of the supernatant was subsequently isolated by ultracentrifugation at 310,000 rcf for 50 min.

The *E. coli* membranes were washed three times in 200 mM Tris/Mes pH 7.5, 20% glycerol buffer in the presence of 10mM DTT to remove endogenous Leu bound to LeuT during expression. 40 mM (2% w/v) DDM (Anatrace) was used to extract LeuT mutants from the native membranes. Solubilized mutants were purified by Ni^{2+} affinity chromatography with a 50mM imidazole wash step and elution with 250mM imidazole. Immediately following, single Cys mutants were labeled with a total of 40x MTSSL (Toronto Research Chemicals, Inc) over 4 hrs at 23°C and placed on ice overnight. Double Cys mutants were labeled with a total of 80x MTSSL over a 6hr period. To generate the Apo intermediate and remove unbound spin label, LeuT mutants were subjected to size exclusion chromatography on a Shodex KW-803 column (Supplemental Figure 22B) and subsequent desalting on a HiTrap desalting column (GE Healthcare) into 200 mM Tris/Mes pH 7.2 buffer containing 0.025% (w/v) DDM and 20% (v/v) glycerol. SDS-PAGE analysis indicated that LeuT is highly purified under these conditions (Supplemental Figure 22C). Protein concentration was determined using an extinction coefficient of 1.91 cm^2/mg at 280 nm.

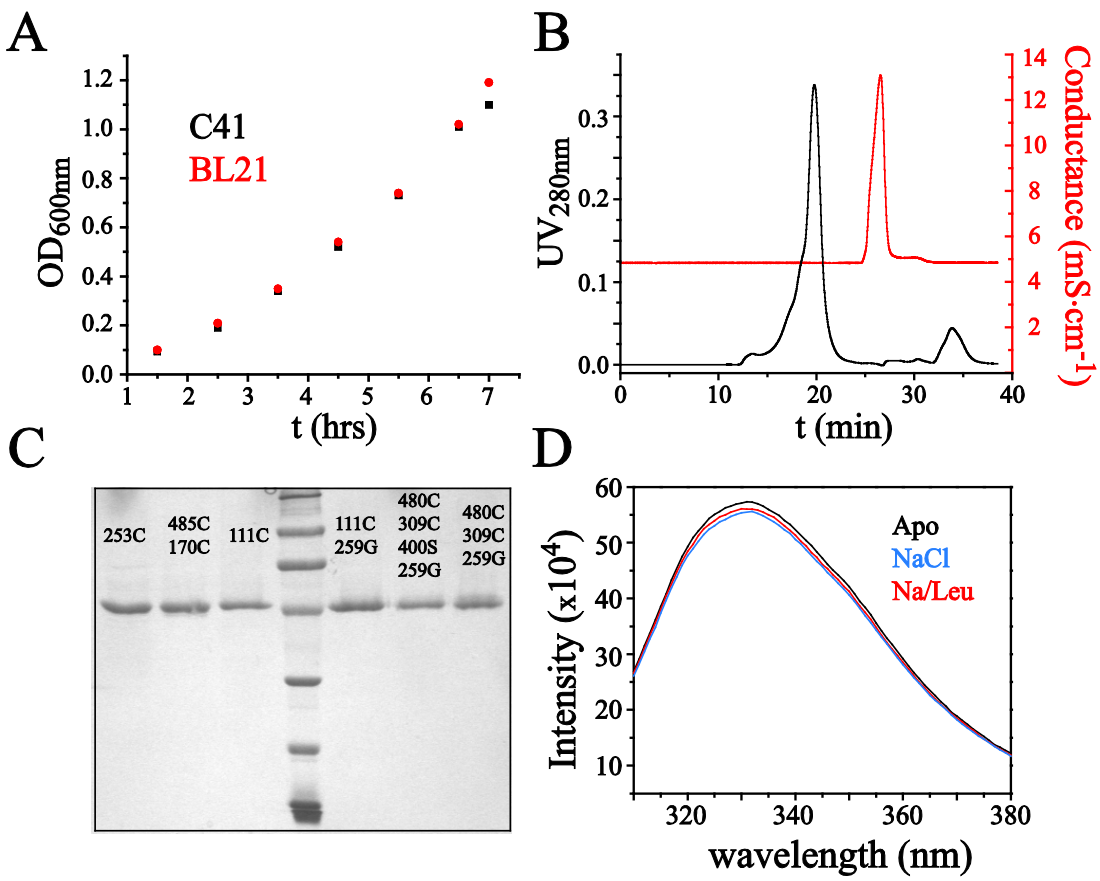

Supplemental Figure 22. Expression and purification of LeuT. (**A**) Time-dependent increase in E. coli optical density using either C41(DE3) or BL21(DE3) cells. (**B**) Gel filtration profile of LeuT-WT showing the separation of protein from solution salts. (**C**) SDS-PAGE of a variety of LeuT mutants. (**D**) The Trp fluorescence profile of LeuT is consistent with a folded protein in all biochemical conditions tested.

Reconstitution

Apo-LeuT mutants were reconstituted into 200 nm unilamellar liposomes made from a 3:1 (w/w) ratio of *E. coli* polar lipids and phosphatidylcholine (Avanti Polar Lipids, Inc) loaded with 0.1 M KP_i pH 6.5 buffer using a 5000:1 (mol/mol) lipid-to-DDM ratio. Detergent was removed during reconstitution by three hourly additions of 60 $mg \cdot mL^{-1}$ SM-2 bio-beads (Bio-Rad) to the protein/lipid mixture. After overnight incubation at 4° C, proteoliposomes were filtered to remove the bio-beads, harvested by ultracentrifugation at 310,000 rcf and re-suspended

in 200 mM Tris/Mes pH 7.2 buffer. For EPR lineshape and solvent accessibility analysis, single cysteine mutants were reconstituted with a 1000:1 (mol/mol) lipid-to-protein ratio. For DEER analysis, the lipid-to-protein ratio was increased to 2000:1 to reduce non-specific intermolecular dipolar coupling.

Scintillation Proximity Assay

Binding studies were performed by scintillation proximity assay (SPA) with 100 nM [^{3}H]-Leu (112 Ci mmol^{-1}) and 50 mM NaCl, with and without spin label. 25 ng of Ni^{2+} affinity purified LeuT was bound to Cu^{2+} chelate YSi scintillation beads (GE Healthcare). Upon [^{3}H]-Leu binding, the scintillation beads emit light which is detected by a photomultiplier tube. Since binding of LeuT to the beads is facilitated by the N-terminal His_{10} tag, nonspecific radiolabeled ligand binding can be determined in the presence of a high concentration (400 mM) of imidazole. A standard curve was generated to convert the counts per minute (cpm) into pmol. The Leu equilibrium binding constant (EC_{50}) and molar stoichiometry were determined by varying the [^{3}H]-Leu concentration from 0.5 – 1000 nM and performing a nonlinear regression fitting of the data in Prism 4.

Transport Assay

The time course of 1 µM [^{3}H]-Ala uptake was performed with proteoliposomes containing LeuT-WT or –F253C and with control liposomes in the presence of an inwardly-directed Na^+ electrochemical gradient (25 mM external NaCl) or by dissipation of the gradient with gramicidin, yielding the total accumulation and specific binding, respectively. Specific substrate transport was determined by the difference between total accumulation and specific binding.

EPR Spectroscopy

Lineshape Analysis

EPR spectra were collected at room temperature on a Bruker EMX spectrometer (X-band) at an incident power of 10 mW and 1.6 Gauss modulation amplitude in DDM micelles or

proteoliposomes. Substrates were allowed to incubate with LeuT mutants on ice for at least 20 minutes before collection of EPR spectra. The addition of 200 mM NaCl to the Apo intermediate was used to create the Na^+ state. The Na^+/Leu state was produced by adding Leu to the Na^+ state.

Solvent Accessibility

Proteoliposome samples were loaded into a gas permeable TPX capillary tube and subjected to either 20% O_2 (g) or 50 mM Ni(II)ethylenediaminediacetic acid (NiEDDA) equilibrated with N_2 (g) on a Bruker Elexsys E500 spectrometer to generate power saturation curves. $P_{1/2}$ was determined from a nonlinear least-squares fit of the power saturation curves in the program Origin (OriginLab Inc.) to the equation:

$$A = IP^{1/2}[1 + \frac{(2^{1/\varepsilon} - 1)P}{P_{1/2}}]^{-\varepsilon}$$

Where A is the signal amplitude, I is a scaling factor, P is the microwave power and ε reports the degree of homogeneous saturation. Signal saturation in the absence of fast-relaxing agents was measured under N_2 (g). $\Delta P_{1/2}$ for O_2 and NiEDDA was determined by subtracting the $P_{1/2}(N_2)$ from the $P_{1/2}(O_2)$ and $P_{1/2}$ (NiEDDA). The accessibility parameter Π was normalized using spin labeled T4L-K135C as a standard. The experimental error was less than 20% based on the mean ± S.D. of three independently determined Π values (denoted as (*) in Table 3).

Double Electron Electron Resonance

Distance measurements were carried out on a Bruker 580 pulsed EPR spectrometer operating at X-band frequency (9.5 GHz) using double electron electron resonance (DEER) with a standard four-pulse protocol. Glycerol was added to 30% (w/w) prior to cooling for both detergent and liposome samples. Deuterated buffer and glycerol was used to enhance the phase memory time for liposome samples. All DEER experiments were performed at 83K. The DEER signals were analyzed by Tikhonov regularization to yield the distance distributions. Some of the resulting distributions were subjected to multiple Gaussian peak picking to model the changes in the distance and width of the distributions.

REFERENCES

1. Nelson, N. (1998) *J Neurochem* 71, 1785-1803

2. Rudnick, G. (ed) (2002) *Mechanisms of biogenic amine neurotransmitter transporters*, Humana Press Inc., Totowa, New Jersey

3. Edwards, R. H. (2007) *Neuron* 55, 835-858

4. Torres, G. E., and Amara, S. G. (2007) *Curr Opin Neurobiol* 17, 304-312

5. Beuming, T., Shi, L., Javitch, J. A., and Weinstein, H. (2006) *Mol Pharmacol* 70, 1630-1642

6. Rose, E. M., Koo, J. C., Antflick, J. E., Ahmed, S. M., Angers, S., and Hampson, D. R. (2009) *J Neurosci* 29, 8143-8155

7. Torres, G. E., Gainetdinov, R. R., and Caron, M. G. (2003) *Nat Rev Neurosci* 4, 13-25

8. Erreger, K., Grewer, C., Javitch, J. A., and Galli, A. (2008) *J Neurosci* 28, 976-989

9. Gu, H., Wall, S. C., and Rudnick, G. (1994) *J Biol Chem* 269, 7124-7130

10. Tzingounis, A. V., and Wadiche, J. I. (2007) *Nat Rev Neurosci* 8, 935-947

11. Loo, D. D., Eskandari, S., Boorer, K. J., Sarkar, H. K., and Wright, E. M. (2000) *J Biol Chem* 275, 37414-37422

12. Adams, S. V., and DeFelice, L. J. (2003) *Biophys J* 85, 1548-1559

13. Zhao, Y., Quick, M., Shi, L., Mehler, E. L., Weinstein, H., and Javitch, J. A. *Nat Chem Biol* 6, 109-116

14. Ryan, R. M., and Mindell, J. A. (2007) *Nat Struct Mol Biol* 14, 365-371

15. Gu, H. H., Wall, S., and Rudnick, G. (1996) *J Biol Chem* 271, 6911-6916

16. Rudnick, G. (2006) *J Membr Biol* 213, 101-110

17. Sonders, M. S., and Amara, S. G. (1996) *Curr Opin Neurobiol* 6, 294-302

18. Adams, S. V., and DeFelice, L. J. (2002) *Biophys J* 83, 3268-3282

19. Galli, A., Blakely, R. D., and DeFelice, L. J. (1996) *Proc Natl Acad Sci U S A* 93, 8671-8676

20. Mager, S., Min, C., Henry, D. J., Chavkin, C., Hoffman, B. J., Davidson, N., and Lester, H. A. (1994) *Neuron* 12, 845-859

21. Sonders, M. S., Zhu, S. J., Zahniser, N. R., Kavanaugh, M. P., and Amara, S. G. (1997) *J Neurosci* 17, 960-974

22. Ingram, S. L., Prasad, B. M., and Amara, S. G. (2002) *Nat Neurosci* 5, 971-978

23. Kanner, B. I., and Zomot, E. (2008) *Chem Rev* 108, 1654-1668

24. Hucho, F., Jarv, J., and Weise, C. (1991) *Trends Pharmacol Sci* 12, 422-426

25. Lester, H. A., Cao, Y., and Mager, S. (1996) *Neuron* 17, 807-810

26. Chiu, C. S., Jensen, K., Sokolova, I., Wang, D., Li, M., Deshpande, P., Davidson, N., Mody, I., Quick, M. W., Quake, S. R., and Lester, H. A. (2002) *J Neurosci* 22, 10251-10266

27. Lehre, K. P., and Danbolt, N. C. (1998) *J Neurosci* 18, 8751-8757

28. Galli, A., Petersen, C. I., deBlaquiere, M., Blakely, R. D., and DeFelice, L. J. (1997) *J Neurosci* 17, 3401-3411

29. Zahniser, N. R., and Doolen, S. (2001) *Pharmacol Ther* 92, 21-55

30. Amara, S. G., and Fontana, A. C. (2002) *Neurochem Int* 41, 313-318

31. Arriza, J. L., Eliasof, S., Kavanaugh, M. P., and Amara, S. G. (1997) *Proc Natl Acad Sci U S A* 94, 4155-4160

32. Ciliax, B. J., Drash, G. W., Staley, J. K., Haber, S., Mobley, C. J., Miller, G. W., Mufson, E. J., Mash, D. C., and Levey, A. I. (1999) *J Comp Neurol* 409, 38-56

33. Pickel, V. M., and Chan, J. (1999) *J Neurosci* 19, 7356-7366

34. Zhou, F. C., Tao-Cheng, J. H., Segu, L., Patel, T., and Wang, Y. (1998) *Brain Res* 805, 241-254

35. Giros, B., Jaber, M., Jones, S. R., Wightman, R. M., and Caron, M. G. (1996) *Nature* 379, 606-612

36. Starke, K., Gothert, M., and Kilbinger, H. (1989) *Physiol Rev* 69, 864-989

37. Bengel, D., Murphy, D. L., Andrews, A. M., Wichems, C. H., Feltner, D., Heils, A., Mossner, R., Westphal, H., and Lesch, K. P. (1998) *Mol Pharmacol* 53, 649-655

38. Fabre, V., Beaufour, C., Evrard, A., Rioux, A., Hanoun, N., Lesch, K. P., Murphy, D. L., Lanfumey, L., Hamon, M., and Martres, M. P. (2000) *Eur J Neurosci* 12, 2299-2310

39. Xu, F., Gainetdinov, R. R., Wetsel, W. C., Jones, S. R., Bohn, L. M., Miller, G. W., Wang, Y. M., and Caron, M. G. (2000) *Nat Neurosci* 3, 465-471

40. Przedborski, S., and Vila, M. (2003) *Ann N Y Acad Sci* 991, 189-198

41. Langston, J. W., Ballard, P., Tetrud, J. W., and Irwin, I. (1983) *Science* 219, 979-980

42. Javitch, J. A., D'Amato, R. J., Strittmatter, S. M., and Snyder, S. H. (1985) *Proc Natl Acad Sci U S A* 82, 2173-2177

43. Drevets, W. C., Gautier, C., Price, J. C., Kupfer, D. J., Kinahan, P. E., Grace, A. A., Price, J. L., and Mathis, C. A. (2001) *Biol Psychiatry* 49, 81-96

44. Nnadi, C. U., Mimiko, O. A., McCurtis, H. L., and Cadet, J. L. (2005) *J Natl Med Assoc* 97, 1504-1515

45. Zahniser, N. R., and Sorkin, A. (2004) *Neuropharmacology* 47 Suppl 1, 80-91

46. United Nations Office on Drugs and Crime (2009) World drug report 2009.

47. Gawin, F. H. (1991) *Science* 251, 1580-1586

48. Sulzer, D., Sonders, M. S., Poulsen, N. W., and Galli, A. (2005) *Prog Neurobiol* 75, 406-433

49. United Nations Office on Drugs and Crime (2008) Amphetamines and ecstasy: global ATS assessment

50. Mazei-Robison, M. S., Bowton, E., Holy, M., Schmudermaier, M., Freissmuth, M., Sitte, H. H., Galli, A., and Blakely, R. D. (2008) *J Neurosci* 28, 7040-7046

51. Berman, S. M., Kuczenski, R., McCracken, J. T., and London, E. D. (2009) *Mol Psychiatry* 14, 123-142

52. United Nations Office on Drugs and Crime (2009) Economic and social consequences of drug abuse and illicit trafficking

53. Ritz, M. C., Lamb, R. J., Goldberg, S. R., and Kuhar, M. J. (1987) *Science* 237, 1219-1223

54. Rocha, B. A., Fumagalli, F., Gainetdinov, R. R., Jones, S. R., Ator, R., Giros, B., Miller, G. W., and Caron, M. G. (1998) *Nat Neurosci* 1, 132-137

55. Sora, I., Wichems, C., Takahashi, N., Li, X. F., Zeng, Z., Revay, R., Lesch, K. P., Murphy, D. L., and Uhl, G. R. (1998) *Proc Natl Acad Sci U S A* 95, 7699-7704

56. Sora, I., Hall, F. S., Andrews, A. M., Itokawa, M., Li, X. F., Wei, H. B., Wichems, C., Lesch, K. P., Murphy, D. L., and Uhl, G. R. (2001) *Proc Natl Acad Sci U S A* 98, 5300-5305

57. Mateo, Y., Budygin, E. A., John, C. E., and Jones, S. R. (2004) *Proc Natl Acad Sci U S A* 101, 372-377

58. Chen, R., Tilley, M. R., Wei, H., Zhou, F., Zhou, F. M., Ching, S., Quan, N., Stephens, R. L., Hill, E. R., Nottoli, T., Han, D. D., and Gu, H. H. (2006) *Proc Natl Acad Sci U S A* 103, 9333-9338

59. Ward, A., Walker, V. J., Feng, Z., and Xu, X. Z. (2009) *PLoS One* 4, e5946

60. Fleckenstein, A. E., Metzger, R. R., Wilkins, D. G., Gibb, J. W., and Hanson, G. R. (1997) *J Pharmacol Exp Ther* 282, 834-838

61. Kokoshka, J. M., Metzger, R. R., Wilkins, D. G., Gibb, J. W., Hanson, G. R., and Fleckenstein, A. E. (1998) *Brain Res* 799, 78-83

62. Zaczek, R., Culp, S., and De Souza, E. B. (1991) *J Pharmacol Exp Ther* 257, 830-835

63. Dipace, C., Sung, U., Binda, F., Blakely, R. D., and Galli, A. (2007) *Mol Pharmacol* 71, 230-239

64. Hilber, B., Scholze, P., Dorostkar, M. M., Sandtner, W., Holy, M., Boehm, S., Singer, E. A., and Sitte, H. H. (2005) *Neuropharmacology* 49, 811-819

65. Wall, S. C., Gu, H., and Rudnick, G. (1995) *Mol Pharmacol* 47, 544-550

66. Jones, S. R., Joseph, J. D., Barak, L. S., Caron, M. G., and Wightman, R. M. (1999) *J Neurochem* 73, 2406-2414

67. Sitte, H. H., and Freissmuth, M. *J Neurochem* 112, 340-355

68. Khoshbouei, H., Wang, H., Lechleiter, J. D., Javitch, J. A., and Galli, A. (2003) *J Biol Chem* 278, 12070-12077

69. Sulzer, D., Chen, T. K., Lau, Y. Y., Kristensen, H., Rayport, S., and Ewing, A. (1995) *J Neurosci* 15, 4102-4108

70. Kahlig, K. M., Binda, F., Khoshbouei, H., Blakely, R. D., McMahon, D. G., Javitch, J. A., and Galli, A. (2005) *Proc Natl Acad Sci U S A* 102, 3495-3500

71. Sitte, H. H., Huck, S., Reither, H., Boehm, S., Singer, E. A., and Pifl, C. (1998) *J Neurochem* 71, 1289-1297

72. Sulzer, D., and Rayport, S. (1990) *Neuron* 5, 797-808

73. Peter, D., Jimenez, J., Liu, Y., Kim, J., and Edwards, R. H. (1994) *J Biol Chem* 269, 7231-7237

74. Daws, L. C., Callaghan, P. D., Moron, J. A., Kahlig, K. M., Shippenberg, T. S., Javitch, J. A., and Galli, A. (2002) *Biochem Biophys Res Commun* 290, 1545-1550

75. Kahlig, K. M., and Galli, A. (2003) *Eur J Pharmacol* 479, 153-158

76. Kahlig, K. M., Javitch, J. A., and Galli, A. (2004) *J Biol Chem* 279, 8966-8975

77. Saunders, C., Ferrer, J. V., Shi, L., Chen, J., Merrill, G., Lamb, M. E., Leeb-Lundberg, L. M., Carvelli, L., Javitch, J. A., and Galli, A. (2000) *Proc Natl Acad Sci U S A* 97, 6850-6855

78. Kahlig, K. M., Lute, B. J., Wei, Y., Loland, C. J., Gether, U., Javitch, J. A., and Galli, A. (2006) *Mol Pharmacol* 70, 542-548

79. Nemeroff, C. B. (1998) *Biol Psychiatry* 44, 517-525

80. Mann, J. J., Malone, K. M., Diehl, D. J., Perel, J., Cooper, T. B., and Mintun, M. A. (1996) *Am J Psychiatry* 153, 174-182

81. Rogers, M. A., Bradshaw, J. L., Pantelis, C., and Phillips, J. G. (1998) *Brain Res Bull* 47, 297-310

82. Owens, M. J., and Nemeroff, C. B. (1994) *Clin Chem* 40, 288-295

83. Gardier, A. M. (2009) *Behav Pharmacol* 20, 18-32

84. Haenisch, B., Bilkei-Gorzo, A., Caron, M. G., and Bonisch, H. (2009) *J Neurochem* 111, 403-416

85. Lesch, K. P., Bengel, D., Heils, A., Sabol, S. Z., Greenberg, B. D., Petri, S., Benjamin, J., Muller, C. R., Hamer, D. H., and Murphy, D. L. (1996) *Science* 274, 1527-1531

86. Pan, W. H., Yang, S. Y., and Lin, S. K. (2004) *Synapse* 53, 44-52

87. Henry, L. K., Meiler, J., and Blakely, R. D. (2007) *Mol Interv* 7, 306-309

88. Anderson, I. M. (2000) *J Affect Disord* 58, 19-36

89. Rudnick, G. (2007) *ACS Chem Biol* 2, 606-609

90. Nemeroff, C. B., and Owens, M. J. (2009) *Clin Chem* 55, 1578-1579

91. Zhou, Z., Zhen, J., Karpowich, N. K., Law, C. J., Reith, M. E., and Wang, D. N. (2009) *Nat Struct Mol Biol*

92. Guastella, J., Nelson, N., Nelson, H., Czyzyk, L., Keynan, S., Miedel, M. C., Davidson, N., Lester, H. A., and Kanner, B. I. (1990) *Science* 249, 1303-1306

93. Pacholczyk, T., Blakely, R. D., and Amara, S. G. (1991) *Nature* 350, 350-354

94. Giros, B., el Mestikawy, S., Godinot, N., Zheng, K., Han, H., Yang-Feng, T., and Caron, M. G. (1992) *Mol Pharmacol* 42, 383-390

95. Blakely, R. D., Berson, H. E., Fremeau, R. T., Jr., Caron, M. G., Peek, M. M., Prince, H. K., and Bradley, C. C. (1991) *Nature* 354, 66-70

96. Kyte, J., and Doolittle, R. F. (1982) *J Mol Biol* 157, 105-132

97. von Heijne, G. (1992) *J Mol Biol* 225, 487-494

98. Krogh, A., Larsson, B., von Heijne, G., and Sonnhammer, E. L. (2001) *J Mol Biol* 305, 567-580

99. Bruss, M., Hammermann, R., Brimijoin, S., and Bonisch, H. (1995) *J Biol Chem* 270, 9197-9201

100. Hersch, S. M., Yi, H., Heilman, C. J., Edwards, R. H., and Levey, A. I. (1997) *J Comp Neurol* 388, 211-227

101. Bennett, E. R., and Kanner, B. I. (1997) *J Biol Chem* 272, 1203-1210

102. Vaughan, R. A., and Kuhar, M. J. (1996) *J Biol Chem* 271, 21672-21680

103. Olivares, L., Aragon, C., Gimenez, C., and Zafra, F. (1997) *J Biol Chem* 272, 1211-1217

104. Ferrer, J. V., and Javitch, J. A. (1998) *Proc Natl Acad Sci U S A* 95, 9238-9243

105. Yu, N., Cao, Y., Mager, S., and Lester, H. A. (1998) *FEBS Lett* 426, 174-178

106. Chen, J. G., Liu-Chen, S., and Rudnick, G. (1997) *Biochemistry* 36, 1479-1486

107. Wang, J. B., Moriwaki, A., and Uhl, G. R. (1995) *J Neurochem* 64, 1416-1419

108. Rasmussen, J. R. (1992) *Current Opinion in Structural Biology* 2, 682-686

109. Nunez, E., and Aragon, C. (1994) *J Biol Chem* 269, 16920-16924

110. Olivares, L., Aragon, C., Gimenez, C., and Zafra, F. (1995) *J Biol Chem* 270, 9437-9442

111. Tate, C. G., and Blakely, R. D. (1994) *J Biol Chem* 269, 26303-26310

112. Li, L. B., Chen, N., Ramamoorthy, S., Chi, L., Cui, X. N., Wang, L. C., and Reith, M. E. (2004) *J Biol Chem* 279, 21012-21020

113. Vaughan, R. A., Huff, R. A., Uhl, G. R., and Kuhar, M. J. (1997) *J Biol Chem* 272, 15541-15546

114. Batchelor, M., and Schenk, J. O. (1998) *J Neurosci* 18, 10304-10309

115. Foster, J. D., Pananusorn, B., and Vaughan, R. A. (2002) *J Biol Chem* 277, 25178-25186

116. Qian, Y., Galli, A., Ramamoorthy, S., Risso, S., DeFelice, L. J., and Blakely, R. D. (1997) *J Neurosci* 17, 45-57

117. Daniels, G. M., and Amara, S. G. (1999) *J Biol Chem* 274, 35794-35801

118. Granas, C., Ferrer, J., Loland, C. J., Javitch, J. A., and Gether, U. (2003) *J Biol Chem* 278, 4990-5000

119. Giambalvo, C. T., and Wagner, R. L. (1994) *J Neurochem* 63, 169-176

120. Mayfield, R. D., and Zahniser, N. R. (2001) *Mol Pharmacol* 59, 113-121

121. Blakely, R. D., and DeFelice, L. J. (2007) *Mol Pharmacol* 71, 1206-1208

122. Bolan, E. A., Kivell, B., Jaligam, V., Oz, M., Jayanthi, L. D., Han, Y., Sen, N., Urizar, E., Gomes, I., Devi, L. A., Ramamoorthy, S., Javitch, J. A., Zapata, A., and Shippenberg, T. S. (2007) *Mol Pharmacol* 71, 1222-1232

123. Lee, F. J., Pei, L., Moszczynska, A., Vukusic, B., Fletcher, P. J., and Liu, F. (2007) *EMBO J* 26, 2127-2136

124. Zapata, A., Kivell, B., Han, Y., Javitch, J. A., Bolan, E. A., Kuraguntla, D., Jaligam, V., Oz, M., Jayanthi, L. D., Samuvel, D. J., Ramamoorthy, S., and Shippenberg, T. S. (2007) *J Biol Chem* 282, 35842-35854

125. Deken, S. L., Beckman, M. L., Boos, L., and Quick, M. W. (2000) *Nat Neurosci* 3, 998-1003

126. Quick, M. W. (2003) *Neuron* 40, 537-549

127. Sung, U., Apparsundaram, S., Galli, A., Kahlig, K. M., Savchenko, V., Schroeter, S., Quick, M. W., and Blakely, R. D. (2003) *J Neurosci* 23, 1697-1709

128. Binda, F., Dipace, C., Bowton, E., Robertson, S. D., Lute, B. J., Fog, J. U., Zhang, M., Sen, N., Colbran, R. J., Gnegy, M. E., Gether, U., Javitch, J. A., Erreger, K., and Galli, A. (2008) *Mol Pharmacol* 74, 1101-1108

129. Ciccone, M. A., Timmons, M., Phillips, A., and Quick, M. W. (2008) *Neuropharmacology* 55, 763-770

130. Fog, J. U., Khoshbouei, H., Holy, M., Owens, W. A., Vaegter, C. B., Sen, N., Nikandrova, Y., Bowton, E., McMahon, D. G., Colbran, R. J., Daws, L. C., Sitte, H. H., Javitch, J. A., Galli, A., and Gether, U. (2006) *Neuron* 51, 417-429

131. Khoshbouei, H., Sen, N., Guptaroy, B., Johnson, L., Lund, D., Gnegy, M. E., Galli, A., and Javitch, J. A. (2004) *PLoS Biol* 2, E78

132. Gnegy, M. E., Khoshbouei, H., Berg, K. A., Javitch, J. A., Clarke, W. P., Zhang, M., and Galli, A. (2004) *Mol Pharmacol* 66, 137-143

133. Sorkina, T., Doolen, S., Galperin, E., Zahniser, N. R., and Sorkin, A. (2003) *J Biol Chem* 278, 28274-28283

134. Miranda, M., Sorkina, T., Grammatopoulos, T. N., Zawada, W. M., and Sorkin, A. (2004) *J Biol Chem* 279, 30760-30770

135. Farhan, H., Reiterer, V., Kriz, A., Hauri, H. P., Pavelka, M., Sitte, H. H., and Freissmuth, M. (2008) *J Cell Sci* 121, 753-761

136. Kilic, F., and Rudnick, G. (2000) *Proc Natl Acad Sci U S A* 97, 3106-3111

137. Schmid, J. A., Scholze, P., Kudlacek, O., Freissmuth, M., Singer, E. A., and Sitte, H. H. (2001) *J Biol Chem* 276, 3805-3810

138. Scholze, P., Freissmuth, M., and Sitte, H. H. (2002) *J Biol Chem* 277, 43682-43690

139. Lakowicz, J. R. (2006) *Principles of fluorescence spectroscopy*, 3rd ed., Springer, New York

140. Ivanov, V., Li, M., and Mizuuchi, K. (2009) *Biophys J* 97, 922-929

141. Just, H., Sitte, H. H., Schmid, J. A., Freissmuth, M., and Kudlacek, O. (2004) *J Biol Chem* 279, 6650-6657

142. Hastrup, H., Karlin, A., and Javitch, J. A. (2001) *Proc Natl Acad Sci U S A* 98, 10055-10060

143. Hastrup, H., Sen, N., and Javitch, J. A. (2003) *J Biol Chem* 278, 45045-45048

144. Bartholomaus, I., Milan-Lobo, L., Nicke, A., Dutertre, S., Hastrup, H., Jha, A., Gether, U., Sitte, H. H., Betz, H., and Eulenburg, V. (2008) *J Biol Chem* 283, 10978-10991

145. Torres, G. E., Yao, W. D., Mohn, A. R., Quan, H., Kim, K. M., Levey, A. I., Staudinger, J., and Caron, M. G. (2001) *Neuron* 30, 121-134

146. Gonzalez, M. I., and Robinson, M. B. (2004) *Curr Opin Pharmacol* 4, 30-35

147. Sitte, H. H., Farhan, H., and Javitch, J. A. (2004) *Mol Interv* 4, 38-47

148. Ozaslan, D., Wang, S., Ahmed, B. A., Kocabas, A. M., McCastlain, J. C., Bene, A., and Kilic, F. (2003) *J Biol Chem* 278, 43991-44000

149. Seidel, S., Singer, E. A., Just, H., Farhan, H., Scholze, P., Kudlacek, O., Holy, M., Koppatz, K., Krivanek, P., Freissmuth, M., and Sitte, H. H. (2005) *Mol Pharmacol* 67, 140-151

150. Scholze, P., Norregaard, L., Singer, E. A., Freissmuth, M., Gether, U., and Sitte, H. H. (2002) *J Biol Chem* 277, 21505-21513

151. Galli, A., Blakely, R. D., and DeFelice, L. J. (1998) *Proc Natl Acad Sci U S A* 95, 13260-13265

152. Henry, L. K., Defelice, L. J., and Blakely, R. D. (2006) *Neuron* 49, 791-796

153. DeFelice, L. J., Adams, S. V., and Ypey, D. L. (2001) *Biosystems* 62, 57-66

154. Su, A., Mager, S., Mayo, S. L., and Lester, H. A. (1996) *Biophys J* 70, 762-777

155. Jardetzky, O. (1966) *Nature* 211, 969-970

156. Doyle, D. A., Morais Cabral, J., Pfuetzner, R. A., Kuo, A., Gulbis, J. M., Cohen, S. L., Chait, B. T., and MacKinnon, R. (1998) *Science* 280, 69-77

157. Long, S. B., Campbell, E. B., and Mackinnon, R. (2005) *Science* 309, 897-903

158. Tate, C. G. (2001) *FEBS Lett* 504, 94-98

159. Teng, Q. (2005) *Structural biology : practical NMR applications*, Springer, New York

160. Zhang, Y. W., and Rudnick, G. (2006) *J Biol Chem* 281, 36213-36220

161. Norregaard, L., Loland, C. J., and Gether, U. (2003) *J Biol Chem* 278, 30587-30596

162. Chen, J. G., and Rudnick, G. (2000) *Proc Natl Acad Sci U S A* 97, 1044-1049

163. Smicun, Y., Campbell, S. D., Chen, M. A., Gu, H., and Rudnick, G. (1999) *J Biol Chem* 274, 36058-36064

164. Stephan, M. M., Chen, M. A., Penado, K. M., and Rudnick, G. (1997) *Biochemistry* 36, 1322-1328

165. Goldberg, N. R., Beuming, T., Soyer, O. S., Goldstein, R. A., Weinstein, H., and Javitch, J. A. (2003) *Eur J Pharmacol* 479, 3-12

166. Abramson, J., Smirnova, I., Kasho, V., Verner, G., Kaback, H. R., and Iwata, S. (2003) *Science* 301, 610-615

167. Yernool, D., Boudker, O., Jin, Y., and Gouaux, E. (2004) *Nature* 431, 811-818

168. Yamashita, A., Singh, S. K., Kawate, T., Jin, Y., and Gouaux, E. (2005) *Nature* 437, 215-223

169. Zhou, Z., Zhen, J., Karpowich, N. K., Goetz, R. M., Law, C. J., Reith, M. E., and Wang, D. N. (2007) *Science* 317, 1390-1393

170. Quick, M., Yano, H., Goldberg, N. R., Duan, L., Beuming, T., Shi, L., Weinstein, H., and Javitch, J. A. (2006) *J Biol Chem* 281, 26444-26454

171. Forrest, L. R., Tavoulari, S., Zhang, Y. W., Rudnick, G., and Honig, B. (2007) *Proc Natl Acad Sci U S A* 104, 12761-12766

172. Zomot, E., Bendahan, A., Quick, M., Zhao, Y., Javitch, J. A., and Kanner, B. I. (2007) *Nature* 449, 726-730

173. Singh, S. K., Piscitelli, C. L., Yamashita, A., and Gouaux, E. (2008) *Science* 322, 1655-1661

174. Singh, S. K., Yamashita, A., and Gouaux, E. (2007) *Nature* 448, 952-956

175. Screpanti, E., and Hunte, C. (2007) *J Struct Biol* 159, 261-267

176. Field, J. R., Henry, L. K., and Blakely, R. D. *J Biol Chem* 285, 11270-11280

177. Gedeon, P. C., Indarte, M., Surratt, C. K., and Madura, J. D. *Proteins* 78, 797-811

178. Kaufmann, K. W., Dawson, E. S., Henry, L. K., Field, J. R., Blakely, R. D., and Meiler, J. (2009) *Proteins* 74, 630-642

179. Sinning, S., Musgaard, M., Jensen, M., Severinsen, K., Celik, L., Koldso, H., Meyer, T., Bols, M., Jensen, H. H., Schiott, B., and Wiborg, O. *J Biol Chem* 285, 8363-8374

180. Wein, T., and Wanner, K. T. (2009) *J Mol Model*

181. Kniazeff, J., Shi, L., Loland, C. J., Javitch, J. A., Weinstein, H., and Gether, U. (2008) *J Biol Chem* 283, 17691-17701

182. Beuming, T., Kniazeff, J., Bergmann, M. L., Shi, L., Gracia, L., Raniszewska, K., Newman, A. H., Javitch, J. A., Weinstein, H., Gether, U., and Loland, C. J. (2008) *Nat Neurosci* 11, 780-789

183. Krishnamurthy, H., Piscitelli, C. L., and Gouaux, E. (2009) *Nature* 459, 347-355

184. Shimamura, T., Weyand, S., Beckstein, O., Rutherford, N. G., Hadden, J. M., Sharples, D., Sansom, M. S., Iwata, S., Henderson, P. J., and Cameron, A. D. *Science* 328, 470-473

185. Weyand, S., Shimamura, T., Yajima, S., Suzuki, S., Mirza, O., Krusong, K., Carpenter, E. P., Rutherford, N. G., Hadden, J. M., O'Reilly, J., Ma, P., Saidijam, M., Patching, S. G., Hope, R. J., Norbertczak, H. T., Roach, P. C., Iwata, S., Henderson, P. J., and Cameron, A. D. (2008) *Science* 322, 709-713

186. Faham, S., Watanabe, A., Besserer, G. M., Cascio, D., Specht, A., Hirayama, B. A., Wright, E. M., and Abramson, J. (2008) *Science* 321, 810-814

187. Forrest, L. R., Zhang, Y. W., Jacobs, M. T., Gesmonde, J., Xie, L., Honig, B. H., and Rudnick, G. (2008) *Proc Natl Acad Sci U S A* 105, 10338-10343

188. Shi, L., Quick, M., Zhao, Y., Weinstein, H., and Javitch, J. A. (2008) *Mol Cell* 30, 667-677

189. Quick, M., Winther, A. M., Shi, L., Nissen, P., Weinstein, H., and Javitch, J. A. (2009) *Proc Natl Acad Sci U S A* 106, 5563-5568

190. Karpowich, N. K., and Wang, D. N. (2008) *Science* 321, 781-782

191. Cuello, L. G., Cortes, D. M., and Perozo, E. (2004) *Science* 306, 491-495

192. Jiang, Y., Lee, A., Chen, J., Ruta, V., Cadene, M., Chait, B. T., and MacKinnon, R. (2003) *Nature* 423, 33-41

193. Weil, J. A., Bolton, J. R., and Wertz, J. E. (1994) *Electron paramagnetic resonance : elementary theory and practical applications*, Wiley, New York

194. Carrington, A., & McLachlan, A.D. . (1967) *Introduction to magnetic resonance with applications to chemistry and chemical physics*, Harper & Row, Inc., New York

195. Van Horn, W. D., Kim, H. J., Ellis, C. D., Hadziselimovic, A., Sulistijo, E. S., Karra, M. D., Tian, C., Sonnichsen, F. D., and Sanders, C. R. (2009) *Science* 324, 1726-1729

196. Hubbell, W. L., Cafiso, D. S., and Altenbach, C. (2000) *Nat Struct Biol* 7, 735-739

197. Hubbell, W. L., McHaourab, H. S., Altenbach, C., and Lietzow, M. A. (1996) *Structure* 4, 779-783

198. Berliner, L. J. (1976) *Spin labeling : theory and applications*, Academic Press, New York

199. Berliner, L. J. (1979) *Spin labeling II : theory and applications*, Academic Press, New York

200. Eaton, S. S., Eaton, G. R., and Berliner, L. J. (2004) *Biomedical EPR*, Kluwer Academic/Plenum Publishers, New York

201. Fleissner, M. R., Brustad, E. M., Kalai, T., Altenbach, C., Cascio, D., Peters, F. B., Hideg, K., Peuker, S., Schultz, P. G., and Hubbell, W. L. (2009) *Proc Natl Acad Sci U S A* 106, 21637-21642

202. Mchaourab, H. S., Lietzow, M. A., Hideg, K., and Hubbell, W. L. (1996) *Biochemistry* 35, 7692-7704

203. Columbus, L., and Hubbell, W. L. (2002) *Trends Biochem Sci* 27, 288-295

204. Columbus, L., Kalai, T., Jeko, J., Hideg, K., and Hubbell, W. L. (2001) *Biochemistry* 40, 3828-3846

205. Mchaourab, H. S., Kalai, T., Hideg, K., and Hubbell, W. L. (1999) *Biochemistry* 38, 2947-2955

206. Volkov, A., Dockter, C., Bund, T., Paulsen, H., and Jeschke, G. (2009) *Biophys J* 96, 1124-1141

207. Altenbach, C., Froncisz, W., Hemker, R., McHaourab, H., and Hubbell, W. L. (2005) *Biophys J* 89, 2103-2112

208. Claxton, D. P., Zou, P., and McHaourab, H. S. (2008) *J Mol Biol* 375, 1026-1039

209. Hubbell, W. L., Gross, A., Langen, R., and Lietzow, M. A. (1998) *Curr Opin Struct Biol* 8, 649-656

210. Dong, J., Yang, G., and McHaourab, H. S. (2005) *Science* 308, 1023-1028

211. Zou, P., and McHaourab, H. S. (2009) *J Mol Biol* 393, 574-585

212. Alexander, N., Bortolus, M., Al-Mestarihi, A., McHaourab, H., and Meiler, J. (2008) *Structure* 16, 181-195

213. Borbat, P. P., Surendhran, K., Bortolus, M., Zou, P., Freed, J. H., and McHaourab, H. S. (2007) *PLoS Biol* 5, e271

214. Berliner, L. J., Eaton, G. R., and Eaton, S. S. (2000) *Distance measurements in biological systems by EPR*, Kluwer Academic/Plenum Publishers, New York

215. Rabenstein, M. D., and Shin, Y. K. (1995) *Proc Natl Acad Sci U S A* 92, 8239-8243

216. Hustedt, E. J., Stein, R. A., Sethaphong, L., Brandon, S., Zhou, Z., and Desensi, S. C. (2006) *Biophys J* 90, 340-356

217. McHaourab, H. S., Oh, K. J., Fang, C. J., and Hubbell, W. L. (1997) *Biochemistry* 36, 307-316

218. Steinhoff, H. J., Radzwill, N., Thevis, W., Lenz, V., Brandenburg, D., Antson, A., Dodson, G., and Wollmer, A. (1997) *Biophys J* 73, 3287-3298

219. Jeschke, G. (2002) *Chemphyschem* 3, 927-932

220. Jeschke, G., Wegener, C., Nietschke, M., Jung, H., and Steinhoff, H. J. (2004) *Biophys J* 86, 2551-2557

221. Chiang, Y. W., Borbat, P. P., and Freed, J. H. (2005) *J Magn Reson* 172, 279-295

222. Zou, P., Surendhran, K., and McHaourab, H. S. (2007) *Biophys J* 92, L27-29

223. Zou, P., Bortolus, M., and McHaourab, H. S. (2009) *J Mol Biol* 393, 586-597

224. Bridges, M. D., Hideg, K., and Hubbell, W. L. *Appl Magn Reson* 37, 363

225. Altenbach, C., Kusnetzow, A. K., Ernst, O. P., Hofmann, K. P., and Hubbell, W. L. (2008) *Proc Natl Acad Sci U S A* 105, 7439-7444

226. Smirnova, I., Kasho, V., Choe, J. Y., Altenbach, C., Hubbell, W. L., and Kaback, H. R. (2007) *Proc Natl Acad Sci U S A* 104, 16504-16509

227. Ward, A., Reyes, C. L., Yu, J., Roth, C. B., and Chang, G. (2007) *Proc Natl Acad Sci U S A* 104, 19005-19010

228. Quick, M., and Javitch, J. A. (2007) *Proc Natl Acad Sci U S A* 104, 3603-3608

229. Owenius, R., Engstrom, M., Lindgren, M., and Huber, M. (2001) *The Journal of Physical Chemistry A* 105, 10967-10977

230. Celik, L., Schiott, B., and Tajkhorshid, E. (2008) *Biophys J* 94, 1600-1612

231. Harwood, A. J., and Agam, G. (2003) *Biochem Pharmacol* 66, 179-189

232. Treiser, S. L., Cascio, C. S., O'Donohue, T. L., Thoa, N. B., Jacobowitz, D. M., and Kellar, K. J. (1981) *Science* 213, 1529-1531

233. Ni, Y. G., Chen, J. G., Androutsellis-Theotokis, A., Huang, C. J., Moczydlowski, E., and Rudnick, G. (2001) *J Biol Chem* 276, 30942-30947

234. Meinild, A. K., Loo, D. D., Skovstrup, S., Gether, U., and MacAulay, N. (2009) *J Biol Chem* 284, 16226-16235

235. MacAulay, N., Zeuthen, T., and Gether, U. (2002) *J Physiol* 544, 447-458

236. Zhou, Y., Zomot, E., and Kanner, B. I. (2006) *J Biol Chem* 281, 22092-22099

237. Noskov, S. Y., and Roux, B. (2008) *J Mol Biol* 377, 804-818

238. Caplan, D. A., Subbotina, J. O., and Noskov, S. Y. (2008) *Biophys J* 95, 4613-4621

239. Torres-Altoro, M. I., Kuntz, C. P., Nichols, D. E., and Barker, E. L. *J Biol Chem* 285, 15369-15379

240. Torres-Altoro, M. I., White, K. J., Rodriguez, G. J., Nichols, D. E., and Barker, E. L. (2008) *Protein Sci* 17, 1761-1770

241. Mitchell, S. M., Lee, E., Garcia, M. L., and Stephan, M. M. (2004) *J Biol Chem* 279, 24089-24099

242. Zomot, E., and Kanner, B. I. (2003) *J Biol Chem* 278, 42950-42958